TECHNISCHE UNIVERSITÄT MÜNCHEN
Lehrstuhl für Carbon Composites

Multiscale Analysis of the Mechanical Response of Triaxial Braided Composites

Tobias Wehrkamp-Richter

Vollständiger Abdruck der von der Fakultät für Maschinenwesen der Technischen Universität München zur Erlangung des akademischen Grades eines

Doktor-Ingenieurs

genehmigten Dissertation.

Vorsitzender:	Prof. Dr.-Ing. Wolfram Volk
Prüfer der Dissertation:	Prof. Dr.-Ing. Klaus Drechsler
	Prof. Silvestre T. Pinho, Ph.D.
	(Imperial College London, Vereinigtes Königreich)

Die Dissertation wurde am 28.02.2018 bei der Technischen Universität München eingereicht und durch die Fakultät für Maschinenwesen am 19.06.2018 angenommen.

Technische Universität München
Fakultät für Maschinenwesen
Lehrstuhl für Carbon Composites
Boltzmannstraße 15
D-85748 Garching bei München

Tel.:+ 49 (0) 89 / 289 - 15092
Fax: + 49 (0) 89 / 289 - 15097
Email: info@lcc.mw.tum.de
Web: www.lcc.mw.tum.de

Declaration

Ich erkläre hiermit ehrenwörtlich, dass ich die vorliegende Arbeit selbstständig und ohne Benutzung anderer als der angegebenen Hilfsmittel angefertigt habe; die aus fremden Quellen (einschließlich elektronischer Quellen) direkt oder indirekt übernommenen Gedanken sind ausnahmslos als solche kenntlich gemacht.

Die Arbeit wurde in gleicher oder ähnlicher Form noch keiner anderen Prüfungsbehörde vorgelegt.

.....	.....
Ort, Datum	Unterschrift

Acknowledgements

I would like to thank my academic supervisor Prof. Dr.-Ing. Klaus Drechsler for giving me the opportunity to work on this thesis and for providing the research environment that enabled this work.

I want to express my deepest gratitude to Prof. Silvestre T. Pinho for his continuous support and academic supervision throughout this thesis. He has been an excellent mentor and a source of invaluable expertise way beyond my research visit at Imperial College London.

Equally, I would like to thank Dr. Nelson V. De Carvalho for his guidance despite the large physical distance.

I would like to thank my colleagues and friends at LCC for making this work such an enjoyable experience: Jörg Cichosz, Jonathan Ölhafen, Roland Hinterhölzl and Johannes Neumayer to name a few. During my time in London, I had the pleasure of meeting many outstanding colleagues who quickly became friends: André Wilmes, Luigi Gigliotti and Gaël Grail.

I am very much indebted to Prof. Dr.-Ing. Jörg Middendorf for his academic guidance. His kind support and teaching had a major impact on my decision to pursue a career in the field of composites.

Most importantly, I wish to thank my family for their encouragement and for making my thesis possible.

Nothing is impossible. Not if you can imagine it. That's what being a scientist is all about.

Professor Hubert J. Farnsworth

Abstract

New lightweight materials, such as carbon fibre reinforced plastics (CFRP) allow a significant reduction in structural weight. Specifically in high-volume production areas, such as the automotive industry, current manufacturing technologies face a twofold challenge: cost and cycle time. State-of-the-art composite braiding features a highly automated and reproducible process combined with an excellent rate of material deposition for mass-production at minimum waste, making it extremely economic. As a result of deficient design experience and sizing methods for braided composites, engineers rely on approaches developed for traditional unidirectional composites. However, such a methodology cannot be applied to highly non-linear problems, such as impact and crash, where the material exhibits a complex failure behaviour as a result of its inherent textile nature including out-of-plane waviness, interacting fibre bundles, and nesting of compacted plies.

In this work, a high-fidelity simulation framework for virtually predicting the non-linear mechanical response of triaxial braided composites is developed. In the first step, multiple braid architectures are investigated experimentally in order to understand the driving mechanisms of damage initiation and propagation. Subsequently, meso-scale finite element unit cell models with a realistic internal geometry are generated through an automated simulation work-flow by explicitly modelling the manufacturing process: after resolving initial interpenetration by means of a fictitious thermal step, a compaction simulation is performed to the desired target fibre volume fraction. For improved computational efficiency, special out-of-plane periodic boundary conditions allow an implicit consideration of the compaction of multiple braid plies in different nesting configurations. After validating the simulation framework against experimental data in terms of internal geometry, elastic properties, non-linear behaviour and damage morphology, the material response is predicted under variable uni-axial off-axis load cases. Finally, the effect of the textile topology on the ultimate strength of the material is investigated.

Kurzfassung

Der Einsatz neuer Leichtbauwerkstoffe, wie beispielsweise Faserverbundwerkstoffe, findet aufgrund von potentiellen Gewichtseinsparungen ein immer breiteres Anwendungsfeld. Jedoch stellen hohe Produktionsvolumina, wie beispielsweise in der Automobilindustrie, heutige Fertigungstechnologien hinsichtlich Kosten und Zykluszeiten vor große Herausforderungen. Dort gewinnen textile Preformverfahren, darunter insbesondere das Flechten mit seinem hohen Automatisierungspotential, hohen Ablegeraten und geringem Materialverschnitt, immer mehr an Bedeutung.

Gleichzeitig erfordert die dabei entstehende textile Faserarchitektur eine komplexere und weitreichendere strukturmechanische Betrachtung als bei vergleichbaren unidirektional verstärkten Laminaten. Für einen robusten Einsatz in hochgradig nichtlinearen Anwendungen, wie beispielsweise Fahrzeugcrash, ist eine Berechnungsmethodik zur Vorhersage des komplexen Werkstoffverhaltens, welches durch Faserwelligkeiten, Interaktion von Faserbündeln, starker Heterogenität und dem Kompaktierungsverhalten einzelner Lagen beeinflusst wird, zwingend erforderlich.

In der vorliegenden Arbeit wird eine Berechnungsmethodik zur Vorhersage des nichtlinearen Konstitutivverhaltens von Triaxialgeflechten entwickelt. In einem ersten Schritt wird dazu das Versagensverhalten mehrerer Geflechtarchitekturen experimentell untersucht. Anschließend wird eine Methodik entwickelt, um mesoskopische finite Elemente Einheitszellenmodelle automatisiert zu erstellen. Eine realistische Vorhersage der defektbehafteten textilen Geometrie wird durch eine explizite Abbildung des Fertigungsprozesses mithilfe von Kompaktierungssimulationen erreicht. Der Einsatz von periodischen Randbedingungen ermöglicht eine implizite Betrachtung des Kompaktierungsverhaltens von Geflechten in verschiedenen Ablagekonfigurationen bei minimaler Rechenzeit. Nach einer umfangreichen Validierung der Vorhersagegüte hinsichtlich textiler Geometrie, Steifigkeit, nichtlinearem Verhalten und zugehörigen Schägdigungsmechanismen, findet eine Vorhersage des Materials unter variablen Belastungszuständen statt. Abschließend wird der Einfluss der textilen Architektur auf die Festigkeit untersucht.

Table of Contents

List of Figures

List of Tables

Nomenclature

Symbols

Lower case Roman letters

a_{12}	(MPa)	non-linear shear hardening parameter
a_2	(MPa)	non-linear transverse hardening parameter
b_{12}	-	non-linear shear hardening parameter
b_2	-	non-linear transverse hardening parameter
c	-	crimp factor
c_{12}	-	non-linear shear hardening parameter
c_2	-	non-linear transverse hardening parameter
d		scalar damage variable
$d_{\mathrm{f,kink}}$	-	damage variable (fibre kinking)
$d_{\mathrm{f,split}}$	-	damage variable (fibre splitting)
$d_{\mathrm{f,t}}$	-	damage variable (fibre tensile)
d_{M}	(mm)	mandrel diameter
d_{mat}	-	damage variable (matrix cracking)
f_{hg}	(1/s)	horn gear frequency
h_{rUC}	(μm)	reduced unit cell height
h_{u}	(μm)	braid yarn undulation amplitude
k_{f}	-	load proportional stiffness factor
l_{char}	(μm)	characteristic material length
l_{cycle}	(mm)	projected axial length of yarn during a full carrier rotation
$l_{\mathrm{F,yarn}}$	(mm)	yarn length
l_{M}	(mm)	mandrel length
l_{mesh}	(μm)	average finite element length
m_{F}	(to)	total fibre mass
$m_{\mathrm{F,a}}$	(to)	total axial yarn fibre mass
$m_{\mathrm{F,b}}$	(to)	total braid yarn fibre mass
$m_{\mathrm{F,yarn}}$	(to)	single yarn fibre mass

$m_{\mathrm{F,yarn,a}}$	(to)	single axial yarn fibre mass
$m_{\mathrm{F,yarn,b}}$	(to)	single braid yarn fibre mass
n_{a}	-	axial yarn cross-sectional shape exponent
n_{b}	-	braid yarn cross-sectional shape exponent
r	-	bi-linear softening strength ratio
s_{a}	(μm)	axial yarn spacing
s_{b}	(μm)	braid yarn spacing
t	(μm)	thickness
$\mathbf{t}$	(MPa)	nominal traction vector
t_{a}	(μm)	axial yarn thickness
t_{b}	(μm)	braid yarn thickness
t_{biax}	(μm)	average biaxial ply thickness
t_{crit}	(μm)	critical contact cut-off thickness for cohesive mesh
t_{F}	(μm)	homogenised fibre volume thickness
$t_{\mathrm{F,a}}$	(μm)	axial yarn homogenised fibre volume thickness
$t_{\mathrm{F,b}}$	(μm)	braid yarn homogenised fibre volume thickness
t_{lam}	(mm)	total laminate thickness
t_{m}	(μm)	matrix pockets thickness
$\bar{t}_{\mathrm{rUC,c}}$	(μm)	average compacted reduced unit cell ply thickness
t_{triax}	(μm)	average triaxial ply thickness
$\mathbf{u}(A)$	(μm)	displacement field of equivalent points at a periodic boundary expressed by coordinate vector A
$\mathbf{u}(\hat{A})$	(μm)	displacement field of equivalent points at a periodic boundary expressed by coordinate vector $\hat{A}$
v_{M}	(mm/s)	mandrel take-up velocity
w_{a}	(μm)	axial yarn width
w_{b}	(μm)	braid yarn width
$w_{\mathrm{b,min}}$	(μm)	minimum braid yarn width
$w_{\mathrm{b,max}}$	(μm)	maximum braid yarn width
w_{rUC}	(μm)	reduced unit cell width
$\mathbf{x}^{\mathbf{O}_{\hat{\mathbf{E}}}}$	(μm)	unit cell translation vector
t_{n}	(MPa)	normal traction component
t_{shear}	(MPa)	effective shear traction component

Upper case Roman letters

A_{a}	(mm^2)	axial yarn cross-sectional area
A_{b}	(mm^2)	braid yarn cross-sectional area

A_{biax}	(mm^2)	minimum size biaxial braid unit cell surface area
A_{F}	(mm^2)	homogenised fibre volume cross-sectional area
$A_{\mathrm{F,yarn}}$	(mm^2)	single yarn fibre cross-sectional area
$A_{\mathrm{F,yarn,a}}$	(mm^2)	single axial yarn fibre cross-sectional area
$A_{\mathrm{F,yarn,b}}$	(mm^2)	single braid yarn fibre cross-sectional area
A_{M}	(mm^2)	mandrel surface area
A_{sf}	($\mu\mathrm{m}^2$)	single fibre cross-sectional area
A_{triax}	(mm^2)	minimum size triaxial braid unit cell surface area
A_{u}	(mm^2)	minimum size biaxial braid unit cell uncovered surface area
$A_{\mathrm{u,1}}$	(mm^2)	minimum size triaxial braid unit cell uncovered surface area zone 1
$A_{\mathrm{u,2}}$	(mm^2)	minimum size triaxial braid unit cell uncovered surface area zone 2
$A_{\mathrm{u,3}}$	(mm^2)	minimum size triaxial braid unit cell uncovered surface area zone 3
A_{yarn}	(mm^2)	single yarn cross-sectional area
$\mathbf{C}$	(MPa)	elasticity tensor
CF	(%)	cover factor
CF_{biax}	(%)	biaxial braid cover factor
CF_{triax}	(%)	triaxial braid cover factor
E_1	(MPa)	axial secant modulus
E_0	(MPa)	initial elastic modulus in cycle 0
$E_{\mathrm{1,c}}$	(MPa)	yarn axial Young's modulus (compression)
$E_{\mathrm{1,c,lin}}$	(MPa)	linear axial Young's modulus (compression)
$E_{\mathrm{1,t}}$	(MPa)	yarn axial Young's modulus (tension)
$E_{\mathrm{1,t,lin}}$	(MPa)	linear axial Young's modulus (tension)
$E_{\mathrm{1f,c}}$	(MPa)	fibre axial Young's modulus (compression)
$E_{\mathrm{1f,t}}$	(MPa)	fibre axial Young's modulus (tension)
E_2	(MPa)	yarn transverse Young's modulus
E_2^{nl}	(MPa)	non-linear transverse secant modulus (2 direction)
E_{2f}	(MPa)	fibre transverse Young's modulus
E_3^{nl}	(MPa)	non-linear transverse secant modulus (3 direction)
E_{i}	(MPa)	unloading modulus in cycle i
E_{m}	(MPa)	matrix Young's modulus
$\mathbf{F}$	-	deformation gradient tensor
FAW	($\mathrm{g/m}^2$)	fibre areal weight
FAW_{biax}	($\mathrm{g/m}^2$)	biaxial braid fibre areal weight
FAW_{triax}	($\mathrm{g/m}^2$)	triaxial braid fibre areal weight

$FI_{\mathrm{f,kink}}$	-	failure index (fibre kinking)
$FI_{\mathrm{f,split}}$	-	failure index (fibre splitting)
$FI_{\mathrm{f,t}}$	-	failure index (fibre tensile)
FI_{mat}	-	failure index (matrix cracking)
G_{12}	(MPa)	yarn in-plane shear modulus
G_{12}^{nl}	(MPa)	non-linear shear secant modulus (12 direction)
$G_{12\mathrm{f}}$	(MPa)	fibre in-plane shear modulus
G_{13}^{nl}	(MPa)	non-linear shear secant modulus (13 direction)
G_{23}	(MPa)	yarn out-of-plane shear modulus
$G_{23\mathrm{f}}$	(MPa)	fibre out-of-plane shear modulus
G_{Ic}	(J/m^2)	interlaminar fracture toughness (Mode I)
$G_{\mathrm{Ic}}^{\mathrm{f,kink}}$	(J/m^2)	interlaminar fracture toughness (fibre kinking)
$G_{\mathrm{Ic}}^{\mathrm{f,t}}$	(J/m^2)	intralaminar fracture toughness (fibre tensile)
$G_{\mathrm{Ic}}^{\mathrm{m}}$	(J/m^2)	intralaminar fracture toughness (matrix Mode I)
G_{IIc}	(J/m^2)	interlaminar fracture toughness (Mode II)
$G_{\mathrm{IIc}}^{\mathrm{m}}$	(J/m^2)	interlaminar fracture toughness (matrix Mode II)
$\mathbf{I}$	(mm^4)	second area moment tensor
K_{n}	(N/mm^3)	interface normal stiffness
K_{shear}	(N/mm^3)	interface shear stiffness
L_{u}	(μm)	projected braid yarn undulation length
$L_{\mathrm{u'}}$	(μm)	curved braid yarn undulation length
N	(MPa)	interface normal strength
N_{c}	-	braid yarn carrier number
N_{F}	-	yarn fibre count
$N_{\mathrm{F,a}}$	-	axial yarn fibre count
$N_{\mathrm{F,b}}$	-	braid yarn fibre count
N_{hg}	-	horn gear number
S	(MPa)	interface shear strength
S_{L}	(MPa)	yarn in-plane shear strength
S_{T}	(MPa)	yarn out-of-plane shear strength
$\mathbf{T}$	-	transformation matrix
$\mathbf{T}_{\psi}$	-	transformation matrix for off-axis loading
T_{cycle}	(s)	full carrier rotation cycle time
T_{hg}	(s)	half horn gear rotation cycle time
U_{M}	(mm)	mandrel circumference
V	(μm^3)	volume
V_{a}	(μm^3)	axial yarn volume
V_{b}	(μm^3)	braid yarn volume

V_{F}	(μm^3)	fibre volume
$V_{\mathrm{F,a}}$	(μm^3)	axial yarn fibre volume
$V_{\mathrm{F,b}}$	(μm^3)	axial yarn fibre volume
$V_{\mathrm{F,yarn}}$	(μm^3)	single yarn fibre volume
V_{m}	(μm^3)	matrix pockets volume
V_{yarn}	(μm^3)	single yarn volume
X_{c}	(MPa)	yarn axial compressive strength
X_{t}	(MPa)	yarn axial tensile strength
Y_{c}	(MPa)	yarn transverse compressive strength
Y_{t}	(MPa)	yarn transverse tensile strength

Greek letters

Γ^{mat}	(J/m^2)	mixed-mode fracture toughness on the fracture surface
$\Gamma^{\mathrm{mat}}_{\mathrm{init}}$	(J/m^2)	mixed-mode initiation fracture toughness on the fracture surface
$\Gamma^{\mathrm{mat}}_{\mathrm{prop}}$	(J/m^2)	mixed-mode propagation fracture toughness on the fracture surface
α	($^\circ$)	matrix cracking fracture angle
α_0	($^\circ$)	matrix cracking fracture angle under pure transverse compression
α_{a}	($^\circ$)	axial yarn twist angle
α_{b}	($^\circ$)	braid yarn twist angle
α_{i}	$1/K$	coefficient of thermal expansion in direction $i = 1, 2, 3$
α_{pl}	($^\circ$)	power law coefficient
γ	-	load reversal factor
δ_{n}	μm	interface normal displacement
δ_{shear}	μm	interface effective shear displacement
$\boldsymbol{\varepsilon}$	-	strain tensor
$\boldsymbol{\varepsilon}_{\mathrm{pl}}$	-	plastic strain tensor
$\varepsilon_{\mathrm{el}}$	-	elastic strain
$\varepsilon_{\mathrm{eq}}$	-	irreversible equivalent strain
$\varepsilon^{\mathrm{max}}_{\mathrm{eq}}$	-	maximum irreversible equivalent strain over time
ε^{0}	-	onset failure strain
ε^{i}	-	intermediate failure strain
ε^{f}	-	final failure strain
$\langle\varepsilon\rangle$	-	homogenised strain
$\langle\varepsilon_{\mathrm{i}}\rangle$	-	homogenised strain in cycle i

$\langle \varepsilon_{\mathrm{ie,i}} \rangle$	-	accumulated inelastic strain in cycle i
ζ	(%)	braid yarn relative non-undulating length
η_{L}	-	longitudinal friction coefficient
η_{T}	-	transverse friction coefficient
θ	(°)	braiding angle
κ	(%)	intra-yarn fibre volume fraction (packing density)
κ_{a}	(%)	axial yarn intra-yarn fibre volume fraction (packing density)
κ_{b}	(%)	braid yarn intra-yarn fibre volume fraction (packing density)
$\mu_{F,yarn}$	(tex)	linear yarn density
$\mu_{F,yarn,a}$	(tex)	axial yarn linear yarn density
$\mu_{F,yarn,b}$	(tex)	braid yarn linear yarn density
ν_{12}	-	yarn in-plane Poisson's ratio
$\nu_{12\mathrm{f}}$	-	fibre in-plane Poisson's ratio
ν_{23}	-	yarn out-of-plane Poisson's ratio
$\nu_{23\mathrm{f}}$	-	fibre out-of-plane Poisson's ratio
ν_{m}	-	matrix Poisson's ratio
ξ_{a}	(%)	axial yarn relative side run-out thickness
ξ_{b}	(%)	braid yarn relative side run-out thickness
ρ_{F}	(to/mm^3)	volumetric fibre density
$\rho_{\mathrm{F,a}}$	(to/mm^3)	axial yarn volumetric fibre density
$\rho_{\mathrm{F,b}}$	(to/mm^3)	braid yarn volumetric fibre density
$\boldsymbol{\sigma}$	(MPa)	stress tensor
σ_{ψ}	(MPa)	applied stress under uni-axial loading at an off-axis angle ψ
σ_{i}	(MPa)	maximum nominal stress in cycle i
σ^0_{mat}	(MPa)	effective traction acting on the fracture surface at matrix cracking failure onset
σ_{N}	(MPa)	normal traction component acting on the fracture plane
σ^0_{N}	(MPa)	normal traction component acting on the fracture plane at failure onset
σ_{yield}	(MPa)	von Mises yield stress
τ_{L}	(MPa)	shear traction (L) component acting on the fracture plane
τ^0_{L}	(MPa)	shear traction (L) component acting on the fracture plane at failure onset
τ_{T}	(MPa)	shear traction (T) component acting on the fracture plane
τ^0_{T}	(MPa)	shear traction (T) component acting on the fracture plane at failure onset
φ_{F}	(%)	global fibre volume fraction
$\varphi_{\mathrm{F,rUC}}$	(%)	reduced unit cell global fibre volume fraction

ψ	(°)	off-axis angle
ω	(μm)	braid yarn localised phase shift (positive or negative)
ω_{hg}	rad/s	horn gear angular speed

Coordinate systems

x,y,z	cartesian coordinate system aligned with the axial yarn (take-up) direction
$1F$,$2F$,$3F$	cartesian coordinate system aligned with the braid yarn direction
$1\psi, 2\psi, 3\psi$	cartesian coordinate system aligned with the off-axis loading direction
x_{a},y_{a},z_{a}	cartesian coordinate system with respect to the axial yarn path
x_{b},y_{b},z_{b}	cartesian coordinate system with respect to the braid yarn path
x'_{a},y'_{a},z'_{a}	cartesian coordinate system with respect to the cross-section area centroid of axial yarns
x'_{b},y'_{b},z'_{b}	cartesian coordinate system with respect to the cross-section area centroid of braid yarns
1a,2a,3a	cartesian coordinate system aligned with the local axial fibre direction
1b,2b,3b	cartesian coordinate system aligned with the local braid fibre direction

Mathematical operators

$\langle \bullet \rangle$	homogenised property
$\langle \bullet \rangle_+$	McCauley brackets $\langle x \rangle_+ = \max\{0, x\}$

Abbreviations

μCT	micro-computed tomography
API	application programming interface
ASTM	american society for testing and materials
CAD	computer aided design
CFRP	carbon fibre reinforced plastics
CLT	classical lamination theory
CSYS	coordinate system

DIC	digital image correlation
FE	finite-element
FVF	fibre volume fraction
HT	high tenacity
PBCs	periodic boundary conditions
RTM	resin transfer moulding
rUC	reduced unit cell
RVE	representative volume element
UC	unit cell
VAP	vacuum membrane assisted process
CV	coefficient of variation
STDV	standard deviation
UD	unidirectional
WWFE	world wide failure exercise

1 Introduction

1.1 Motivation

Applying new lightweight materials, such as carbon fibre reinforced plastics (CFRP) allows a significant reduction in structural weight and carbon dioxide emissions. Specifically in high-volume production areas, such as the automotive industry, current manufacturing technologies face a twofold challenge: cost and cycle time. State-of-the-art composite braiding features a highly automated and reproducible process combined with an excellent rate of material deposition for mass-production at minimum waste, making it extremely economic. Yarns of several thousand carbon fibres are intertwined and positioned on a mandrel to produce geometries with variable cross-sections which can subsequently be infused with a polymer resin. Triaxial braids comprise an integrated structure of yarns oriented in three in-plane directions, which makes them a well-suited choice for multi-axial loading. Their natural through-thickness reinforcement promises excellent specific energy absorption characteristics in combination with a high degree of delamination resistance. Following the increasing usage of composites in general, braiding has recently received particular attention from the automotive industry. In addition to applications in the chassis of current electric vehicle platforms, such as the i3 or i8, BMW has implemented a braided A pillar structure in their latest 7-series (G12), as is shown in Fig. 1.1.

As a result of deficient design experience and sizing methods for braided composites, engineers rely on approaches developed for traditional unidirectional composites. Safety critical aerospace composite parts for example are typically not sized to experience cracking in-service. In case textile composites are used, empirical knock-down or safety factors on stiffness and strength can be incorporated during the design phase in order to account for the textile architecture. However, such a methodology cannot be applied to highly non-linear problems, such as determining the catastrophic failure load of a structure or simulating its impact and crash behaviour. Since the material exhibits a complex failure and damage behaviour as a result of its inherent textile nature with its out-of-plane waviness, interacting fibre

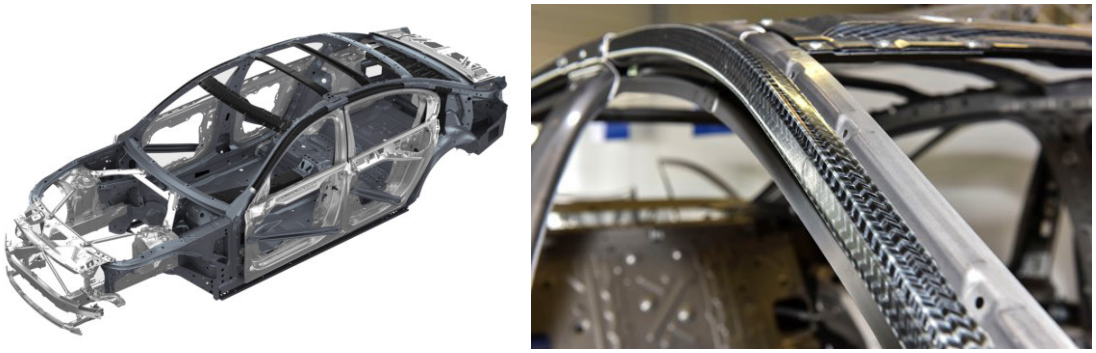

(a) (b)

Fig. 1.1: Application of triaxial braided composites in the automotive industry (a) Body-in-White (BiW) of the G12 BMW 7-series (b) braided A pillar

bundles, resin pockets, and nesting of compacted plies, the constitutive response experiences significant non-linearity before final failure. Additionally, the textile architecture can vary significantly on a composite component with a multitude of parameters effecting the material properties, such as braiding angle, yarn geometry, waviness, and fibre volume fraction. Hence, the determination of robust material properties by experimental test campaigns is highly cost- and time-intensive. The experimental characterisation of a single material configuration may easily produce costs of up to 100,000 € and take up several months.

1.2 Thesis scope

The primary aim of this thesis is to develop a high-fidelity simulation tool for virtually predicting the non-linear mechanical response of triaxial braided composites. Therefore, following a detailed literature study in chapter 2, a modelling strategy was developed, which is outlined in Fig. 1.2. In the first step, multiple braid architectures are investigated experimentally under multi-axial stress states. Digital image correlation measurement (DIC) techniques and a high-speed camera are used to quantify the effects of the textile architecture and its heterogeneity on the surface strain fields, to identify and locate constituent failure mechanisms and to understand the physics of damage initiation and propagation as a basis for modelling in chapter 3. With the the driving physical mechanisms behind the material non-linearity identified, a meso-scale simulation framework is developed in chapter 4 which generates unit cell models of triaxial braided composites with a realistic internal geometry by explicitly modelling the manufacturing process. After validating the simulation framework against experimental data in terms of

internal geometry, elastic properties, non-linear behaviour and damage morphology, the material response is predicted under variable uni-axial off-axis load cases. Finally, the effect of the textile topology on the ultimate strength of the material is investigated in chapter 5.

The multiscale framework described in this thesis can be used as a general modelling approach for conducting numerical simulations of other textile composites. Aside from providing a valuable insight into how damage propagation is affected by the underlying meso-structure, the predicted stress-strain curves can be used to calibrate macroscopic material models suitable for large-scale impact and crash simulations of braided composites.

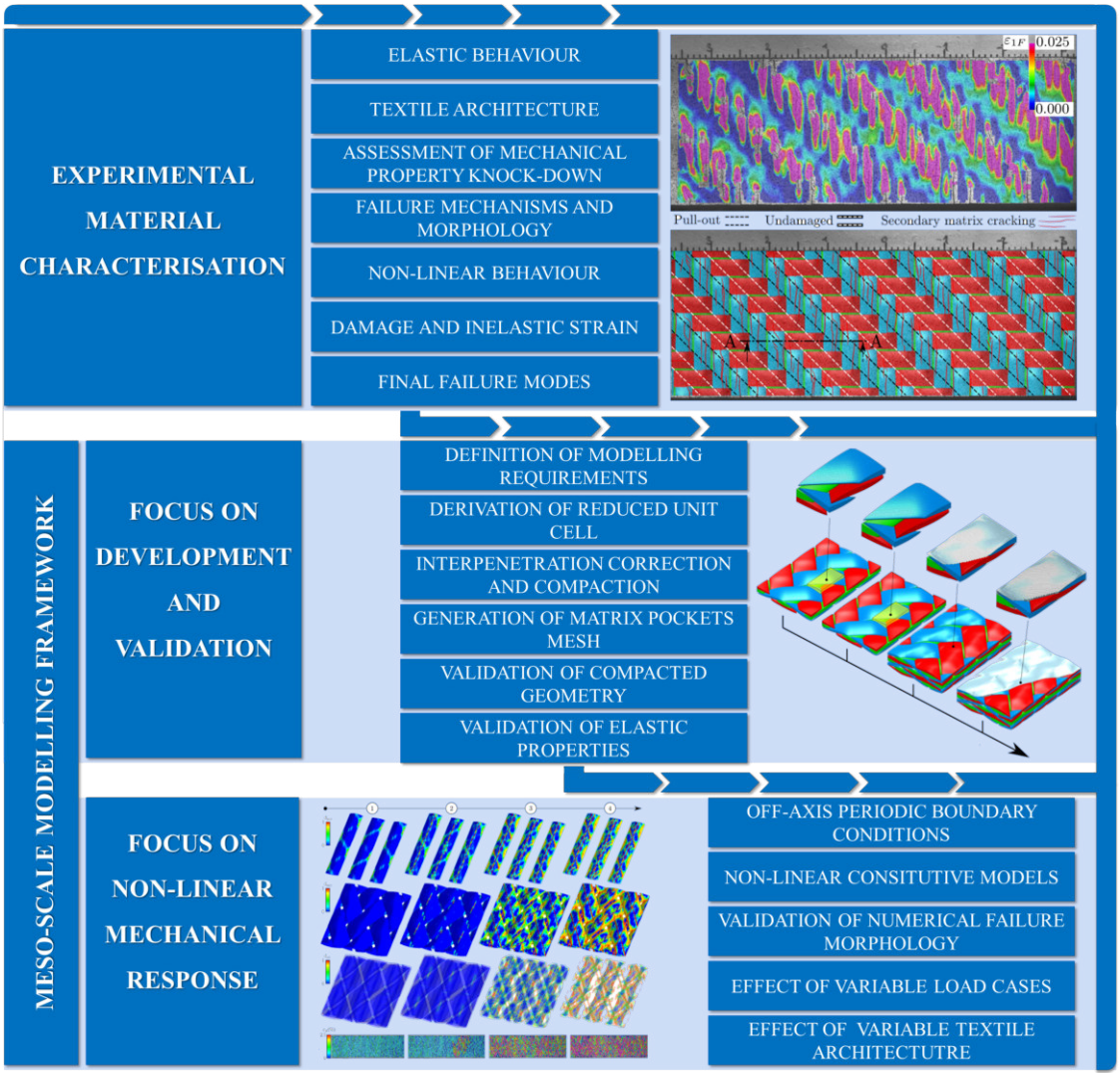

Fig. 1.2: Overall modelling strategy

1.3 Thesis outline

This thesis is subdivided into several chapters which address the step-by-step development of a high-fidelity simulation tool for virtually predicting the non-linear mechanical response of triaxial braided composites:

Chapter 2: *Introduction to braiding technology*

In chapter 2, an introduction to the braiding process technology is given, including the determination of typical textile parameters and a discussion of the main technological advantages and disadvantages of the process.

Chapter 3: *Experimental material characterisation*

Chapter 3 provides the experimental baseline for the modelling methodology by investigating damage and failure of triaxial braided composites under multi-axial stress states. Three braid architectures, comprising braiding angles of 30°, 45° and 60° are each loaded parallel to their axial, transverse and braid yarn direction. Digital image correlation measurement techniques are used to quantify the effects of the textile architecture and its heterogeneity on the strain field, to identify and locate constituent failure mechanisms and to investigate damage initiation and development. In order to identify the driving physical mechanisms behind the material non-linearity, the evolution of the damage variable and the accumulated inelastic strain are quantified using incremental loading/unloading experiments. A high-speed camera is employed in order to study the dynamic nature of catastrophic failure. This information further serves as a baseline for the development of a numerical model for predicting the non-linear constitutive behaviour of braided composites. Having identified the failure morphology to be severely affected by the underlying textile architecture, the necessity of a meso-scale modelling approach becomes evident.

Chapter 4: *Development of a meso-scale simulation framework*

Based on the modelling requirements and material behaviour identified in the previous experimental work, a novel simulation framework for accurate predictions of the the mechanical response of triaxial braided composites is proposed in chapter 4. A simulation roadmap is introduced and the individual steps are explained in detail: Realistic finite element unit cell models are generated through an automated bottom-

up simulation work-flow: local volumetric interpenetrations present in the initial stage of the model are resolved in a fictitious thermal step. Subsequently, a compaction simulation is performed to the desired target fibre volume fraction using flexible membranes for improved computational efficiency. Special out-of-plane periodic boundary conditions allow an implicit consideration of the compaction of multiple braid plies in different nesting configurations in order to capture global FVFs of $55 - 60\%$ while using intra-yarn fibre volume fractions obtained from experiments. In the last step, a tetrahedral matrix pocket mesh is created from a CAD reconstruction of the deformed textile. A novel meshing methodology is developed to incorporate branching cohesive yarn-to-yarn and yarn-to matrix interfaces without the need of introducing an artificial matrix mesh of finite thickness. The framework is validated by a detailed comparison with experimental results. The unit cell geometry is compared to the detailed reconstruction of the actual bundle geometry from μCT measurements for three braid architectures under consideration. The excellent correlation of experiments and unit cell predictions underlines the framework's potential for future damage modelling.

Chapter 5: *Non-linear mechanical response*

In chapter 5, the previously developed simulation framework is extended to the prediction of the the non-linear mechanical response of triaxial braided composites. Numerical predictions are made by three-dimensional finite element unit cells in two nesting configurations and validated against experimental stress-strain curves and damage mechanisms. The progressive development of matrix cracks manifested in a smooth degradation of the stress-strain curve up to the formation of a plateau for matrix dominated load cases, while the underlying textile architecture acted as a crack arresting grid and inhibited catastrophic failure. The second damage mechanism was found to be intrinsic to the textile architecture and prevailed in the presence of severe interfacial stresses. A stable plateau in the stress-strain curves was correlated with the rapid formation of large-scale delaminations followed by progressive bundle pull-out, which was predicted qualitatively by the numerical model. Although the investigated braid topologies exhibited considerable geometric variability, the unit cell modelling approach with a compacted geometry model built from average input parameters was capable of correctly predicting the homogenised constitutive response,

localisation, and damage evolution. Further, the mechanical response was predicted under variable uni-axial off-axis load cases and the effect of the textile topology on the ultimate strength of the material was investigated. The meso-scale framework described in this paper can be used as a general modelling approach for conducting numerical simulations of other textile composites. Aside from providing a valuable insight into how damage propagation is affected by the meso-structure, the predicted stress-strain curves can be used to calibrate macroscopic material models suitable for large-scale impact and crash simulations of braided composites.

Chapter 6: *Conclusions and future work*

Chapter 6 concludes the experimental and numerical work presented in this thesis. Finally, the developments achieved within this thesis are addressed, the capabilities and limitations of the modelling approach are discussed, and possible future improvements are highlighted.

2 Introduction to braiding technology

2.1 Manufacturing of braided composites

2.1.1 Manufacturing process

Braiding is a textile manufacturing process that creates a reinforcing fibrous architecture composed of interlacing yarns which is subsequently impregnated with a polymeric resin and cured to form a braided composite material. Based on the orientations of the majority of the yarns which can be tailored to a specific application, they are classified as three-dimensional (3D) or two-dimensional (2D) braids [7]. Following the basic principle of a traditional maypole dance, the latter are produced as either flat or tubular preforms on circular braiding machines.

Around the centre of a maypole braider, the horn gears, which are notched discs that serve as a transportation device for the yarn carriers are positioned around an orbital ring. In these notches, two groups of yarn spool carriers move in opposing directions on intersecting serpentine paths, with one half following a clockwise and the other half a counterclockwise direction. Each time their paths intersect, two yarns are intertwined in the conversion zone. As the carriers proceed along the circumference of the machine, more and more interlacement points form an interlocked fibre mesh that converges progressively towards the deposition plane in the centre of the machine, where a pulling or take-up mechanism advances the finished braid.

Two-dimensional braids can be manufactured without a mandrel, resulting in closed sleeves that can be flattened, or as an helical overwrap on a mandrel in an over-braiding process. Depending on the application, the mandrel remains within the part as a permanent core or serves as a temporary moulding tool for subsequent resin infusion of hollow structures. Automated braiding machines, such as the radial machine for producing the rim base of CFRP wheels on a Porsche 911 shown

Fig. 2.1: Radial braiding machine with 288 carriers for CFRP wheel production

in Fig. 2.1 use industrial six-axis robots to control the velocity and trajectory of complex mandrel shapes through the convergence point for further tailoring of the textile architecture. Multiple braided layers are achieved by either repeated passing of the mandrel through a single machine, or by a continuous process through multiple machines in series. Forming or guide rings ensure a consistent convergence point of the yarns on the mandrel and allow reversing the braid direction during the process [8]. Flat braided tapes can be accomplished without a mandrel by inserting terminal horn gears at specific locations in a braiding machine. Here, by reversing the direction of each carrier, a complete rotation cycle is prevented.

2.1.2 Braid parameters

The large variety of parameters offers many degrees of freedom in designing and tailoring the material to the requirements of individual components. In addition to the customisation of the constituent bundles, including the choice of the fibre type, linear density, the number of filaments, and the twist, the textile architecture and geometry are a product of several interconnected production process variables.

2.1.2.1 Braid type and pattern

Similar to woven composites, braids are classified in terms of their characteristic interlacement pattern shown in Fig. 2.2, which refers to the number of bias yarns between each cross-over point. In case a braiding machine with four slots in each horn gear is used, a diamond (1×1) or regular (2×2) pattern is achieved with a full load configuration, where half of the available horn gear slots are populated with yarn carriers. By selecting different initial positions of the carriers on the track during the machine set-up, either of the two patterns can be realised [9]. A hercules (3×3) and 4×4 architecture are manufactured on braiding machines with six and eight slots per horn gear, respectively. In a diamond architecture, each positively oriented braid yarn alternately passes over a bias yarn and vice versa. As the number of bridging bias yarns between two cross-over points increases, the ratio of undulating to straight yarn path is minimised. Thus, the degree of degradation of mechanical in-plane properties is expected to decrease [10–12]. On the other hand, however, both the dimensional stability of the preform and the mechanical out-of plane properties benefit from more intertwining points in the textile, with the latter being desirable when designing impact critical structures [13]. Regular braids offer a good compromise between their in-plane and out-of-plane mechanical properties, which makes them one of the most commonly used braid patterns.

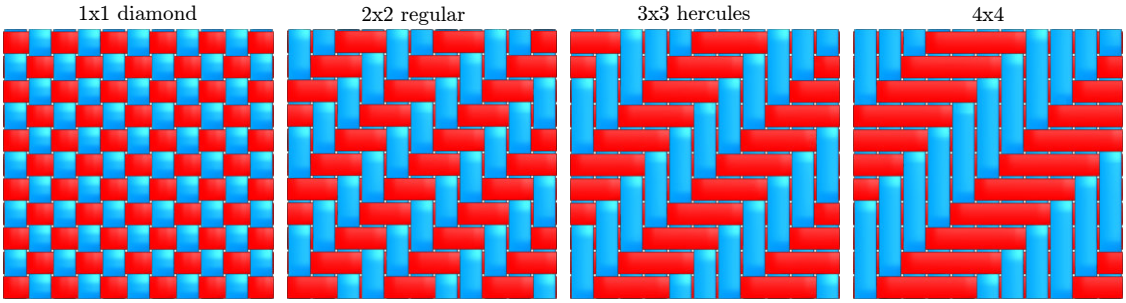

Fig. 2.2: Braid patterns referring to the number of bias yarns between each cross-over point

Whereas biaxial braids consist of two interlacing braid yarn directions, triaxial braids are manufactured by incorporating additional axial bundles into the braiding process from stationary guides. Fig. 2.3 underlines differences between a biaxial and a triaxial braid for a tubular structure with a mandrel diameter of d_{M}. The braid yarns are coloured in red and blue, and the entrapped axial yarns are highlighted in green. Since the axial yarns are enclosed between the cross-overs of undulating braid yarns, they are mostly devoid of crimp. While biaxial braids with their two in-plane fibre directions benefit from predominantly uniaxial load cases, such as a torque shaft, the reinforcing three in-plane fibre directions of triaxial

braids make them a well-suited choice for multi-axial loading. Furthermore, the mechanical properties can be further optimised by the choice of the axial yarns, e.g. by controlling the relative axial yarn size, by using commingled bundles, or by creating glass/carbon hybrid braids.

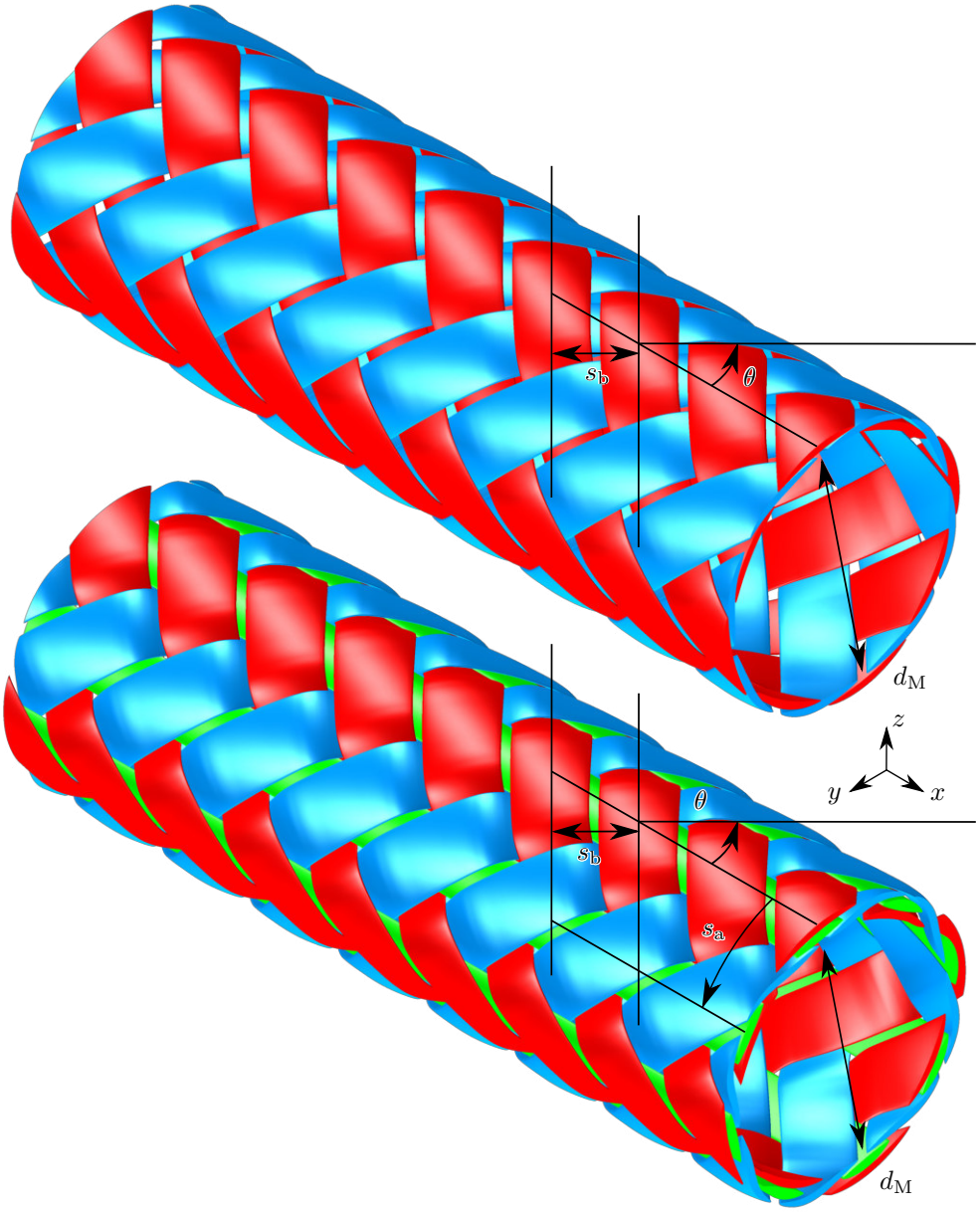

Fig. 2.3: Comparison of biaxial and triaxial braid architectures for a regular braid pattern

2.1.2.2 Braiding angle

In contrast to weaves, where warp and weft bundles interlace orthogonally, the bias yarns in braids overlap at an inclined angle with respect to the axial take-up

direction. This additional degree of freedom in designing the material, denoted as the braiding angle θ in Fig. 2.3 critically affects the mechanical properties of braided composites and is directly controlled by the manufacturing process. Considering the simplest case of a tubular mandrel guided through the centre of a braiding machine, the braiding angle θ is determined geometrically by relating a bundle's projected axial length l_{cycle} during a full carrier rotation to the circumference of the mandrel U_{M} with diameter d_{M}. Assuming a constant axial take-up velocity v_{M}, the braiding angle is obtained from

$$\theta = \arctan\left(\frac{U_{\text{M}}}{l_{\text{cycle}}}\right) = \arctan\left(\frac{U_{\text{M}}}{v_{\text{M}} T_{\text{cycle}}}\right). \tag{2.1}$$

The cycle time T_{cycle} for a full carrier rotation considering the number of horn gears in the machine N_{hg} is

$$T_{\text{cycle}} = N_{\text{hg}} T_{\text{hg}}, \tag{2.2}$$

and the time required for a carrier to travel half of the circumference of a single horn gear T_{hg} can be calculated from

$$T_{\text{hg}} = \frac{\pi}{\omega_{\text{hg}}} = \frac{1}{2\, f_{\text{hg}}}. \tag{2.3}$$

With the horn gear frequency f_{hg} and angular velocity ω_{hg} defined by the manufacturing process, Equation 2.1 is rewritten as

$$\theta = \arctan\left(\frac{2\, U_{\text{M}}\, f_{\text{hg}}}{v_{\text{M}}\, N_{\text{hg}}}\right) = \arctan\left(\frac{2\, d_{\text{M}}\, \pi\, f_{\text{hg}}}{v_{\text{M}}\, N_{\text{hg}}}\right). \tag{2.4}$$

Subsequently, the yarn spacing, which is the normal distance between the centre-lines of two adjacent yarns as defined in Fig. 2.3 for circular cross-sections yields:

$$s_{\text{a}} = \frac{2\,\pi\, d_{\text{M}}}{N_{\text{c}}} \quad ; \quad s_{\text{b}} = s_{\text{a}} \cos(\theta). \tag{2.5}$$

When the mandrel is guided through the braiding point at an arbitrary trajectory, including eccentricity and angling of the centre-line, or for complex shapes mandrels, the resulting braiding angle varies across the entire component. Due to the need to minimise cost- and time-intensive trial and error manufacturing iterations, various process simulation models have been developed. Kinematic models [12, 14, 15] neglect many important process parameters, such as yarn interaction

and shape, contact with the guide ring, friction and gravity. However, their computational efficiency allows to obtain acceptable process settings quickly, or even optimise the machine and robot take-up speed profile for a desired target braiding angle distribution. Many of the aforementioned modelling limitations are overcome by performing FE simulations of the over-braiding process, although at the cost of significant computational time [1, 16]. Using an explicit time integration scheme, Hans et al. [1] discretised each yarn centre-line with chains of truss elements and incorporated experimentally determined friction coefficients for potential contacts of yarns, mandrel, and the guide-ring in order to predict the local braiding angle and yarn spacing. When applied to a generic mandrel displayed in Fig. 2.4, the simulation results showed a good correlations with experimental measurements, with a maximum error between measured and predicted braiding angle of less than 5° at all points. When a constant fibre volume fraction (FVF) is assumed, the braid ply thickness for biaxial braids can be estimated from the local spacing and braiding angle of two adjacent braid yarns [17]. Thus, for the case of a pre-defined mandrel, the design of an outer rigid tool greatly benefits from an available preform thickness distribution. In case the outer shape of the part is known a priori, a tailored mandrel can be derived from the process simulation. Typical braiding angles range from 20° to 70°, allowing for significant optimisation of the fibre directions for structural design. The minimum and maximum braid angles are limited by jamming of the yarns, which is related to the maximum shear distortion the braid can sustain [9].

2.1.2.3 Cover factor

The textile architecture of braided composites can be open or closed, depending on the ratio of spacing to yarn width. The cover factor CF quantifies the surface area covered by fibres on a mandrel. For a 2D triangular unit cell of minimum size highlighted in Fig. 2.5, in which the surface areas of the constituent yarns are correctly represented, the cover factor is obtained by relating the covered to the total area, or equally by the ratio of uncovered area A_o to the total area A_t. With the local braid yarn spacing s_b and width w_b, the cover factor for a biaxial architecture is described by:

$$CF_\mathrm{biax} = 1 - \frac{A_\mathrm{u}}{A_\mathrm{biax}} = 1 - \frac{(s_\mathrm{b} - w_\mathrm{b})^2}{s_\mathrm{b}^2} = \frac{2\,w_\mathrm{b}}{s_\mathrm{b}} - \left(\frac{w_\mathrm{b}}{s_\mathrm{b}}\right)^2 . \tag{2.6}$$

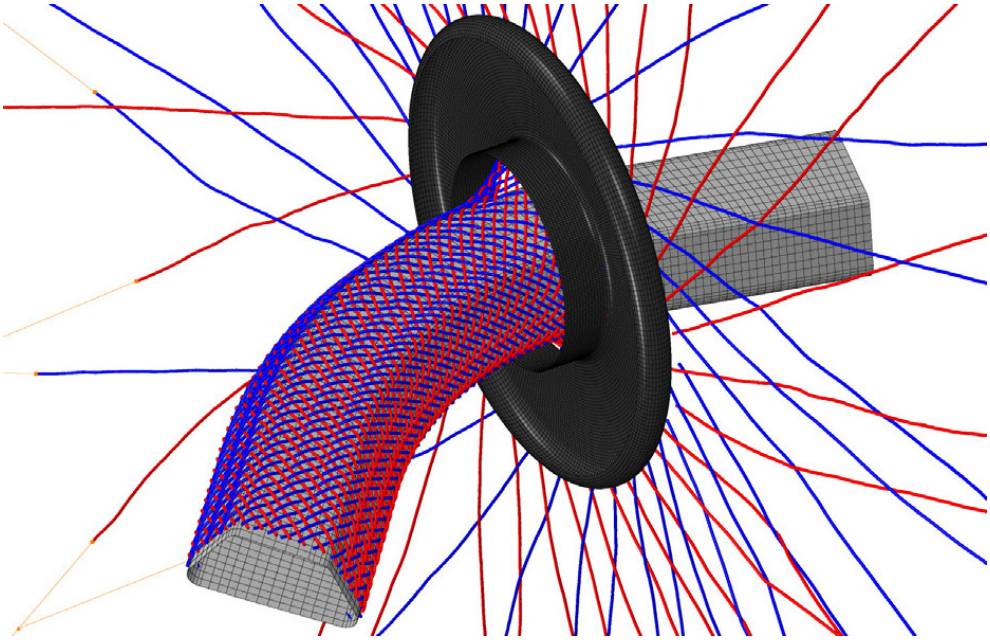

Fig. 2.4: FE simulation model of the braiding process for a generic curved mandrel using truss elements [1]

For a triaxial topology, the additional coverage of the axial yarns must be taken into account. Considering a minimum unit cell of twice the original size of the biaxial case, the uncovered area is subdivided into three potential zones:

$$CF_{\text{triax}} = 1 - \frac{A_{\text{u},1} + A_{\text{u},2} + A_{\text{u},3}}{A_{\text{triax}}}. \tag{2.7}$$

A potential overlapping of braid and axial bundles is considered by a relative contribution of each zone to the overall cover factor defined as:

$$\begin{aligned} CF_{\text{triax}} = 1 - \frac{1}{s_{\text{b}}^2}\Bigg[& \frac{1}{8}\max\Big(0, s_{\text{b}} - 2w_{\text{b}} - 2w_{\text{a}}\cos(\theta)\Big)^2 \;\rightarrow\; A_{\text{u},1} \\ & + \frac{1}{8}\max\Big(0, s_{\text{b}} - 2w_{\text{a}}\cos(\theta)\Big)^2 \;\rightarrow\; A_{\text{u},2} \\ & + \frac{1}{2}\max\Big(0, s_{\text{b}} - 2w_{\text{a}}\cos(\theta)\Big)\Big(s_{\text{b}} - w_{\text{b}} - \frac{1}{2}\max\Big(0, s_{\text{b}} - 2w_{\text{a}}\cos(\theta)\Big)\Big) \;\rightarrow\; A_{\text{u},2} \\ & + \frac{1}{2}\min\Big(s_{\text{b}} - w_{\text{b}}, \frac{3}{2}s_{\text{b}} - w_{\text{b}} - w_{\text{a}}\cos(\theta)\Big)^2\Bigg]. \;\rightarrow\; A_{\text{u},3} \end{aligned} \tag{2.8}$$

When superior mechanical properties are desired, braids are commonly designed to be closed, which implies a cover factor of close to one. While gaps in between the bundles are closed, the overall fraction of resin pockets is minimised. Following

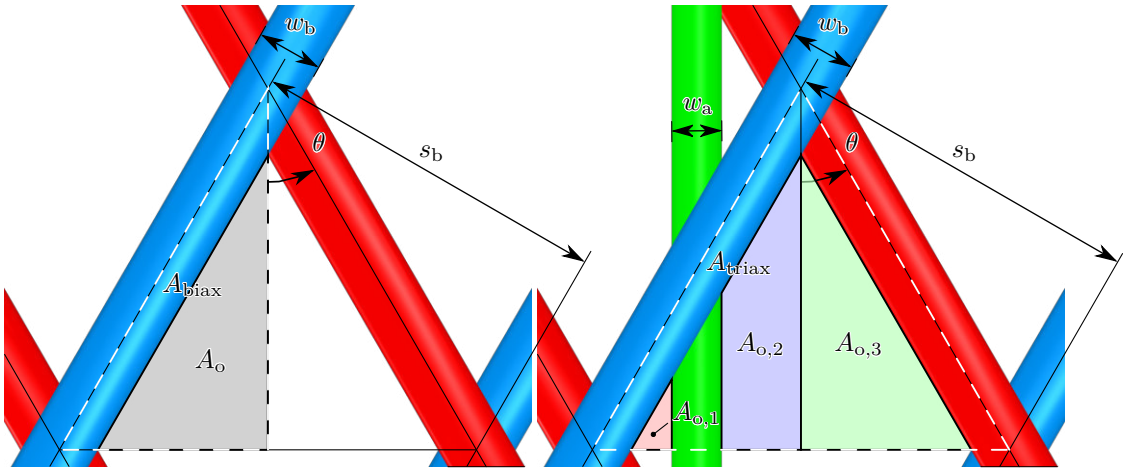

Fig. 2.5: Geometrical derivation of the cover factor for biaxial (left) and triaxial (right) braids

a successive gain in FVF, the mechanical properties improve [18]. Although the extent of this increase is hard to quantify directly, the cover factor provides a valuable qualitative assessment of a potential degradation and the corresponding location during over-braiding of the first ply. In addition, it can be applied to maximise local fibre coverage particularly for complex mandrels with geometrical discontinuities and high curvature by optimising the transient process parameters.

Dry yarns consist of thousands of contacting filaments. When subjected to external forces, their cross-sectional shape can change significantly. Specific to a combination of process parameters and material properties, including for example local yarn tension and twist, the bundle width and thickness can vary between an upper and a lower bound. As a consequence, three potential states can be distinguished in Fig. 2.6 for a braid depositing on a circular mandrel. Jamming occurs, in case the core diameter decreases, the fibre bundles try to accommodate to the underlying mandrel by squeezing together laterally. After the bundles reach their minimum width $w_{b,min}$ and maximum thickness, they will no longer be able to adjust to the core and form a closed sleeve with a diameter bigger than that of the core. The optimum process point is achieved, when the cover factor just approaches a value of one. Yet, yarns are highly spread and cover the perimeter with their maximum width and minimum thickness, resulting in a reduced undulation amplitude and hence excellent mechanical properties. For open braids, the perimeter of the core cannot be fully covered by the yarns, although they are depositioned at their maximum width $w_{b,max}$. Gaps and a high amount of resin pockets in combination with low FVF then correlate with poor mechanical properties.

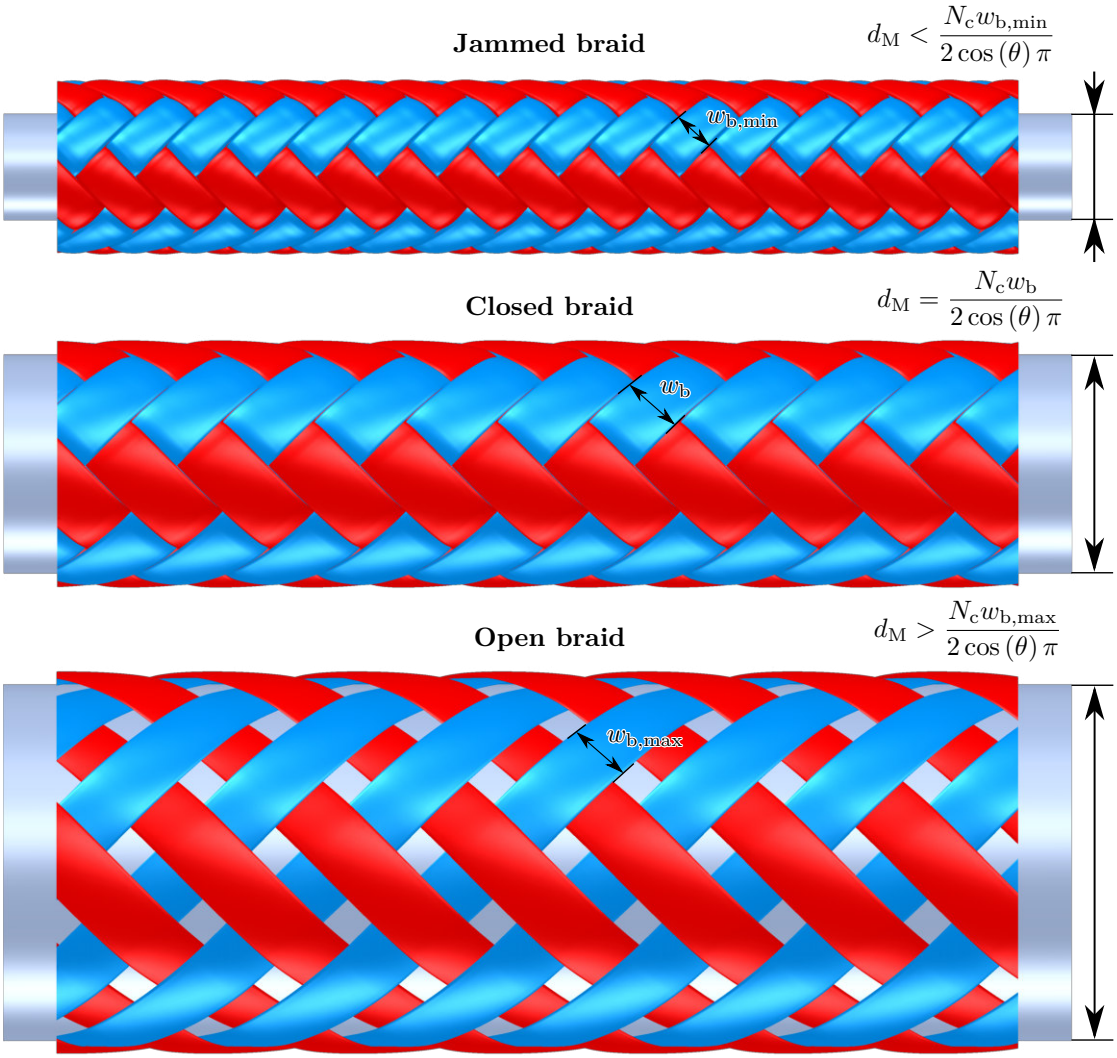

Fig. 2.6: Jammed, closed, and open braid deposition state on a circular mandrel

2.1.2.4 Volume fractions and areal weight

Since the fibres are the main load carrying elements in the composite, their percentage has a direct effect on mechanical properties of the material. The global FVF φ_F relates the fibre volume V_F to the total volume V according to:

$$\varphi_F = \frac{V_F}{V}. \tag{2.9}$$

Braided composites are composed of impregnated fibre bundles and neat resin pockets. Thus, the FVF must be homogenised over a large enough domain of at least one unit cell to be representative of the material. Additionally, the local intra-yarn FVF κ, also denoted as the yarn packing density [19, 20] is defined as the fraction of fibre volume $V_{F,yarn}$ to total volume V_{yarn} inside the bundles:

$$\kappa = \frac{V_{\mathrm{F,yarn}}}{V_{\mathrm{yarn}}}. \tag{2.10}$$

For a triaxial braided composites, the global FVF and the intra-yarn FVF are interconnected through the relative contribution of the yarns in axial V_{a} and braid direction V_{b} as

$$\varphi_{\mathrm{F}} = \frac{V_{\mathrm{a}}\,\kappa_{\mathrm{a}} + V_{\mathrm{b}}\,\kappa_{\mathrm{b}}}{V}, \tag{2.11}$$

where the total volume V is the sum of axial yarns, braid yarns, and matrix pockets V_{m}:

$$V = V_{\mathrm{a}} + V_{\mathrm{b}} + V_{\mathrm{m}}. \tag{2.12}$$

Contrarily to the global FVF which can be experimentally measured by several techniques, e.g. by physically removing the matrix by digestion or ignition [21], the determination of the intra-yarn FVF is hindered by the complexity of a reliable segmentation and measurement of the yarn volume. As a workaround, the calculation can be performed on individual bundle cross-sections obtained from microsections or X-ray computed tomography. Thus, Equation 2.10 can be rewritten to instead account for the total cross-sectional area A_{yarn} and fibre cross-sectional area $A_{\mathrm{F,yarn}}$ which contains a known quantity of N_{F} fibres of cross-sectional area A_{sf}:

$$\kappa = \frac{V_{\mathrm{F,yarn}}}{V_{\mathrm{yarn}}} = \frac{A_{\mathrm{F,yarn}}}{A_{\mathrm{yarn}}} = \frac{N_{\mathrm{F}}\,A_{\mathrm{sf}}}{A_{\mathrm{yarn}}}. \tag{2.13}$$

The fibre areal weight FAW quantifies the mass of fibres m_{F} per surface area A_{F} of the preform as

$$FAW = \frac{m_{\mathrm{F}}}{A_{\mathrm{F}}} = \frac{\rho_{\mathrm{F}}\,V_{\mathrm{F}}}{A_{\mathrm{F}}} = \rho_{\mathrm{F}}\,t_{\mathrm{F}} = \rho_{\mathrm{F}}\,\varphi_{\mathrm{F}}\,t \tag{2.14}$$

where the average ply thickness t can be calculated for a desired target FVF φ_{F} or vice versa, in case the fibre density ρ_{F} is known and equal for both bias directions. With the definition of the linear yarn density $\mu_{F,yarn}$ as the ratio of yarn mass $m_{\mathrm{F,yarn}}$ per length $l_{\mathrm{F,yarn}}$ written as

$$\mu_{F,yarn} = \frac{m_{\mathrm{F,yarn}}}{l_{\mathrm{F,yarn}}}, \tag{2.15}$$

and the crimp factor c, which is the ratio of undulating yarn length $L_{\mathrm{u'}}$ to projected length L_{u} given as

$$c = \frac{L_{\mathrm{u'}}}{L_{\mathrm{u}}}, \tag{2.16}$$

the fibre areal weight of a biaxial braided composite FAW_{biax} can be expressed after eliminating the length of the braid on the mandrel l_{M}:

$$\begin{aligned} FAW_{\mathrm{biax}} &= \frac{m_{\mathrm{F,b}}}{A_{\mathrm{M}}} = \frac{N_{\mathrm{c}}\, m_{\mathrm{F,yarn,b}}}{d_{\mathrm{M}}\, \pi\, l_{\mathrm{M}}} \\ &= \frac{N_{\mathrm{c}}\, \mu_{\mathrm{F,yarn,b}}\, \dfrac{c}{\cos(\theta)}}{d_{\mathrm{M}}\, \pi} \\ &= \frac{2\, c\, \mu_{\mathrm{F,yarn,b}}}{s_{\mathrm{b}}}. \end{aligned} \tag{2.17}$$

The thickness of a single biaxial ply t_{biax} can then be obtained after substituting Equation 2.14:

$$t_{\mathrm{biax}} = \frac{2\, c\, \mu_{\mathrm{F,yarn,b}}}{s_{\mathrm{b}}\, \rho_{\mathrm{F,b}}\, \varphi_{\mathrm{F}}}. \tag{2.18}$$

For a triaxial braided composite with equal bias yarns, the fibre areal weight FAW_{triax} is

$$\begin{aligned} FAW_{\mathrm{triax}} &= \frac{m_{\mathrm{F,a}} + m_{\mathrm{F,b}}}{A_{\mathrm{M}}} = \frac{\dfrac{N_{\mathrm{c}}}{2}\, m_{\mathrm{F,yarn,a}} + N_{\mathrm{c}}\, m_{\mathrm{F,yarn,b}}}{d_{\mathrm{M}}\, \pi\, l_{\mathrm{M}}} \\ &= \frac{\dfrac{N_{\mathrm{c}}}{2}\, \mu_{\mathrm{F,yarn,a}} + N_{\mathrm{c}}\, \mu_{\mathrm{F,yarn,b}}\, \dfrac{c}{\cos(\theta)}}{d_{\mathrm{M}}\, \pi} \\ &= \frac{\mu_{\mathrm{F,yarn,a}}\, \cos(\theta) + 2\, c\, \mu_{\mathrm{F,yarn,b}}}{s_{\mathrm{b}}}. \end{aligned} \tag{2.19}$$

Due to the axial bundles commonly exhibiting only minor undulations, the application of the crimp factor is confined to the braid bundles. Equation 2.14 is valid for triaxial braided composites only if the fibre density in the axial and the braid bundles are identical. In order to obtain a more generalised formulation, the ratio of axial fibre volume $V_{\mathrm{F,a}}$ to global fibre volume content V_{F} is derived first as a

function of the braiding angle, the crimp ratio, and the respective linear yarn and fibre densities, or equally, as a function of the cross-sectional yarn ratios:

$$\begin{aligned}
\frac{V_{\mathrm{F,a}}}{V_{\mathrm{F}}} = \frac{t_{\mathrm{F,a}}}{t_{\mathrm{F}}} &= \frac{\dfrac{N_{\mathrm{c}}\,\mu_{\mathrm{F,yarn,a}}}{2\,\rho_{\mathrm{F,a}}}}{\dfrac{N_{\mathrm{c}}\,\mu_{\mathrm{F,yarn,a}}}{2\,\rho_{\mathrm{F,a}}} + \dfrac{N_{\mathrm{c}}\,\mu_{\mathrm{F,yarn,b}}\,c}{\rho_{\mathrm{F,b}}\,\cos(\theta)}} \\
&= \frac{1}{1 + \dfrac{2\,c}{\cos(\theta)}\,\dfrac{\rho_{\mathrm{F,a}}\,\mu_{\mathrm{F,yarn,b}}}{\rho_{\mathrm{F,b}}\,\mu_{\mathrm{F,yarn,a}}}} \\
&= \frac{1}{1 + \dfrac{2\,c}{\cos(\theta)}\,\dfrac{A_{\mathrm{F,yarn,b}}}{A_{\mathrm{F,yarn,a}}}} \\
&= \frac{1}{1 + \dfrac{2\,c}{\cos(\theta)}\,\dfrac{N_{\mathrm{F,b}}\,A_{\mathrm{sf,b}}}{N_{\mathrm{F,a}}\,A_{\mathrm{sf,a}}}}.
\end{aligned} \tag{2.20}$$

The average thickness of a single triaxial ply t_{triax} is then calculated by

$$t_{\mathrm{triax}} = \frac{1}{s_{\mathrm{b}}\,\varphi_{\mathrm{F}}} \left(\frac{\mu_{\mathrm{F,yarn,a}}\,\cos(\theta)}{\rho_{\mathrm{F,a}}} + \frac{2\,c\,\mu_{\mathrm{F,yarn,b}}}{\rho_{\mathrm{F,b}}} \right). \tag{2.21}$$

It is important to note, however, that Equation 2.18 and Equation 2.21 provide only an estimation of the ply thickness in a multi-layered braided composite laminate. When multiple layers are stacked and compacted during the resin infusion process, the final cured ply thickness is controlled by a phenomenon called nesting. Depending on the geometrical alignment of layers, their textile architecture, and the compaction behaviour of the constituent dry yarns, inter-yarn voids can be closed. Thus, an irregularly shaped interface in between plies is created and the global FVF increases. Lomov et al. [22] concluded that nesting in triaxial braids is a compromise between two competing effects: on the one side, the axial yarns increase the overall waviness in the braid yarns and hence promote nesting. On the other side, they also prevent ultimate nesting, similar to long floats in twill weaved. Although the outcome of a single simulation in maximum nesting configuration suggested that the axial yarns tend to prevent effective nesting compared to biaxial braided composites, no clear trend was visible in the results obtained from Monte-Carlo simulations. Endruweit and Long [23] found that due to the significant periodic thickness in triaxial braids caused by the insertion of axial yarns, nesting is more pronounced for triaxial than for biaxial braids. In this case

denoted 'structural nesting', sections devoid of axial bundles are filled by their adjacent layer's equivalent. Additional nesting can occur, in case bundles of adjacent plies are shifted in such a way that voids in between the undulating braid bundles are filled. Then, local bending effects can give rise to additional fibre waviness in the axial yarns and an overall increase of nesting. Birkefeld et al. [24] confirmed this tendency by measuring significantly higher nesting factors in triaxial braids compared to biaxial braids for multiple braiding angles.

Finally, by rewriting Equation 2.20 to account for the total volume instead of the fibre volume of the axial yarns, with

$$\frac{V_\mathrm{a}\,\kappa_\mathrm{a}}{V\,\varphi_\mathrm{F}} = \frac{t_\mathrm{a}\,\kappa_\mathrm{a}}{t_\mathrm{triax}\,\varphi_\mathrm{F}} = \frac{1}{1+\dfrac{2\,c}{\cos(\theta)}\,\dfrac{\rho_\mathrm{F,a}\,\mu_\mathrm{F,yarn,b}}{\rho_\mathrm{F,b}\,\mu_\mathrm{F,yarn,a}}}, \tag{2.22}$$

an expression for the relative volume and thickness ratio of the axial yarns, the braid yarns, and the matrix pockets can be derived:

$$\begin{aligned}
\frac{V_\mathrm{a}}{V} &= \frac{t_\mathrm{a}}{t_\mathrm{triax}} = \frac{\varphi_\mathrm{F}}{\kappa_\mathrm{a}\left(1+\dfrac{2\,c}{\cos(\theta)}\,\dfrac{\rho_\mathrm{F,a}\,\mu_\mathrm{F,yarn,b}}{\rho_\mathrm{F,b}\,\mu_\mathrm{F,yarn,a}}\right)} \\
\frac{V_\mathrm{b}}{V} &= \frac{t_\mathrm{b}}{t_\mathrm{triax}} = \frac{\varphi_\mathrm{F}}{\kappa_\mathrm{b}\left(1+\dfrac{2\,c}{\cos(\theta)}\,\dfrac{\rho_\mathrm{F,a}\,\mu_\mathrm{F,yarn,b}}{\rho_\mathrm{F,b}\,\mu_\mathrm{F,yarn,a}}\right)} \\
\frac{V_\mathrm{m}}{V} &= \frac{t_\mathrm{m}}{t_\mathrm{triax}} = 1 - \frac{V_\mathrm{a}+V_\mathrm{b}}{V} = 1 - \frac{t_\mathrm{a}+t_\mathrm{b}}{t_\mathrm{triax}}.
\end{aligned} \tag{2.23}$$

2.1.3 Advantages and constraints

The use of braided composites offers a variety of unique advantages, such as:

- a high potential for process automation allows for part mass production, such that recurring costs and cycle time can be significantly reduced compared to hand lay-up methods. In order to achieve a completely integrated manufacturing process chain, a single or multiple braiding machines can be incorporated in a fully automated work cell. Collaborating robots continuously guide the mandrel, starting from over-braiding of multiple layers at an optimised take-up trajectory. Yarn tension and horn gear speeds are controlled electronically by an on-line inspection system which continuously assesses the finished textile architecture. Additional circumferential fibres can be intro-

duced by integral hoop winding. The finished preform is then automatically cut and further passed to the injection station that employs e.g. a resin transfer moulding (RTM) step. After subsequent curing, de-moulding, and final machining, the finished component is measured and checked in an automatic quality assurance system. Such an integrated system was successfully built by A&P Technology for over-braiding large composite structures. The 'Mantis' work cell incorporates fully automated control over all braiding parameters, a vision system for on-line inspection, a laser projection system, and circumferential winding [25].

- near-net shape manufacturing, minimising expensive scrap material and the need for additional machining.
- geometric flexibility with the capability to accommodate to complex and varying cross-sectional shapes. Typical applications comprise elliptical, triangular, rectangular, trapezoidal and asymmetric shapes. Using folding or cutting techniques, open cross-sections can be realised.
- possibility to directly integrate load introduction and functional elements during the preforming process, including bushings, connectors, and flanges, thus minimising subsequent machining and assembly steps [12].
- hybridisation of the textile architecture, with the goal of achieving advantages in the manufacturing process or tailoring the mechanical properties. By using glass fibre yarns with a lower cross-sectional area and material cost compared to carbon fibres for the braid direction, the time in between reloading of the carriers in a continuous process can be drastically extended. Additionally, the combination of glass and carbon fibre bundles can also be exploited for designing composite materials that exhibit a high strain to failure [26].
- the textile architecture can function as a natural crack arresting grid, resulting in a higher strain to failure and damage tolerance compared to tape laminates [27, 28]. The accompanying mechanical behaviour can be desirable in designing structures for crashworthiness with a high specific energy absorption [29].

Despite the many advantages, the design and manufacturing of braided composites also poses a number of challenges:

- despite its high flexibility, the manufacturing process imposes several constraints on the textile architecture. With a fixed number of yarns involved in braiding and their geometric shape varying within certain boundaries, the fibre coverage and the braiding angle are interdependent parameters. Hence,

for a given arbitrarily shaped component, it is not possible to optimise both parameters at the same time in order to obtain specifically tailored mechanical properties [9].

- concave parts cannot be manufactured directly.
- minimum and maximum practical braid angles are commonly confined to 20° and 70°, respectively [9].
- the braiding process produces considerable variability in the textile architecture and hence in the resulting mechanical properties [13].
- frictional forces between sliding yarns causes several fibres to break at each cross-over point until each bundle deposits on the mandrel. Hence, some fibre dominated mechanical properties are diminished [30]. The severity of this degradation is amplifies by increasing yarn tension and machine diameter, as the latter is typically accompanied by a higher carrier count that produces more bundle cross-over points.
- a specific mandrel or core must be developed for each individual component. Additional complexity is added to manufacturing process, in case the core is removed after curing.
- with a given diameter and carrier number, each braiding machine is optimised for parts of a specific size. For a given pattern, yarn type and coverage, only mediocre variations in part dimensions are possible.
- for conventional braiding machines without an automated spool changing system, the duration of a single production run is governed by the amount of material that can be contained on the spools. While the inertia forces generated by their rotation either limit the horn gear speed or the fibre mass on each spool, the latter additionally succumbs to space constraints during carrier movement.
- the complexity of the development process, including an iterative machine set-up to obtain full coverage of the mandrel and the need to characterise the mechanical and geometrical properties of a variety of textile architectures. To address this challenge, the development of a virtual process chain, including braiding process simulation and the prediction of the mechanical properties by means of virtual testing is key to address the high variability in the textile architecture.

3 Experimental material characterisation

In this chapter, damage and failure of triaxial braided composites under multi-axial stress states is investigated. In order to introduce different multi-axial stress states in the material, uni-axial tensile tests are performed at different off-axis orientations. Three braid architectures, comprising braiding angles of 30°, 45° and 60° are each loaded parallel to their axial, transverse and braid yarn direction. Digital image correlation measurement techniques are used to quantify the effects of the textile architecture and its heterogeneity on the strain field, to identify and locate constituent failure mechanisms and to investigate damage initiation and development. In order to identify the driving physical mechanisms behind the material non-linearity, the evolution of the damage variable and the accumulated inelastic strain are quantified using incremental loading/unloading experiments. A high-speed camera is employed in order to study the dynamic nature of catastrophic failure.

The triaxial braids within this study exhibited severe non-linearities in the mechanical response before final failure as a result of extensive matrix cracking. While the underlying textile architecture was found to slightly reduce the elastic properties compared to equivalent tape laminates, it functions as a natural crack arresting grid. As a result of this mechanism, braids under certain load conditions were capable of withstanding a higher strain to failure, even if a large portion of the specimen surface was saturated with matrix cracks. The accompanying mechanical behaviour can be desirable in the design of crash absorbing or pseudo-ductile materials. An additional failure mode intrinsic to the textile architecture was encountered for loading in the heavily undulated braid yarn direction. Due to yarn straightening and out-of-plane movements, braided composites were found to fail as a result of large scale delaminations accompanied by progressive fibre bundle pull-out.

3.1 Introduction

In high-volume production areas, such as the automotive industry, current manufacturing technologies face a twofold challenge: cost and cycle time. Two-dimensional (2D) triaxial braids comprise an integrated structure of yarns oriented in three in-plane directions, which makes them a well-suited choice for multi-axial loading. Their natural through-thickness reinforcement promises excellent specific energy absorption characteristics [28] in combination with higher delamination resistance compared to tape laminates [30, 31]. Mechanical in-plane properties, however, suffer from the textile nature of braids, as the intertwining yarns inevitably exhibit a certain degree of out-of-plane and in-plane waviness. Hence, a reduction of stiffness and strength can be observed compared to unidirectional composites. The inherent textile nature, which includes a multitude of curved yarn interfaces, resin rich areas and nesting of multiple plies, yields a complex damage and failure behaviour. In addition, the manufacturing process creates a heterogeneous fibre assembly which can cause significant variations of the material properties across a braided composite structure. As a result, investigations on multiple textile architectures are usually inevitable for the development of robust design allowables.

The determination of representative mechanical properties for braided composites remains a challenging task. Due to the complex textile architecture of braided composites, standard test methods developed for tape laminates may not be applicable. To address this issue, modified specimen dimensions for textile composites based on the ASTM D3039 standard [32] were proposed by [33]. Masters and Ifju [11] conducted an experimental programme to characterise the mechanical response of triaxial braided composites. Using Moiré interferometry to obtain the displacement field on the specimen's surface and X-ray radiography, the damage development was investigated under longitudinal and transverse loading conditions. Multiple matrix cracks and delaminations were observed, in particular when loading occurred transverse to the axial yarns. Falzon and Herszberg [30] compared the performance of triaxial braid architectures to laminates manufactured from fabrics and prepreg tape. A considerable strength reduction in the longitudinal direction was observed, which was attributed to a combination of out-of-plane waviness as well as fibre damage in the yarns as a result of the braiding process. Littell et al. [34] investigated the effect of the resin system on damage development in braided composites using digital image correlation (DIC) techniques. A reduced onset and extent of damage was observed when applying a toughened instead of an untoughened epoxy system. Lomov et al. [35] proposed a methodology to study damage initiation and development in different textile composites using a combination of

full-field strain measurement obtained through DIC, acoustic emission (AE), X-ray computed tomography (CT) and microsections on flat coupons exposed to specific load levels. Ivanov et al. [27, 36] applied this approach to a 45° 1x1 triaxial braided composite and investigated damage mechanisms in different off-axis directions under tensile loading.

The present experimental study serves two major objectives. The first goal is to investigate the non-linear mechanical response of different triaxial braided carbon/epoxy composites under multi-axial stress states, which are achieved through off-axis tensile tests. For this purpose, straight-sided specimens of three braid architectures shown in Fig. 3.1, comprising a braiding angle θ of 30°, 45° and 60° are each tested in their axial (x), transverse (y) and braid fibre direction ($1F$).

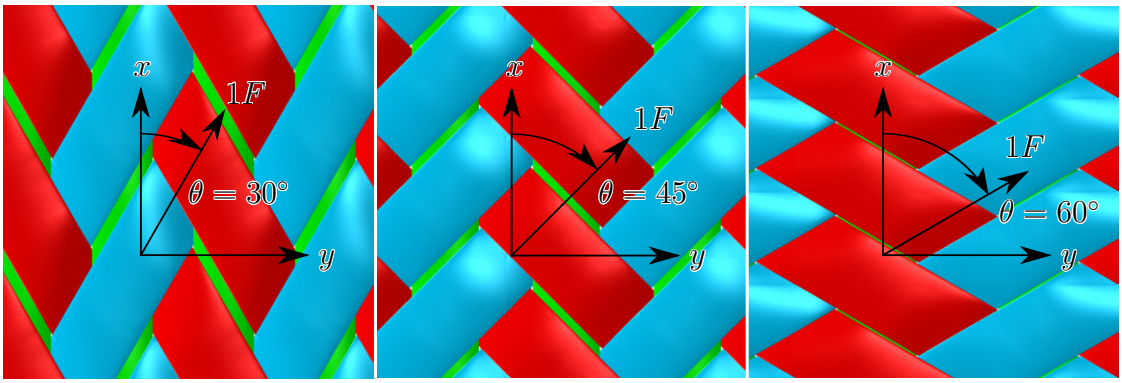

Fig. 3.1: Triaxial braid architectures under investigation: [0/±30],[0/±45] and [0/±60]

An overview of the test cases and their corresponding stress state is displayed in Fig. 3.2. The configurations aim to represent the characteristic manufacturing variability encountered across a typical braided component [1]. After monotonically loading an initial test series up to final failure, a subsequent series employed incremental load cycles, which include loading, unloading and reloading. Following the approach described by [37], the evolution of macroscopic damage and inelastic strain is investigated, as it provides an insight into the physical mechanisms driving non-linearities within the material. Secondly, strong emphasis is put on the characterisation of the complex material damage and failure behaviour. DIC measurement techniques are used to quantify the effects of the textile architecture and its heterogeneity on the strain field, identify and locate constituent failure mechanisms and investigate damage initiation and development. Microsections of the specimen are analysed for the geometrical material characterisation and assessment of failure mechanisms in the thickness direction. A high-speed camera is employed in order to study the dynamic nature of catastrophic failure by identifying the consecutive short-term failure events. This information can serve as baseline for the

development of a simulation model capable of predicting the constitutive behaviour of triaxial braided composites.

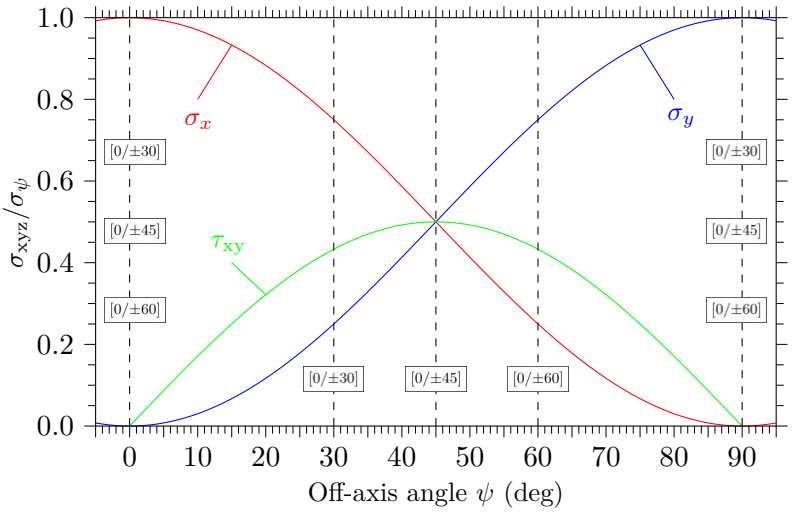

Fig. 3.2: Test cases with the corresponding multi-axial stress states in principal coordinates (xyz) as a function of uni-axial loading σ_ψ at an off-axis angle ψ

3.2 Experiments

3.2.1 Material systems

The materials investigated in this study feature two-dimensional 2×2 triaxial braided preforms manufactured from Toho-Tenax HTS40 F13 12K (800 tex) untwisted yarns for both the axial and braid yarn direction in combination with a Hexcel HexFlow RTM 6 epoxy resin. All three braid architectures, with a nominal braiding angle of 30°, 45° and 60° were manufactured on a Herzog radial braiding machine with 176 bobbins. Single layers of triaxial braid were produced by overbraiding on a cylindrical mandrel which was guided through the braiding point by a robot at constant axial take-up speed as shown in Fig. 3.3. For each braiding angle, a different mandrel diameter was used in order to obtain a closed braid with full fibre coverage and hence avoid resin-rich areas. As a result, similar fibre areal weights were achieved. This allows a comparison of different braiding angles. Machine parameters were optimised such that the yarn dimensions of all braid architectures match as closely as possible. In order to produce flat panels, each braid layer was cut along the axial yarn direction, removed from the mandrel and subsequently flattened. Before cutting, a temperature-resistant tape was applied to all

preform edges, such that fibre distortions during subsequent handling operations were minimised.

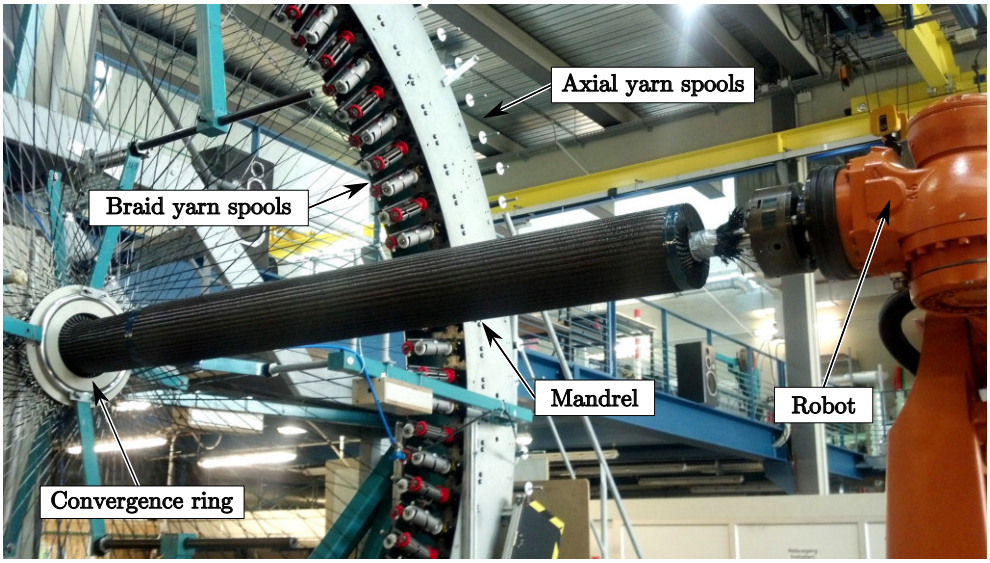

Fig. 3.3: Overbraiding process

Composite plates were produced with a total of four triaxial braid plies each. The shift between unit cells (UC) in each ply was not controlled and can be considered to be random. For resin infusion, the Vacuum membrane Assisted Process (VAP) technology was selected to minimise void content and to yield similar fibre volume fractions (FVFs) in all plates as a result of constant compaction pressure. The resin system for all braid architectures consisted of a Hexcel HexFlow RTM 6 resin. This matrix material is a one-part untoughened 180° C cure epoxy system designed for the RTM process. After degassing, the resin was infused at 80° C and then cured at 180° C for 120 minutes. FVF measurements were obtained from three locations on each panel in accordance with ASTM D3171 [21]. The intra-yarn FVFs were determined by optical microscopy on polished cross-sections. For quality control and estimation of the textile architecture, each specimen was inspected with a photometric stereo sensor [38]. Based on fibre reflectance values from multiple images under different lighting conditions, the braiding angle distribution was measured over the entire specimen surface. In a subsequent step, the raw sensor pictures were processed with an image segmentation algorithm in order to extract features of the underlying meso-structure, such as yarn width and spacing. The averaged geometrical properties are summarised in Table 3.1 together with the FVF measurements. Using an idealised model to render the measured geometrical data, the three braid architectures are visualised in Fig. 3.1.

Table 3.1: Properties of braid architectures under investigation

Braiding angle θ (deg)	Mandrel diameter d_M (mm)	FVF φ_F (%)	Thickness t_{lam} (mm)	Axial yarn spacing (mm)	Braid yarn spacing (mm)	Braid yarn width (mm)	Axial yarn FVF (%)	Braid yarn FVF (%)	Axial yarn content (%)
29.95 ± 2.35	100	58.7 ± 0.9	3.02 ± 0.04	3.63 ± 0.13	3.10 ± 0.57	2.91 ± 0.23	66 ± 6	70 ± 5	29.1 ± 0.4
45.04 ± 2.09	120	55.9 ± 0.8	2.99 ± 0.10	4.37 ± 0.38	3.05 ± 0.38	2.91 ± 0.21	66 ± 4	70 ± 6	25.0 ± 0.3
57.47 ± 2.44	160	57.0 ± 0.2	2.91 ± 0.09	5.30 ± 1.50	2.82 ± 0.23	2.85 ± 0.17	63 ± 5	70 ± 5	19.3 ± 0.4

3.2.2 Test set-up

The selection of a test method to obtain representative material properties for braided composites is not straightforward. Littell et al. [34] and Kohlman et al. [39] highlighted differences in damage propagation for straight-sided and tubular specimens due to edge-initiated failure of a 60° triaxial braided composite subjected to transverse tension. A notched coupon geometry was proposed which yielded significantly larger strengths in relation to the standard tests. Contrarily, Ivanov et al. [27] found no significant influence of edge effects on the damage development for straight-sided specimens. The difference between cut and uncut coupon edges was investigated by [28] for biaxial braided composites. A substantial increase in strain to failure was observed for the case of uncut edges that preserve fibre continuity, together with a highly non-linear specimen dependent Poisson's effect and significant fibre reorientation. Within the presented study, we follow the methodology proposed by [35] and focus on straight-sided coupons based on ASTM D3039. In order to obtain a representative material response and minimise the effect of possible localised edge cracking, the specimen width must be large in relation to the size of the representative material unit cell. A width of 25 mmwas selected in order to cover a minimum of two UCs, as proposed in [40]. For proper load introduction, glass fibre fabric tabs of 50 mmlength were bonded to the specimen grip region, leaving a total gage length of 150 mm. In case the applied load direction was not aligned with one of the orthotropic axes, oblique tabs according to [41] were used to minimise stress concentrations due to the presence of material shear-extension coupling.

An electromechanical Hegewald & Peschke testing machine with hydraulic grips capable of loading 250 kNwas operated at a constant head speed of 2 mm/min. All monotonic tests were performed under displacement control. The incremental loading tests were performed under load control, with the exception of the $[0/\pm 30]$ configuration under transverse tension due to a plateau-like stress-strain response. A maximum of seven loading, unloading and reloading cycles was selected in or-

der to avoid the possibility of low-cycle fatigue phenomena [37]. Since Kelkar and Whitcomb [10] found viscous effects in biaxial carbon/epoxy braided composites to be of minor importance, each specimen was reloaded immediately after a preceding unloading cycle. The final loading cycle caused failure of the specimen. The maximum load levels of individual cycles were selected such that they specifically correspond to transition regions in the material response identified a priori in the monotonic tests. For all tests, full field measurement of surface strains was undertaken using the commercial DIC system GOM ARAMIS in 3D mode with a maximum camera resolution of 4 mega-pixels. A comprehensive description of DIC can be found in [42]. The field of view was centred at the coupon mid-section and covered approximately 70 mmof the gage length and the entire specimen width. A facet size of 17x17 pixels with a 2 pixels overlap yielded a good compromise between measurement noise level and local field resolution. The linear strain in each facet was computed over a 3x3 subset window. In case not all adjacent facets exist, the strain in the centre facet was determined with a default validity quote of 55% [43]. Stress-strain curves were generated by averaging the full surface strain field, except for cases of significant surface cracking. Here, the macroscopic strain was calculated using a virtual extensometer over the complete measurement window to avoid any influence of artificial high strain computations in facets with underlying surface cracks. Final failure of the specimens was investigated with a PHOTRON SA5 high-speed camera operated at a rate of 20000 frames per second. For a field of view of similar size to the DIC, a maximum camera resolution of 384x880 pixels was achieved, with appropriate lighting provided by a 400 W flood light.

3.2.3 Experimental Methodology

For the monotonic tests, the elastic modulus was determined by a moving window least squares fit of the stress-strain curve. In the case of incremental loading, damage was characterised in terms of a macroscopic modulus degradation for each braided material. The corresponding scalar damage variable d was obtained after each unloading cycle according to [37]:

$$d_{\mathrm{i}} = 1 - \frac{E_{\mathrm{i}}}{E_0} \tag{3.1}$$

where E_{i} is the unloading modulus calculated from the end points of the loading and unloading part of cycle i as is shown in Fig. 3.4, such that the effects of a potential unloading/reloading hysteresis are minimised. The initial elastic modulus E_0 is calculated from a moving least squares fit in the first loading cycle. The

accumulated inelastic strain component $\langle\varepsilon_{\mathrm{ie,i}}\rangle$ was determined from the maximum nominal stress σ_{i} in cycle i by

$$\langle\varepsilon_{\mathrm{ie,i}}\rangle = \langle\varepsilon_{\mathrm{i}}\rangle - \frac{\sigma_{\mathrm{i}}}{E_{\mathrm{i}}}, \tag{3.2}$$

where $\langle\cdot\rangle$ denotes a volume averaged variable. The scalar damage variable and the inelastic residual strain represent homogenised material quantities caused by a combination of plasticity and failure modes occurring within the material, such as matrix cracking inside the yarns as well as in the resin pockets, intra- and inter-yarn delaminations, fibre-matrix debonding, and progressive fibre failure.

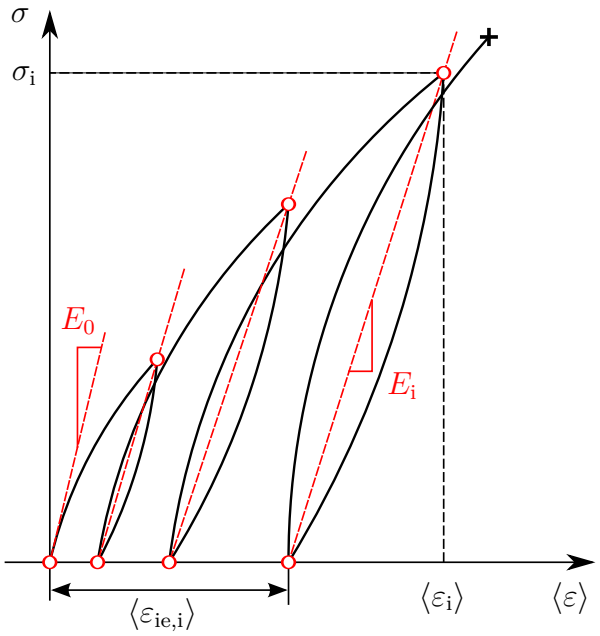

Fig. 3.4: Determination of damage and inelastic strain from loading/unloading cycles

3.2.4 Analytical Modelling

The overall impact of the textile architecture on the elastic properties is approximated by comparing experimental data with equivalent tape laminates using classical lamination theory (CLT). Several modelling approaches exist for predicting the effect of waviness on the elastic properties of braided composites [19, 44, 45]. By comparing the experimental results to equivalent laminates without crimp, however, the possible knock-down of mechanical properties can be quantified directly. For triaxial braided composites, an equivalent laminate can be constructed by virtually separating the axial yarns, the braid yarns and the pure resin pockets. Each constituent is then modelled either with a single unidirectional ply in the respective

fibre direction or represented by an isotropic layer, as is the case for the matrix pockets. The relative yarn ply thicknesses in the laminate model correspond to the volume fractions of axial and braid yarn content given in Table 3.1. With the intra-yarn FVFs determined from microscopy, the relative thickness of the matrix ply is selected such that the overall FVF is satisfied. As a result of this approach, no textile architecture is considered, and a quantitative assessment of the mechanical property knock-down can be made in the linear-elastic regime. The homogenised elastic properties of the plies given in Table 3.3 were derived from the fibre and matrix properties given in Table 4.6 using the micromechanical equations from [46].

Table 3.2: Elastic properties for fibre and resin [2]

Fibre: Tenax HTS40 12k (800 tex)				Resin: RTM 6	
E_{1f} (MPa)	E_{2f} (MPa)	G_{12f} (MPa)	ν_{12f}	E_m (MPa)	ν_m
210000	18000	21800	0.305	2890	0.35

Table 3.3: Homogenised elastic properties of the unidirectional plies

Intra-yarn FVF (%)	E_1 (MPa)	E_2 (MPa)	G_{12} (MPa)	ν_{12}
63	133369	8660	4364	0.322
66	139583	9087	4705	0.320
70	147867	9709	5236	0.319

3.3 Results and Discussion

3.3.1 Elastic behaviour

The linearised elastic moduli of the three braid architectures are compared to their respective CLT predictions in Fig. 3.5(a) as a function of the off-axis angle ψ. Assuming orthotropic material behaviour, the missing experimental in-plane shear modulus G_{xy} can be calculated from the off-axis Young's modulus in braid yarn direction ($1F$). This enables us to highlight differences between experiments and analytical predictions under arbitrary off-axis angles through a mere transformation of the stiffness matrix. To compare the three braided configurations, the elastic

moduli were normalised to a FVF of 56 %, and error bars indicate one standard deviation.

Due to CLT neglecting any undulation, it generally predicts larger moduli in relation to the experimental results. For loading in the x direction, only a minor decrease of the material properties can be observed. Here, the total homogenised stiffness is composed of a substantial contribution of the predominantly straight axial yarns superimposed by the load carrying capability of the undulated braid yarns. Most of the stiffness drop in this direction may be attributed to a combination of multiple textile phenomena: the presence of minor fibre in-plane and out-of-plane waviness in the axial yarns caused by the braiding process in combination with nesting and uneven compaction. Additionally, the axial fibre bundles tend to spread in regions where they are primarily surrounded by matrix pockets and lack support from adjacent braid yarns. Despite having the highest ratio of axial fibre volume content, the [0/±30] configuration exhibits the largest knockdown in x direction. This tendency is consistent with a higher contribution of the wavy braid yarns to the overall stiffness. As expected, this configuration yields the highest modulus in the x direction, which makes it a preferable choice for structures primarily subjected to bending loads.

The Young's moduli in the 1F direction are significantly lower compared to their equivalent laminate counterparts. This case yields the most severe reduction of the overall mechanical properties, as the heavily undulated braid yarns are loaded in their longitudinal direction. With increasing braiding angle, experimental and predicted moduli in 1F direction deviate progressively. The accompanying increase in braid yarn volume fraction combined with a larger bias orientation of the axial yarns contribute more and more to a degradation of the elastic properties, with a maximum relative error of 15.2 % for the [0/±60] braid. The stiffness reduction observed in the y direction is slightly larger than in the x direction. Here, no fibres are directly aligned with the load. In particular the axial yarns only contribute to the overall stiffness through their matrix-dominated transverse properties. Hence, any slight longitudinal contribution provided by the undulating braid yarns is amplified, even if the bias angle between the load direction and the braid fibre orientation is considerably high. A maximum relative error of 9.3 % can be observed for the [0/±30] case, in which the elastic modulus of 10 GPa is only slightly higher than the transverse properties of the yarns.

Fig. 3.5(b) summarises the results from the Poisson's ratio measurements. Given that only ν_{xy} serves as input for the homogenised stiffness matrix, the experimental results for other load directions diverge from those obtained by transformation.

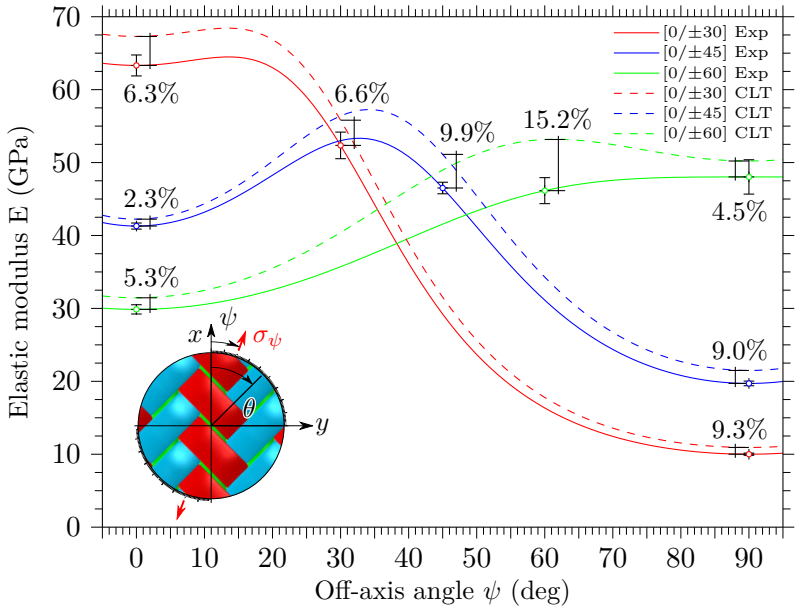

(a)

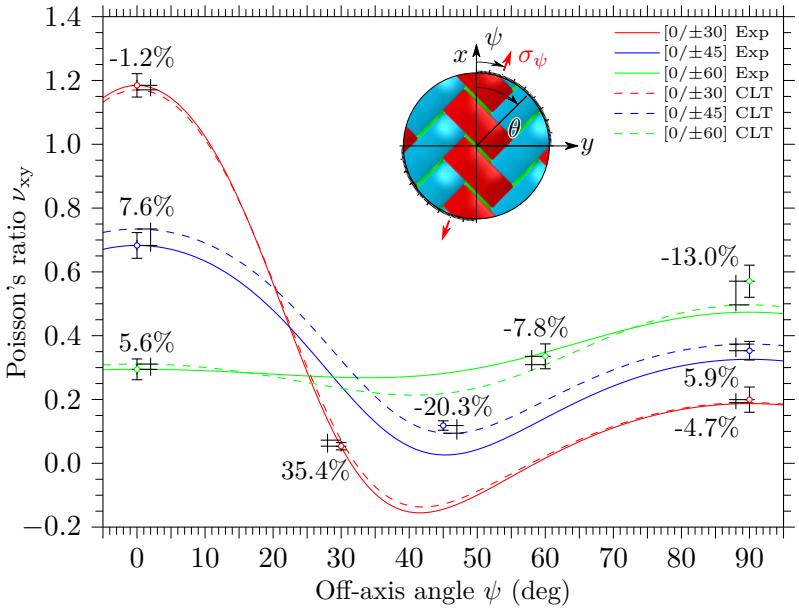

(b)

Fig. 3.5: Comparison of experimental and predicted Young's moduli (a) and Poisson's ratios (b) as a function of the off-axis angle ψ

The [0/±30] architecture exhibits the largest Poisson's ratio in the x direction due to the severe discrepancy of longitudinal and transverse stiffness and is comparable to results obtained by [30]. Furthermore, its specific lay-up induces an auxetic behaviour close to an off-axis angle of 40°, with a negative Poisson's ratio of approximately −0.1. As the braiding angle increases, the mismatch between longitudinal

and transverse stiffness becomes less pronounced, with a tendency towards balanced Poisson's ratios for the [0/±60] material. Except for the 1F direction, where the large relative error is connected to the Poisson's ratio converging to a value close to zero, the deviations between experiments and predictions are comparable to those of the elastic moduli. However, with the Poisson's effect comprising a ratio of transverse and longitudinal strain, no direct contribution of fibre waviness can be extracted. As a general observation, the analytical model provides a simple and robust method for approximating the elastic in-plane properties of all braid configurations. While it is not capable of directly capturing any fibre waviness and generally over-predicts the mechanical properties, it represents a viable tool for the determination of stiffness properties within a preliminary design phase, where usually only limited data on the detailed textile architecture is available.

3.3.2 Non-linear behaviour and damage characterisation

The non-linear mechanical behaviour of triaxial braided composites is highly anisotropic. Depending on the external state of loading, a variation of the tangent modulus can be attributed to a combination of material and geometrical mechanisms. The application of DIC allows us to investigate strain concentrations and characteristic damage morphology in terms of crack initiation and propagation on the specimen surface, and to assess their impact on the homogenised stress-strain response. The results of this investigation are discussed in the following sections for three different monotonic loading conditions.

3.3.2.1 Loading in the axial (x) direction

Typical stress-strain curves are presented in Fig. 3.6 for loading the three braid architectures in the axial (x) direction. In addition, the superimposed strain fields on the specimen surface are displayed for load levels of primary interest, such as transition regions in the stress-strain curve, the appearance of a first visible surface crack, and ultimately before final failure of the specimen. If not directly visible, surface crack locations are indicated by artificially high local strains due to the underlying displacement discontinuity which, for large crack openings, also causes automatic removal of the underlying facet. The grey dashed lines represent the elastic properties and allow us to emphasise the non-linearities in the stress-strain curves for progressive loading.

For the [0/±30] and the [0/±45] architecture, only a slight decrease in tangent modulus is observed. The surface strain fields for both configurations show strain

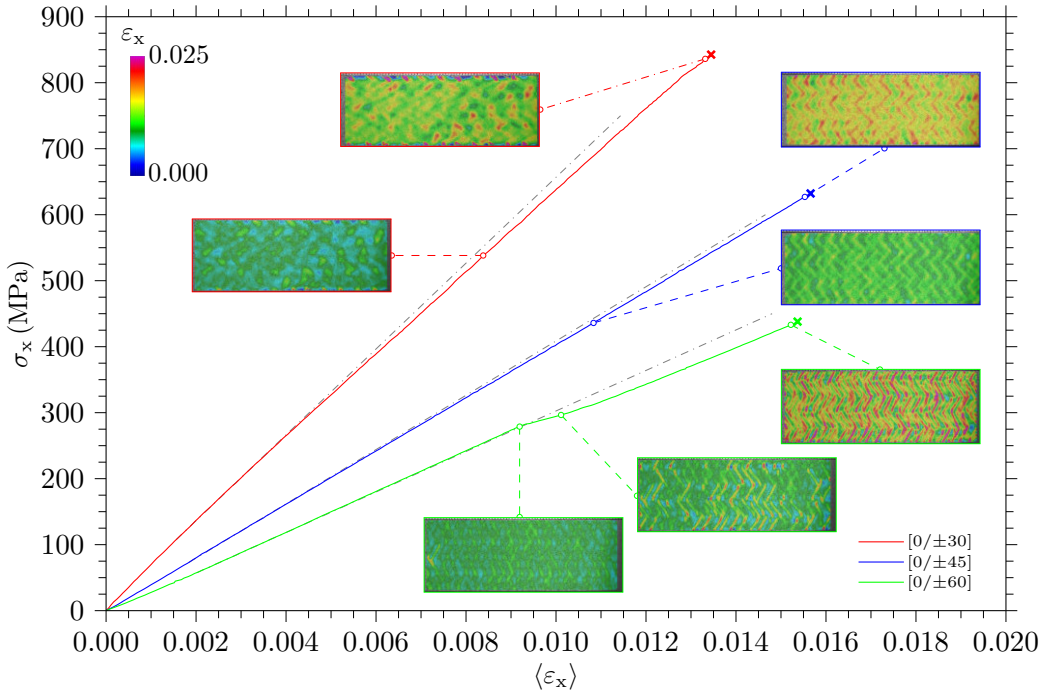

Fig. 3.6: Representative stress-strain curves and local strain fields for loading in axial (x) direction

concentrations at the resin-rich yarn-to-yarn junctions of the textile, but no evidence for matrix cracks except for localised edge damage shortly before final failure. As the overall mechanical response until final failure is dominated by the large stiffness contribution of the axial yarns loaded in the fibre direction, any possible geometrical and material non-linearity originating from the mesoscopic building blocks - the yarns and the matrix pockets - was found to have a negligible impact on the predominantly linear stress-strain response. Furthermore, while some of these phenomena are associated with a decrease in modulus, such as plasticity and damage, a competing stiffening effect on the stress-strain curve is induced by others. In the case of loading in the x direction, the primary load carrying carbon fibres in the axial yarns exhibit stiffening due to their non-Hookean constitutive behaviour [47–49]. At the same time, minor undulations in axial bundles caused by nesting effects of multiple braid plies diminish as the fibres align progressively with the load. The braid bundles are subjected to a state of multi-axial stress, particularly in-plane shear in the case of a braiding angle of 45°. The resulting non-linear contribution, however, is small, also due to fact that it is simultaneously counteracted by a lateral fibre reorientation in load direction.

The [0/±60] architecture exhibits almost linear behaviour up to a global threshold strain level of approximately 0.9 %. Up to this point, strain concentrations intensify

at the yarn cross-over points until first matrix cracks nucleate at multiple locations on the specimen surface parallel to the braid fibre direction, as a result of their combined shear and transverse tensile loading. Within each braid yarn, they propagate along one fibre direction until they are arrested at the adjacent intersecting bundle. Subsequently, a crack appears in the other braid fibre direction - possibly promoted by the stress concentrations of the preceding crack tip - thus creating a zig-zag crack pattern across the specimen width. Unlike in a tape laminate, for example in a cross-ply laminate where matrix cracks may easily propagate across the entire coupon width, the textile architecture of braids acts as a crack stopper. Similar findings are also reported in [27].

Above the threshold strain, crack development can be directly correlated with a bulge in the stress-strain curve, accompanied by a sudden decrease in modulus. As the specimen is further loaded and saturating with cracks, the crack density increases from a single crack per yarn to an average of 2-3 cracks while the tangent modulus subsequently converges back to its initial magnitude. This stiffening effect may be the product of two overlying mechanisms: Firstly, after the braid yarns crack and become more compliant, more loads are redistributed back into the axial fibres. Secondly, the formation of multiple cracks removes constraints in the material, which promotes further alignment of fibres in the load direction. A post-mortem micrograph normal to the axial yarns in Fig. 3.7 highlights the through-thickness crack formation in the [0/±60] braid. In contrast to the undamaged axial bundles, a maximum density of three matrix cracks per yarn is evident in the braid direction, with some additional cracking inside the resin pockets. These findings are consistent with the DIC results. Depending on the stacking configuration, dry yarns of adjacent plies and equal orientation nest into each other during compaction and create a locally merging fibre bundle without a visible interface. Hence, crack growth from one ply to another is facilitated in the through-thickness direction. Coalescing cracks of non-aligned fibre direction are rarely observed, except for a single case in which a crack migrates into a thin resin pocket and further into an adjacent yarn. Generally, a very limited number of delaminations confined to small regions around crack tips were observed for loading in longitudinal direction.

3.3.2.2 Loading in the transverse (y) direction

Severe non-linearities exist in all materials for loading in the transverse (y) direction as shown in Fig. 3.8. The [0/±45] and the [0/±60] braid exhibit a gradual decrease in stiffness. For the latter, no discrete cracks appear on the specimen surface, again with the exception of edge initiated damage. However, multiple sites of

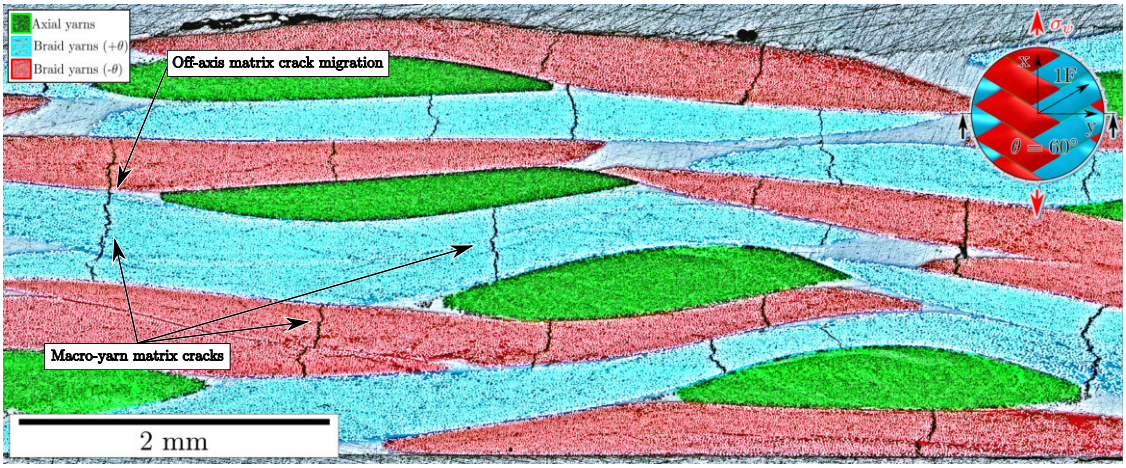

Fig. 3.7: Crack pattern in a [0/±60] configuration subjected to axial loading obtained by optical microscopy

high strain concentrations at elevated load levels correlate with the positions of the underlying axial yarns, indicating subsurface failure events as a result of transverse tensile stresses. Considering the absence of any gaps between adjacent braid yarns, as can be seen in Fig. 3.1, their formation cannot be directly monitored, yet an investigation of the respective microsections confirmed their presence. A similar damage morphology was observed for the [0/±45] material. Initially, a gradual decrease in tangent modulus is attributed to the primary contribution of the braid fibre direction to the overall stress-strain curve through its non-linear shear behaviour. Unlike the previous case, the mechanical response is now not controlled by the large fibre stiffness in the load direction. Above a threshold stress of approximately 120 MPa, initial cracks appear in the axial yarns. Contrary to the [0/±60] braid, minor gaps in the textile allow local camera vision onto small segments of axial fibre bundles where most of the initial occurrences of cracks are identified. In the DIC image, a straight crack opens, running parallel to the axial fibre direction across the entire length of the visible uncovered section at the location of the gap between two braid yarns. Consecutively, both crack tips develop into the braid fibre direction at their opposing ends until they get arrested at the next cross-over point, again highlighting the step-wise crack development in braided composites. Supported by evidence from the micrographs in Fig. 3.9, the cracks in the axial yarns extend along their entire thickness. In case they contact an adjacent braid yarn, they further follow along the interface and create a localised delamination. After a certain length, a crack migration into this braid yarn can occur. Gradually, a complex crack network is created. This comprises several matrix cracks in neighbouring bundles connected by a multitude of delaminations or branching into the neat resin. As a consequence of this phenomenon, the stress-strain curve ex-

hibits a significant degradation until final failure occurs when the tangent modulus approaches approximately a quarter of its initial magnitude.

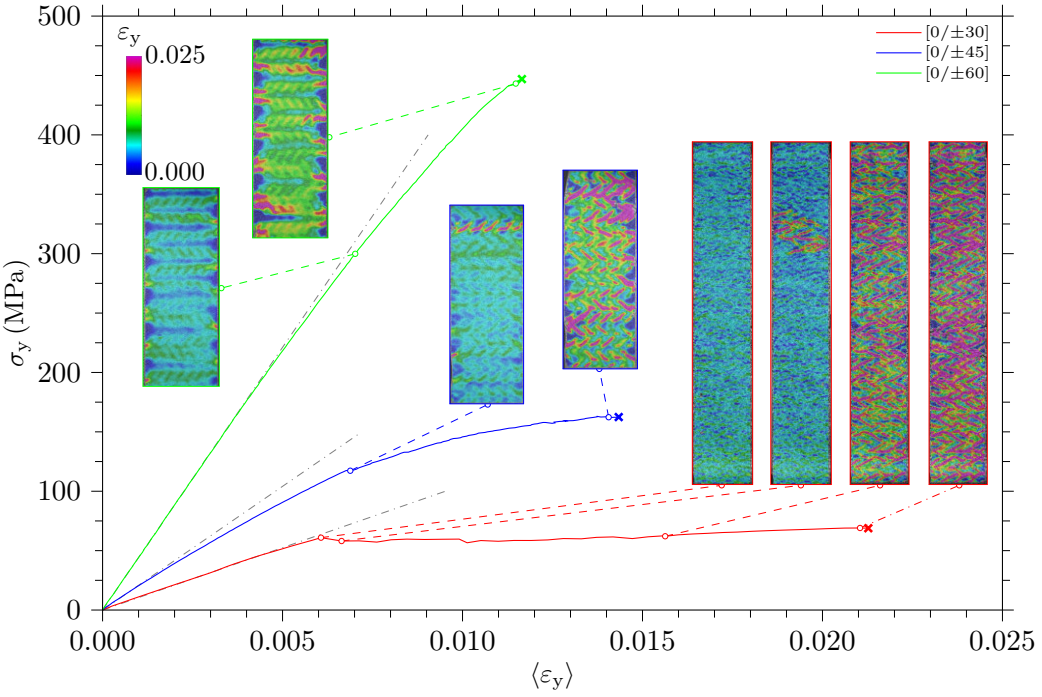

Fig. 3.8: Representative stress-strain curves and local strain fields for loading in transverse (y) direction

The [0/±30] braid features the most complex damage behaviour for this load condition. Here, the material response can be separated into three distinct domains up to final failure: an approximately linear domain, a damage progression domain, and a saturation domain. As the applied load is increased in the linear domain, strain concentrations arise in the resin-rich areas between adjacent yarns, thus exposing the underlying textile architecture. When a critical load level is reached, the first matrix cracks form at the boundaries of adjacent yarns at a specific location across the specimen length. Their initial appearance can be correlated with the first major load drop, which marks the point of damage initiation at the end of the linear domain. While the damage morphology follows a similar pattern to the previous [0/±45] case, the effect on the stress-strain curve is considerably larger. In light of the fact that the [0/±30] material features the largest bias angle with respect to the fibres and the load direction, the compliance introduced by the formation of each crack can be correlated with small load drops. As the strain is further increased, the loads are redistributed and the stress level exhibits a stable plateau as a result of progressive damage development. This behaviour is associated with the continuing development of matrix cracks, originating from the initiation location on the

coupon. When the entire specimen is saturated with cracks, a small increase in load can be observed. In this domain, the existing cracks exhibit further opening. Final failure of the specimen is induced when multiple cracks coalesce across the specimen width.

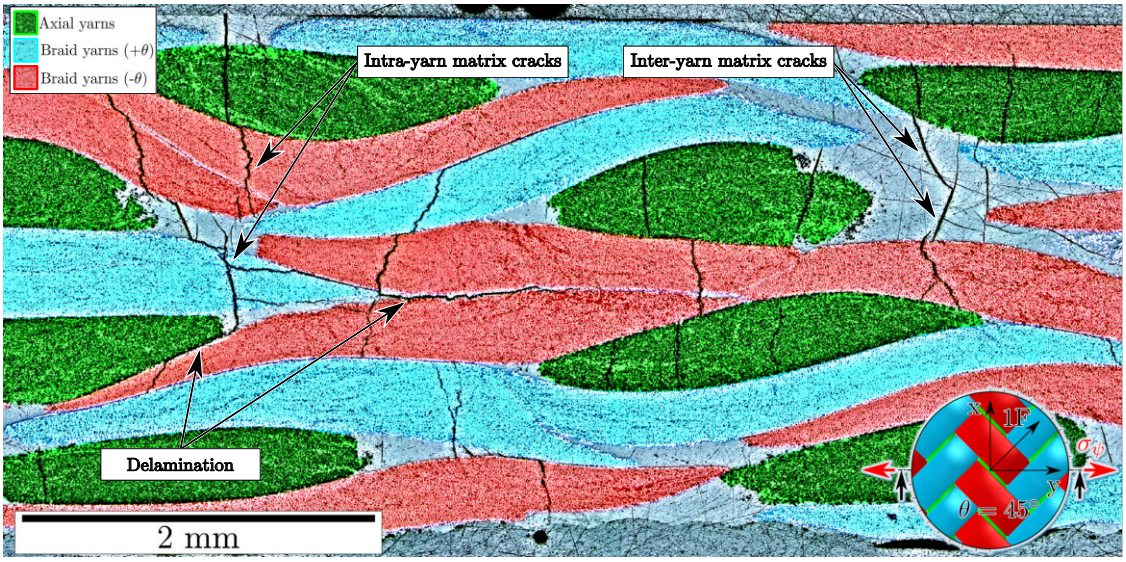

Fig. 3.9: Crack pattern in a [0/±45] configuration subjected to transverse loading obtained by optical microscopy

3.3.2.3 Loading in braid yarn ($1F$) direction

The textile architecture has the greatest effect on the mechanical response for loading in the braid fibre direction ($1F$), as is shown in Fig. 3.10. Up to a homogenised strain level of $\langle \varepsilon_{1F} \rangle \approx 0.6\%$, all braid architectures exhibit approximately linear stress-strain behaviour.

Beyond this threshold point, distinct load drops can be attributed to a progressive failure mechanism intrinsic to the textile architecture: as the highly crimped braid yarns are aligned with the external load, they straighten along their longitudinal direction. Hence, intersecting axial fibre bundles are subjected to an out-of-plane displacement which is at first inhibited by the overlying braid yarns and the support of adjacent plies in the through-thickness direction. Once the resulting out-of-plane stresses trigger failure in the interface, a large delamination zone is created and extends across the entire specimen width along a single subsurface axial yarn. Simultaneously, the localised loss of through-thickness support causes an abrupt pull-out of this fibre bundle, accompanied by several secondary matrix cracks in the overlying braid yarns. The DIC images in Fig. 3.10 detail

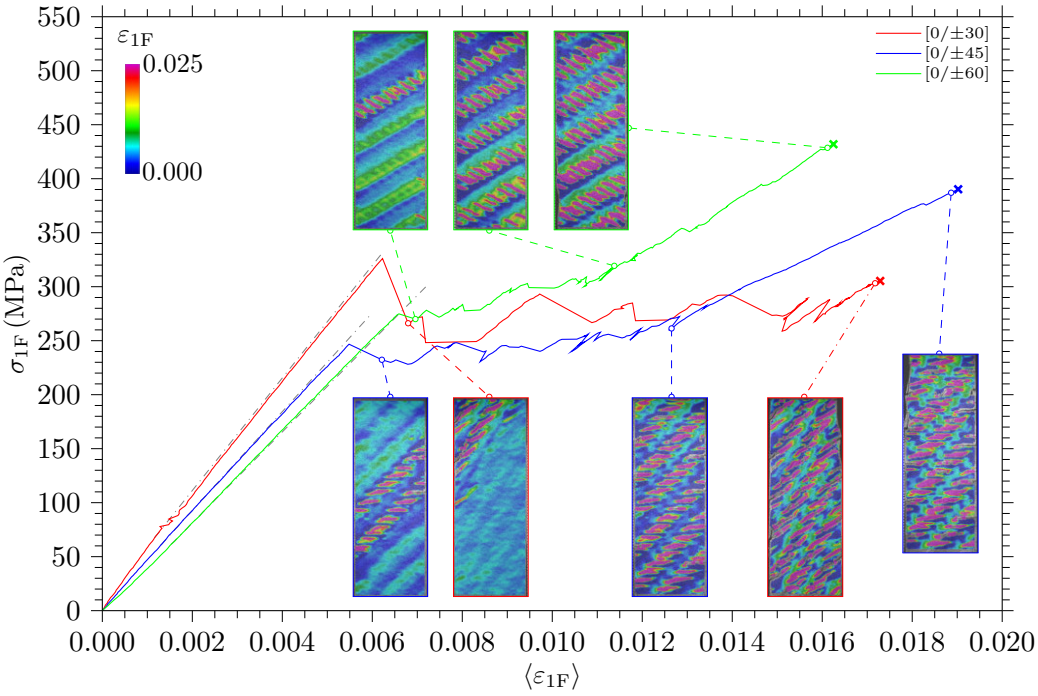

Fig. 3.10: Representative stress-strain curves and local strain fields for loading in braid yarn ($1F$) direction

the strain field after an initial pull-out event for each braid configuration. Due to the abrupt and unstable nature of this failure mode, a sudden increase in the homogenised strain combined with a slight load drop can be observed. When the applied strain is further increased, the progressive pull-out of fibre bundles fabricates a plateau-like stress-strain response. This behaviour shows similarities to the previously mentioned [0/±30] transverse load case, but originates from a different failure mechanism and at considerably higher stress.

Fig. 3.11 displays a detailed view of the strain field for the [0/±45] material after several axial yarns have debonded. The secondary matrix cracks are clearly visible and the heterogeneous shading on the coupon surface underlines the mismatch of out-of-plane displacement of adjacent axial yarns. When a nominal textile geometry derived from Table 3.1 is mapped onto the specimen surface, the locations of matrix cracks reveal that the pull-out effect is confined to every second axial bundle. If we consider the cross-sectional cut A-A, it becomes evident that the braid yarns oriented along the coupon width provide only limited resistance against out-of-plane deformations at the coupon surface. Without the through-thickness support of an adjacent layer, the outer plies tend to promote the initial formation of delamination and subsequent bundle pull-out in regions where the out-of-plane deformation is oriented to the outside of the specimen. While the first event was

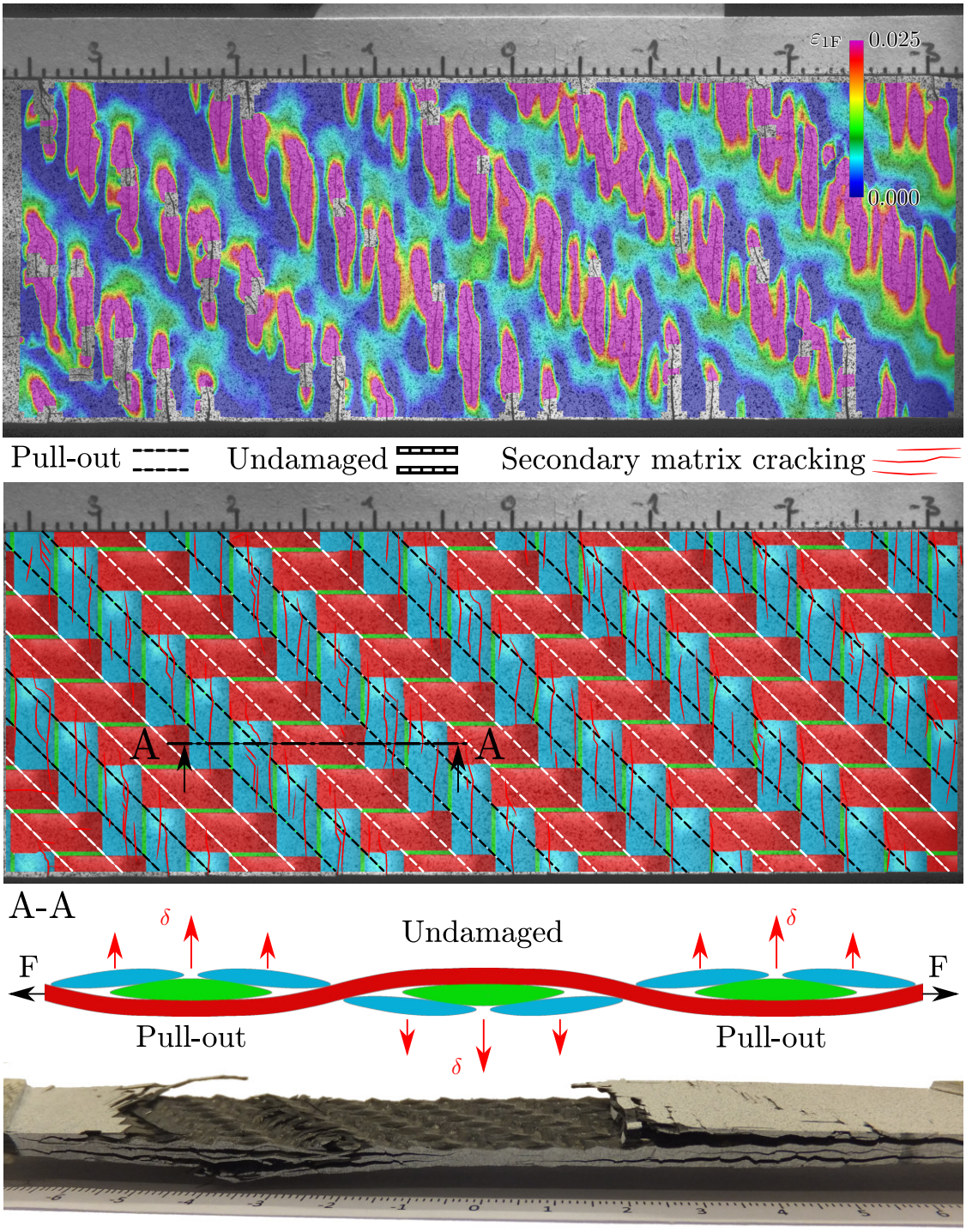

Fig. 3.11: DIC surface strain field, crack pattern, failure mechanism and ply separation during ultimate failure of a $[0/\pm45]$ braid subjected to loading in braid yarn ($1F$) direction

observed at a random location, probably triggered by the weakest unit cell, subsequent pull-outs progressively occur in direct proximity at the next but one bundle and propagate along the specimen gage length in both directions until a saturation stage is reached. The cascading nature of this failure mechanism indicates some

weakening influence of braid yarns with multiple secondary matrix cracks. As a result of the textile architecture, these yarns are oriented along the specimen width, with some of them again inhibiting pull-out of the next potential axial bundle after one undulation interval. At the end of the plateau strain, the delaminations have completely interconnected in each of the three ply interfaces. After a full separation of the braided layers along the entire gage length, each of them acts as a separate entity, and the mechanical response is again governed by the braid fibres aligned with the load. For the [0/±45] and the [0/±60] architecture, the sustainable load can be approximately doubled compared to the plateau initiation before final failure. In addition to the many advantages of applying DIC measurement techniques to textile composites summarised in [36], the 3D DIC set-up allowed us to identify and measure the out-of-plane deformation of the braid bundles during the progressive pull-out mechanism.

3.3.3 Evolution of damage and inelastic strain

In order to identify the driving physical mechanisms behind the material non-linearity, the evolution of the homogenised damage variable and the accumulated inelastic strain is quantified as a function of the total strain in Fig. 3.13(a) and (b), respectively. Each of the data points corresponds to a completed cycle and a polynomial fit illustrates the average evolution of both variables up to the failure strain of the corresponding test series. Due to a problem in the data acquisition during the incremental loading/unloading tests parallel to the braid fibre direction of the [0/±30]material, this test case is not included. The stress-strain response and strength of all loading/unloading tests were very similar to their monotonic counterparts, indicating that unloading and reloading had no substantial effect on the constituent failure mechanisms, as is highlighted in Fig. 3.12. Depending on the degree of damage, the unloading and reloading cycles reveal hysteresis loops, possibly due to frictional effects at crack interfaces and failed fibre/matrix interfaces [28].

Consistently with the monotonic tests, only minor non-linearities are present in the material for cases in which the load is aligned with the axial fibre direction (x). Independently of the braiding angle, the damage variable for the [0/±30] and the [0/±45] braided composite remains at a steady level below 5 %. The inelastic strain shows a gradual increase. However, with a maximum magnitude of 0.05 % at an average failure strain of about 1.3 %, the total contribution for all braid configurations in axial direction remains negligible. The [0/±60] configuration exhibits a negative damage variable which indicates a slight stiffening effect upon loading

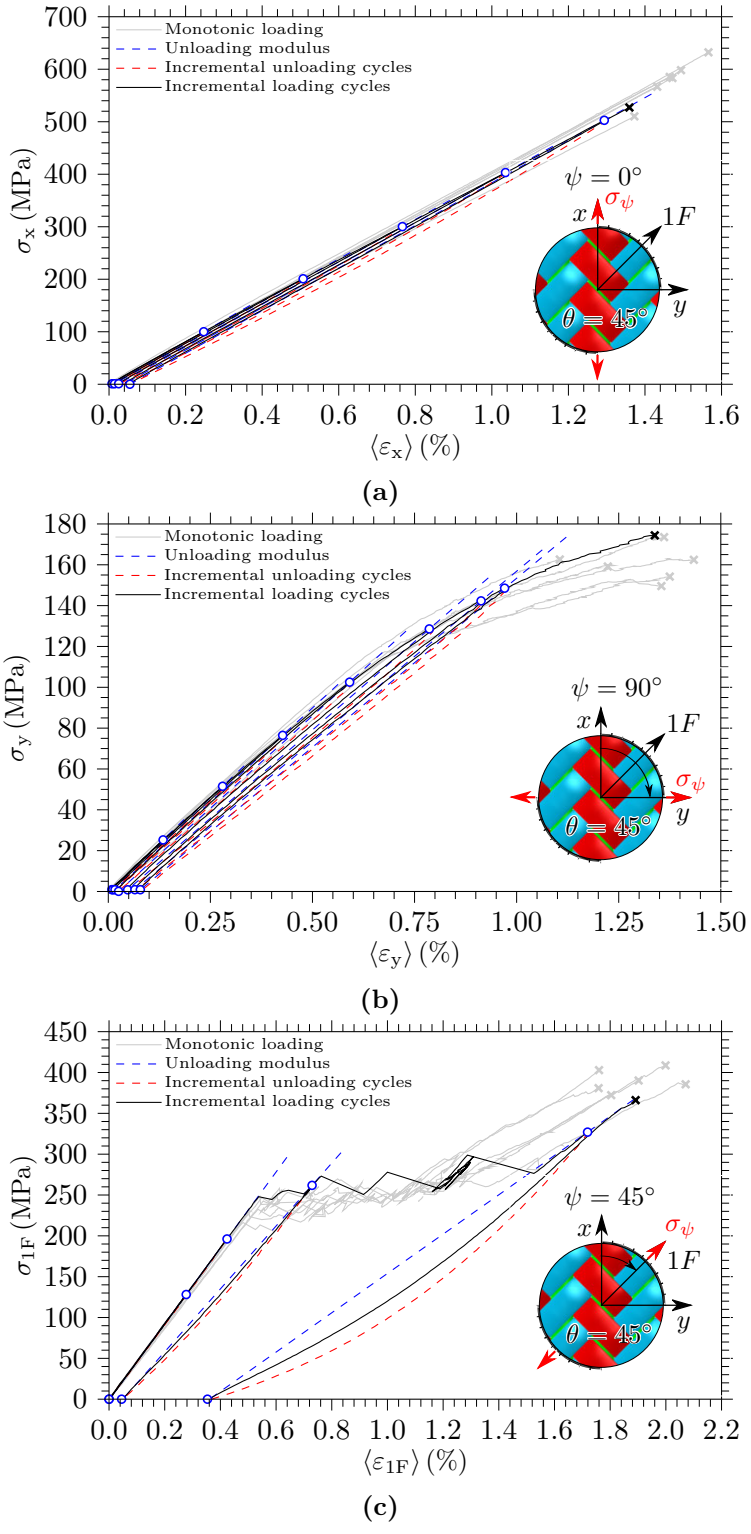

Fig. 3.12: Comparison of monotonic and representative incremental loading/unloading stress-strain curves for the $[0/\pm45]$ architecture loaded in the (a) axial (x), (b) transverse (y), (c) braid fibre direction ($1F$)

from a combination of initial axial yarn straightening. After the degradation at the onset of matrix cracking inside the braid yarns, the superimposed stiffening due to load redistribution and lateral fibre reorientation translates into a slight increase in both the damage variable and the accumulated inelastic strain until final failure. Recalling the stress-strain curves from Fig. 3.8, significant non-linearities occur for loading in the transverse direction. For both the [0/±60] and the [0/±45] cases, the damage variable and the inelastic strain grow steadily as a function of the applied strain. An accompanying increase of the damage variable at low strains suggests the presence of microscopic damage events. When the first macroscopic cracks appear in the axial and braid yarns at an applied strain of approximately 0.6 %, the rate of growth of the damage variable and the inelastic strain are amplified. Two separate domains in the mechanical response of the [0/±30] are clearly visible in the loading/unloading experiments. In the first domain, the highest gradual increase in damage amongst all architectures is accompanied by a negligible increase in inelastic strain. Here, strain concentrations arise at the yarn interfaces, but no macroscopic cracks are visible on the specimen surface yet. Following their first appearance at the initiation site and the subsequent propagation across the entire coupon, the increasing crack density can be correlated with an abrupt increase in both the damage variable and the inelastic strain. As the applied strain is further increased, and the coupon is saturating with cracks, the rate of damage and inelastic strain growth recedes consistently. Now, crack growth is replacing the formation of new cracks as the driving damage mechanism. Before final failure of the specimen, the modulus has degraded to almost 50 % of its initial value, at a considerable inelastic strain of 0.35 %.

Subdividing the mechanical response into two separate domains is also viable in the case of loading in braid fibre direction ($1F$). Before the first pull-out event, all materials follow an almost identical path, including negligible damage and inelastic strain accumulation. As soon as the first delamination zone forms and induces axial yarn pull-out, both the damage variable and the inelastic strain increase drastically. The transition into this failure mode is triggered at a slightly lower strain of 0.5 % for the [0/±45] case in comparison to the [0/±60] configuration. During the progressive ply separation in both materials, the evolution of the damage variable again follows a very similar path. Due to its higher failure strain of more than 1.7 % and its earlier failure mode transition, the [0/±45] case is capable of sustaining a comparably larger loss in modulus and accumulation of inelastic strain before final failure than the [0/±30] braid subjected to transverse loading. If we consider that the increase in inelastic strain is negligible before the initial appearance of cracks in the [0/±45] transverse load case, where both braid yarn directions are predom-

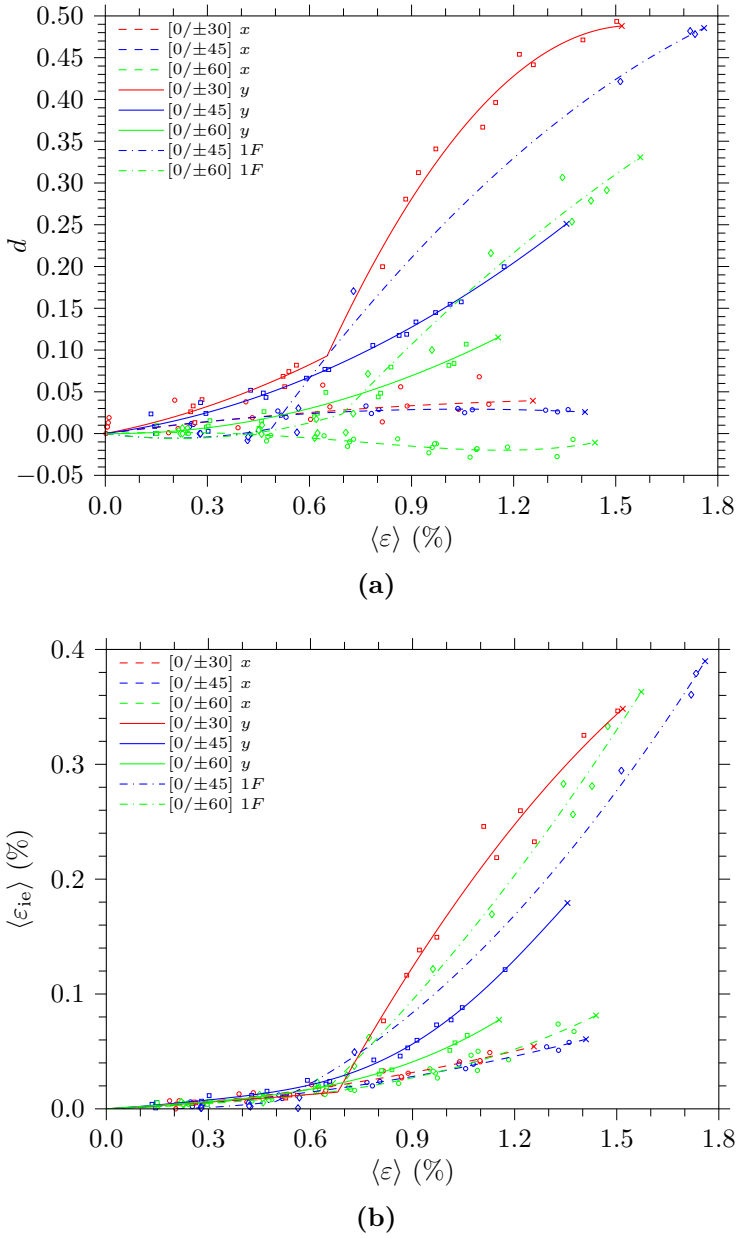

Fig. 3.13: Evolution of the scalar damage variable d (a) and the accumulated inelastic strain $\langle\varepsilon_{\text{ie}}\rangle$ (b) as a function of applied strain

inantly loaded in shear and contribute significantly to the overall stiffness, we can conclude that the overall impact of plasticity in the yarns is small compared to the effects of matrix cracking. Having identified matrix cracking and delaminations as the primary source of non-linearities in triaxial braids, we observe that both of these failure modes introduce significant damage and inelastic strain into the material.

3.3.4 Final failure modes

After investigating the non-linear mechanical behaviour, a better understanding of the mechanisms which trigger catastrophic failure is key to the design of more damage-tolerant braided composite materials. In Fig. 3.14, the development of final failure for a representative specimen of each test case is studied using a sequence of three images recorded with a high-speed camera. The first one highlights the state of the specimen immediately before failure with a maximum resolution of 0.05 ms. The second image captures the short-term formation of a fracture zone propagating across the entire coupon width. This process allows for very rapid movement of the fracture surfaces and is typically accompanied by a certain degree of motion blur. Lastly, the third image represents the post-mortem state. Since no data was available for the [0/±30] y configuration, we focus solely on the post-mortem inspection in this case.

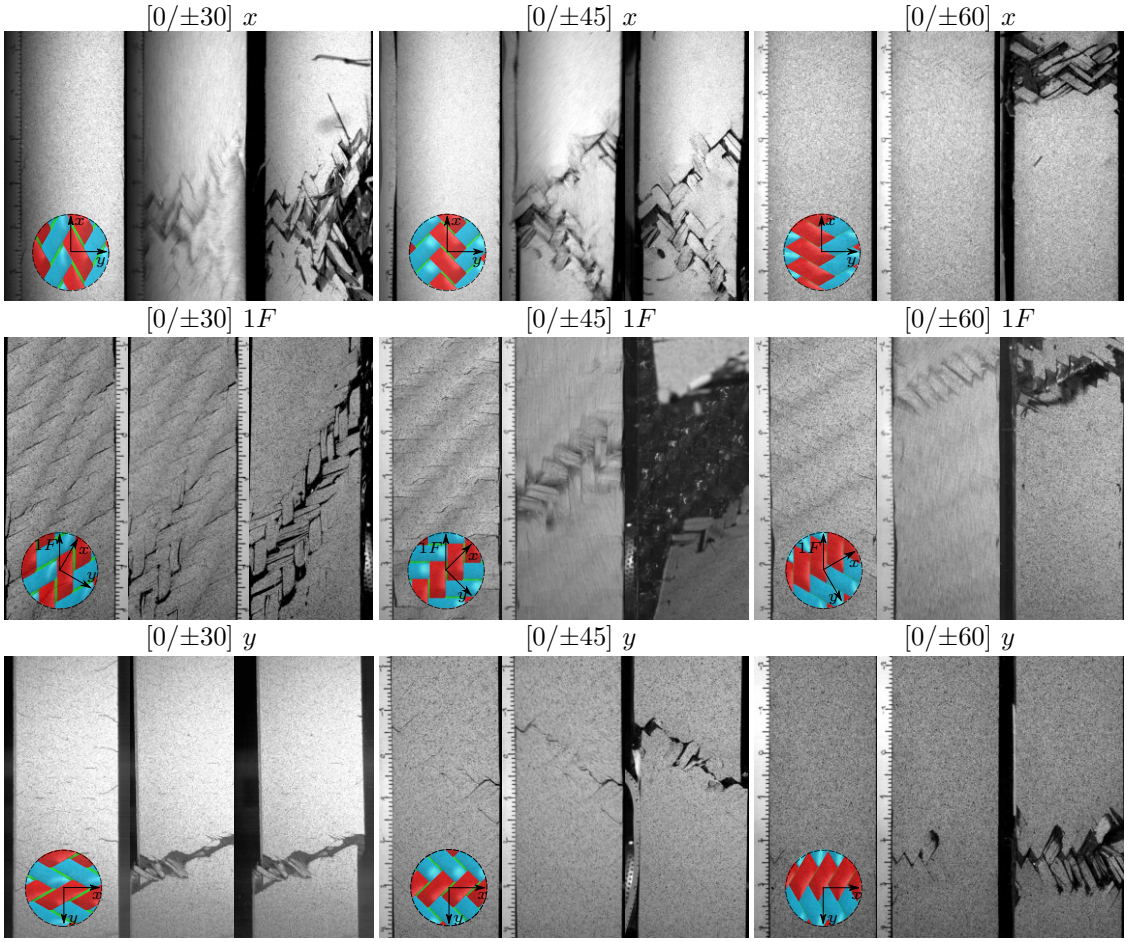

Fig. 3.14: Final failure process recorded with a high-speed camera

All braid architectures loaded in take-up direction develop a bidirectional V-shaped fracture zone which extends across the coupon width along both intersecting braid fibre directions. The absence of visible surface cracks and the initial axial movement of the specimen suggests that catastrophic failure for a braiding angle of 30° and 45° is triggered by rupture of axial yarns. Due to the resulting high amount of energy getting released, several additional fibre bundles disintegrate and large pieces of debris are explosively separated from the specimen. For the [0/±60] case, several matrix cracks propagate rapidly in a zig-zag pattern across the coupon immediately before catastrophic failure and further promote failure of the underlying axial yarns at the same location. Final failure of all materials loaded in 1F direction is dominated by fibre fracture in the load aligned braid yarns. After all plies have completely delaminated and the load is further increased, fibre bundles break at their respective yarn cross-over point. When viewed from the top, each yarn ruptures at an angle coincident with the intersecting braid fibre direction. With the ply losing its primary load carrying capability, a stair-case shaped band of cracked braid yarns propagates rapidly across the coupon width. Due to the excessive recoil, large pieces of individual layers may disintegrate and allow camera vision the fractured braid ply interface.In contrast to the previous cases, the final failure for the transverse load cases is confined to a small region. Here, a single macroscopic crack develops along one of the braid fibre directions, promoted by the previously existing matrix cracks. The intersecting braid yarns initially prevent a complete coupon separation. However, due to the opposing lateral movements of the fracture surfaces, they fail as a result of excessive rotation.

3.4 Conclusions on experimental material characterisation

Within this study, the damage and failure behaviour of triaxial braided composites was investigated under multi-axial stress states introduced through uni-axial off-axis tests. Digital image correlation measurement techniques were used to quantify the effects of the textile architecture and its heterogeneity on the strain field, to identify and locate constituent failure mechanisms and to investigate damage initiation and development. Microsections of the specimen were analysed for the purpose of geometrical material characterisation and assessment of failure mechanisms in the thickness direction. The evolution of the damage variable and the accumulated inelastic strain was quantified using incremental loading/unloading experiments. A high-speed camera was employed in order to study the dynamic

nature of catastrophic failure. The triaxial braids within this study exhibited severe non-linearities in the mechanical response before final failure. This phenomenon was primarily attributed to a complex damage behaviour composed of two characteristic mechanisms. In the first one, matrix cracks developed progressively in the yarns that were not aligned with the load direction. While we found the underlying textile architecture to slightly reduce the elastic properties compared to equivalent tape laminates, we conclude that it functions as a natural crack arresting grid and restricts the propagation of cracks to in between adjacent intersecting yarns, thus reducing their criticality. Loads can be redistributed without catastrophic failure of the material. In addition, a possible crack deflection can cause additional energy absorption. As a result of this mechanism, braids under certain load conditions were capable of withstanding a high strain to failure, even if a large portion of the specimen surface was saturated with matrix cracks. The accompanying mechanical behaviour can be desirable in the design of crash absorbing or pseudo-ductile materials. An additional failure mode intrinsic to the textile architecture was encountered for loading in the heavily undulated braid yarn direction. Due to yarn straightening induced out-of-plane deformations, braided composites were found to fail as a result of large scale delaminations accompanied by progressive fibre bundle pull-out.

This information can further serve as a baseline for the development of a numerical model for predicting the non-linear constitutive behaviour of braided composites. Having identified the failure morphology to be severely affected by the underlying textile architecture, the necessity of a meso-scale modelling approach becomes evident. In addition to a realistic representation of the internal geometry after compaction of multiple braided layers, the potential development of a bundle pull-out mode requires failure to not only be captured inside the yarns or matrix pockets, but also at their respective interfaces.

4 Development of a meso-scale simulation framework

In this chapter, a novel simulation framework is proposed for accurately predicting the mechanical response of highly compacted triaxial braided composites using meso-scale finite element models. Unit cells with a realistic internal geometry are generated within an automated simulation work-flow. Local volumetric interpenetrations are removed from a nominal geometry in a fictitious thermal simulation step. A compaction simulation of a single textile layer is performed to the desired target fibre volume fraction while implicitly considering multiple plies in different nesting configurations through periodic boundary conditions. For mechanical simulation, a matrix pocket mesh is created from a reconstruction of the deformed textile. A novel meshing methodology incorporates branching cohesive yarn-to-yarn and yarn-to matrix interfaces for modelling delamination. The framework was validated by detailed comparison with experimental results for three braid architectures. The excellent correlation of the internal geometry and the elastic properties underlines the framework's potential for future damage modelling.

4.1 Introduction

Braiding combines an automated and reproducible process together with an excellent rate of material deposition for mass-production of high performance structures [50]. Accurately modelling the mechanical response of 2D braided composites, however, remains a challenging task due to their textile nature, which includes out-of-plane waviness, interactions between intertwining bundles and nesting of multiple plies in the through-thickness direction. Numerical modelling using meso-scale finite-element (FE) unit cell models provides a powerful tool to study the material behaviour of braided composites. Typically, a representative domain of the internal textile geometry is considered, wherein the constituent reinforcing yarns are explicitly modelled as solid continua. This approach can be applied to a variety of problems, ranging from determining dry fabric permeability or draping characteris-

tics to the composite mechanical response, including the prediction of stress-strain fields, macroscopic mechanical properties, and the investigation of the non-linear behaviour with damage initiation and development.

The fidelity of unit cell models is largely affected by a realistic representation of the underlying textile geometry. Geometry pre-processors, such as WiseTex [51] or TexGen [52] provide good results for a variety of textile architectures, but modelling highly compacted triaxial braided composites with global fibre volume fractions (FVFs) of $55 - 60\%$ remains challenging. Here, the non-orthogonal interlacing of three in-plane fibre directions yields a complex internal geometry. After compacting multiple textile layers, the fabric features severely distorted yarns with multiple contact zones, locally varying intra-yarn FVF and fibre orientations.

Recently, increased research emphasis has been put on extending established textile modelling strategies [53] to more realistic geometry models [54]. Hivet and Boisse [55] developed a consistent 3D CAD formulation devoid of interpenetrations for the forming simulation of 2D woven fabrics in which contact zones between yarns are represented by shared geometrical faces. Using a hypoelastic material model for the yarns, the compaction and nesting behaviour of stacked 2D woven fabrics was investigated by [56]. In addition, Grail et al. [57] developed a mesh distortion algorithm to remove the resulting mesh inconsistency between orthogonal yarns after forming and investigated the mechanical performance of the resulting composite unit cell. Other researcher have tried to mimic the dry fabric behaviour by representing each bundle through several chains of one-dimensional finite elements in contact, thus explicitly rendering the effect of inter-fibre sliding [58, 59]. While results of the investigated 3D woven geometry agree well with microâ€“computed tomography (μCT) scans, a sophisticated post-processing technique is necessary to reconstruct yarn surfaces and generate a volumetric mesh for further mechanical analysis. Additionally, the multitude of contacts in the model is accompanied by a high computational expense and limits the degree of model parallelisation. Green et al. [60] studied the mechanical response of the above mentioned geometry using FE voxel discretisation and found significant differences between nominal and deformed geometry. Further studies on voxel modelling of textile composites [61, 62] concluded that although the elastic properties are in good agreement with a conventional mesh discretisation, the potential for simulating damage initiation and propagation is limited due to artificial stress concentrations induced by the staircase-like representation of the geometry. Additionally, the inadequate representation of the yarn interfaces impedes the possibility to model delamination in the unit cell. Another approach for obtaining a representative geometry model is the direct reconstruction of image data. Compared to a nominal geometry model,

Naouar et al. [63] obtained an improved correlation with forming experiments of a single layer of dry woven fabric obtained from μCT images. Faes et al. [64] created a detailed 2D representative volume element (RVE) model of microscopic images taken from polished specimen edges to study the stress distribution in multiple nested layers. Considering the high geometrical characterisation effort for a single localised geometry, these inverse modelling approaches provide only limited capabilities for predicting the mechanical response of multiple textile architectures. In the presented work, the authors propose a modelling framework for predicting the mechanical response of triaxial braided composites using mesoscopic FE unit cells with a realistic internal geometry. The general procedure and the outline of the framework are derived from a list of key modelling requirements condensed from the previously mentioned literature:

1. Increased computational efficiency or modelling detail by
    - minimisation of the simulation domain through the use of reduced unit cell (rUCs) models and application of advanced in-plane periodic boundary conditions (PBCs) [65, 66]
    - implicit consideration of nesting and stacking effects in a single layer model through out-of-plane PBCs during an explicit compaction simulation to obtain highly compacted textile architectures
2. Accurate representation of the textile geometry, interface and properties without unsound assumptions by
    - an interpenetration-free geometry model without over-idealisations [67]
    - an improved representation of the yarn-to-yarn and yarn-to-matrix interface without the need of introducing and artificial matrix layer [68–71]
    - correct representation of the global FVF through a realistic axial and braid intra-yarn FVF [27, 57, 72]
3. High fidelity in the prediction of the non-linear mechanical response by
    - the capability to capture typical failure modes encountered in the yarns, in the matrix pockets, and at their respective interface [27]
    - a high quality structured hexahedral mesh in the yarns for accurate predictions of stress-strain fields suitable for the application of 3D continuum damage models [5]
    - a matrix mesh without severely distorted tetrahedral elements
4. High degree of automation in model generation through

- scripting for objectivity and easy accessibility to other users
- relying on software packages widely used and available within the research community. Throughout this work, all models are generated and solved in the unified FE package Abaqus controlled by MATLAB and the Abaqus Python scripting API [73].

This paper is structured as follows: in Section 2, the meso-scale modelling framework is introduced. The four key steps implemented in the simulation work-flow are outlined. From an initial idealised geometry model, a reduced unit cell domain is extracted, it's periodic boundary conditions are derived, and two subsequent process simulation steps are addressed, including the elimination of volumetric interpenetrations and the explicit compaction to the desired FVF. A novel algorithm for the generation of the complex matrix pocket mesh is introduced. In Section 3, the numerical model is validated against experimental data by comparing internal geometry features and elastic properties for three braid architectures. Finally, the capabilities and limitations of the modelling approach are discussed, highlighting possible future improvements.

4.2 Modelling framework

4.2.1 Roadmap and data flow

The modelling procedure is schematically shown in Fig. 4.1. Based on a reduced unit cell (rUC) concept to minimise computational expense [65], a compacted and interpenetration-free composite geometry is created within a three stage simulation process. In the first step, a nominal textile geometry is constructed from user-defined input parameters, such as braiding angle, yarn spacing and cross-sectional shape. As a result of the absence of initial contact between intertwining fibre bundles at this stage, local volumetric interpenetrations are resolved in a subsequent fictitious thermal step in which contact is established within the entire unit cell. In the subsequent compaction simulation step to the desired target FVF, flexible membranes which model the support of adjacent layers are added in through-thickness direction. By applying different sets of periodic boundary conditions to the latter, the compaction of multiple plies in different stacking and nesting configurations is implicitly considered at at reduced computational cost. This approach further enables us to render global FVFs of $55 - 60\%$ through intra-yarn FVFs obtained from experiments for the axial and braid bundles. Finally, the deformed hexahedral yarn mesh is used in a series of boolean operations to create a tetrahedral matrix

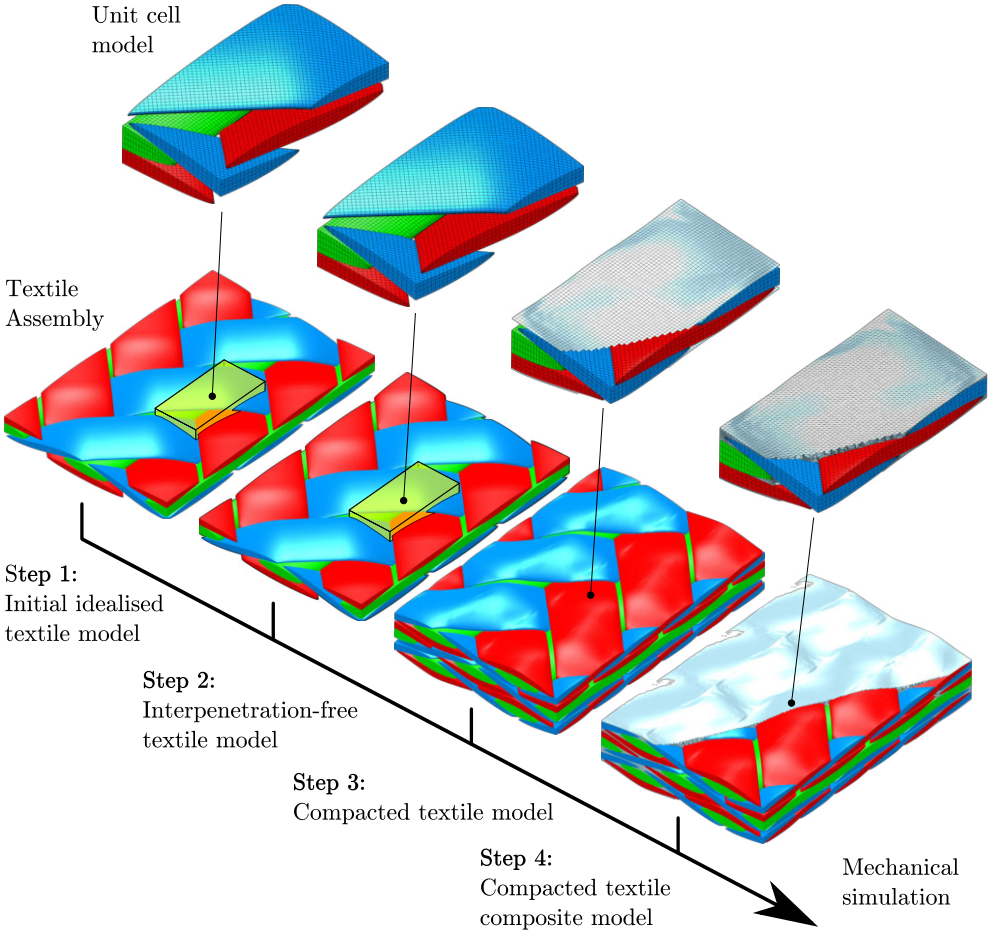

Fig. 4.1: Roadmap and data flow for generating a realistic unit cell model

pocket mesh with continuous yarn-to-yarn and yarn-to-matrix cohesive interfaces for modelling delaminations.

By obtaining the final geometry in a step-by-step approach, as opposed to inversely reconstructing geometry directly from μCT measurements [67], the overall robustness of the unit cell generation algorithm improves drastically for a broader range of textile geometries. Instead of dealing with all the complexity of a compacted textile at once, the task is subdivided and accounted for by several simulation steps. While the interpenetration correction step takes care of any potential overlaps in the initial analytical geometry model, mostly independent of the geometry input by the user, the compaction step further ensures consistency of both the global target and intra-yarn FVFs. The framework's high robustness is a key capability in order to cope with the large manufacturing variability in braided composites, where braiding angles in between 20° and 70° are commonly encountered across a typical component [1, 9].

4.2.2 Idealised geometry

In the step 1 of the framework, a surface mesh of the textile is generated from user-defined input parameters. Aside from the global braiding angle θ and the geometry of axial and bias bundles, including height, width, spacing and FE mesh size, their intra-yarn FVFs and the global target FVF are defined. Initially, a constant idealised cross-section is selected. Axial bundles indicated by the subscript a are assumed to be straight and their surface is described by a modified sinusoidal function

$$z_\mathrm{a} = \pm\frac{t_\mathrm{a}\,(1-\xi_\mathrm{a})}{2}\,\cos\left(\frac{y'_\mathrm{a}\,\pi}{w_\mathrm{a}}\right)^{n_\mathrm{a}} \pm \frac{\xi_\mathrm{a}\,t_\mathrm{a}}{2}, \quad \rightarrow \quad \text{cross-sectional term} \tag{4.1}$$

for which the required geometrical and global input parameters are displayed in Fig. 4.2, where the coordinate system $x_\mathrm{a,b}$,$y_\mathrm{a,b}$,$z_\mathrm{a,b}$ describes the master yarn surface and $x'_\mathrm{a,b}$,$y'_\mathrm{a,b}$,$z'_\mathrm{a,b}$ refers to the area centroid of a cross-section. The sign change indicates separate equations for the top and bottom surface. In a textile composite, the cross-sectional shape of a yarn is the product of the local preforming and compaction history and hence varies along its path. The sinusoidal term with a shape exponent n enables the generation of an adaptive cross-section capable of mimicking an arbitrary geometry through progressive morphing along its centre-line. Within an optimisation framework, it can also be used to minimise initial volumetric interpenetrations. Here, we exploit this geometrical degree of freedom to capture experimentally determined cross-sectional areas of bundles in addition to their width and height, such that consistency of FVF, fibre count and diameter are achieved. The effect of different magnitudes of the shape exponent n on the cross-sectional shape and area A for a typical yarn aspect ratio are highlighted in Fig. 4.3 (a) and (b), respectively. For $n = 1.0$, a nearly lenticular shape is reproduced, while the function closely resembles an ellipse with an exponent of $n = 0.5$. As n tends to zero, a rectangular cross-section with rounded corners is generated and the maximum area is achieved. For subsequent mesh quality purposes, the cross-section is truncated at a predefined side thickness of $\xi \cdot t$.

For both the positively (b+) and negatively (b−) oriented braid yarn surfaces, an adapted formulation of the model developed for biaxial braids [74] is implemented. The total yarn path is assembled by a straight and an undulated segment. The latter is constructed by superimposing the cross-sectional term by an additional sinusoidal function responsible for the waviness of amplitude $h_\mathrm{u} = t_\mathrm{a} + t_\mathrm{b}$:

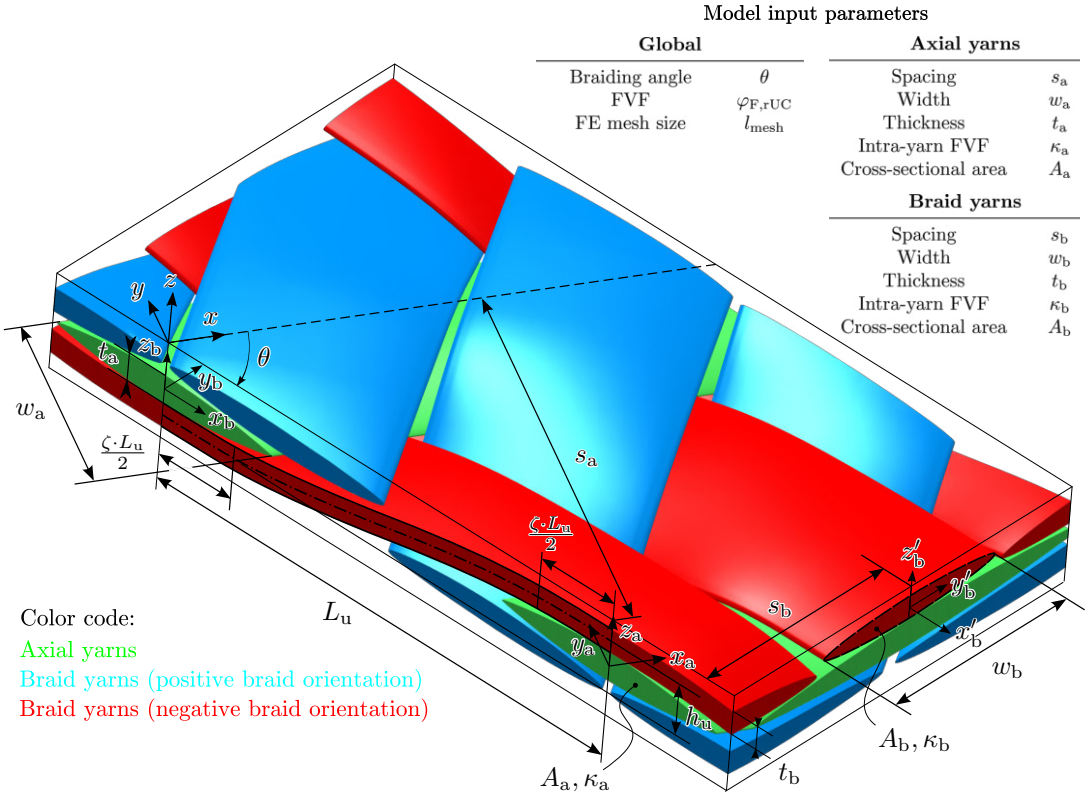

Fig. 4.2: Initial geometry representation and model input data

$$
\begin{aligned}
z_{\mathrm{b+,b-}}^{\mathrm{top,bottom}} = &\pm \frac{t_{\mathrm{b}}\,(1-\xi_{\mathrm{b}})}{2} \left|\cos\left(\frac{y'_{\mathrm{b}}\,\pi}{w_{\mathrm{b}}}\right)\right|^{n_{\mathrm{b}}} \pm \frac{\xi_{\mathrm{b}}\,t_{\mathrm{b}}}{2} \quad \rightarrow \quad \text{cross-sectional term} \\
&+ h_{\mathrm{u}}\,\sin\left(\frac{(x_{\mathrm{b}} - \omega_{\mathrm{b+,b-}})\,\pi}{L_{\mathrm{u}}\,(1-\zeta)}\right). \quad \rightarrow \quad \text{undulation term}
\end{aligned}
\tag{4.2}
$$

The opposite signs in Equation 4.2 create the top and bottom master yarn surface. The straight undulation segment is obtained from:

$$
\begin{aligned}
z_{\mathrm{b+,b-}}^{\mathrm{top,bottom}} = &\pm \frac{t_{\mathrm{b}}\,(1-\xi_{\mathrm{b}})}{2} \left|\cos\left(\frac{y'_{\mathrm{b}}\,\pi}{w_{\mathrm{b}}}\right)\right|^{n_{\mathrm{b}}} \pm \frac{\xi_{\mathrm{b}}\,t_{\mathrm{b}}}{2} \quad \rightarrow \quad \text{cross-sectional term} \\
&+ h_{\mathrm{u}}\,\mathrm{sign}\left(\sin\left(\frac{x_{\mathrm{b}}\,\pi}{L_{\mathrm{u}}\,(1-\zeta)}\right)\right). \quad \rightarrow \quad \text{straight term}
\end{aligned}
\tag{4.3}
$$

Both the positive and negative braid master yarn incorporate a braiding angle dependent localised phase shift given by

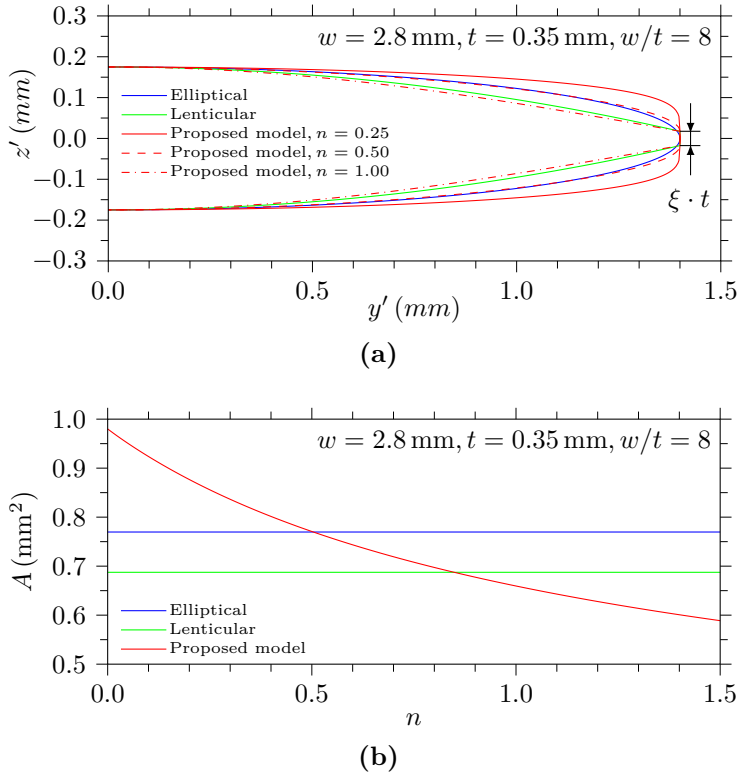

Fig. 4.3: (a) Comparison of cross-sectional yarn shapes (b) Effect of shape exponent n on resultant area

$$\omega_{\mathrm{b}+,\mathrm{b}-} = \pm y'_{\mathrm{b}} \tan\left(\frac{\pi}{2} - 2\,\theta\right) \cos\left(\frac{x_{\mathrm{b}}\,\pi}{L_{\mathrm{u}}}\right)^2 \tag{4.4}$$

into the undulation term, the volumetric shape can be analytically distorted while retaining a constant cross-sectional area. A key advantage of this approach lies in the significant reduction of mutual braid yarn interpenetrations compared to a fixed cross-section for braiding angles $\neq 45°$, as is exemplified for the non-orthogonal bundle intersections of a [0/±60] braid in Fig. 4.4 [74]. Each braid yarn is gradually distorted along its transverse direction by linearly increasing the phase shift. While the distortion term vanishes periodically at the intersection points of axial and braid yarns for minimised overlapping, it grows quadratically along the yarn path, until a maximum is reached at half of the wavelength L_{u}. Due to the closest proximity of braid yarns at their kinematic intersection point, the highest phase shift is introduced here.

It is worth mentioning that a pure rotation of cross-sections, as is often performed in woven composites [52], has shown only limited potential for an application in triaxial braids. In many cases, this procedure may reduce the interference with one entity on one side of a cross-section while causing a severe overlap on the opposite

side. Since no in-plane waviness is considered in the bundles, the transverse position in each cross-section $y'_{\mathrm{a,b}}$ is coincident to its representation within the master yarn $y_{\mathrm{a,b}}$.

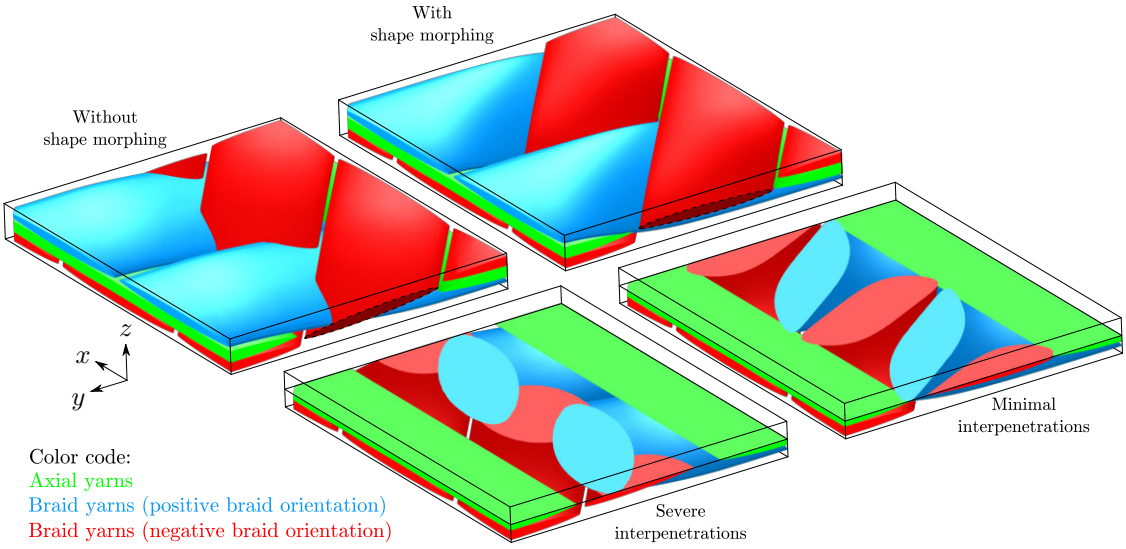

Fig. 4.4: Effect of shape morphing on volumetric interpenetrations for [0/±60] braid

From the analytical surface description, an undulated master yarn is constructed in MATLAB through a series of blended cross-sections. Each cross-section is discretised symmetrically about its y' and z' axis with the user-defined FE mesh size which will later serve as a blueprint for the structured hexahedral unit cell mesh. Furthermore, several pieces along the master bundle are extracted and assembled in the desired textile pattern. Unlike in a periodic biaxial braids, the three interlacing fibre directions in a periodic triaxial braid induce a geometrical interdependency of the braiding angle θ, the axial yarn spacing s_{a} and the braid yarn spacing s_{b} for a given textile pattern, independent of the subsequent unit cell size and type. Out of these three parameters, only two can be chosen arbitrary. By satisfying the geometrical compatibility equation defined as

$$s_{\mathrm{b}} = s_{\mathrm{a}} \cos(\theta) , \tag{4.5}$$

a correct representation of cross-over points within a given braid undulation interval is ensured. Apart from restricting the yarn width to be equal or smaller than its corresponding spacing, there are no limitations on the geometry. In the last step, the assembled textile is rendered in 3D space. This allows a direct visual inspection of the geometry, an early detection of interpenetrations by geometric slicing and, if desired, a quick modification of parameters. Finally, an arbitrary unit cell shape can be selected for extraction.

4.2.3 Reduced unit cell domain and mesh generation

In order to minimise computational effort, a rUC for triaxial braided composites is derived on the basis of the equivalence framework for periodic structures [65] in Fig. 4.5. This approach allows us to reduce the modelling domain to a quarter of a smallest translational unit cell by exploiting internal symmetries of the textile topology. The width and height of the rUC are given by

$$w_{\mathrm{rUC}} = \frac{s_{\mathrm{a}}}{2} \quad ; \quad h_{\mathrm{rUC}} = \frac{s_{\mathrm{b}}}{\sin(\theta)}. \tag{4.6}$$

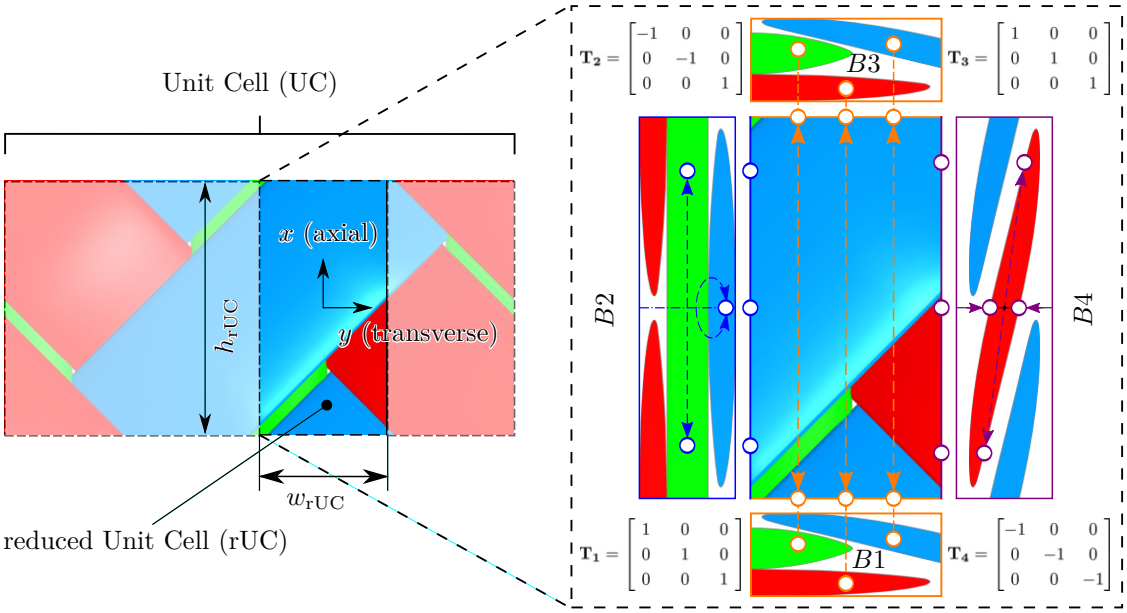

Fig. 4.5: Reduced unit cell with periodic boundaries

With the rUC dimensions defined and using spline interpolation along the fibre direction, the surface mesh is automatically converted into a solid CAD geometry. For the transverse direction, a linear interpolation based on the preceding symmetric discretisation of cross-sections is selected. This methodology enables us to retain the spatial information on predefined mesh seeds through geometric edges. By automatically creating a native Abaqus/CAE format with Python, any issues arising from external software import, such as imprecise geometry or unconnected faces are avoided. Hence, a high robustness of the overall procedure is guaranteed. Working on CAD geometry as opposed to discrete meshes provides many key benefits, such as granting access to volumetric boolean operations that are particularly useful for mesoscopic modelling. For an arbitrary unit cell selected by the user,

an exact CAD representation is obtained, independent of the angle of intersection between yarns and the periodic boundaries of the unit cell.

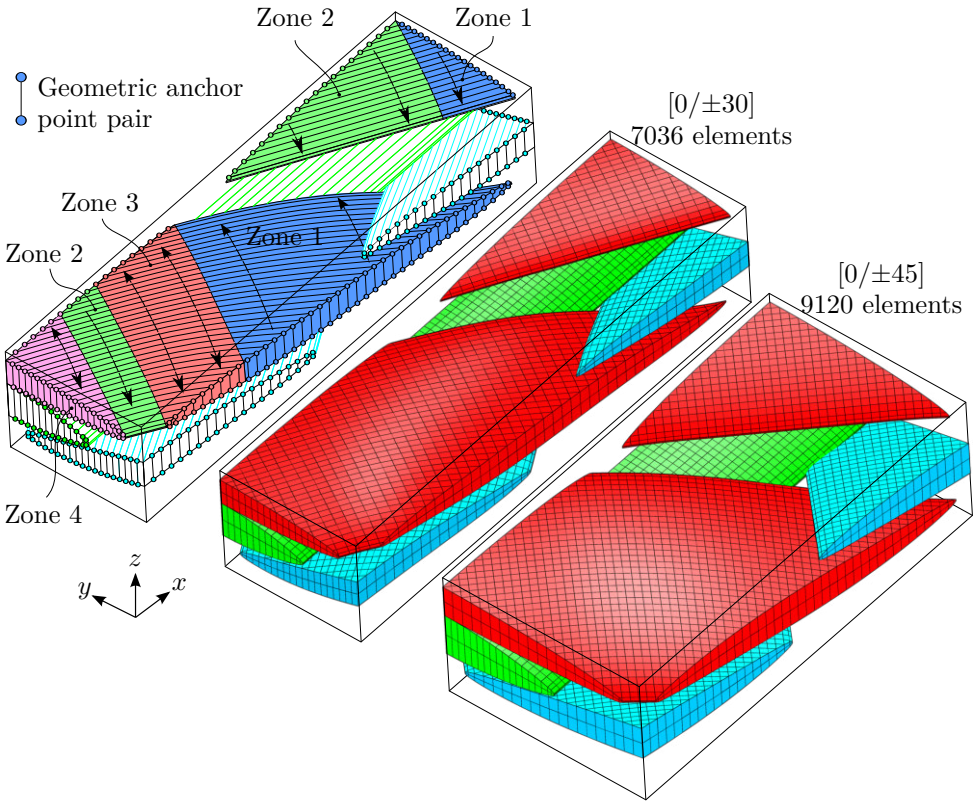

Fig. 4.6: Meshing procedure and structured hexahedral mesh for [0/±30] and [0/±45] rUC, 40 elements per yarn width, 2 elements per yarn thickness, $\xi = 5\%$

In light of the fact that a structured first-order hexahedral mesh provides an accurate solution at significantly less cost compared to a second-order tetrahedral mesh and the use of linear tetrahedral elements should be avoided as much as possible due their overly stiff behaviour [73], an automatic hexahedral meshing algorithm was developed for arbitrary yarn geometries.

A regular mesh is aligned with the fibre direction, as it offers many key advantages. Firstly, for a subsequent application of smeared crack models [75], crack bands may easily propagate along the fibre direction after strain localisation. Secondly, as a result of shape morphing, the fibre undulation varies not only along the yarn path, but also within each cross-section. Nevertheless, the local orientation tensor can be conveniently calculated on an element by element basis.

The biggest advantage of the presented approach, however, lies in the resulting inherent mesh periodicity caused by the boundary cut operation on the symmetric yarn discretisation. Geometric edges representing the transversal mesh seeds are cropped at the unit cell boundaries in a way that a periodic structure of boundary

vertices is created, independent of the unit cell size or its type of periodicity. These anchor points highlighted in Fig. 4.6 are coincident with nodal positions and ensure the periodic nature of each boundary discretisation during the following mesh generation.

The outcome of this initial step is depicted in Fig. 4.6 for a [0/±30] rUC. Now that all periodic boundaries are fully defined, the nodal positions inside the unit cell can be established. Depending on their relative position, length, and the number of periodic seed and target anchor points, each yarn is subdivided into logical meshing zones featuring up to two periodic boundaries. For single-sided periodic zones, e.g. zone 1 and zone 2, an orthogonal partition originating from each pair of seed anchor points produces a rectangular mesh pattern. Compatibility with the non-orthogonal boundary is satisfied by inserting single wedge elements per element row. In Fig. 4.6, zone 3 and 4 feature two periodic boundaries and hence must be treated separately. These two boundaries are subdivided into a target and a source side, with the latter determined by the minimum anchor point number. For each through-thickness pair of vertices positioned on the source side, a corresponding pair of target vertices is found, such that the aspect ratio of the mesh is optimised. By partitioning the yarns through a connection of these four corner points, the periodic boundaries remain unchanged. Finally, a user defined number of element rows is generated in through-thickness direction by a mere subdivision that preserves the periodic nature of the boundaries.

At the side edges of the bundles, the predefined thickness of $\xi \cdot t$ allows a compatible run-out of the hexahedral mesh. Here, the insertion of wedge elements was found to be disadvantageous, as they perform poorly in contact when large forces are introduced over a sharp edge in the fictitious thermal step. Additionally, the mesh is refined in close proximity to the side edges for optimised contact performance and element aspect ratio. An ideal choice for solid meshes with a high width to thickness aspect ratio are special purpose continuum elements with incompatible modes available in the commercial FE solver Abaqus [73]. In addition to the displacement degrees of freedom, incompatible deformation modes are added internally to improve the bending behaviour and eliminate parasitic shear locking. A slight increase in computational expense is nullified by the fact that significantly less elements are required in thickness direction leading in the consequence to an improved aspect ratio. While the meshing procedure was applied to the case of triaxial braided composites, it can be easily adapted to treat any kind of textile composite.

The periodic response is ensured by applying periodic displacement boundary conditions. Following the nomenclature of [65], they can be written for a deformable periodic body including arbitrary symmetries as

$$\mathbf{u}(A) - \gamma\,\mathbf{T}\,\mathbf{u}(\hat{A}) = -\,\langle\mathbf{F}\rangle\;\mathbf{T}\,\mathbf{x}^{\mathbf{O}_{\hat{\mathbf{E}}}} \tag{4.7}$$

where $\mathbf{u}$ denotes the displacement field of equivalent points A and $\hat{A}$ at a periodic boundary. The coordinate transformation matrix $\mathbf{T}$ and the translation vector $\mathbf{x}^{\mathbf{O}_{\hat{\mathbf{E}}}}$ define the tessellation of adjacent sub-domains, $\gamma = \pm 1$ describes their load reversal factor and $\langle\mathbf{F}\rangle$ is the volume averaged deformation gradient tensor tensor. Considering the rUC shown in Fig. 4.5, the PBCs are implemented by enforcing a series of linear constraint equations between displacements of equivalent nodes on the previously created periodic boundary mesh. Following the procedure described in [65], a set of master equations for the in-plane boundaries is derived in Table 5.1 where $\langle\cdot\rangle$ denotes a volume-averaged variable. For edges and vertices sharing more than one periodic boundary, a system of linearly independent constraint equations is assembled.

Table 4.1: Master equations for implementation of in-plane periodic boundary conditions

$$\text{B1}\quad \begin{bmatrix} u_{\mathrm{x}}(h_{\mathrm{rUC}}/2,y,z) \\ u_{\mathrm{y}}(h_{\mathrm{rUC}}/2,y,z) \\ u_{\mathrm{z}}(h_{\mathrm{rUC}}/2,y,z) \end{bmatrix} - \begin{bmatrix} u_{\mathrm{x}}(-h_{\mathrm{rUC}}/2,y,z) \\ u_{\mathrm{y}}(-h_{\mathrm{rUC}}/2,y,z) \\ u_{\mathrm{z}}(-h_{\mathrm{rUC}}/2,y,z) \end{bmatrix} = \begin{bmatrix} \langle\varepsilon_x\rangle\; h_{\mathrm{rUC}} \\ \langle\varepsilon_{xy}\rangle\; h_{\mathrm{rUC}} \\ 0 \end{bmatrix}$$

$$\text{B2}\quad \begin{bmatrix} u_{\mathrm{x}}(-x,-w_{\mathrm{rUC}}/2,z) \\ u_{\mathrm{y}}(-x,-w_{\mathrm{rUC}}/2,z) \\ u_{\mathrm{z}}(-x,-w_{\mathrm{rUC}}/2,z) \end{bmatrix} - \begin{bmatrix} -u_{\mathrm{x}}(x,-w_{\mathrm{rUC}}/2,z) \\ -u_{\mathrm{y}}(x,-w_{\mathrm{rUC}}/2,z) \\ u_{\mathrm{z}}(x,-w_{\mathrm{rUC}}/2,z) \end{bmatrix} = \begin{bmatrix} -\langle\varepsilon_{xy}\rangle\; w_{\mathrm{rUC}} \\ -\langle\varepsilon_{y}\rangle\; w_{\mathrm{rUC}} \\ 0 \end{bmatrix}$$

$$\text{B3}\quad \begin{bmatrix} u_{\mathrm{x}}(-h_{\mathrm{rUC}}/2,y,z) \\ u_{\mathrm{y}}(-h_{\mathrm{rUC}}/2,y,z) \\ u_{\mathrm{z}}(-h_{\mathrm{rUC}}/2,y,z) \end{bmatrix} - \begin{bmatrix} u_{\mathrm{x}}(h_{\mathrm{rUC}}/2,y,z) \\ u_{\mathrm{y}}(h_{\mathrm{rUC}}/2,y,z) \\ u_{\mathrm{z}}(h_{\mathrm{rUC}}/2,y,z) \end{bmatrix} = \begin{bmatrix} -\langle\varepsilon_x\rangle\; h_{\mathrm{rUC}} \\ -\langle\varepsilon_{xy}\rangle\; h_{\mathrm{rUC}} \\ 0 \end{bmatrix}$$

$$\text{B4}\quad \begin{bmatrix} u_{\mathrm{x}}(-x,w_{\mathrm{rUC}}/2,-z) \\ u_{\mathrm{y}}(-x,w_{\mathrm{rUC}}/2,-z) \\ u_{\mathrm{z}}(-x,w_{\mathrm{rUC}}/2,-z) \end{bmatrix} + \begin{bmatrix} u_{\mathrm{x}}(x,w_{\mathrm{rUC}}/2,z) \\ u_{\mathrm{y}}(x,w_{\mathrm{rUC}}/2,z) \\ u_{\mathrm{z}}(x,w_{\mathrm{rUC}}/2,z) \end{bmatrix} = \begin{bmatrix} \langle\varepsilon_{xy}\rangle\; w_{\mathrm{rUC}} \\ \langle\varepsilon_{y}\rangle\; w_{\mathrm{rUC}} \\ 0 \end{bmatrix}$$

By exploiting the internal material symmetry at the periodic boundary B4 in Table 5.1, a symmetric undulation path about the z axis is implied throughout the subsequent simulation steps. In addition, homogenised in-plane shear $\langle\varepsilon_{xy}\rangle$ and

out-of-plane shear $\langle \varepsilon_{xz} \rangle$ must be applied separately in order to satisfy the admissibility of all sub-domains [65]. Since the rUC can only be extracted at specific positions of the periodic textile, potential ply shifts in an explicit compaction simulation of multiple layers are restricted to integer multiples of half of the rUC width and height.

4.2.4 Interpenetration correction and compaction

With the sole geometric constraint that the yarn width cannot exceed its corresponding spacing, the initial idealised geometry directly represents the user input data. Although the degree of interpenetrations in the case of non-orthogonal interlacing can be minimised by using the previously described analytical formulation, there is no guarantee that any combination of input data will always yield an interpenetration free geometry model. In order to achieve a high robustness of the presented modelling framework for a large variety of textile geometries, potential volumetric interpenetrations are resolved by means of a fictitious explicit thermal disturbance step before the textile can be compacted to the desired FVF. The procedure is highlighted in Fig. 4.7. Initially, the rUC is subjected to a decrease in temperature accompanied by volumetric shrinkage of the yarns up to a point where all parts are distinctively separated. While the latter are subsequently reset to their initial temperature, they are now capable of interacting with each other by means of activated contact conditions. Considering the gradual expansion, a smooth transition into a compatible deformed geometric state is achieved. As this is a purely geometrical procedure of contraction and subsequent expansion, the constitutive law implemented is fictitious. An isotropic dummy material ($E = 20\,\mathrm{GPa}$, $\nu = 0.45$) obtained from numerical sensitivity studies ensures an approximately constant bundle volume due to a quasi-incompressible material response without deteriorating the stable time increment in non-hybrid solid elements. Orthotropic coefficients of thermal expansion eliminate axial stretching ($\alpha_1 = 0,\ \alpha_2 = \alpha_3 = 1$), and a perfectly-plastic constitutive law with a von Mises yield criterion ($\sigma_{\mathrm{yield}} = 250\,\mathrm{MPa}$) allows local yielding at critical contact locations, in particular at the convergence point of axial, positive and negative braid yarn depicted in Fig. 4.7. Here, they are tightly interlocked, and this clinching effect can give rise to high localised contact penetrations. With the applied strains eliminated in the in-plane PBC implementation, the rUC volume does not change during the simulation. Still, the periodic boundaries can deform freely, and geometrical coupling effects during the orthotropic contraction and expansion are averted.

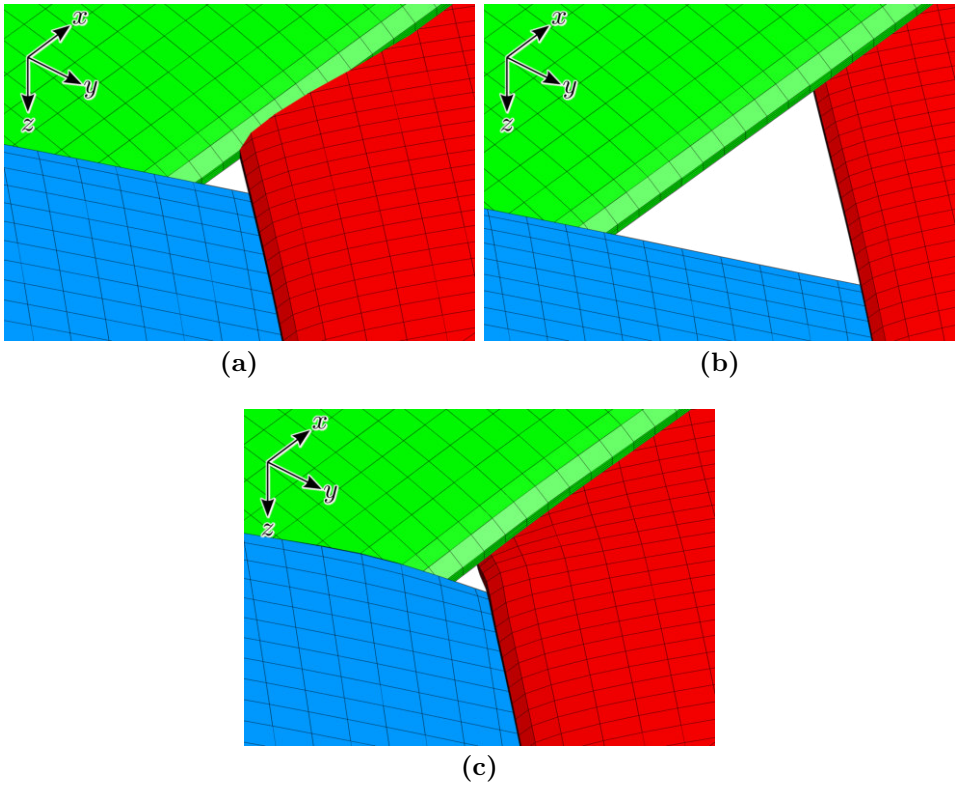

Fig. 4.7: Resolving interpenetrations at the critical yarn convergence point (a) initial state (b) separation after contraction (c) interlock after expansion

A key feature of the presented work is the subsequent compaction simulation. Instead of explicitly modelling the forming process using a finite number of fabric layers in combination with a tool, we rely solely on the application of out-of-plane PBCs during an explicit compaction simulation of a single textile layer to further minimise computational effort. Flexible membranes of unit thickness which implicitly simulate the support of adjacent layers by means of PBCs are introduced on the top and bottom of the rUC. With the equivalence framework introduced previously, the effects of different nesting conditions such as ply shifting or flipping are studied by means of two stacking configurations shown in their compacted state in Fig. 4.8. The corresponding out-of-plane master equations are summarised in Table 4.2. As the membranes represent the support of adjacent layers, they comprise the material properties of the fibre bundles. Considering both the top and bottom cell assembled with a rotation of 180°about the z axis (flipped layer), axial fibre bundles of adjacent layers are positioned such that they are capable of closing large initial voids originating from the variable braid thickness. In this case of structural nesting described by [23], sections devoid of axial bundles are filled by their adjacent layer's equivalent. As a consequence, a rUC with locally varying

thickness is produced. An identical nesting case can be obtained by incorporating a translational offset of w_{rUC} for the top and bottom rUC.

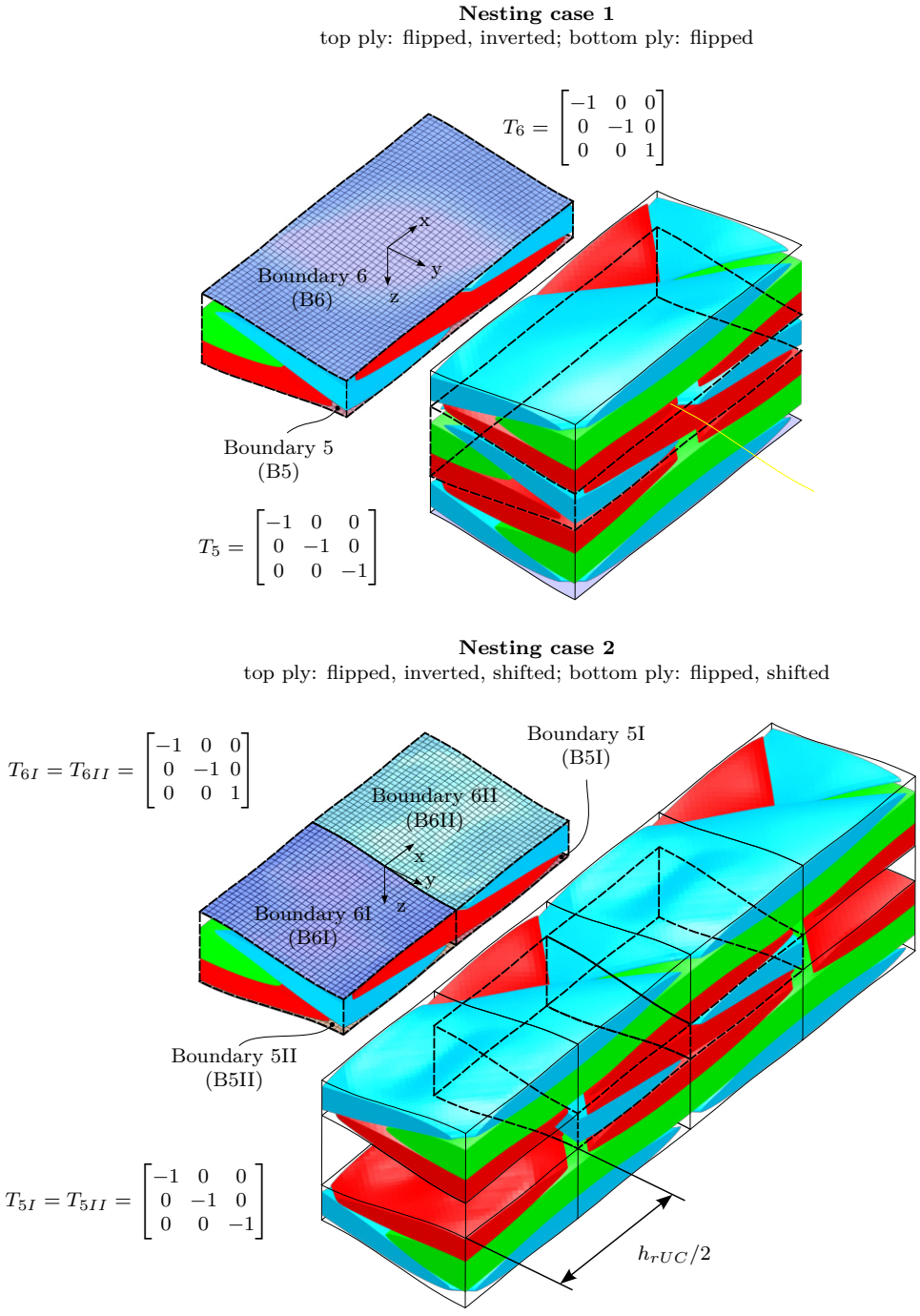

Fig. 4.8: Out-of-plane PBCs considering nesting case in unshifted and shifted nesting case configuration

However, a specific set of out-of-plane PBCs may not be chosen arbitrarily. Since rotational and mirror symmetries are exploited simultaneously in B2 and B4, the

flipped top and bottom layers in Fig. 4.8 must be arranged inversely in order to satisfy the overall compatibility of the periodic structure. In the second nesting case, the plies are additionally shifted in axial (x) direction by a magnitude of $h_{\mathrm{rUC}}/2$. In contrast to the first nesting case, the braid bundles are now positioned directly on top of each other. Hence, regions of high packing densities are supplemented by local resin rich areas in the textile after compaction.

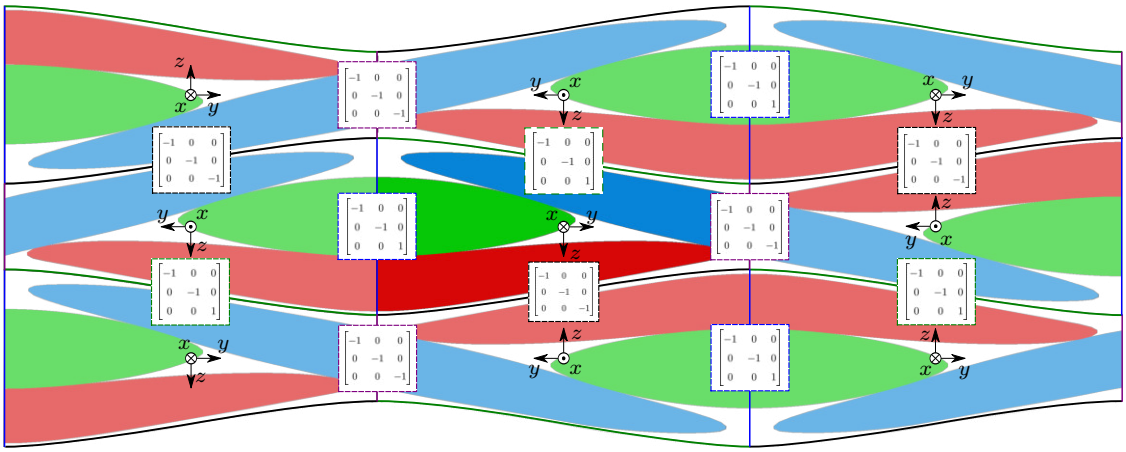

Fig. 4.9: Interdependency of in-plane and out-of-plane PBCs for nesting case 1 satisfying periodic compatibility

It is important to note that the purpose of the model at this stage is not to represent a dry fabric. The input parameters shown in Fig. 4.2 should be chosen to match the finished composite as closely as possible. Since we implicitly consider the yarn compaction behaviour by measuring the finished product rather than explicitly simulate the physical constitutive response of the dry fibre bundles, several localised deformation modes, such as yarn flattening, interactions with the tool, and the compaction force are not directly captured. Instead, we focus on quickly generating compacted unit cells for mechanical simulations by means of mimicking global compaction phenomena, such that any artificial scaling of intra-yarn FVF is avoided, The compaction step's primary mechanism comprises the shape distortion and repositioning of yarns due to mutual contact during compaction, such that large resin rich regions are closed and direct contact is established between individual fibre bundles. Finally, a more realistic geometry model of variable thickness enriched by a multitude of defects and imperfections is obtained, without the need of characterizing the complex mechanical behaviour of the dry fibre bundles. Nevertheless, the modular approach of the framework further allows for an additional implementation of physical compaction phenomena, for example by implementing a transversely-isotropic hypo-elastic constitutive law for the yarns [76, 77].

During the compaction operation, all yarn volumes V and hence intra-yarn FVFs κ remain approximately constant, enabling a priori determination of the average compacted ply thickness $\bar{t}_{\mathrm{rUC,c}}$ to achieve the global target FVF $\varphi_{\mathrm{F,rUC}}$:

$$\begin{aligned} \bar{t}_{\mathrm{rUC,c}} &= \frac{V_{\mathrm{a}}\,\kappa_{\mathrm{a}} + V_{\mathrm{b}}\,\kappa_{\mathrm{b}}}{4\,\varphi_{\mathrm{F,rUC}}\,h_{\mathrm{rUC}}\,w_{\mathrm{rUC}}} \\ &= \frac{h_{\mathrm{rUC}}\,A_{\mathrm{a}}\,\kappa_{\mathrm{a}} + 2\,L_{\mathrm{u'}}\,A_{\mathrm{b}}\,\kappa_{\mathrm{b}}}{2\,\varphi_{\mathrm{F,rUC}}\,h_{\mathrm{rUC}}\,w_{\mathrm{rUC}}} \end{aligned} \tag{4.8}$$

The yarn volumes V_{a} and V_{b} within the rUC are directly determined from the actual mesh discretisation, meaning that the target FVF is achieved independently of the element size. Further mesh refinement in order to obtain FVF convergence, as is commonly performed in voxel models [61], or a discretisation error due to mismatching geometry and mesh are eliminated. As the overall layer thickness gradually decreases over time, the global fibre volume fraction increases up to its target value. For a [0/±45] braid under investigation, the process is visualised using an assembly of several rUCs in Fig. 4.10. From the initial state at $\varphi_{\mathrm{F,rUC}} = 0.38$, the flat membranes are subjected to a prescribed displacement. Once interacting with the fabric, mutual deformations occur. Upon further compaction, they tend to locally accommodate to the underlying geometric shapes, thus increasing the contact area and the resulting compaction pressure. The final stage features a tightly packed structure of deformed bundles in direct contact. Here, the initially straight axial yarns exhibit a minor degree of crimp accompanied by a reduction in crimp in the braid yarns.

Considering that the assumption of a periodic stacking during the compaction process neglects a potential influence of rigid tool boundaries on the internal geometry of the outer layers, its applicability should be verified against the actual manufacturing process and the ply count of the braided component. In case of a severe impact of the tool on the yarn geometry, as in the case of laminates with few plies manufactured by resin transfer moulding (RTM), an explicit representation of the full stack and the tool may be necessary in order to capture their mutual mechanical interactions, such as flatting of the surface yarns [78]. For higher numbers of braided layers [24], however, or for vacuum infusion processes with a single-sided flexible membrane [2, 79], the advantages of drastically reducing computational expense can outweigh the loss in modelling detail.

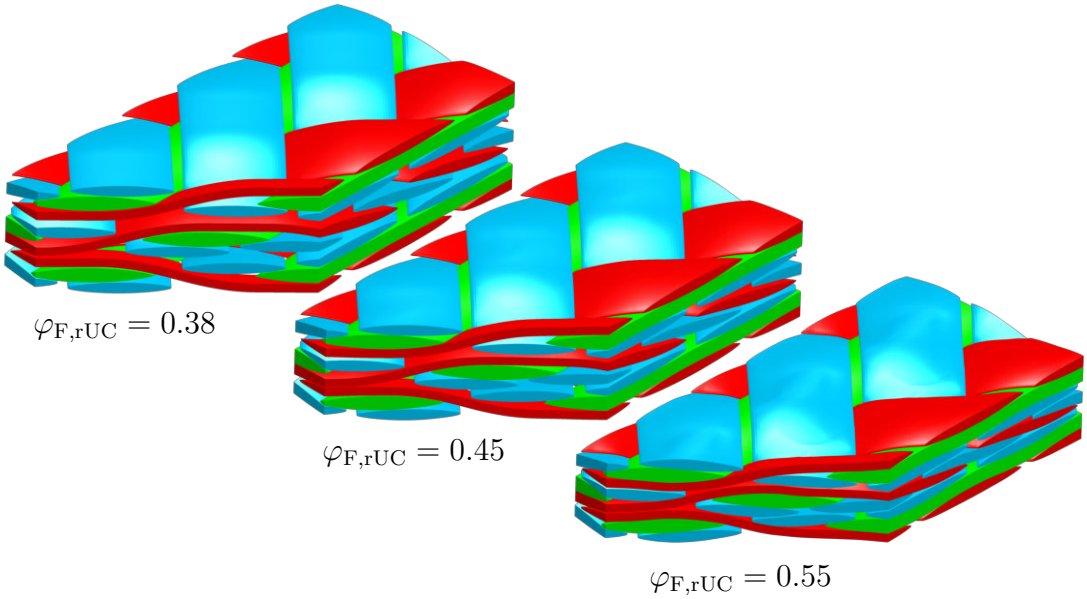

Fig. 4.10: Evolution of global fibre volume fraction $\varphi_{\mathrm{F,rUC}}$ during compaction simulation for nesting case 1

4.2.5 Generation of matrix pocket mesh for mechanical simulation

Now that the geometry of the yarns is defined in its final state, the addition of a matrix pocket mesh enables us to perform mechanical simulations of the composite unit cell. Particularly due to the non-orthogonal bundle interlacement and for highly compacted braids with their inherent complexity of the matrix pocket geometry, this step remains a major challenge in meso-FE modelling. Our approach relies on two basic principles: Firstly, an exact CAD representation of the matrix pocket geometry which serves as a surrogate for a solid tetrahedral mesh is constructed through a series of boolean operations. Secondly, a search algorithm detects regions of mutual bundle contact and subsequently establishes interfacial cohesive zones. Thus, the introduction of an artificial matrix layer or a poor tetrahedral element quality is avoided. A seamless connection of the cohesive zones in the direct yarn-to-yarn and the yarn-to-matrix contact regions is achieved by merging coincidently positioned nodes. As a result, the meshing methodology allows us to create a coherent three-dimensional cohesive zone with local branching.

The overall procedure is explained in detail in Fig. 4.11. Initially, the deformed mesh is tessellated in close proximity of the rUC with respect to its symmetries at the periodic boundaries. Using spline interpolation in axial and transverse direction, a solid CAD representation of the textile is reconstructed based on the deformed nodal coordinates, as is shown in Fig. 4.11 (a) for a [0/±60] configura-

Table 4.2: Out-of-plane PBC master equations

Nesting case 1: top ply: flipped, inverted; bottom ply: flipped

$$\text{B5}\quad \begin{bmatrix} u_\mathrm{x}(-x,-y,\bar{t}_\mathrm{rUC}/2) \\ u_\mathrm{y}(-x,-y,\bar{t}_\mathrm{rUC}/2) \\ u_\mathrm{z}(-x,-y,\bar{t}_\mathrm{rUC}/2) \end{bmatrix} + \begin{bmatrix} u_\mathrm{x}(x,y,\bar{t}_\mathrm{rUC}/2) \\ u_\mathrm{y}(x,y,\bar{t}_\mathrm{rUC}/2) \\ u_\mathrm{z}(x,y,\bar{t}_\mathrm{rUC}/2) \end{bmatrix} = \begin{bmatrix} 0 \\ 0 \\ \langle\varepsilon_z\rangle\ \bar{t}_\mathrm{rUC} \end{bmatrix}$$

$$\text{B6}\quad \begin{bmatrix} u_\mathrm{x}(-x,-y,\bar{t}_\mathrm{rUC}/2) \\ u_\mathrm{y}(-x,-y,\bar{t}_\mathrm{rUC}/2) \\ u_\mathrm{z}(-x,-y,\bar{t}_\mathrm{rUC}/2) \end{bmatrix} + \begin{bmatrix} u_\mathrm{x}(x,y,-\bar{t}_\mathrm{rUC}/2) \\ u_\mathrm{y}(x,y,-\bar{t}_\mathrm{rUC}/2) \\ -u_\mathrm{z}(x,y,-\bar{t}_\mathrm{rUC}/2) \end{bmatrix} = \begin{bmatrix} 0 \\ 0 \\ \langle\varepsilon_z\rangle\ \bar{t}_\mathrm{rUC} \end{bmatrix}$$

Nesting case 2: top ply: flipped, inverted, shifted; bottom ply: flipped, shifted

$$\text{B5I}\quad \begin{bmatrix} u_\mathrm{x}(-x+h_\mathrm{rUC}/2,-y,\bar{t}_\mathrm{rUC}/2) \\ u_\mathrm{y}(-x+h_\mathrm{rUC}/2,-y,\bar{t}_\mathrm{rUC}/2) \\ u_\mathrm{z}(-x+h_\mathrm{rUC}/2,-y,\bar{t}_\mathrm{rUC}/2) \end{bmatrix} + \begin{bmatrix} u_\mathrm{x}(x,y,\bar{t}_\mathrm{rUC}/2) \\ u_\mathrm{y}(x,y,\bar{t}_\mathrm{rUC}/2) \\ u_\mathrm{z}(x,y,\bar{t}_\mathrm{rUC}/2) \end{bmatrix} = \begin{bmatrix} \langle\varepsilon_x\rangle\ h_\mathrm{rUC}/2 \\ \langle\varepsilon_{xy}\rangle\ h_\mathrm{rUC}/2 \\ \langle\varepsilon_z\rangle\ \bar{t}_\mathrm{rUC} \end{bmatrix}$$

$$\text{B5II}\quad \begin{bmatrix} u_\mathrm{x}(-x-h_\mathrm{rUC}/2,-y,\bar{t}_\mathrm{rUC}/2) \\ u_\mathrm{y}(-x-h_\mathrm{rUC}/2,-y,\bar{t}_\mathrm{rUC}/2) \\ u_\mathrm{z}(-x-h_\mathrm{rUC}/2,-y,\bar{t}_\mathrm{rUC}/2) \end{bmatrix} + \begin{bmatrix} u_\mathrm{x}(x,y,\bar{t}_\mathrm{rUC}/2) \\ u_\mathrm{y}(x,y,\bar{t}_\mathrm{rUC}/2) \\ u_\mathrm{z}(x,y,\bar{t}_\mathrm{rUC}/2) \end{bmatrix} = \begin{bmatrix} -\langle\varepsilon_x\rangle\ h_\mathrm{rUC}/2 \\ -\langle\varepsilon_{xy}\rangle\ h_\mathrm{rUC}/2 \\ \langle\varepsilon_z\rangle\ \bar{t}_\mathrm{rUC} \end{bmatrix}$$

$$\text{B6I}\quad \begin{bmatrix} u_\mathrm{x}(-x-h_\mathrm{rUC}/2,-y,\bar{t}_\mathrm{rUC}/2) \\ u_\mathrm{y}(-x-h_\mathrm{rUC}/2,-y,\bar{t}_\mathrm{rUC}/2) \\ u_\mathrm{z}(-x-h_\mathrm{rUC}/2,-y,\bar{t}_\mathrm{rUC}/2) \end{bmatrix} + \begin{bmatrix} u_\mathrm{x}(x,y,-\bar{t}_\mathrm{rUC}/2) \\ u_\mathrm{y}(x,y,-\bar{t}_\mathrm{rUC}/2) \\ -u_\mathrm{z}(x,y,-\bar{t}_\mathrm{rUC}/2) \end{bmatrix} = \begin{bmatrix} -\langle\varepsilon_x\rangle\ h_\mathrm{rUC}/2 \\ -\langle\varepsilon_{xy}\rangle\ h_\mathrm{rUC}/2 \\ \langle\varepsilon_z\rangle\ \bar{t}_\mathrm{rUC} \end{bmatrix}$$

$$\text{B6II}\quad \begin{bmatrix} u_\mathrm{x}(-x+h_\mathrm{rUC}/2,-y,\bar{t}_\mathrm{rUC}/2) \\ u_\mathrm{y}(-x+h_\mathrm{rUC}/2,-y,\bar{t}_\mathrm{rUC}/2) \\ u_\mathrm{z}(-x+h_\mathrm{rUC}/2,-y,\bar{t}_\mathrm{rUC}/2) \end{bmatrix} + \begin{bmatrix} u_\mathrm{x}(x,y,-\bar{t}_\mathrm{rUC}/2) \\ u_\mathrm{y}(x,y,-\bar{t}_\mathrm{rUC}/2) \\ -u_\mathrm{z}(x,y,-\bar{t}_\mathrm{rUC}/2) \end{bmatrix} = \begin{bmatrix} \langle\varepsilon_x\rangle\ h_\mathrm{rUC}/2 \\ \langle\varepsilon_{xy}\rangle\ h_\mathrm{rUC}/2 \\ \langle\varepsilon_z\rangle\ \bar{t}_\mathrm{rUC} \end{bmatrix}$$

tion. Owing to the actual mesh discretisation and small interpenetrations due to the previous penalty contact formulation, a direct boolean operation between two contacting yarns is not adequate. Independent of their mesh size, such a procedure would generate a ill-conditioned geometry features, including voids, self-intersecting surfaces or very sharp angles that are impractical to mesh [57]. With the definition of a critical contact cut-off thickness t_crit, the presented algorithm automatically detects three-dimensional contact surfaces for every possible yarn interaction by performing geometric boolean operations on slightly thickened dummy bundles. For the envelopes of the resulting contact domains shown in Fig. 4.12, the distance between the CAD representation of two adjacent bundles is equal to the predefined cut-off thickness. If we move progressively to the centre of the contact area, the

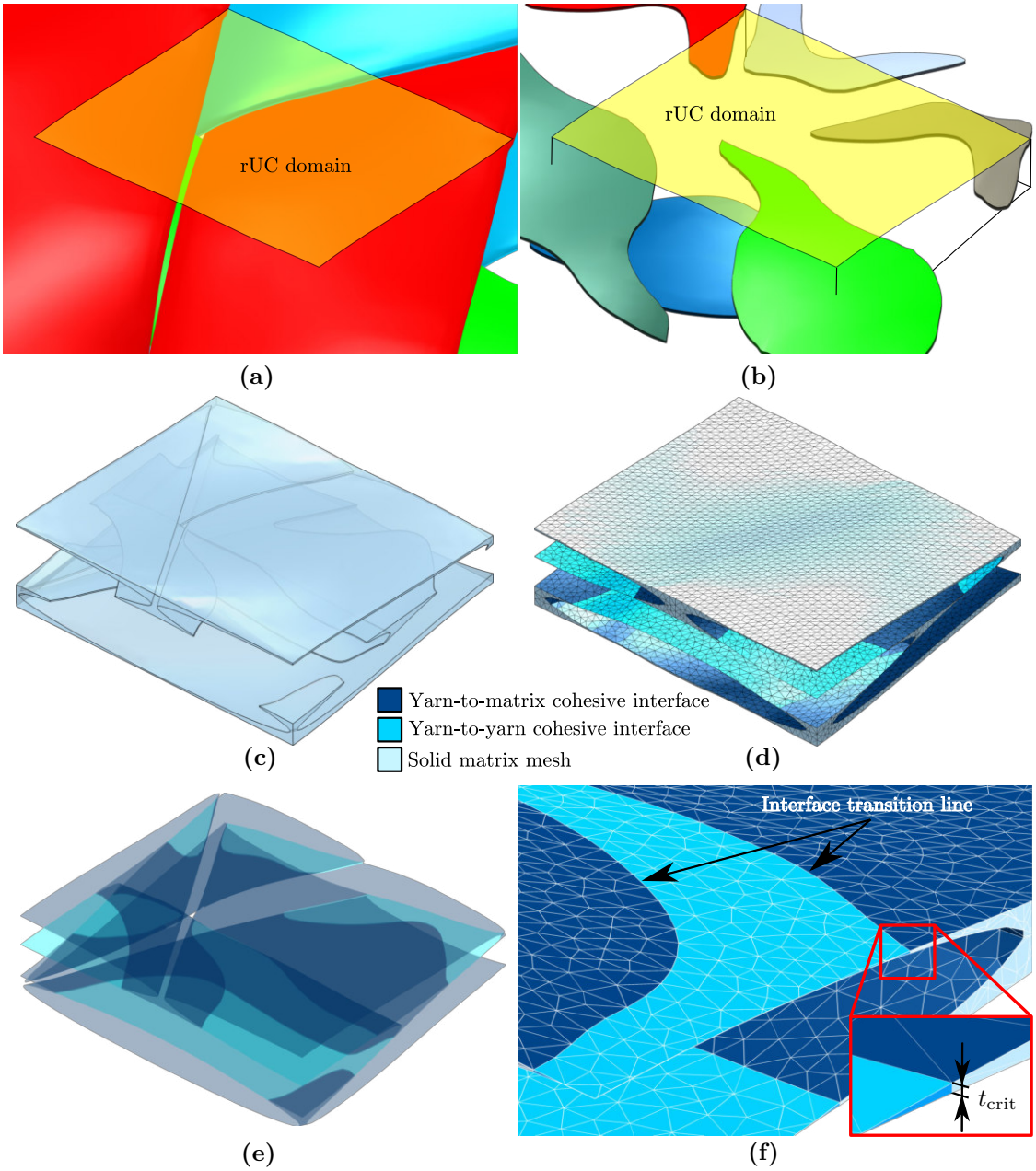

Fig. 4.11: Algorithm for generation of matrix pockets mesh: (a) CAD reconstruction of compacted yarn mesh, (b) determination of direct yarn-to-yarn direct contact zones, (c) CAD model of matrix pockets, (d) final mesh of matrix pockets, (e) cohesive zones highlighted and (f) detailed view of a transition zone of the yarn-to-yarn and yarn-to-matrix cohesive mesh

proximity decreases until both bodies locally interpenetrate each other. In case the geometric proximity between two potential contact partners exceeds the specified distance, the boolean operation yields a body of zero volume, indicating that no direct yarn-to-yarn contact is required. Now that the boundaries are defined, their automatic extraction is followed by the construction of the contact bodies as

shown in Fig. 4.11 (b). Since this process extends over neighbouring unit cells, the assembled contact surfaces intrude into the simulation domain in such a way that all periodicity requirements are automatically satisfied at the boundaries. Now, the determination of the matrix pocket geometry is straightforward. At first, the contact bodies are removed from the rUC volume enclosed by the flexible membranes, then the yarns are subtracted from the remainder to obtain the final CAD geometry highlighted in Fig. 4.11 (c).

With the critical contact regions eliminated, the default meshing algorithm is now capable of generating a high quality solid tetrahedral mesh. To satisfy the periodicity requirements, a two-dimensional mesh is initially created at predefined seed faces at the boundaries. By applying the coordinate transformation matrices, this source mesh seed is transformed into its corresponding target morphology and then copied accordingly. The top and bottom surfaces of the completed mesh highlighted in Fig. 4.11 (d) are assembled from the deformed nodal coordinates of the flexible membranes which retain their periodicity during the compaction process.

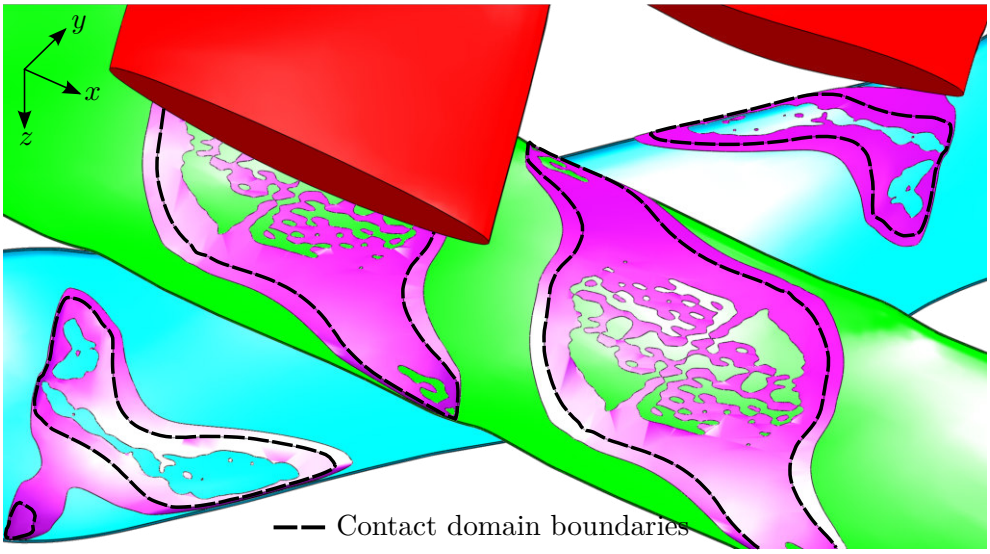

Fig. 4.12: Determination of yarn-to-yarn contact regions and extraction of domain cut-off boundaries

For the purpose of modelling delamination between the yarns and the bulk resin, a layer of three-dimensional cohesive elements is extruded on top of the tetrahedral mesh, much like an interior coating. Subsequently, the direct yarn-to-yarn cohesive interfaces are added to the global mesh. After cropping their geometries to the rUC boundaries, these regions are discretised with cohesive elements separately. However, due to consistent mesh seed sizes, the coordinates of nodes created at the outer circumference of each contact domain match those generated by the

tetrahedral meshing algorithm. Along this transition line between the yarn-to-yarn and yarn-to-matrix interaction shown in Fig. 4.11 (f), a single cohesive interface branches into two diverging interfaces with underlying tetrahedral elements. By merging the outer yarn-to-yarn interface nodes with the respective upper and lower nodes of adjacent yarn-to-matrix cohesive elements, a consistent mesh coupling is achieved. Consequently, this smooth interfacial transition enables us to capture cohesive crack propagation and branching. While the cohesive elements share nodes with the underlying tetrahedral mesh on one side, their inner surfaces displayed in Fig. 4.11 (e) and the yarn surfaces are coupled in order to ensure displacement continuity of the incompatible hexahedral and tetrahedral element types [73]. A surface-to-surface tie formulation guarantees a smooth and accurate stress distribution as opposed to a mere node-to-surface algorithm at the interface. The inner nodes of the cohesive elements are excluded from the PBC definition at the periodic boundaries. Otherwise, over-constraints would either issue an input error or lead to a drastic increase in simulation run time, depending on whether the implicit or explicit solver is used. Here, periodicity of the nodal displacements is implicitly enforced through the master role of adjacent yarn nodes in the tie formulation.

The effect of the presented methodology on the interfacial stress distribution is shown in Fig. 4.13 for an axial yarn of the [0/±45] braid loaded in transverse direction. Owing to the stiffness discontinuity at the interface transition line, where a single cohesive element branches into a stack of tetrahedral matrix elements covered by a thin cohesive zone on both sides, these regions develop minor stress concentrations compared to their undisturbed surroundings. However, the overall distribution of the traction components is preserved well. Given the low intensity of the artificial stress concentrations at the interface junction, it can be concluded that the overall stress distribution in the interface is captured well by the meshing methodology. Similar to the yarn meshing procedure, this methodology may be easily adapted to a variety of textile composites, allowing for a more realistic representation of branching interfaces without the need of introducing a dummy matrix mesh of finite thickness in between contacting yarns. In addition, the proposed methodology offers several advantages:

- since a spline-based CAD geometry is employed in the procedure, contacting meshes are not required to match, and the results are less sensitive to mesh refinement
- no modifications or distortions of the yarn mesh are required
- by working on CAD geometry, error prone nodal search algorithms are avoided

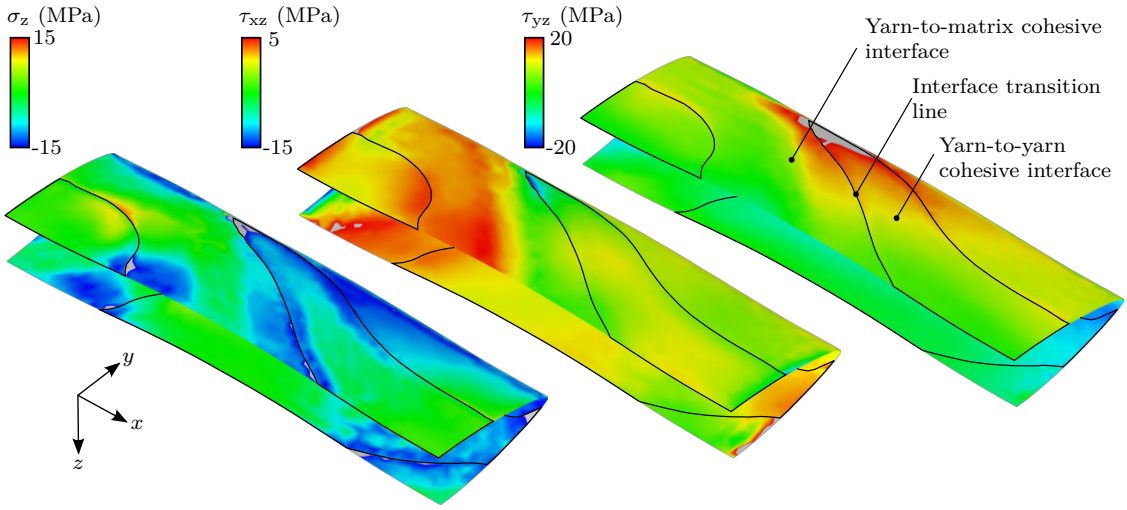

Fig. 4.13: Effect of the proposed yarn-to-yarn and yarn-to-matrix cohesive meshing methodology on the interfacial stress distribution of half of an axial yarn of a [0/±45] braid loaded in transverse direction

4.3 Validation and application

With the simulation framework defined, we apply our methodology to predict the elastic properties of triaxial braided composites. The materials in this study are manufactured from Toho-Tenax HTS40 F13 12K (800 tex) untwisted yarns for both the axial and braid direction in combination with a Hexcel HexFlow RTM 6 epoxy resin. In order to demonstrate the framework, various unit cells are generated for braiding angles ranging from 25° to 65° in increments of 5°. For validation purposes, tensile tests of straight-sided specimens with a total of four layers are performed in accordance with ASTM D3039 [32]. Three braid architectures, with a nominal braiding angle of 30°, 45° and 60° are each tested in their longitudinal (x), transverse (y) and braid yarn direction ($1F$). Details on the manufacturing process and the elastic properties are summarised in [79].

Based on a mesh refinement study, an average element seed size of 70 μm is selected for all unit cells. Given the geometrical properties of the bundles under investigation, this discretisation yields approximately 40 hexahedral elements with incompatible modes over the yarn width and two elements in the thickness direction, with a total of 7036 elements for the [0/±30], 9120 for the [0/±45] and 9114 for the [0/±60] configuration. Depending on the braiding angle, roughly 15,000 and 20,000 cohesive elements ensure coupling with the matrix pockets that contain in between 40,000 to 50,000 tetrahedral elements. For all unit cells, a bundle side thickness ratio of $\xi_a = \xi_b = 5\%$ is selected.

4.3.1 Internal geometry

Ensuring that the unit cell models render a realistic representation of the compacted internal textile geometry is key for accurate predictions of the mechanical response. A detailed reconstruction of the actual geometry from μCT measurements enables us to identify key geometrical features and compare them to the model. These parameters comprise the yarn centre-line, thickness, width, spacing, twist, and the intra-yarn FVF calculated from the cross-sectional area for both the axial and braid fibre bundles. In addition, we can study the periodic nature of the internal geometry, evaluate its spatial variability and asses the applicability of a unit cell modelling approach to the problem.

For each textile architecture, samples of $15 \times 15 \times 3\,\mathrm{mm}^3$ were cut from the resin-infused plates in close proximity to the coupons used for the mechanical tests and scanned with a GE Phoenix/X-Ray Nanotom 180 at a voxel size of $9\,\mu\mathrm{m}^3$ at the University of Applied Sciences Upper Austria. Since an automatic segmentation of resin-infused bundles poses significant challenges [80], a semi-automatic segmentation strategy was developed. Initially, the raw CT data is imported into a Matlab script and sliced using three planes, with each of them corresponding to a cut orthogonal to one of the in-plane fibre directions. Within the resulting stacks of CT images, solely the cross-sections normal to the cut plane are segmented manually by a predefined number of points that form a closed polygon line at the bundle perimeter. This procedure is repeated until all cross-sections along each image stack are processed. To minimise the manual input during this cumbersome procedure, existing points are automatically copied to subsequent images where only minor adjustments are required. As the data is progressively visualised and saved, changes to any of the cross-sections can be made at any time via a graphical user interface. A minimum of statistical data is captured along each yarn path by limiting the segmentation to entities that extend at least over a single undulation interval inside the measurement volume. In the presented study, each cross-section is manually discretised with 20 measurement points. The distance between two consecutive cross-sections is $180\,\mu$m for the braid and $540\,\mu$m for the axial direction. In total, the segmentation of the [0/±30] material involves 37900 points, the [0/±45] 43100 points and the [0/±60] braid 40460 points. Finally, the data set is converted into a 3D CAD geometry using spline interpolation in both axial and transverse direction for easy inspection of geometrical features and comparison with the unit cell models. For the generation of the unit cell models at arbitrary braiding angles, we apply a quadratic interpolation function on the basis of the averaged

μCT geometry that is summarised in Table 4.3. The global FVF measurements $\varphi_{\mathrm{F,rUC}}$ were obtained using acid digestion in accordance with ASTM D3171 [21].

Table 4.3: Averaged μCT geometry used for the generation of the unit cell models

Global		Axial yarns					
θ	$\varphi_{\mathrm{F,rUC}}$	s_{a}	w_{a}	t_{a}	κ_{a}	A_{a}	n_{a}
(deg)	(%)	(μm)	(μm)	(μm)	(%)	(mm^2)	
30	56 ± 0.9	3354 ± 123	2122 ± 131	452 ± 90	66 ± 6	0.674 ± 0.029	0.76
45	55 ± 0.8	4232 ± 118	2340 ± 157	440 ± 43	66 ± 4	0.726 ± 0.041	0.74
60	56 ± 0.2	6003 ± 259	2888 ± 203	350 ± 45	63 ± 5	0.742 ± 0.059	0.63

Global		Braid yarns					
θ	$\varphi_{\mathrm{F,rUC}}$	s_{b}	w_{b}	t_{b}	κ_{b}	A_{b}	n_{b}
(deg)	(%)	(μm)	(μm)	(μm)	(%)	(mm^2)	
30	56 ± 0.9	3052 ± 583	2695 ± 267	326 ± 59	70 ± 5	0.660 ± 0.048	0.58
45	55 ± 0.8	3047 ± 288	2716 ± 187	327 ± 50	70 ± 6	0.661 ± 0.054	0.60
60	56 ± 0.2	2799 ± 233	2767 ± 175	317 ± 59	70 ± 5	0.663 ± 0.060	0.56

The centre-lines shown in Fig. 4.14 for the [0/±45] braid are extracted from the geometrical area centroid of consecutive cross-sections along the axial and braid fibre undulation path. After segmentation, the individual curves are superimposed and averaged locally to allow a comparison with the compacted unit cell geometry. For the braid yarns displayed in Fig. 4.14 (a), the periodic nature of the fibre waviness is clearly evident. When following individual bundle loci, we encounter greater deviations from the experimental average, particularly in close proximity to regions of peak amplitude. Here, the nesting configuration during compaction plays a key role in the formation of the overall internal geometry. When braid bundles of equal orientation are positioned on top of each other, the mutual interaction can flatten their undulation path over a finite contact length. During compaction and subsequent resin infusion, they merge into a bundle devoid of a visible interface in this region. If we analyse each of the centre-lines separately, we observe a certain degree of geometric variability induced by manufacturing process chain, much like superimposed high frequency noise. However, as soon as a critical number of yarn loci is combined in a statistical analysis, the average path follows a clear periodic trend with a comparable standard deviation bandwidth. If the first nesting case is considered in the simulations, the average experimental shape is captured very well. Here, the positioning of the braid yarns in the thickness direction promotes nesting into cavities that form in regions where the bundles progressively thin out along their width. Due to the lack of a supporting yarn at about half of the distance

between the point of maximum and zero undulation amplitude, the braid yarns are compacted inwards and the yarn path exhibits a slight kink. In the second nesting case, the centre-lines of the braid yarns are arranged directly on top of each other. Using coincident geometric input parameters, they develop an undulation plateau with a slightly smaller amplitude at the intersection with an axial bundle. At this point, the yarn are tightly packed. Hence, large compaction stresses translate into yarn flattening and hence a higher degree of geometrical defects in the textile architecture.

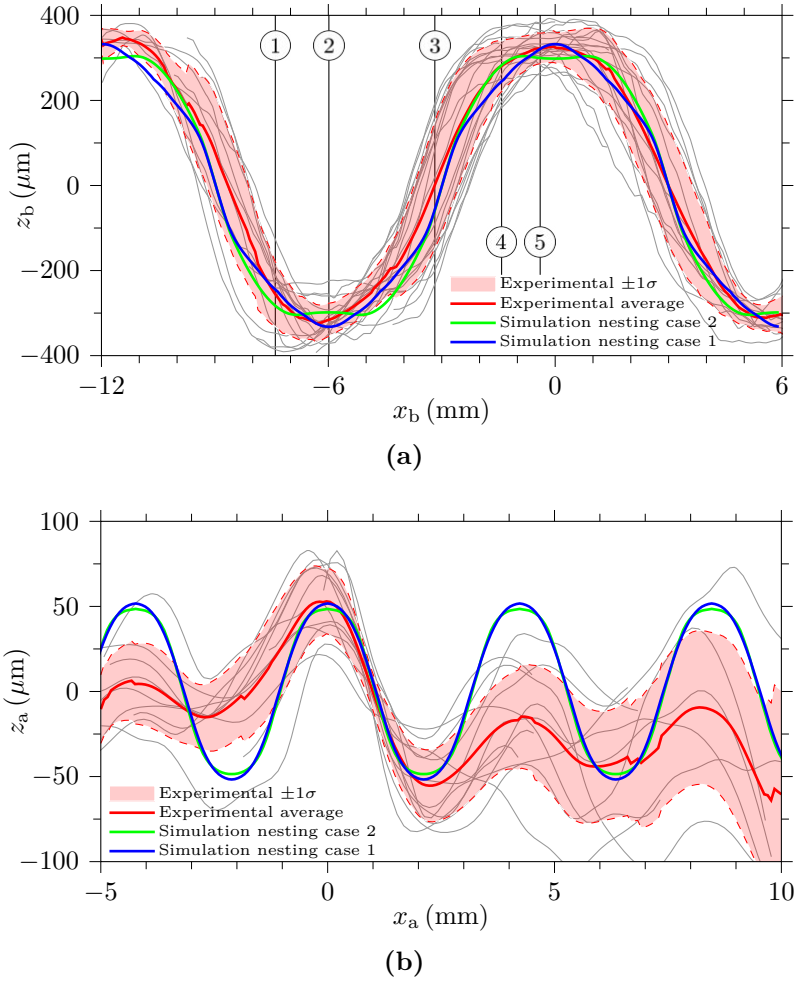

Fig. 4.14: Comparison of experimental and simulated yarn path of the [0/±45] braid for (a) braid yarns (b) axial yarns (see Fig. 4.16 for braid yarn cross-sections at positions (1) to (5))

The experimental findings in Fig. 4.14 (b) confirm the existence of additional fibre waviness in the axial bundles, although at a significantly reduced amplitude compared to the bias direction. The individual experimental curves are shifted to achieve an optimum correlation in their first positive undulation interval. Here,

the average undulation path and the simulations with both nesting cases match extremely well in terms of wavelength and amplitude. As we progressively move away from the correlation point, fundamental changes in the shape of the centre-lines are accompanied by a sky-rocketing standard deviation. These findings indicate that the degree of fibre waviness in the axial yarns is driven by local bending effects dominated by the nesting configuration. The simulated nesting cases were found to have only minor impact on the yarn path of the unit cell. During the compaction, the initially straight axial bundles are subjected to local bending from their entangling braid counterparts, independent of the applied out-of-plane boundary conditions. While we cannot identify a clear periodic trend of axial fibre waviness in the experiments, the unit cell model captures this geometrical phenomenon in terms of amplitude and wavelength and hence also renders possible effects on the mechanical response.

In addition to the centre-lines, the textile architecture is characterised by a variety of geometrical parameters. As exemplarily displayed in Fig. 4.15 for the braid bundles of the [0/±45] configuration, the yarn width w_b, thickness t_b, intra-yarn FVF κ_b and twist angle α_b are analysed along the average experimental undulation path. Assuming an undamaged 12k bundle and a fibre diameter of $7\,\mu m$, the intra-yarn FVF is obtained for each cross-section by relating the total filament area to the total segmented area. Each cross-section and the corresponding yarn thickness are calculated orthogonal to the local yarn path direction.

When we investigate the evolution of the average braid yarn width w_b along its undulation path z'_b in Fig. 4.15 (a), we discover a periodic increase each time it converges to its peak amplitude. Looking at the distribution of the average thickness t_b in Fig. 4.15 (b) at the same time, an opposite trend is clearly visible. This change in aspect ratio is further accompanied by a repeating growth of the intra-yarn FVF in Fig. 4.15 (c) at coincident positions along the undulation path. These finding underline the impact of the compaction process on the bundle geometry. In regions where yarns of adjacent plies are in direct contact, their cross-sections are flattened under the applied pressure. In these regions where the elevated intra-yarn FVF levels are consistent with a tight fibre packing, dry contacting filaments are subjected to a transverse movement and the bundles are subsequently widened. Recalling that the primary focus of the simulation framework is to construct a defect enriched geometry model based on average geometrical parameters of the finished composite, only minor variations of the geometrical parameters are rendered in the unit cell. While the bundle width is largely unaffected by the compaction simulation and its stacking configuration, the second nesting case produces a slight variation in the thickness and intra-yarn FVF distribution. Again, with bias bundles of adjacent

plies positioned directly on top of each other, a flattening mechanism similar to the one found in the μCT experiments is introduced.

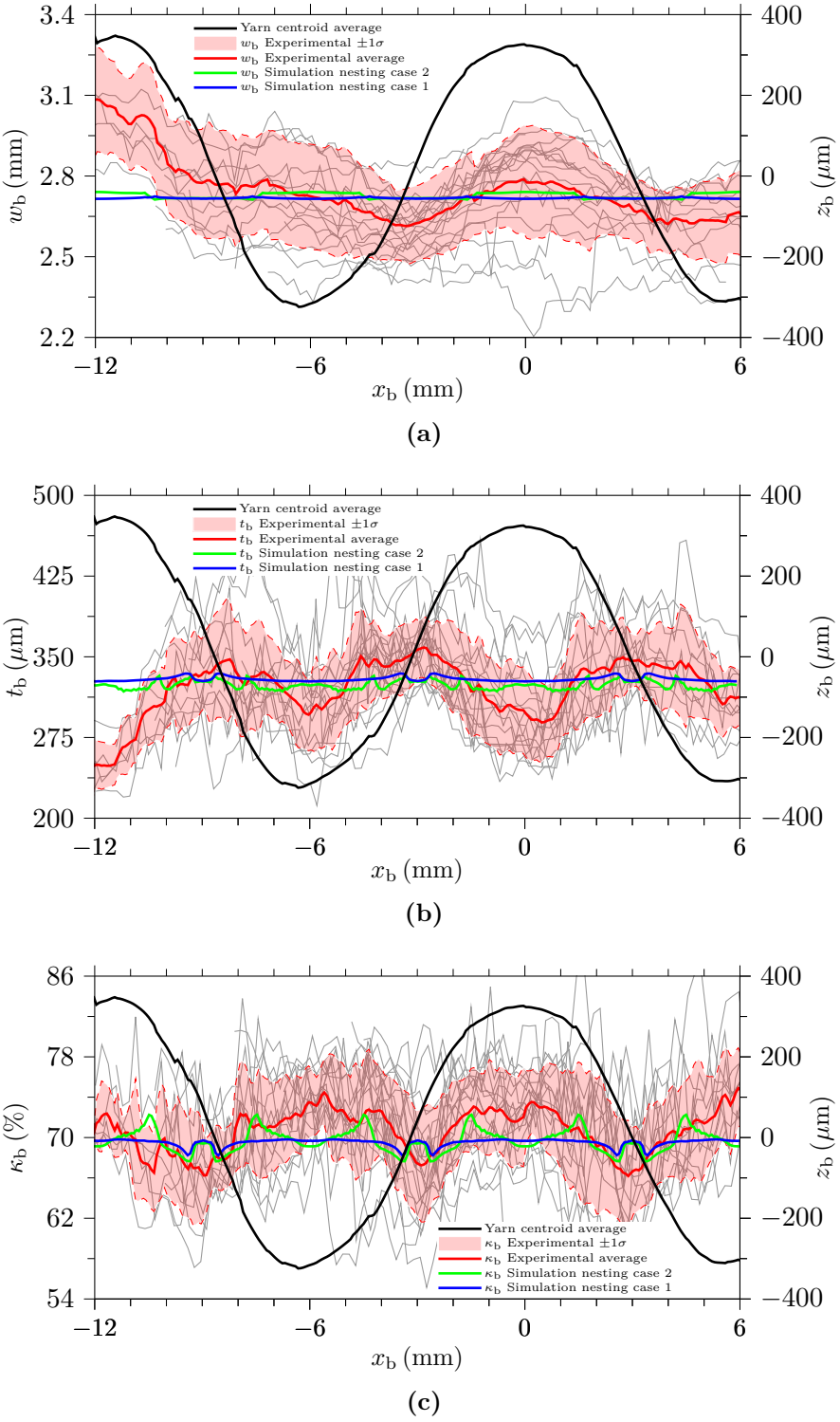

Fig. 4.15: Comparison of experimental and simulated yarn architecture of the [0/±45] braid (a) bundle width w_b (b) bundle thickness t_b (c) intra-yarn FVF κ_b, (d) twist angle α_b

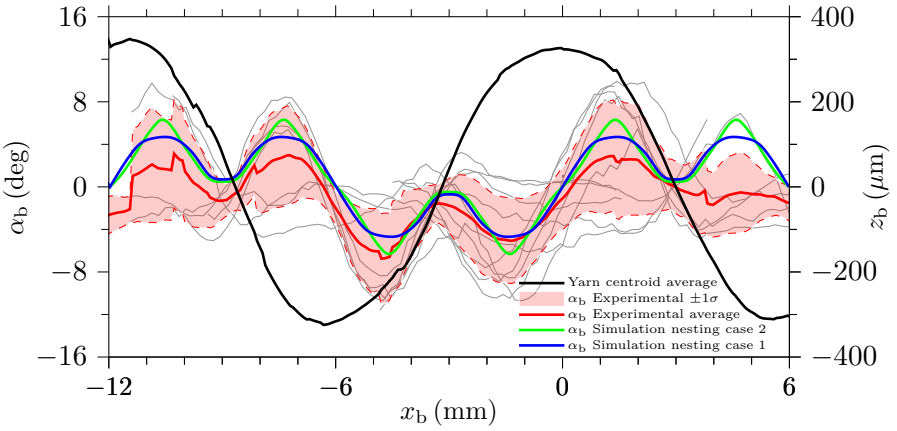

(d)

Fig. 4.15: continued: Comparison of experimental and simulated yarn architecture of the [0/±45] braid (a) bundle width w_b (b) bundle thickness t_b (c) intra-yarn FVF κ_b, (d) twist angle α_b

The distortion of fibre bundles along their undulation path is hard to quantify, especially since the cross-sections typically do not exhibit uniform twisting. For a more detailed comparison of the experimental and the simulated topology, we introduce a twist angle α derived from the orientation of the principal axes of the second area moment tensor defined as:

$$\alpha = \frac{1}{2} \arctan\left(\frac{2\, I_{y'z'}}{I_{y'} - I_{z'}}\right), \tag{4.9}$$

where the tensor components $I_{y'}$, $I_{z'}$ and $I_{y'z'}$ with respect to the yarn cross-sectional area centroid are obtained from numerical integration and the sign of α follows a right-handed coordinate system. When looking at the distortion of positively oriented braid yarns in Fig. 4.15 (d), we notice a periodic response characteristic of their waviness. At the point of maximum path amplitude, they are located directly on top of their axial counterparts. During the transition into the downwards undulation segment, the mutual contact induces a gradual distortion in the braid bundles as they are forced to accommodate to the underlying cross-section. This phenomenon is consistent with the first sinusoidal peak of the twist angle α_b. At the point of maximum out-of-plane curvature, the fibres further pass through the gap of two neighbouring longitudinal bundles. Owing to the absence of an interacting axial bundle at this point, the overall distortion is minimised. Although the bundle now continues on the opposite side of the textile, a second peak is created by the identical kinematics near the successive intertwining region. Further along the centre-line, the mechanism is continuously repeated, with the exception that

the orientation of the twist angle changes sign in the upwards path segment. The unit cell model captures this phenomenon accurately. Consistent with the higher overall distortion, the second nesting predicts a sharper shape of the twist angle distribution.

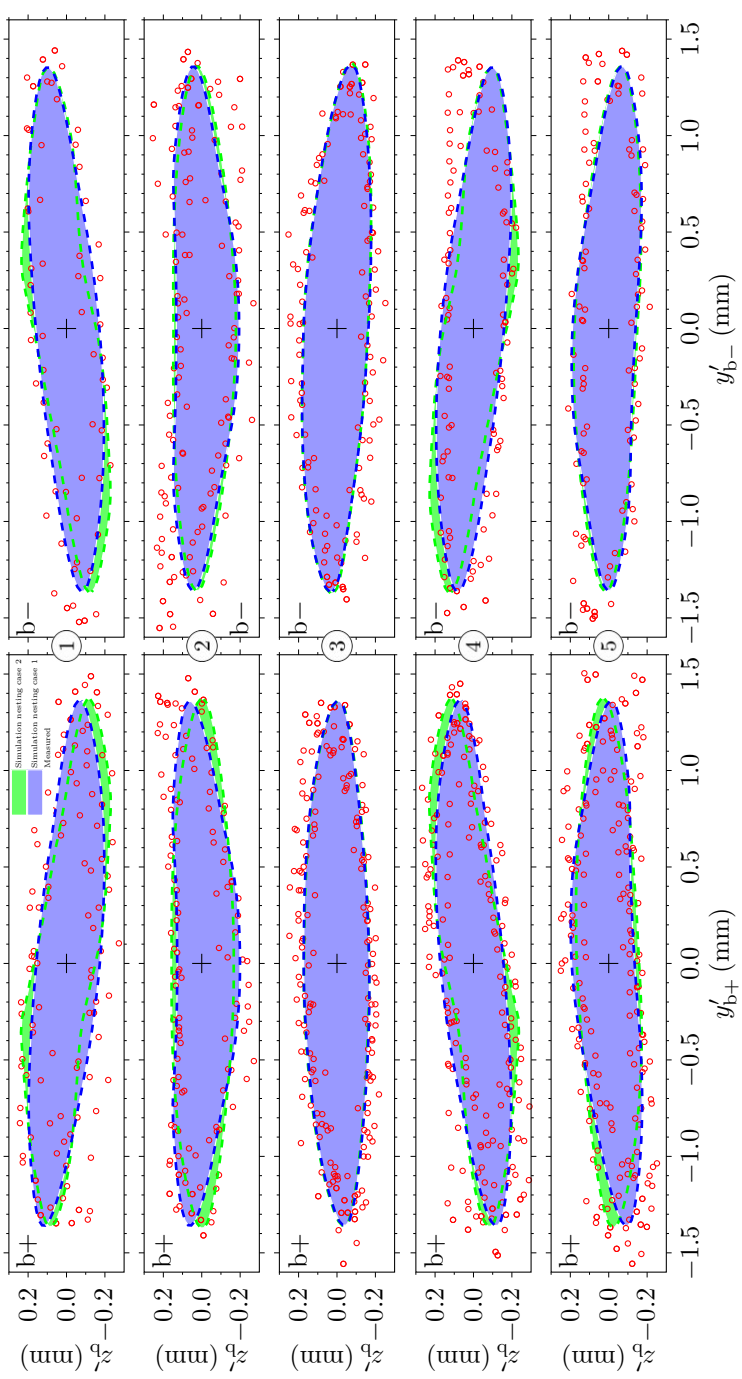

Fig. 4.16: Comparison of experimental and simulated cross-sections for positively (b+) and negatively (b−) oriented braid yarns of the [0/±45] braid at position ① to ⑤

A detailed comparison of the experimental and the simulated yarn cross-sections in both braid directions is shown in Fig. 4.16 at different locations along the centrelines indicated in Fig. 4.14 (a). Superposition of the cross-sections is achieved by

shifting each area centroid to the origin of the local coordinate system. The first virtual cut (1) is made halfway between the point of maximum and zero undulation amplitude, where the simulated yarn shapes experience the largest degree of twisting. While the magnitude and the opposing twist directions in the positive and negative braid bundles agree well with the μCT measurements, we observe considerable scatter in the latter, further indicating that their deformation during compaction is sensitive to the local nesting configuration. Moving further along the centre-line, the second cut (2) investigates the point of maximum undulation amplitude. Here, the braid yarns are pressed against their axial counterparts as a result of direct contact with bundles from neighbouring layers. While the unshifted stacking configuration in nesting case 2 produces a flattened top and bottom surface, additional bending is introduced across the yarn width as a result of the shifted locations of braid bundles through-the-thickness in nesting case 1. The resultant asymmetric shape correlates well with the characteristic deformation mode of the actual cross-sections at this location, similar to the mechanism found in woven composites [67]. Contrarily to the previous cases, we observe mostly undistorted yarn-shapes and a low scatter near the point of zero undulation amplitude (3), where the fibres exhibit their maximum crimp angle. As a bundle crosses from one side of the textile to the other, the degree of interaction with adjacent plies and subsequent deformation are minimised. Position (4) coincides with the first cut in the upwards undulation segment and repeats the characteristic deformation pattern, although the sign of twist deformation changes. In the final cross-section (5) slightly before the peak amplitude, the gradual development of the yarn flattening mechanism is again encountered in opposite direction.

In Fig. 4.17, the evolution of the average ply thickness $\bar{t}_{\mathrm{rUC,c}}$ is outlined as a function of the global FVF $\varphi_{\mathrm{F,rUC}}$. At the beginning of the compaction simulation, all three braid architectures comprise a global FVF of approximately 37%. During their initial interaction, the bundles reposition freely and fill up large voids while the overall thickness drops considerately.

Close to the target FVF, the mutual contacts multiply. Due to the inherent growth in compaction resistance, the slope of the thickness reduction declines consistently. In comparison to the experimental data obtained from calliper measurements of the plate thickness, the simulated target values agree well. To validate the quasi-incompressible material behaviour during the compaction simulation, the total change in yarn volume is investigated in Fig. 4.18. For configurations involving the first nesting case, a negligible volumetric change is encountered. More pronounced but still in an acceptable range, the second nesting case induces a total volumetric shrinkage of approximately 0.5%. Here, the direct contact of two over-

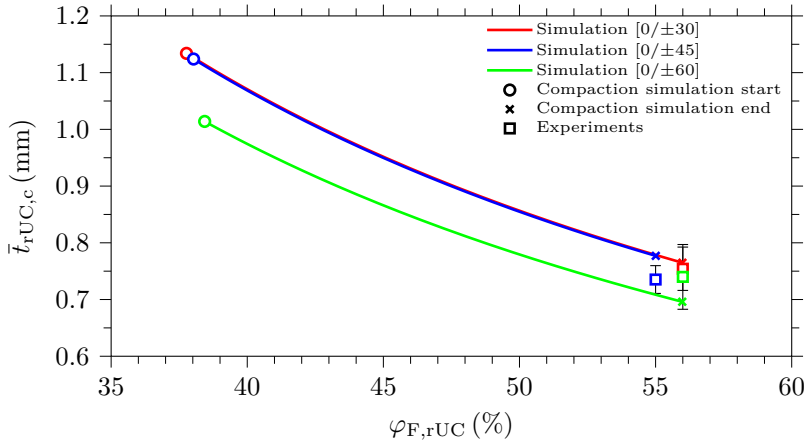

Fig. 4.17: Evolution of average ply thickness $\bar{t}_{\mathrm{rUC,c}}$ as a function of the global FVF $\varphi_{\mathrm{F,rUC}}$ during the compaction simulation for nesting case 1

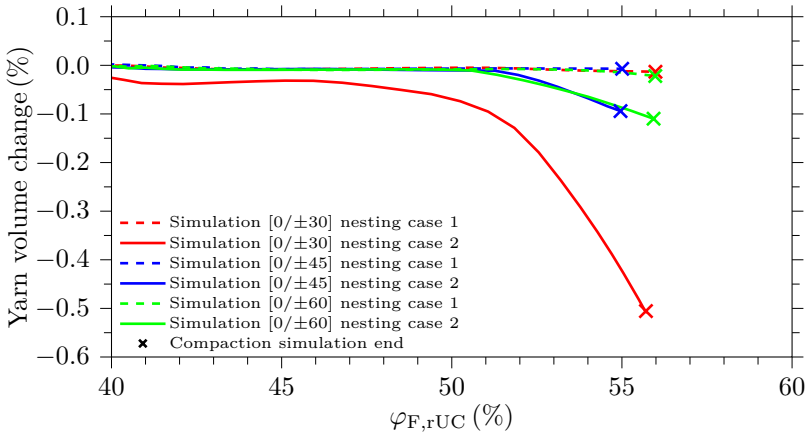

Fig. 4.18: Total yarn volume change as a function of the global FVF $\varphi_{\mathrm{F,rUC}}$ during the compaction simulation

lapping braid bundles from adjacent plies produces excessive contact pressure and local distortion.

In order to assess the sensitivity of the compacted geometry and the resulting stress fields with respect to the mesh density, a mesh refinement study was performed. A total of four unit cells of the same [0/±45] architecture in the first nesting configuration were created with the properties of each mesh highlighted in Table 4.4. In addition to varying the input element seed size l_{mesh} from its nominal value of 70 μm (medium) to 45 μm (fine) and 105 μm (coarse), the number of elements in the yarn through-thickness direction was doubled for the nominal case. As the meshing algorithm in the resin pockets adjusts for this modification at the truncated yarn sides, both medium mesh topologies feature a slightly different discretisation of the

matrix pockets. For the side edges of the bundles, a thickness ratio of $\xi = 5\%$ was selected for all unit cells throughout this work.

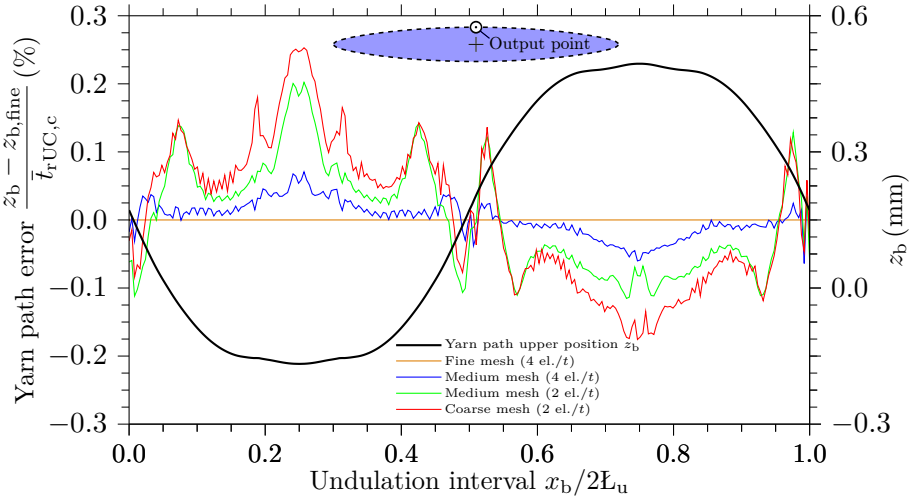

(a)

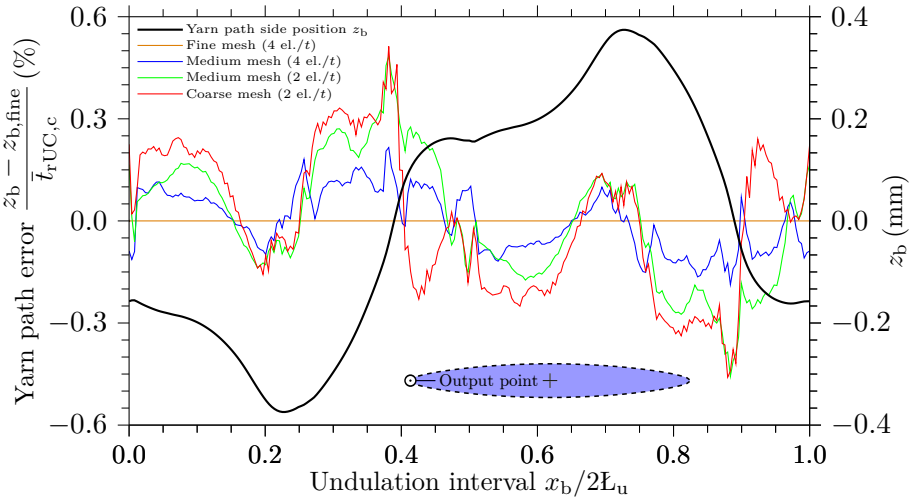

(b)

Fig. 4.19: Relative yarn path error along a single undulation interval (a) at the top position and (b) at the side of the braid bundles

The effect of the different mesh sizes on the compacted yarn path is investigated in Fig. 4.19 along a single undulation interval (a) at the top position and (b) at the side of the braid bundles. We quantify the relative positional error by comparing the nodal coordinates of each mesh with respect to the finest discretisation. Following the nodal coordinates at the top position of the bundle along a single undulation interval in Fig. 4.19 (a), we can identify two characteristic peaks in the geometrical error, with the larger one coinciding to the location of direct contact with an entangled axial bundle close to the minimum path locus. Although the identical

phenomenon is again encountered at the top of the undulation path, its severity is dampened by larger distance to the output location. While the shape of the yarn path deviation is mostly independent of the mesh, the relative error reduces gradually as a function of the mesh refinement. A significantly better convergence, however, is achieved by increasing the element count in the yarn thickness direction, as local deformations at the mutual contact zones can be captured more accurately. The same tendency can be found at the yarn side locus in Fig. 4.19 (b). While still having the highest error magnitude, the path predicted by the coarse mesh changes sign compared to all other configurations near the point of zero undulation amplitude, where axial and braid yarns interlock. Given the low overall sensitivity of the compacted geometry with respect to the mesh density, it can be concluded that the compacted textile architecture can be reliably reproduced with the given normal mesh size of $l_{\text{mesh}} = 70\,\mu\text{m}$.

Table 4.4: Mesh statistics of the [0/±45] braid refinement study ($\xi_\text{a} = \xi_\text{b} = 5\%$)

Mesh density	Fine	Medium	Medium	Coarse
l_{mesh} (μm)	45	70	70	105
Elements per yarn thickness	4	4	2	2
Elements in yarns (hex)	39512	17328	8664	4064
Elements in yarns (wedge)	1392	912	456	312
Elements in matrix pockets (tet)	118187	41776	40787	17016
Elements (3D cohesive)	44295	16564	16234	8977
Elements total	203386	76580	66141	30369
Nodes in yarns	52410	23665	14199	6927
Nodes in matrix pockets	59339	22649	22175	11796
Nodes total	111749	46314	36374	18723

4.3.2 Elastic properties

After updating the local fibre orientations for the compacted yarns, elastic properties can be readily obtained through the application of principal load cases and subsequent homogenisation. The material properties of the linear elastic transversely isotropic bundles summarised in Table 4.5 are calculated from the fibre and matrix properties given in Table 4.6 using Chamis' micromechanical equations [46] at the intra-yarn FVFs κ from Table 4.3. For a rUC subjected to a sequence of four successive linear load cases (E_x, E_y, E_z, G_xy) combined in a single simulation, the model is solved by Abaqus/Implicit (6.14) within seconds on a standard computer.

In order to quantify to effect of the textile architecture in the unit cell, the results are compared to an equivalent tape laminate using classical lamination theory

Table 4.5: Elastic properties of the transversely isotropic yarns for characteristic intra-yarn FVFs

κ (%)	E_1 (MPa)	$E_2 = E_3$ (MPa)	$G_{12} = G_{13}$ (MPa)	$\nu_{12} = \nu_{13}$	ν_{23}
63	133369	8660	4364	0.322	0.388
66	139583	9087	4705	0.320	0.391
70	147867	9709	5236	0.319	0.395

Table 4.6: Elastic properties for fibre and resin [2, 3]

Fibre: Toho-Tenax HTS40 F13 (12K, $\mu_{\mathrm{F,yarn}} = 800\,\mathrm{tex}$)						Resin: RTM 6	
$E_{1\mathrm{f}}$ (MPa)	$E_{2\mathrm{f}}$ (MPa)	$G_{12\mathrm{f}}$ (MPa)	$\nu_{12\mathrm{f}}$	$\nu_{23\mathrm{f}}$	ρ_{F} (g/cm^3)	E_{m} (MPa)	ν_{m}
210000	18000	21800	0.305	0.450	1.76	2890	0.35

(CLT). For triaxial braided composites, we construct an equivalent laminate by virtually separating the axial yarns, the braid yarns and the pure resin pockets. Each of the three constituents is then modelled either with a single unidirectional ply in the respective fibre direction or represented by an isotropic layer, as is the case for the matrix pockets. Assuming no crimp, the relative ply thicknesses t_{a}/t and t_{b}/t in the laminate model correspond to the volume fractions of axial and braid yarn content V_{a}/V and V_{b}/V and vary as a function of the braiding angle θ and the yarn properties. From a 2D unit cell, they are related by:

$$\begin{aligned}
\frac{V_{\mathrm{a}}}{V} = \frac{t_{\mathrm{a}}}{t} &= \frac{\varphi_{\mathrm{F}}}{\kappa_{\mathrm{a}} \left(1 + \dfrac{2}{\cos(\theta)} \dfrac{\rho_{\mathrm{F,a}}\, \mu_{\mathrm{F,yarn,b}}}{\rho_{\mathrm{F,b}}\, \mu_{\mathrm{F,yarn,a}}}\right)} \\
\frac{V_{\mathrm{b}}}{V} = \frac{t_{\mathrm{b}}}{t} &= \frac{\varphi_{\mathrm{F}}}{\kappa_{\mathrm{b}} \left(1 + \dfrac{2}{\cos(\theta)} \dfrac{\rho_{\mathrm{F,a}}\, \mu_{\mathrm{F,yarn,b}}}{\rho_{\mathrm{F,b}}\, \mu_{\mathrm{F,yarn,a}}}\right)} \\
\frac{V_{\mathrm{m}}}{V} = \frac{t_{\mathrm{m}}}{t} &= 1 - \frac{V_{\mathrm{a}} + V_{\mathrm{b}}}{V} = 1 - \frac{t_{\mathrm{a}} + t_{\mathrm{b}}}{t},
\end{aligned} \tag{4.10}$$

where the linear yarn density $\mu_{\mathrm{F,yarn}}$ and the fibre density ρ_{F} for the coincident axial and braid yarns are given in Table 4.6 and the intra-yarn and global FVFs are taken from Table 4.3.

For the longitudinal (x), transverse (y) and braid yarn direction ($1F$), the predicted elastic moduli are compared to their experimental equivalent as a function of the braiding angle θ in Fig. 4.20 (a). Error bars indicate one standard deviation for a total of six specimen tested. While the properties of the first two principal load

directions (x and y) are directly calculated from homogenisation of the unit cell, the modulus in braid fibre direction ($1F$) is obtained by an additional transformation of the macroscopic in-plane stiffness tensor. Consequently, this orientation implicitly incorporates deviations of the shear modulus G_{xy} and the Poisson's ratio ν_{xy}.

Due to the higher degree of overall bundle distortion after compaction, the second nesting case consistently yields the lower stiffness among the two stacking configurations. However, the magnitude of this knock-down is comparably small, since the localised defects are smeared over a finite volume during the subsequent homogenisation step. Nonetheless, the effect on the non-linear response including failure is expected to be significantly larger [81, 82]. For the principal directions, the unit cell predictions match the experiments exceptionally well, with a maximum relative error of 3.4 % in the case of a [0/±30] braid loaded in x direction. A similar trend is encountered in case the applied load is aligned with the braid fibre direction $1F$, with the exception that the stiffness of the [0/±60] architecture is severely over-predicted with a relative error of 10.5 %. While this is the most pronounced case, the predictions generally exceed the experimental results. For minimised computational effort, we assume an infinite stack of plies in through-thickness direction and hence over-estimate their out-of-plane support in comparison to an actual braided laminate [81]. If we now directly introduce the load in the fibre direction of the heavily undulating braid bundles, local out-of-plane deformations develop as a result of non-zero bend-extension coupling terms accompanied by a degradation of the effective modulus E_{1F}.

With the CLT model neglecting any undulation, it generally predicts larger elastic moduli compared to the unit cell results. In the braid's principal directions, an average increase in relative error of approximately 5% compared to the unit cell results is encountered. In the braid fibre direction $1F$, we observe an increase in error of up to 7% for the [0/±45] braid. Clearly, these small improvements in the prediction of the elastic properties do not justify the extensive modelling effort and computational cost of meso-scale unit cell models. For this purpose, the CLT model provides a simple and viable tool within a preliminary design phase, particularly in case only limited data on the detailed textile architecture is available. In addition, several analytical approaches also explicitly account for the effect of fibre waviness on the elastic properties of braided composites [44, 45, 83].

Fig. 4.20 (b) completes the comparison of the elastic properties by a comprehensive summary of the in-plane Poisson's ratios. An excessive Poisson's effect in axial direction is encountered in the [0/±30] material. Here, the discrepancy of the longitudinal and transverse stiffness is most prominent. As the braiding an-

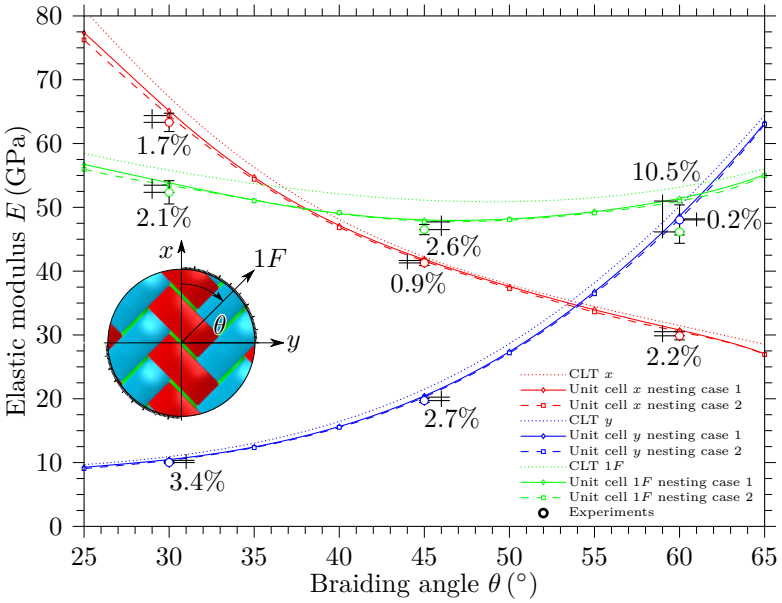

(a)

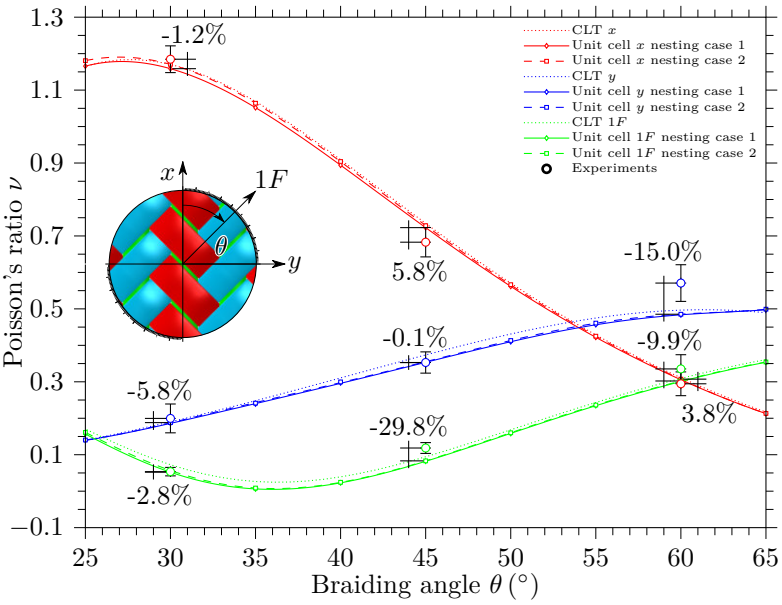

(b)

Fig. 4.20: Comparison of homogenised experimental and predicted (a) elastic moduli (b) Poisson's ratios as a function of the braiding angle θ

gle increases, this mismatch becomes less pronounced, with a tendency towards a balanced Poisson's effect in the [0/±60] architecture. Up to a braiding angle of 45°, experiments and predictions differ by a magnitude comparable to the elastic moduli, with the sole exception of the $1F$ direction. The corresponding jump of the relative error may be attributed to ν converging to a value close to zero. In the [0/±60] braid, the axial experiments are predicted well by the unit cell model.

Contrarily, the remaining load cases exhibit a relative error up to 15 %, possibly originating from a larger mismatch between the unit cell and the actual internal geometry of the composite. Again, the differences between the unit cell and the CLT model predictions are small.

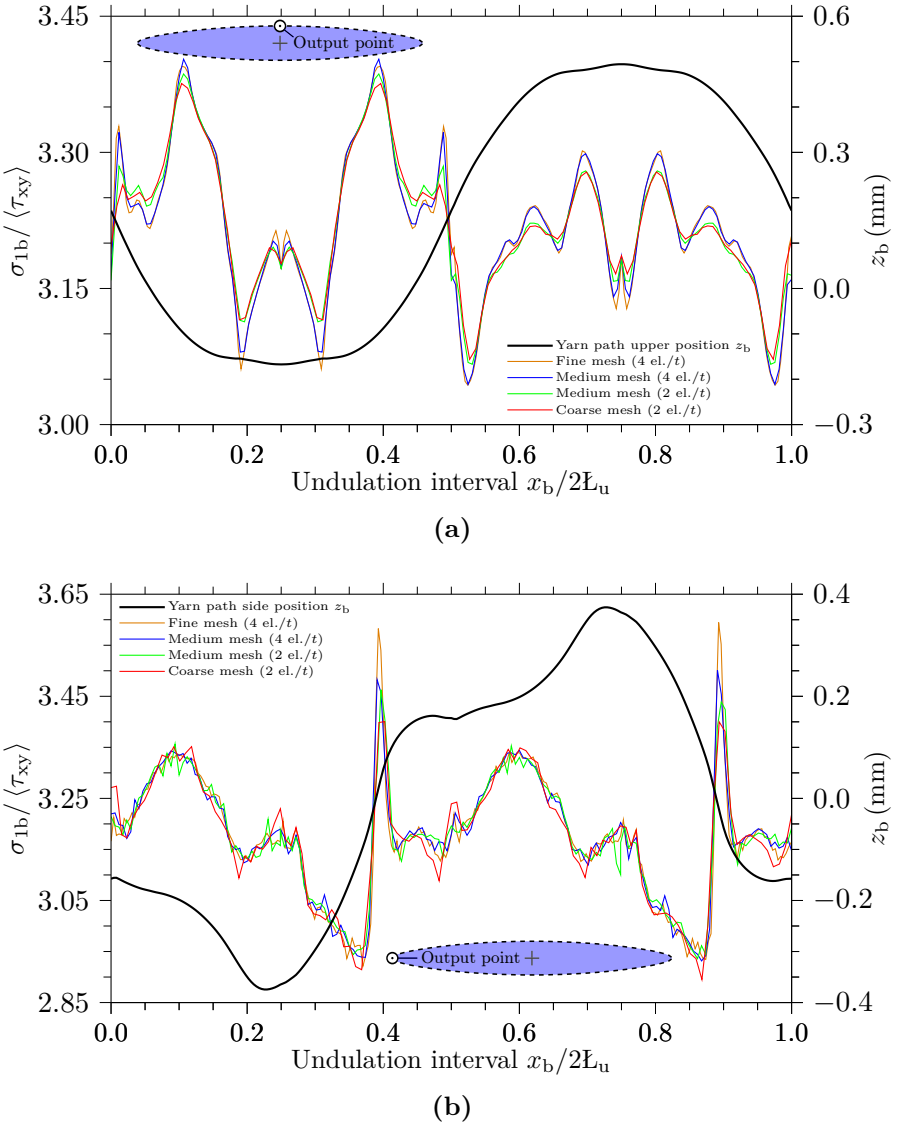

Fig. 4.21: Effect of mesh density on the stress distribution in fibre direction along a single undulation interval (a) at the top position and (b) at the side of the braid bundles

After having successfully demonstrated a minimal sensitivity of the simulated yarn path to the mesh cases under investigation, the preceding refinement study is extended to the stress fields inside the yarns. Coincident with the positions in Fig. 4.19, the stress distribution in the local braid fibre direction σ_{1b} is assessed as a result of the unit cell being subjected to a homogenised shear stress $\langle\tau_{xy}\rangle$ in a linear analysis. For each mesh, the nominal stress is calculated at the centre

and the side nodal position of the actual yarn path by extrapolation of the closest integration points. Hence, we benchmark the net effect of mesh refinement along the complete simulation chain, including both the geometric and actual mesh convergence. Fig. 4.21 (a) compares the linear stress concentration factor $\sigma_{1b}/\langle\tau_{xy}\rangle$ for different mesh densities along the top path of the braid bundles. Aside from the periodic pattern being represented well in all configurations, the element count in the yarn through-thickness direction outweighs the effect of global mesh refinement, particularly with regards to the peak amplitudes. When the bundle thickness is discretised with four elements, a global mesh refinement leads to a negligible change in the stress distribution compared to the medium case. Contrarily to the top position, the effect of a denser global mesh is more pronounced along the side of a braid bundle as shown in Fig. 4.21 (b). While both medium mesh cases yield comparable peak amplitudes here, the stress distribution along the yarn path tends to experience less noise and more distinct peaks with increasing refinement, as local bending effects are reproduced more accurately. Similar to the convergence behaviour during compaction and considering the additional computational expense of a fine mesh, a global mesh size of of $l_{\text{mesh}} = 70\,\mu$m is deemed sufficient to capture local stresses accurately.

4.4 Conclusions on meso-scale simulation framework

In this chapter, a novel simulation framework for accurate predictions of the mechanical response of triaxial braided composites was proposed. Realistic FE unit cell models were generated through an automated bottom-up simulation work-flow: local volumetric interpenetrations present in the initial stage of the model were resolved in a fictitious thermal step. Subsequently, a compaction simulation was performed to the desired target fibre volume fraction using flexible membranes for improved computational efficiency. Special out-of-plane periodic boundary conditions allow an implicit consideration of the compaction of multiple braid plies in different nesting configurations which enabled us to capture global FVFs of $55-60\%$ while using intra-yarn fibre volume fractions obtained from experiments. In the last step, a tetrahedral matrix pocket mesh was created from a CAD reconstruction of the deformed textile. A novel meshing methodology was developed to incorporate branching cohesive yarn-to-yarn and yarn-to matrix interfaces without the need of introducing an artificial matrix mesh of finite thickness. The framework was validated by detailed comparison with experimental results. First, the unit cell geometry was compared to the detailed reconstruction of the actual bundle

geometry from μCT measurements for three braid architectures, with a nominal braiding angle of 30°, 45° and 60°. Subsequently, the predictive capability of the approach and its robustness were demonstrated by successfully generating models in an automatic fashion for braiding angles ranging from 25° to 65°. These models were successfully used to predict the elastic properties obtained experimentally. The excellent correlation of experiments and unit cell predictions underlines the framework's potential for future damage modelling.

5 Non-linear mechanical response

In this chapter, the non-linear mechanical response of 2D triaxial braided composites under multiple tensile loading conditions was investigated with a novel meso-scale simulation framework. Numerical predictions made by three-dimensional finite element unit cells with a realistic internal geometry in two nesting configurations showed excellent correlation to experimental stress-strain curves and damage mechanisms. Triaxial braided composites were found to experience significant non-linearity in their macroscopic constitutive response before final failure, primarily attributed to two characteristic damage mechanisms. In the first one, the progressive development of matrix cracks manifested in a smooth degradation of the stress-strain curve up to the formation of a plateau for matrix dominated load cases, while the underlying textile architecture acted as a crack arresting grid and inhibited catastrophic failure.

The second damage mechanism was found to be intrinsic to the textile architecture and prevailed in the presence of severe interfacial stresses. A stable plateau in the stress-strain curves was correlated with the rapid formation of large-scale delaminations followed by progressive bundle pull-out, which was predicted qualitatively by the numerical model.

Although the investigated braid topologies exhibited considerable geometric variability, the unit cell modelling approach with a compacted geometry model built from average input parameters was capable of correctly predicting the homogenised constitutive response, localisation, and damage evolution. Further, the mechanical response was predicted under variable uni-axial off-axis load cases and the effect of the textile topology on the ultimate strength of the material was investigated. The meso-scale framework described in this chapter can be used as a general modelling approach for conducting numerical simulations of other textile composites. Aside from providing a valuable insight into how damage propagation is affected by the meso-structure, the predicted stress-strain curves can be used to calibrate macroscopic material models suitable for large-scale impact and crash simulations of braided composites.

5.1 Introduction

As a result of tight constraints on manufacturing costs and cycle-time in the industry, braided composites have recently been receiving increased attention. Aside from significant processing advantages over traditional laminates, their high specific energy absorption and excellent damage tolerance characteristics make them an ideal choice for designing primary load-carrying structures [50]. The accurate prediction of their non-linear mechanical response, however, remains a challenging task. Owing to the inherent textile nature with its out-of-plane waviness, interacting fibre bundles, resin pockets, and nesting of compacted plies, the material exhibits a complex failure and damage behaviour. In light of the fact that the textile architecture can vary significantly on a composite component with a multitude of parameters effecting the material properties, the determination of robust material properties by experimental test campaigns is highly cost- and time-intensive.

Finite-element (FE) modelling of mesoscopic unit cells provides powerful means for investigating the material behaviour of braided composites via virtual testing. In textile composites, a representative domain of the internal geometry is considered wherein the constituent reinforcing yarns are explicitly rendered as homogeneous continua. This approach can be applied to a variety of problems, ranging from the simulation of a dry fabric to the composite mechanical response with the accurate prediction of stress-strain fields, the determination of homogenised elastic properties, and the investigation of non-linearities with plasticity, damage initiation and progression up to final failure [53].

A unit cell's potential to accurately predict damage is primarily driven by a realistic representation of the underlying textile geometry. Idealised geometrical models, like for example those created by available pre-processors [51, 52], provide excellent results for a variety of topologies, but modelling highly compacted triaxial braided composites with global fibre volume fractions (FVF) of $55 - 60\%$ remains a challenging task. Here, the non-orthogonal intertwining of three in-plane fibre directions with multiple compacted layers produces a complex internal geometry that features severely distorted bundles with multiple contact zones and locally varying fibre orientations.

The non-linear mechanical response of textile composites was investigated by several researchers based on idealised geometrical models. By exploiting symmetries and periodicity in the material microstructure, Tang and Whitcomb [66, 74] derived a reduced unit cell (rUC) for biaxial braided composites. Owing to the model's computational efficiency, a sensitivity study of the progressive failure behaviour to

the internal geometry was performed. By generalising this approach, Carvalho et al. [65, 70] developed an equivalence framework for arbitrary periodic structures and accurately predicted failure envelopes for woven composites under biaxial compression. For a triaxial braided composite, Ivanov et al. [27] found a good correlation between the experimental and numerical stress-strain curves for tensile loading in axial and transverse direction. Obert et al. [84] introduced multiple discrete cracks in a woven unit cell and applied finite fracture mechanics to simulate the effect of transverse matrix cracks on the energy release rate.

Recently, increased research focus has been dedicated to the generation of more realistic geometry models, either by implementing additional processing simulation steps [60, 61, 85] or by a direct reconstruction of experimentally measured geometries using micro-computed tomography (μCT) images [64, 67]. Green et al. [60] studied the mechanical response of compacted 3D woven composites using a FE voxel discretisation and found significant differences between an idealised geometry model and one obtained from process simulation steps. For the same voxel meshing methodology applied to 2D woven composites, however, Doitrand et al.[61] showed that despite the good agreement of the elastic properties with a conventional mesh discretisation, the potential for simulating damage initiation and propagation is strongly limited due to severe artificial stress concentrations induced by the staircase-like representation of the geometry. After performing a numerical compaction step, Grail et al. [57] developed a nodal distortion algorithm to create matching mesh topologies between orthogonal yarns and investigated the mechanical performance of the resulting composite unit cell. In a subsequent study, Doitrand et al. [78] predicted the occurrence of matrix cracks at similar locations to those observed in experiments and studied their impact on the macroscopic mechanical performance.

The primary aim of this chapter is to provide a high-fidelity simulation tool for predicting the non-linear mechanical response of triaxial braided composites. Therefore, a meso-scale FE simulation framework was developed, which generates unit cell models with a realistic internal geometry by explicitly modelling the compaction process. The article is organised as follows:

- Firstly, the numerical model is described in detail and its key features are summarised, the periodic boundary conditions are introduced for strain controlled off-axis loading, and the constitutive law including plasticity, damage initiation and propagation is addressed.
- Secondly, the numerical results for several test cases under are presented for two nesting conditions and validated against experimental data by compar-

ing stress-strain curves and damage morphology obtained from digital image correlation (DIC) measurements.

- Thirdly, the mechanical response is investigated under multi-axial stress states, and the effect of the textile architecture on the ultimate strength of the material is studied.
- Finally, the capabilities and limitations of the modelling approach are addressed.

5.2 Modelling framework

5.2.1 Key features

Despite their high fidelity, the excessive computational expense of meso-FE models currently confines their potential application to a small niche of engineering applications. The capability to run multiple simulations in a short time frame would allow for more robust predictions by performing sensitivity studies as well as the generation of failure envelopes and optimisation tasks. To maximise computational efficiency, a reduced unit cell model which exploits the inherent material symmetries is generated within an automated simulation work-flow in four key steps for highly compacted braided composites at global FVFs of 55-60%. Following the roadmap outlined in Fig. 4.1, a nominal geometry is constructed a priori from measurable geometric parameters. In the second step, local volumetric interpenetrations are resolved in a fictitious thermal contraction and expansion step to achieve a compatible internal geometry. Subsequently, a compaction simulation is performed to the desired global target FVF using a single textile layer enclosed by flexible membranes. By applying different sets of PBCs, the compaction of multiple plies in different stacking and nesting configurations is implicitly considered at significantly reduced computational cost compared to explicitly modelling the full textile stack. The compacted rUC correctly renders the global FVF through experimentally determined intra-yarn FVFs. In the last step, a tetrahedral matrix pocket mesh is created from a CAD reconstruction of the deformed textile for subsequent mechanical analysis.

The key features of the finished composite rUC model are summarised in Fig. 5.1. Aside from the minimisation of the simulation domain, the use of a hexahedral mesh for the yarns which constitute about 80% of the total volume plays a key role in further improving the computational efficiency. With this discretisation,

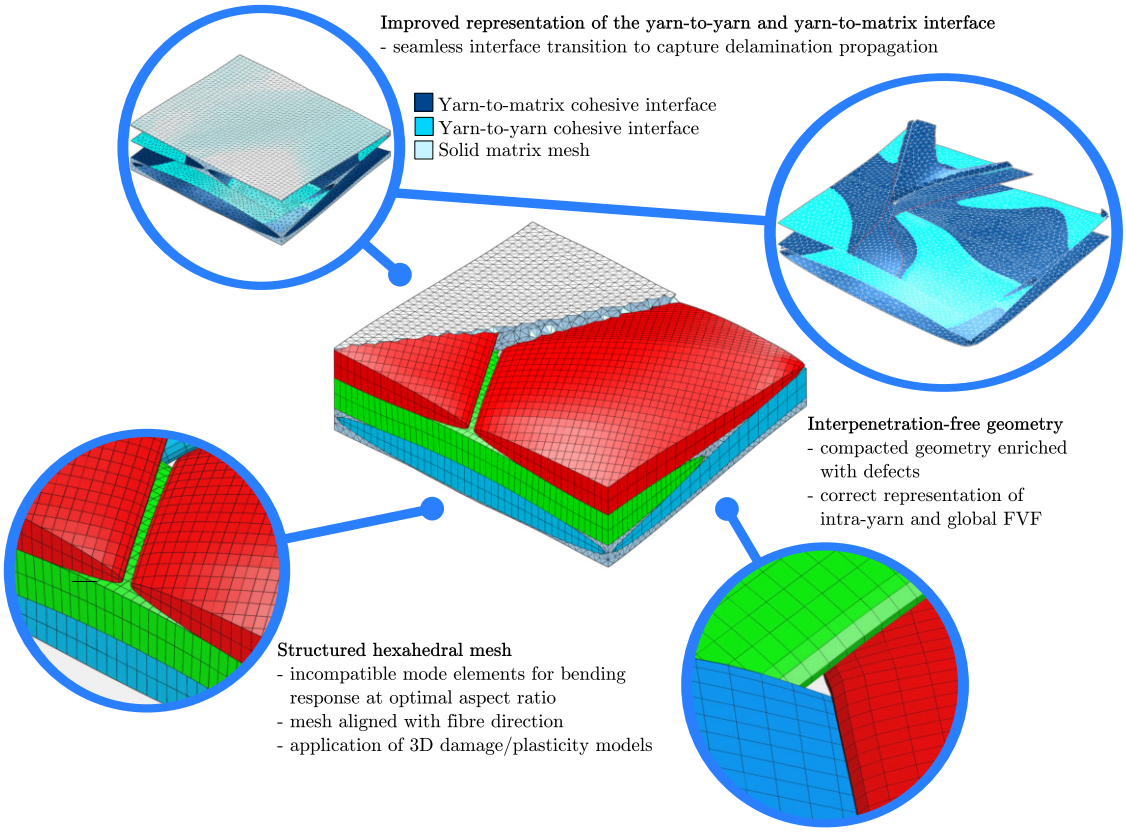

Fig. 5.1: Key modelling features of the simulation framework

an accurate solution at significantly reduced cost compared to a full second-order tetrahedral mesh is obtained [73], while the tetrahedral elements are confined to fill the complex resin pocket topology. The large width-to-thickness aspect ratio of the fibre bundles promotes the use of continuum elements enriched by incompatible modes. In addition to their displacement degrees of freedom, incompatible deformation modes are added internally to improve the bending behaviour and eliminate parasitic shear locking [73]. Despite their cost-intensive numerical formulation, a net decrease in computational expense is achieved by requiring a minimum amount of elements with improved aspect ratio in through-the-thickness direction to capture the bending stress gradient accurately.

In the fibre bundles, the implementation of a state-of-the-art three-dimensional elasto-plastic constitutive law with a set of physically-based damage initiation criteria enables us to capture non-linearities and typical failure modes encountered in textile composites.

In addition to intralaminar damage, the progressive delamination of the fibre bundles at their interface is an important failure mechanism which can trigger catastrophic fracture of the entire braid architecture. By connecting the yarn-to-yarn

and the yarn-to-matrix cohesive interfaces without an artificial matrix layer of finite thickness, delamination propagation is captured through an energy-based traction separation law.

5.2.2 Periodic boundary conditions under off-axis loading conditions

After exploiting the internal material symmetries to minimize the simulation domain, the periodic response of the rUC displayed in Fig. 5.2 is ensured by applying periodic displacement boundary conditions. By extending Equation 4.7 to account for arbitrary off-axis loading conditions, we obtain

$$\mathbf{u}(A) - \gamma\, \mathbf{T}\, \mathbf{u}(\hat{A}) = -\mathbf{T}_{\psi}^{-\mathbf{1}}\, \langle \mathbf{F} \rangle\ \mathbf{T}\, \mathbf{x}^{\mathbf{O}_{\hat{\mathbf{E}}}}, \tag{5.1}$$

where the left side describes the periodic displacement field $\mathbf{u}$ at the boundaries expressed by the complementing points A and $\hat{A}$. The coordinate transformation matrix $\mathbf{T}$ and the translation vector $\mathbf{x}^{\mathbf{O}_{\hat{\mathbf{E}}}}$ define the tessellation of adjacent subdomains, and the volume averaged deformation gradient tensor $\langle \mathbf{F} \rangle$ represents the external forcing function. Since the rUC is constructed by exploiting rotational and mirror symmetries, the load reversal factors $\gamma = \pm 1$ inhibit a simultaneous superposition of in-plane and out-of-plane shear loading. Due to the availability of experimental data, we focus on combined in-plane loading and compare our predictions against experimental off-axis test results. Under load control, this set-up is conveniently modelled by a transformation of the off-axis stress tensor into principal coordinates. Under displacement controlled loading, however, the full strain tensor in off-axis coordinates is not known a priori, as the model must be able to deform freely in any direction other than the load direction, such that Poisson's effects and shear-extension couplings are captured accurately. In order to reproduce this case, the external loading term on the right side of Equation 5.1 is extended by transforming an arbitrary deformation gradient tensor $\langle \mathbf{F} \rangle$ from off-axis coordinates into principal coordinates using the transformation matrix $\mathbf{T}_{\psi}$ with the off-axis loading angle ψ, as is displayed in Fig. 5.4.

The master equations necessary for the implementation of in-plane periodic boundaries are summarised in Table 5.1, and their out-of-plane equivalents are processed with an identical methodology. For edges and vertices sharing more than a single periodic boundary, a system of linearly independent constraint equations is assembled. The PBCs are incorporated into the FE model by coupling nodes at

the periodic boundaries through linear constraint equations in combination with external constraint driver nodes that define the homogenised deformation gradient tensor. It is important to note that under a case of uni-axial loading in off-axis direction, the unknown homogenised displacements of each constraint driver node except for the user-defined forcing term ε_1^{ψ} are determined by the FE solver.

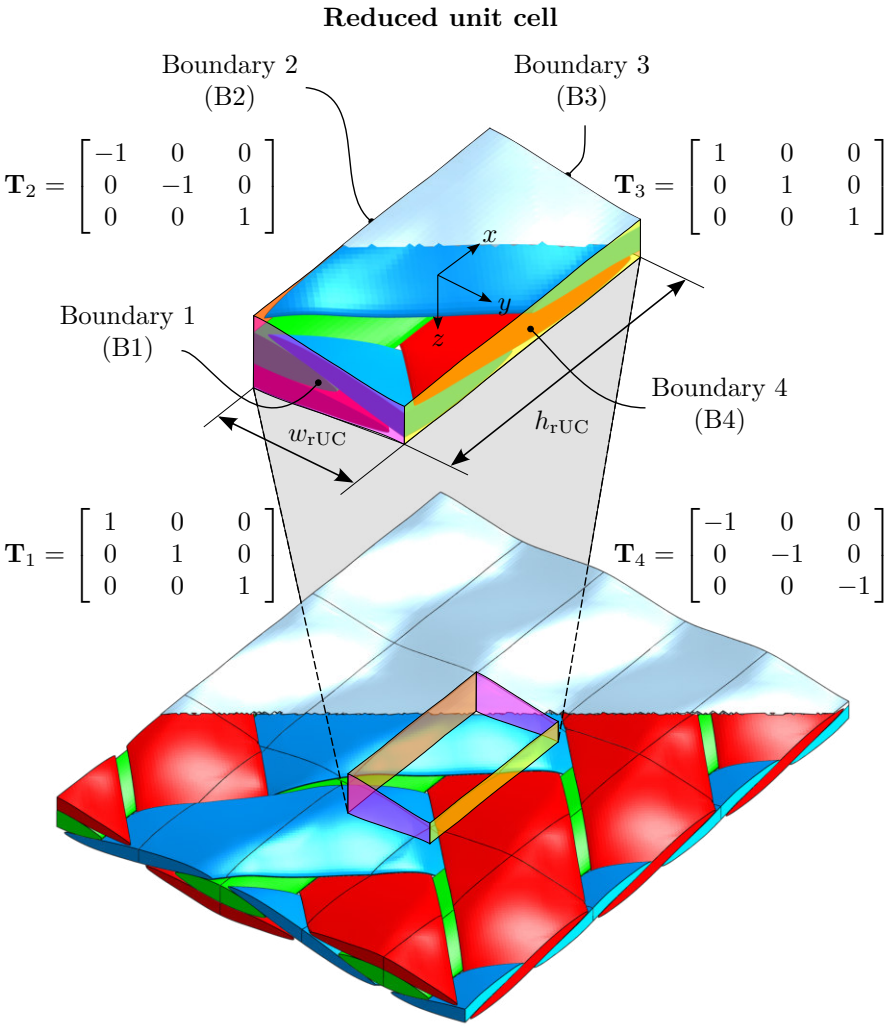

Fig. 5.2: Derivation of rUC domain with periodic in-plane boundaries and corresponding transformation matrices

A key feature of the presented work lies in the high fidelity of the mechanical simulation, since it builds on a compacted and defect-enriched geometry model that is the product of a step-by-step simulation process. In order to minimise computational expense during the compaction step, the out-of-plane behaviour of a periodic laminate is implicitly modelled by adding flexible dummy membranes to the top and bottom of the rUC. PBCs are subsequently applied to both membranes in their initial flat state and remain active throughout the entire compaction proce-

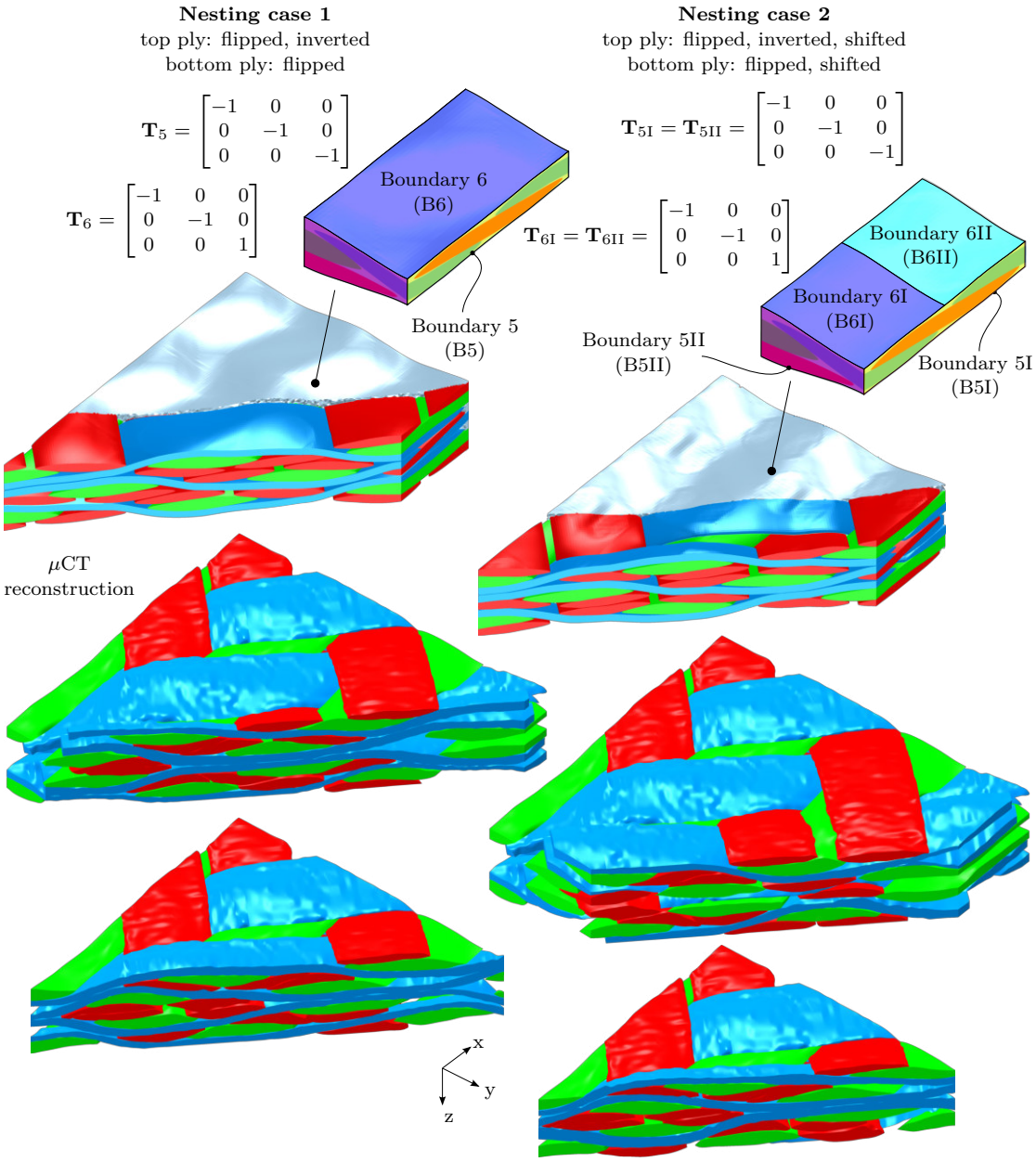

Fig. 5.3: Comparison of simulated nesting cases visualised by multiple tessellated rUCs and experimental μCT reconstruction for the [0/±45] architecture

dure. Finally, the periodically deformed nodal coordinates serve as a blueprint for constructing the solid matrix mesh at the out-of-plane boundaries of the rUC for the mechanical simulation.

The choice of through-the-thickness boundary conditions, including layer shifts and nesting severely affects the compacted geometry and the mesoscopic stress fields [81, 82]. When an actual component is manufactured on a braiding machine with multiple layers and changes in cross-section, the local shifts are hard to control and

hence tend to follow a random pattern. In the presented model, two different nesting configurations are considered implicitly with a special set of out-of-plane PBCs, both during the compaction simulation and the mechanical analysis. In their final state displayed in Fig. 5.3, axial fibre bundles of adjacent layers are positioned such that they are capable of closing the large initial voids originating from the variable braid thickness. In this case of maximum nesting, sections devoid of axial bundles are filled by their adjacent layer's equivalent. In the second nesting case, the stacked layers are additionally shifted in axial direction by a magnitude of half the rUC length. In contrast to the first case, the braid bundles are now positioned directly on top of each other. Hence, regions of high packing densities are supplemented by local resin-rich areas in the textile after compaction. A comparison with several cross-sections of the reconstructed μCT yarn geometry underlines the random nature of layer shifts. While the nesting configurations considered in the numerical can be identified in regions of the reconstructed geometry, they primarily aim to represent bounding intervals to the support provided by the adjacent layers at significantly reduced computational expense. The mechanical simulations of both nesting cases are conducted on two different geometry models that originate from the same compaction simulation being performed under the respective out-of-plane condition.

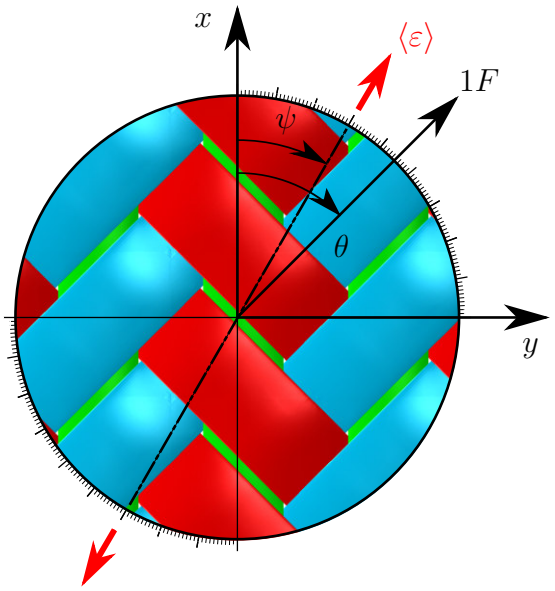

Fig. 5.4: Definition of off-axis load cases

Special care must be taken when PBCs are implemented in the commercial FE solver Abaqus/Explicit with the *Equation keyword. Within this environment, user-defined constraints are assembled in a global matrix for which a solution is obtained in every explicit time increment by means of an embedded penalty based

implicit algorithm. Unlike in the implicit solver, however, the constraint equation solver in Abaqus/Explicit is not parallelised. Hence, a bottleneck controlled by the bandwidth of the constraint matrix is formed in the overall solution procedure. With a standard implementation of the PBCs, the run-time for a non-linear analysis of a single rUC increases by a factor of 20 compared to simple displacement boundary conditions and would nullify all benefits of the periodic model reduction. To overcome this issue, the constraint equation system is fully decoupled by introducing a phantom slave node for each physical node at a periodic boundary. Both entities are coupled using rigid one-dimensional truss elements to ensure displacement equivalence. The constraint equations are now independently formed at the isolated phantom slave nodes in order to obtain a straightforward solution for a minimum bandwidth matrix. As the task of overall coupling of the equation system is now distributed explicitly among several elements, the solution procedure can be subdivided between multiple CPUs. This methodology produces similar run-times with and without activated PBCs and hence ensures the low computational expense of the unit cell. In order to eliminate parasitic stress concentrations at the boundaries from numerical inaccuracies in the nodal displacements, the PBCs are continuously solved in a double precision format.

Table 5.1: Master equations for implementation of in-plane periodic boundary conditions

$$
\begin{array}{cccccc}
 & \begin{bmatrix} u_\mathrm{x}(h_\mathrm{rUC}/2,y,z) \\ u_\mathrm{y}(h_\mathrm{rUC}/2,y,z) \\ u_\mathrm{z}(h_\mathrm{rUC}/2,y,z) \end{bmatrix} & - & \begin{bmatrix} u_\mathrm{x}(-h_\mathrm{rUC}/2,y,z) \\ u_\mathrm{y}(-h_\mathrm{rUC}/2,y,z) \\ u_\mathrm{z}(-h_\mathrm{rUC}/2,y,z) \end{bmatrix} & = & \begin{bmatrix} h_\mathrm{rUC}\left(\left\langle\varepsilon_\mathrm{x}^\psi\right\rangle\cos(\psi)^2+\left\langle\varepsilon_\mathrm{y}^\psi\right\rangle(1-\cos(\psi)^2)-\left\langle\varepsilon_\mathrm{xy}^\psi\right\rangle\sin(2\psi)\right) \\ h_\mathrm{rUC}\left(\left\langle\varepsilon_\mathrm{x}^\psi\right\rangle\sin(2\psi)/2-\left\langle\varepsilon_\mathrm{y}^\psi\right\rangle\sin(2\psi)/2+\left\langle\varepsilon_\mathrm{xy}^\psi\right\rangle\cos(2\psi)\right) \\ 0 \end{bmatrix} \\
\mathrm{B1} & & & & & \\
\mathrm{B2} & \begin{bmatrix} u_\mathrm{x}(-x,-w_\mathrm{rUC}/2,z) \\ u_\mathrm{y}(-x,-w_\mathrm{rUC}/2,z) \\ u_\mathrm{z}(-x,-w_\mathrm{rUC}/2,z) \end{bmatrix} & - & \begin{bmatrix} -u_\mathrm{x}(x,-w_\mathrm{rUC}/2,z) \\ -u_\mathrm{y}(x,-w_\mathrm{rUC}/2,z) \\ u_\mathrm{z}(x,-w_\mathrm{rUC}/2,z) \end{bmatrix} & = & \begin{bmatrix} -w_\mathrm{rUC}\left(\left\langle\varepsilon_\mathrm{x}^\psi\right\rangle\sin(2\psi)/2-\left\langle\varepsilon_\mathrm{y}^\psi\right\rangle\sin(2\psi)/2+\left\langle\varepsilon_\mathrm{xy}^\psi\right\rangle\cos(2\psi)\right) \\ -w_\mathrm{rUC}\left(\left\langle\varepsilon_\mathrm{x}^\psi\right\rangle(1-\cos(\psi)^2)+\left\langle\varepsilon_\mathrm{y}^\psi\right\rangle\cos(\psi)^2+\left\langle\varepsilon_\mathrm{xy}^\psi\right\rangle\sin(2\psi)\right) \\ 0 \end{bmatrix} \\
\mathrm{B3} & \begin{bmatrix} u_\mathrm{x}(-h_\mathrm{rUC}/2,y,z) \\ u_\mathrm{y}(-h_\mathrm{rUC}/2,y,z) \\ u_\mathrm{z}(-h_\mathrm{rUC}/2,y,z) \end{bmatrix} & - & \begin{bmatrix} u_\mathrm{x}(h_\mathrm{rUC}/2,y,z) \\ u_\mathrm{y}(h_\mathrm{rUC}/2,y,z) \\ u_\mathrm{z}(h_\mathrm{rUC}/2,y,z) \end{bmatrix} & = & \begin{bmatrix} -h_\mathrm{rUC}\left(\left\langle\varepsilon_\mathrm{x}^\psi\right\rangle\cos(\psi)^2+\left\langle\varepsilon_\mathrm{y}^\psi\right\rangle(1-\cos(\psi)^2)-\left\langle\varepsilon_\mathrm{xy}^\psi\right\rangle\sin(2\psi)\right) \\ -h_\mathrm{rUC}\left(\left\langle\varepsilon_\mathrm{x}^\psi\right\rangle\sin(2\psi)/2-\left\langle\varepsilon_\mathrm{y}^\psi\right\rangle\sin(2\psi)/2+\left\langle\varepsilon_\mathrm{xy}^\psi\right\rangle\cos(2\psi)\right) \\ 0 \end{bmatrix} \\
\mathrm{B4} & \begin{bmatrix} u_\mathrm{x}(-x,w_\mathrm{rUC}/2,-z) \\ u_\mathrm{y}(-x,w_\mathrm{rUC}/2,-z) \\ u_\mathrm{z}(-x,w_\mathrm{rUC}/2,-z) \end{bmatrix} & + & \begin{bmatrix} u_\mathrm{x}(x,w_\mathrm{rUC}/2,z) \\ u_\mathrm{y}(x,w_\mathrm{rUC}/2,z) \\ u_\mathrm{z}(x,w_\mathrm{rUC}/2,z) \end{bmatrix} & = & \begin{bmatrix} w_\mathrm{rUC}\left(\left\langle\varepsilon_\mathrm{x}^\psi\right\rangle\sin(2\psi)/2-\left\langle\varepsilon_\mathrm{y}^\psi\right\rangle\sin(2\psi)/2+\left\langle\varepsilon_\mathrm{xy}^\psi\right\rangle\cos(2\psi)\right) \\ w_\mathrm{rUC}\left(\left\langle\varepsilon_\mathrm{x}^\psi\right\rangle(1-\cos(\psi)^2)+\left\langle\varepsilon_\mathrm{y}^\psi\right\rangle\cos(\psi)^2+\left\langle\varepsilon_\mathrm{xy}^\psi\right\rangle\sin(2\psi)\right) \\ 0 \end{bmatrix}
\end{array}
$$

5.2.3 Constitutive modelling

5.2.3.1 Yarns

The non-linear mechanical response of the fibre bundles under quasi-static loading is modelled using LaRC05 [5]. As one of the best performing failure theories benchmarked in the World Wide Failure Exercise (WWFE) [86], this physically-based smeared-crack model considers typical failure processes in composites under three-dimensional stress states, such as matrix cracking, fibre kinking, fibre splitting and fibre tensile failure. The constitutive law consists of three basic building blocks, including the elastic-plastic behaviour before failure onset, the prediction of failure initiation by means of physically-based criteria, and damage propagation using a smeared crack model.

Elastic-plastic behaviour

The elastic properties of the transversely-isotropic fibre bundles are calculated from the fibre and matrix properties given in Table 4.6 by means of an analytical micromechanical approach [46] at the corresponding intra-yarn FVFs to obtain the homogenised properties summarised in Table 4.5. Before failure onset, non-linearities due to matrix-induced plasticity are considered in shear and transverse direction through a change of the respective secant moduli that produce plastic strains without damage. The decomposition of the total strain tensor into an elastic and a plastic part yields a constitutive law in the form of

$$\boldsymbol{\sigma} = \mathbf{C}\left(\boldsymbol{\varepsilon} - \boldsymbol{\varepsilon}_{\mathrm{pl}}\right) \tag{5.2}$$

where $\mathbf{C}$ denotes the elasticity tensor of the undamaged material, $\boldsymbol{\sigma}$ is the effective stress tensor and $\boldsymbol{\varepsilon}$ and $\boldsymbol{\varepsilon}_{\mathrm{pl}}$ are the total and plastic strain tensors. The non-zero components of the latter irreversible part at time t are obtained from calculating the maximum over the loading history as

$$\begin{aligned}
\varepsilon_2^{\mathrm{pl}}(t) &= \max_{t^*\leq t}\left\{\left|\varepsilon_2(t)\left(1-\frac{E_2^{\mathrm{nl}}}{E_2}\right)\right|, \left|\varepsilon_2^{\mathrm{pl}}(t^*)\right|\right\} \\
\varepsilon_3^{\mathrm{pl}}(t) &= \max_{t^*\leq t}\left\{\left|\varepsilon_3(t)\left(1-\frac{E_3^{\mathrm{nl}}}{E_3}\right)\right|, \left|\varepsilon_3^{\mathrm{pl}}(t^*)\right|\right\} \\
\gamma_{12}^{\mathrm{pl}}(t) &= \max_{t^*\leq t}\left\{\left|\gamma_{12}(t)\left(1-\frac{G_{12}^{\mathrm{nl}}}{G_{12}}\right)\right|, \left|\gamma_{12}^{\mathrm{pl}}(t^*)\right|\right\} \\
\gamma_{13}^{\mathrm{pl}}(t) &= \max_{t^*\leq t}\left\{\left|\gamma_{13}(t)\left(1-\frac{G_{13}^{\mathrm{nl}}}{G_{13}}\right)\right|, \left|\gamma_{13}^{\mathrm{pl}}(t^*)\right|\right\}.
\end{aligned} \tag{5.3}$$

The transverse isotropy of the material is retained throughout its plastic deformation history by consistently degrading the corresponding shear and transverse moduli, such that $E_3^{\mathrm{nl}} = E_2^{\mathrm{nl}}$ and $G_{13}^{\mathrm{nl}} = G_{12}^{\mathrm{nl}}$. By assuming a negligible contribution of the axial strain to yielding of the matrix, its plastic deformation is further quantified by introducing the current irreversible equivalent strain [5] as

$$\varepsilon_{\mathrm{eq}} = \sqrt{(\varepsilon_2 - \varepsilon_3)^2 + \gamma_{12}^2 + \gamma_{13}^2 + \gamma_{23}^2}. \tag{5.4}$$

Material healing during unloading can be further prevented by defining the history field variable $\varepsilon_{\mathrm{eq}}^{\max}$ at time t as the maximum over the loading history as

$$\varepsilon_{\mathrm{eq}}^{\max}(t) = \max_{t^* \leq t} \left\{ \varepsilon_{\mathrm{eq}}(t^*) \right\}. \tag{5.5}$$

For a maximum equivalent strain greater zero, both non-linear shear secant modulus G_{12}^{nl} and transverse secant modulus E_2^{nl} are defined as the ratio of the current stress state to the maximum equivalent strain under uniaxial loading conditions as

$$G_{12}^{\mathrm{nl}} = \frac{\tau_{12}(\varepsilon_{\mathrm{eq}}^{\max})}{\varepsilon_{\mathrm{eq}}^{\max}} \qquad E_2^{\mathrm{nl}} = \frac{\sigma_2(\varepsilon_{\mathrm{eq}}^{\max})}{\varepsilon_{\mathrm{eq}}^{\max}}. \tag{5.6}$$

The non-linear stress-strain curves $\tau_{12}(\varepsilon_{\mathrm{eq}}^{\max})$ and $\sigma_2(\varepsilon_{\mathrm{eq}}^{\max})$ in Equation 5.6 are determined experimentally under the respective uniaxial loading conditions. An exponential fitting function with three independent constants in the form of

$$\tau_{12}(\varepsilon_{\mathrm{eq}}^{\max}) = a_{12}\left(e^{b_{12}\,\varepsilon_{\mathrm{eq}}^{\max}} - e^{c_{12}\,\varepsilon_{\mathrm{eq}}^{\max}}\right) \qquad \sigma_2(\varepsilon_{\mathrm{eq}}^{\max}) = a_2\left(e^{b_2\,\varepsilon_{\mathrm{eq}}^{\max}} - e^{c_2\,\varepsilon_{\mathrm{eq}}^{\max}}\right) \tag{5.7}$$

captures the non-linear behaviour in the shear and transverse direction adequately. Moreover, the monotonically increasing nature of this analytical formulation ensures a positive tangent stiffness, produces a smooth curve extrapolation for combined load cases and avoids time consuming tabular interpolations during the solution procedure. The plastic coefficients summarised in Table 5.2 are obtained by fitting averaged stress-strain data of shear and transverse compressive coupon tests for the material used in this study.

In the fibre direction (1), the stress-strain response is typically modelled as linearly-elastic up to final failure. Under tension, carbon fibres reveal a non-Hookean constitutive behaviour, in which the Young's modulus increases proportionally with the applied load [48, 49, 87]. This stiffening phenomenon is incorporated into the

Table 5.2: Plastic fitting parameters for the non-linear shear and transverse stress-strain curves

a_{12} (MPa)	b_{12}	c_{12}	a_2 (MPa)	b_2	c_2
73.53	2.53	-72.50	-1957.00	-16.75	-10.76

constitutive law by a simple empirical relation [47] where the stress-proportional modulus in the fibre direction is calculated from

$$E_1 = \begin{cases} E_{1,\mathrm{t,lin}}(1 + k_\mathrm{f}\,\sigma_1) & \text{for } \sigma_1 \geq 0 \\ E_{1,\mathrm{c,lin}} & \text{for } \sigma_1 < 0, \end{cases} \tag{5.8}$$

and $E_{1,\mathrm{t,lin}}$ denotes the linear tensile Young's modulus at zero load. From regression of unidirectional tests, an averaged stress-strain curve is represented with a load proportional stiffness factor of $k_\mathrm{f} = 4.76$. Due to the lack of reliable data under longitudinal compression, we resort to a linear model in this region. Here, potential non-linear effects are implicitly incorporated by an adjustment of the elastic properties. The compressive modulus $E_{1,\mathrm{c,lin}}$ is degraded based on a material characterisation campaign performed by [3] for the fibre/matrix combination utilised within this study.

Failure initiation

The onset of damage in the yarns is predicted by physically-based failure criteria which distinguish four failure modes under three-dimensional stress states, including matrix cracking, fibre kinking, fibre splitting, and fibre tensile failure [5]. Whereas the latter is predicted using a maximum stress criterion, the coincident fibre kinking and splitting failure indices are evaluated on a rotated fracture plane m aligned with the formation of a possible kink band by:

$$FI_{\mathrm{f,kink}} = FI_{\mathrm{f,split}} = \sqrt{\left(\frac{\tau_{23}^{\mathrm{m}}}{S_\mathrm{T} - \eta_\mathrm{T}\,\sigma_2^{\mathrm{m}}}\right)^2 + \left(\frac{\tau_{12}^{\mathrm{m}}}{S_\mathrm{L} - \eta_\mathrm{L}\,\sigma_2^{\mathrm{m}}}\right)^2 + \left(\frac{\langle\sigma_2^{\mathrm{m}}\rangle_+}{Y_\mathrm{T}}\right)^2} \tag{5.9}$$

where S_L and S_T are the longitudinal and transverse shear strengths, Y_t is the transverse tensile strength and η_L and η_T are friction coefficients on the corresponding fracture plane. These two failure modes are then distinguished based on the magnitude of the acting longitudinal compressive stress with $\sigma_1 \leq -X_\mathrm{c}/2$ representing fibre kinking and $-X_\mathrm{c}/2 < \sigma_1 < 0$ indicating fibre splitting [5]. This

distinction is important for further failure propagation. The McCauley brackets $\langle \bullet \rangle_+$ are defined as $\langle x \rangle_+ = \max\{0, x\}$.

Matrix cracking is predicted using a modified version of the Mohr-Coulomb failure criterion with a quadratic stress interaction on a rotated fracture plane given by

$$FI_{\mathrm{mat}} = \sqrt{\left(\frac{\tau_{\mathrm{T}}}{S_{\mathrm{T}} - \eta_{\mathrm{T}}\,\sigma_{\mathrm{N}}}\right)^2 + \left(\frac{\tau_{\mathrm{L}}}{S_{\mathrm{L}} - \eta_{\mathrm{L}}\,\sigma_{\mathrm{N}}}\right)^2 + \left(\frac{\langle \sigma_{\mathrm{N}} \rangle_+}{Y_{\mathrm{t}}}\right)^2}. \tag{5.10}$$

A stress transformation yields the components of the traction vector σ_{N}, τ_{L} and τ_{T} acting on a possible fracture plane, see Fig. 5.5, as

$$\begin{aligned} \sigma_{\mathrm{N}} &= \sigma_2 \cos^2(\alpha) + \sigma_3 \sin^2(\alpha) + \tau_{23} \sin(2\alpha) \\ \tau_{\mathrm{T}} &= \frac{\sigma_3 - \sigma_2}{2} \sin(2\alpha) + \tau_{23} \cos(2\alpha) \\ \tau_{\mathrm{L}} &= \tau_{12} \cos(\alpha) + \tau_{31} \sin(\alpha). \end{aligned} \tag{5.11}$$

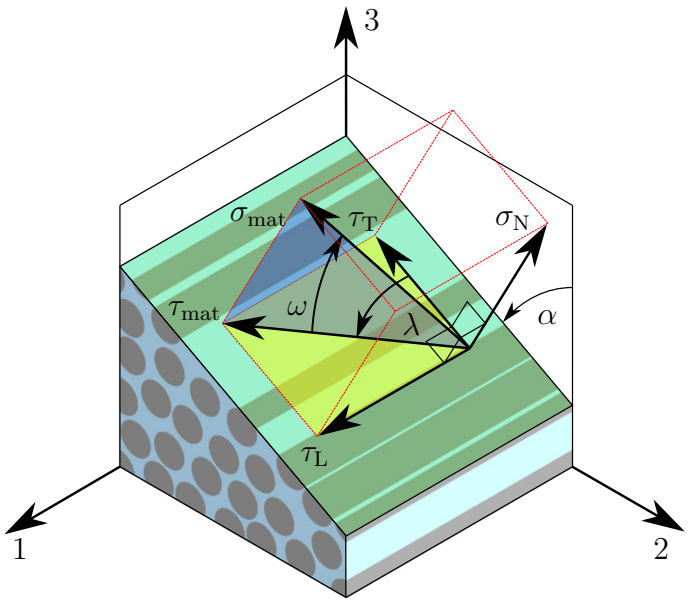

Fig. 5.5: Traction components on the fracture plane for matrix cracking

By iteratively evaluating Equation 5.10 within a range of $0° < \alpha < 180°$ in such a way that the failure index is maximised, the fracture plane is identified when $FI_{\mathrm{mat}} \geq 1$. The normal traction component σ_{N} only contributes to failure onset for positive values attributed to crack opening, whereas a negative or compressive value inhibits failure onset through frictional mechanisms. The longitudinal friction coefficient $\eta_{\mathrm{L}} = 0.082$ is taken from experimental data for a typical carbon/epoxy

composite [5]. Assuming a fracture angle of $\alpha_0 = 53°$ under pure transverse compression, the transverse friction coefficient η_T is calculated from

$$\eta_T = -\frac{1}{\tan(2\,\alpha_0)} \tag{5.12}$$

The matrix failure criterion does not directly incorporate the corresponding unidirectional strength Y_c. However, considering that failure under pure transverse compressive loading is triggered by the transverse shear stress component τ_T on a rotated fracture plane, the transverse shear strength S_T is given by

$$S_T = \frac{Y_c}{2\,\tan(\alpha_0)}. \tag{5.13}$$

Failure propagation

Once a failure criterion is satisfied, the formation of cracks in the material is simulated using a continuum damage mechanics (CDM) approach. By introducing the concept of effective stress [88] and associating an independent scalar damage variable with each of the failure modes fibre tension, matrix cracking and fibre kinking/splitting, the constitutive law is modified in such a way that the tractions on the associated fracture plane are progressively reduced to zero. During this degradation procedure, the energy dissipated by the model corresponds to the fracture toughness of the associated failure mode. Using a linear softening law, the irreversible scalar damage variable for fibre tension and fibre kinking/splitting is defined as a function of the strain tensor as

$$d = \max\left\{0, \min\left\{1, \varepsilon^f \frac{\varepsilon - \varepsilon^0}{\varepsilon(\varepsilon^f - \varepsilon^0)}\right\}\right\}. \tag{5.14}$$

where ε denotes the current elastic driving strain on the fracture plane, ε^0 corresponds to the onset of damage and ε^f to final failure. The latter are obtained based on the smeared crack band model [75] while considering a suitable characteristic size of the band l_{char} in order to alleviate mesh dependency from

$$\begin{aligned} \varepsilon^{\mathrm{f}}_{\mathrm{f,t}} &= \frac{2\,G^{\mathrm{f,t}}_{\mathrm{Ic}}}{X_{\mathrm{t}}\,l_{\mathrm{char}}} \\ \varepsilon^{\mathrm{f}}_{\mathrm{f,kink}} &= \frac{2\,G^{\mathrm{f,kink}}_{\mathrm{Ic}}}{X_{\mathrm{c}}\,l_{\mathrm{char}}} \\ \varepsilon^{\mathrm{f}}_{\mathrm{f,split}} &= \frac{2\,G^{\mathrm{mat}}_{\mathrm{IIc}}}{\tau^{0,m}_{12}\,l_{\mathrm{char}}}. \end{aligned} \tag{5.15}$$

The choice of the characteristic material length l_{char} is affected by the failure mode, the orientation of the fracture plane, the finite element type, and the mesh topology [89, 90]. For the sake of numerical simplicity, the cubic root of the element volume is selected here. Thus, taking into account that the orientation of the hexahedral yarn mesh follows the fibre direction, the most accurate predictions are achieved if the crack band develops either along or perpendicular to the yarn-path. After transforming the stress tensor from principal material coordinates onto the previously identified fracture plane, the nominal traction vector $\mathbf{t}$ including damage is defined as

$$\mathbf{t} = \left\{ \left(1 - d\,\frac{\langle \sigma_{\mathrm{N}} \rangle_{+}}{\sigma_{\mathrm{N}}}\right) \sigma_{\mathrm{N}} \quad (1-d)\,\tau_{\mathrm{L}} \quad (1-d)\,\tau_{\mathrm{T}} \right\}^{T}. \tag{5.16}$$

In the final step, the degraded stress tensor is rotated back to the material coordinate system. Using the material data provided in Table 5.3, the stress-strain response of the braid bundles in the fibre direction is shown for different loading/unloading cases in Fig. 5.6 (a). While macroscopic cyclic loading is not part of this study, the constitutive law's capability to capture unloading is key to accurately render load redistributions after localisation in a non-linear failure analysis.

Unidirectional composites often exhibit an increasing resistance to fracture during matrix crack growth, which is attributed to toughening effects in the wake of the crack tip, such as fibre bridging [91]. By formulating a bi-linear softening law, an increase in the resistance (R)-curve associated with a transition from crack initiation to steady state propagation can be captured [92]. A piecewise definition of damage variable d_{mat} in the initiation and propagation region yields

$$d_{\mathrm{mat}} = \begin{cases} \max\left\{0, \dfrac{(\varepsilon - \varepsilon^{0})(\varepsilon^{\mathrm{i}} - r\,\varepsilon^{0})}{\varepsilon(\varepsilon^{\mathrm{i}} - \varepsilon^{0})}\right\} & \text{for } \varepsilon^{0} < \varepsilon \leq \varepsilon^{\mathrm{i}} \\ \min\left\{1, \dfrac{(r\,\varepsilon^{0}(\varepsilon - \varepsilon^{\mathrm{f}})}{\varepsilon(\varepsilon^{\mathrm{f}} - \varepsilon^{\mathrm{i}})}\right\} & \text{for } \varepsilon^{\mathrm{i}} < \varepsilon \leq \varepsilon^{\mathrm{f}}, \end{cases} \tag{5.17}$$

where the strength ratio r relates the intermediate strength to the initiation strength at which the energy dissipated by the model is coincident to the mixed-mode initiation fracture toughness $\Gamma^{\text{mat}}_{\text{init}}$. The respective intermediate strain ε^{i} and the final failure strain ε^{f} at which the element is deactivated are defined as

$$\begin{aligned} \varepsilon^{\text{i}} &= \frac{2\,\Gamma^{\text{mat}}_{\text{init}}}{\sigma^0\,l_{\text{char}}} + r\,\varepsilon^0 \text{and} \\ \varepsilon^{\text{f}} &= \frac{2\,\Gamma^{\text{mat}}_{\text{prop}}}{r\,\sigma^0\,l_{\text{char}}}. \end{aligned} \tag{5.18}$$

Assuming quadratic mode mixety [90], the fracture toughness on the fracture surface is calculated from

$$\Gamma^{\text{mat}} = G^{\text{mat}}_{\text{Ic}} \left(\frac{\langle \sigma^0_{\text{N}} \rangle_+}{\sigma^0_{\text{mat}}} \right)^2 + G^{\text{mat}}_{\text{IIc}} \left(\frac{\tau^0_{\text{T}}}{\sigma^0_{\text{mat}}} \right)^2 + G^{\text{mat}}_{\text{IIc}} \left(\frac{\tau^0_{\text{L}}}{\sigma^0_{\text{mat}}} \right)^2. \tag{5.19}$$

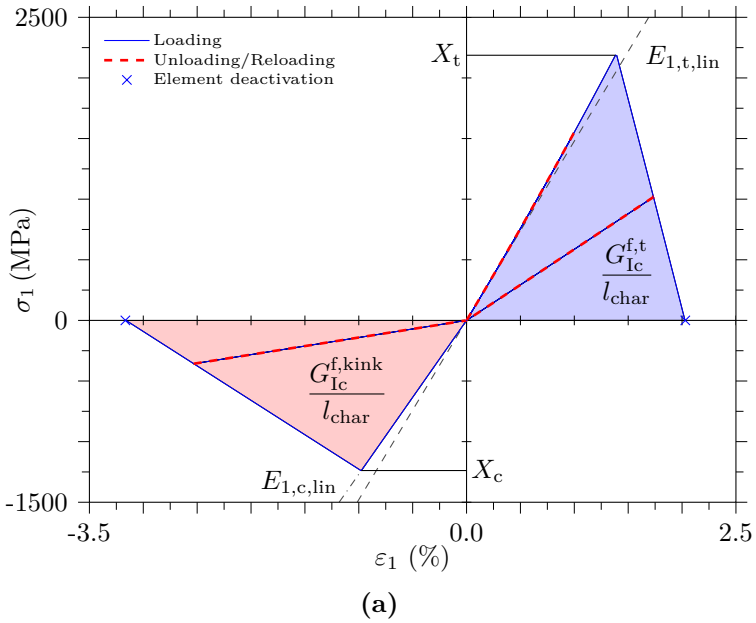

(a)

Fig. 5.6: Stress-strain response of the braid bundles loaded in their (a) fibre direction (1), l_{char}=4 mm, (b) transverse direction (2), l_{char}=150 μm, (c) shear direction (12), l_{char}=250 μm

In addition to the fracture toughness initiation properties given in Table 5.3, the propagation values required for the definition for the bi-linear softening law are based on an experimental R-curve reported in [92]. Due to numerical stability reasons, a value of 0.02 is selected for the strength ratio r. The stress-strain response of the braid bundles is displayed for loading in the transverse direction (2)

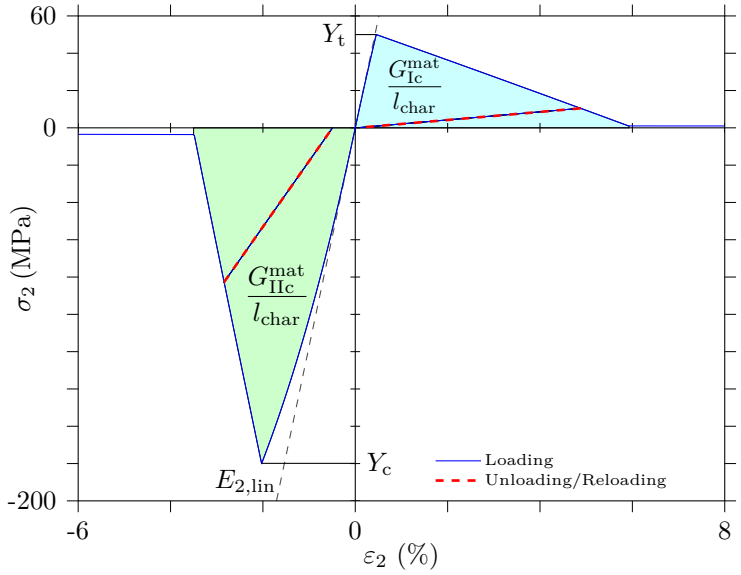

(b)

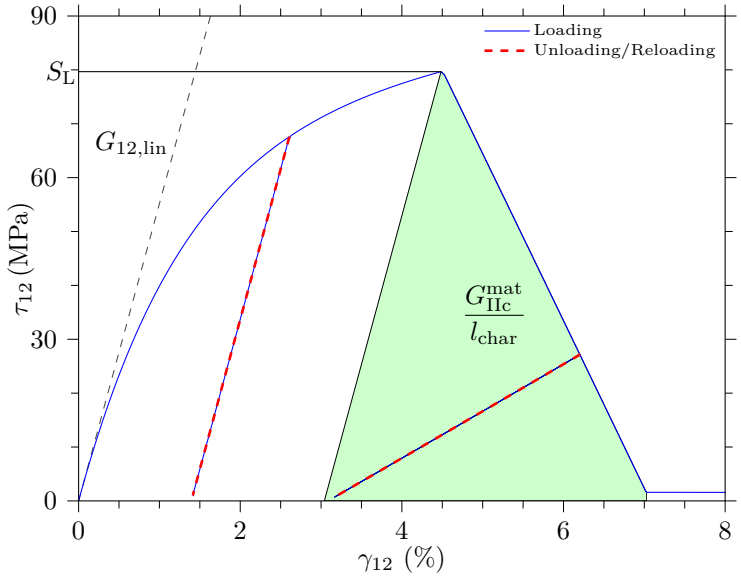

(c)

Fig. 5.6: continued: Stress-strain response of the braid bundles loaded in their (a) fibre direction (1), l_{char}=4 mm, (b) transverse direction (2), l_{char}=150 μm, (c) shear direction (12), l_{char}=250 μm

in Fig. 5.6 (b) and for in-plane shear (12) loading in Fig. 5.6 (c). In the presence of non-linearities due to matrix-induced plasticity, only the elastic part of the strain tensor contributed to the fracture process. In the case of more than a single failure criterion initiating at the same material point during the simulation, the fibre tensile and kinking damage process are treated as the most critical propagation modes and an element is deactivated when each of its integration points is fully

damaged. The material model is implemented in the commercial finite element code Abaqus/Explicit [73] using a user-defined material model (VUMAT). The explicit implementation avoids convergence problems often encountered in implicit implementations during softening.

Table 5.3: Strength and initiation fracture toughness properties for axial and braid yarns [4, 5]

	κ (%)	X_t (MPa)	X_c (MPa)	Y_t (MPa)	Y_c (MPa)	S_L (MPa)	$G_{Ic}^{f,t}$ (J/m^2)	$G_{Ic}^{f,kink}$ (J/m^2)	G_{Ic}^{mat} (J/m^2)	G_{IIc}^{mat} (J/m^2)
Axial yarns	63-66	2100	1240	45	180	70	89800	78300	200	400 [1]
Braid yarns	70	2200	1240	50	180	80	89800	78300	225	400 [1]

[1] estimated

5.2.3.2 Interface

In both the yarn-to-matrix and the yarn-to-yarn interfaces, the possibility of debonding is incorporated through a cohesive zone modelling (CZM) approach. The constitutive response employs a quadratic stress interaction criterion for failure initiation where the opening component of the normal traction t_n and the effective shear traction t_{shear} are evaluated against the interface strength properties N and S in the form of

$$\left(\frac{\langle t_n \rangle_+}{N}\right)^2 + \left(\frac{t_{shear}}{S}\right)^2 = 1. \tag{5.20}$$

Once the onset of failure is reached, damage propagation is modelled using an energy-based linear softening law. The mixed-mode response is governed by a power law interaction of the energies required to cause failure in the individual modes given by

$$\left(\frac{G_I}{G_{Ic}}\right)^{\alpha_{pl}} + \left(\frac{G_{shear}}{G_{IIc}}\right)^{\alpha_{pl}} = 1. \tag{5.21}$$

Using the material properties provided in Table 5.4 and a power law coefficient of $\alpha_{pl} = 1.23$ [**?**], the corresponding bi-linear traction-separation response of the interface is shown under mixed-mode conditions in Fig. 5.7. After complete failure of the interface, normal and post-debonding frictional stresses are transmitted by means of a contact algorithm, where an isotropic friction coefficient of 0.6 [93] between the delaminated surfaces is employed.

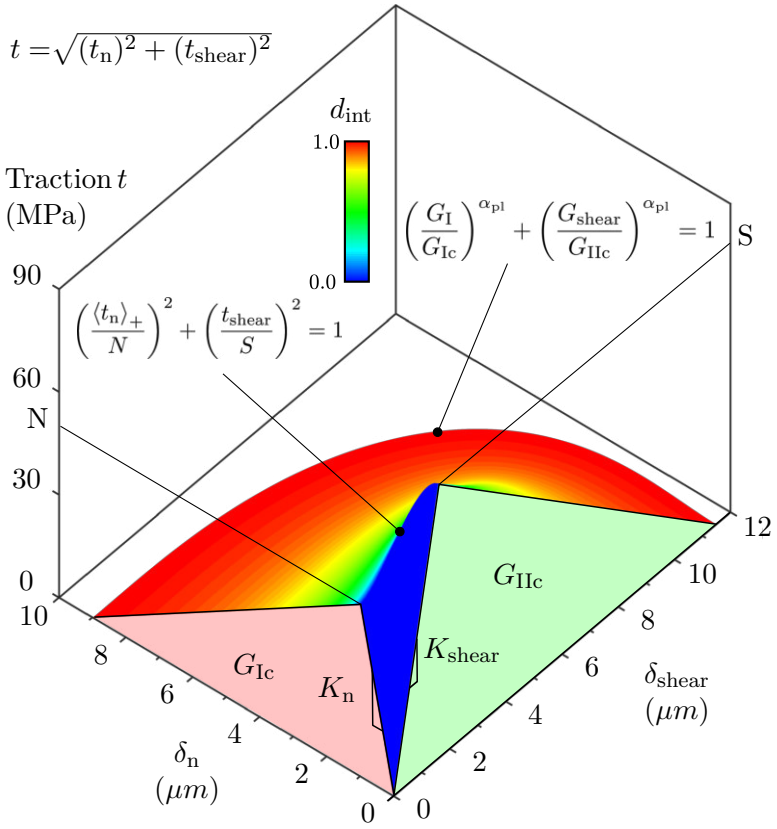

Fig. 5.7: Bi-linear traction-separation law

Table 5.4: Material properties used to define the cohesive interface [6]

$K_n = K_{shear}$ (N/mm^3)	N (MPa)	S (MPa)	G_{Ic} (J/m^2)	G_{IIc} (J/m^2)
$2.5 \cdot 10^6$	50	80	225	460

5.2.3.3 Resin pockets

The non-linear constitutive response of the resin pockets under quasi-static loading is commonly addressed by elastic-plastic material models, such as the Drucker-Prager yield criterion, which accounts for the effect of hydrostatic stress and different hardening responses under tensile and compressive loading encountered in polymers [94, 95]. For the tightly packed braid configurations investigated in this study, the neat resin volume takes up about 20 % of the total unit cell at about four to seven times the amount of finite elements in the fibre bundles. Hence, considering that the latter already contribute the majority of the macroscopic elastic-plastic response and significant savings in computational cost, the resin pockets are assumed to behave linearly elastic, with their material properties given in Table 4.6.

5.3 Applications

In the present section, the non-linear mechanical response for triaxial braided composites manufactured from Toho-Tenax HTS40 F13 12K (800 tex) bundles for both the axial and braid yarns in combination with a Hexcel RTM6 epoxy resin is predicted. In the first part, the numerical results for several test cases are presented and validated against experimental data by addressing their macroscopic and mesoscopic behaviour for three braid architectures, with nominal braiding angles of 30°, 45° and 60°. On top of investigating the correlation of the homogenised stress-strain curves, a detailed comparison of the progressive damage morphology and its effect on the overall mechanical response is performed, and the driving mechanisms behind catastrophic failure are identified.

In a subsequent step, the existing braids are subjected to multi-axial stress states in order to identify transition regions in the overall failure behaviour. Finally, the effect of the textile architecture on the ultimate strength of the material is studied by generating unit cell models for braiding angles ranging from 25° to 65° obtained from interpolated geometrical data.

For the numerical model, a quasi-static analysis under displacement control is performed using an explicit integration scheme in the commercial FE code Abaqus/Explicit (6.14) [73]. Based on a preceding mesh refinement study, an average element seed size of 70 μm is selected for all unit cells. Given the geometrical properties of the bundles under investigation, this discretisation yields approximately 40 hexahedral elements over the yarn width and two elements in the thickness direction, with a total of 7036 elements for the [0/±30], 9120 for the [0/±45] and 9114 for the [0/±60] configuration. Depending on the braiding angle, roughly 15,000 and 20,000 cohesive elements ensure coupling with the matrix pockets that contain in between 40,000 to 50,000 tetrahedral elements.

Appropriate mass scaling is applied carefully to the entire model, such that ultimate failure occurs after 200,000-300,000 explicit time increments at a kinetic to strain energy ratio of less than 5 %. Variable local mass scaling is employed such that the stable time increment of all elements in the model is scaled to a user-defined target value. The latter was determined through a sensitivity analysis, where trial simulations were performed ranging from 1,000,000 increments (slowest run) to 100,000 increments (fastest run) under multiple loading scenarios. The critical time increment, its associated element, and any effects on the predicted stress-strain response and damage pattern were continuously monitored. Appropriate mass scaling was then selected according to the worst case scenario. In order to eliminate

any shock from a sudden initial acceleration on the rUC, the homogenised applied displacements at the constraint driver nodes are ramped over time using a 5^{th} order polynomial function. No filtering or smoothing is applied to any of the stress-strain curves presented in this paper. In a double precision solution format, a single simulation runs in approximately two hours on four CPUs (Intel Core i7-6700K, 4.6 GHz). For a consistent comparison with the experiments, the homogenised stress-strain curves obtained from volume-averaging employ engineering strain and nominal stress measures with $\langle\cdot\rangle$ denoting a volume-averaged variable.

5.3.1 Validation test cases

For validation purposes, the numerical predictions are compared to mechanical tensile tests of straight-sided specimens performed with a total of four layers in accordance with ASTM D3039 [32]. All three braid configurations are each subjected to uni-axial loading aligned with their axial (x), transverse (y) and braid yarn direction ($1F$) until catastrophic failure. Details on the manufacturing process and the test set-up are summarised in chapter 3. The experimental stress-strain curves are generated by averaging the complete DIC surface strain field. The geometry data employed for the generation of the unit cell models is obtained from μCT measurements in close proximity to the mechanical test specimens and is summarised in Table 4.3. Out of the three braid test cases in each section, we focus on the two most interesting ones.

5.3.1.1 Uni-axial loading in the axial direction (x, $\psi = 0°$)

The experimental and numerical stress-strain curves for imposing a uni-axial load in the axial direction (x) are displayed in Fig. 5.8. As the load direction is aligned with the axial fibre bundles regardless of the braiding angle, their dominant contribution to the overall stiffness induces only minor deviations from linearity. Generally, the degree of non-linearity encountered in the stress-strain curve is composed of a relative contribution of the three mesoscopic constituents: the resin pockets and the bundles oriented in the axial and braid direction. In the $[0/\pm45]$ configuration shown in Fig. 5.8 (a), the latter are primarily loaded under in-plane shear. Hence, with a significant amount of plastic strain but negligible damage predicted by the numerical model, their stiffness contribution decreases gradually as the applied load increases. In agreement with these findings, the DIC surface strain fields show strain concentrations at the resin-rich yarn-to-yarn junctions of the textile but no evidence of matrix cracking. At the same time, however, the material non-linearity

is counteracted by a geometrical stiffening phenomenon, as the braid fibres tend to continuously reorient in the direction of the global load. In addition, the carbon fibres in the axial yarns exhibit stiffening due to their non-Hookean constitutive behaviour. In total, these effects only play a minor role in the mechanical behaviour for this case. When catastrophic failure occurs as a result of axial yarn rupture, the second nesting configuration yields the lower failure stress prediction of both cases, which can be attributed to a higher degree of yarn distortion after compaction. Considering the scatter in the experiments, the upper and lower bounds in ultimate strength are well predicted by the two nesting configurations.

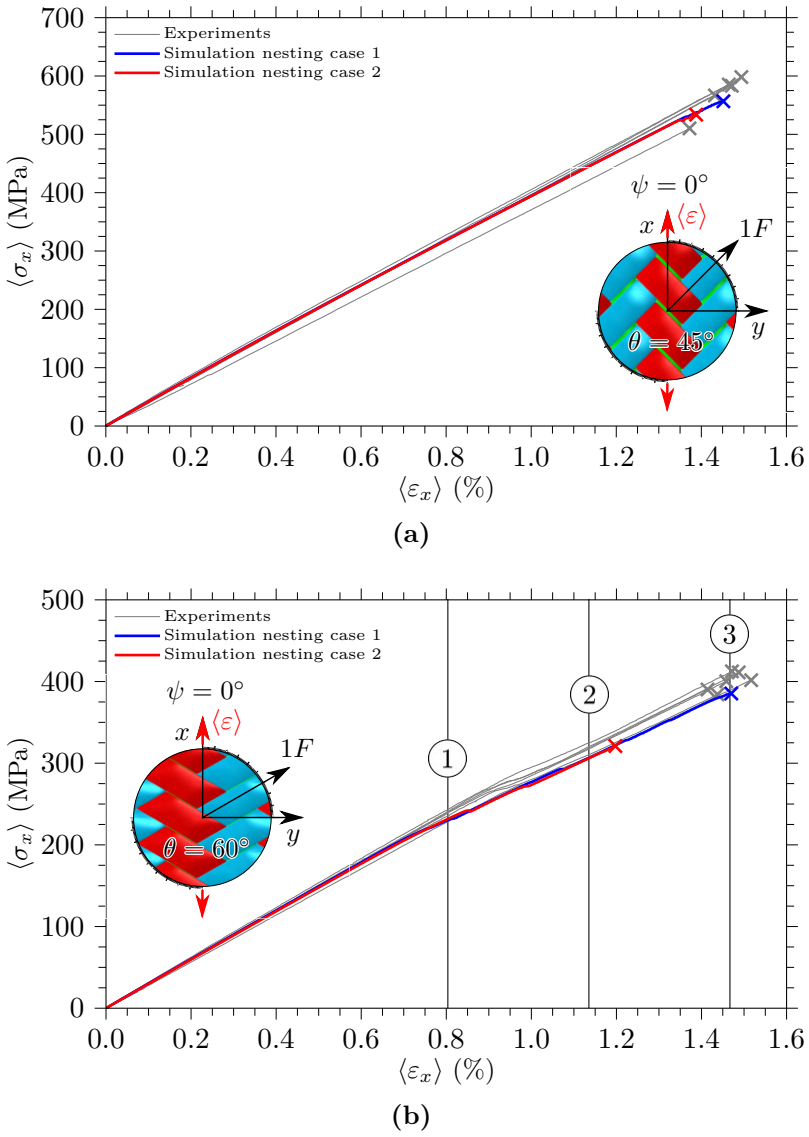

Fig. 5.8: Comparison of experimental and predicted homogenised stress-strain curves in the axial direction (x) for the (a) $[0/\pm45]$ and (b) $[0/\pm60]$ architecture (see Fig. 5.9 and Fig. 5.10 for damage morphology at load levels (1), (2) and (3))

A more severe effect of the braid yarns on the global behaviour is encountered in the [0/±60] architecture displayed in Fig. 5.8 (b). In addition to the stress-strain response, the progressive damage development predicted by the rUC is compared to the formation of cracks during the mechanical tests in Fig. 5.9 at three load levels that correspond to transition regions in the stress-strain curve. For a more convenient interpretation of the predicted damage pattern, the rUC model is tessellated several times with respect to its periodic boundaries such that a piece of a single layer of braid is constructed. In addition, the development of damage predicted in the bundles and the interface during progressive loading is quantified in Fig. 5.10 through a scalar damage variable for each failure mode from volume-averaging calculated as

$$\langle d \rangle = \frac{1}{V} \int_V d \, dV. \tag{5.22}$$

Up to the first load level at approximately 250 MPa, the [0/±60] architecture exhibits almost linear behaviour without damage. When this threshold level is exceeded in the experiments, matrix cracks nucleate in the braid bundles at multiple locations on the specimen and propagate parallel to their fibre direction until they are arrested at an intersecting bundle. A new crack then develops along the intersecting direction, thus creating a saw-tooth crack network. The numerical model captures this matrix cracking failure mode as a result of combined transverse tensile and shear loading in the braid bundles accurately. When a global threshold strain of approximately 0.6 % is exceeded, the first zones of damage tend to initiate in close proximity to the mutual braid bundle interfaces where the maximum fibre waviness and a three-dimensional state of stress prevail. Subsequently, a stable growth observed in the accumulated matrix damage in Fig. 5.10 can be correlated with the simultaneous localisation of the first crack band in the centre of the positively and negatively oriented braid yarns and the subsequent propagation along the respective fibre directions.

Above the first load level, the continuous development of damage in the experiments and the model produces a bulge in the stress-strain curve, accompanied by a sudden decrease in modulus as a result of the stiffness degradation in the braid yarns. After the entire coupon is saturated with a network of matrix cracks, their density increases from a single crack to an average of three cracks per yarn close to the second load level. Apart from a small amount of secondary damage in the interface, the unit cell predicts four parallel localisation bands in regions of higher bundle thickness. While this tendency is in good agreement with the crack loci on the specimen surface, their criticality is slightly over-predicted. Although

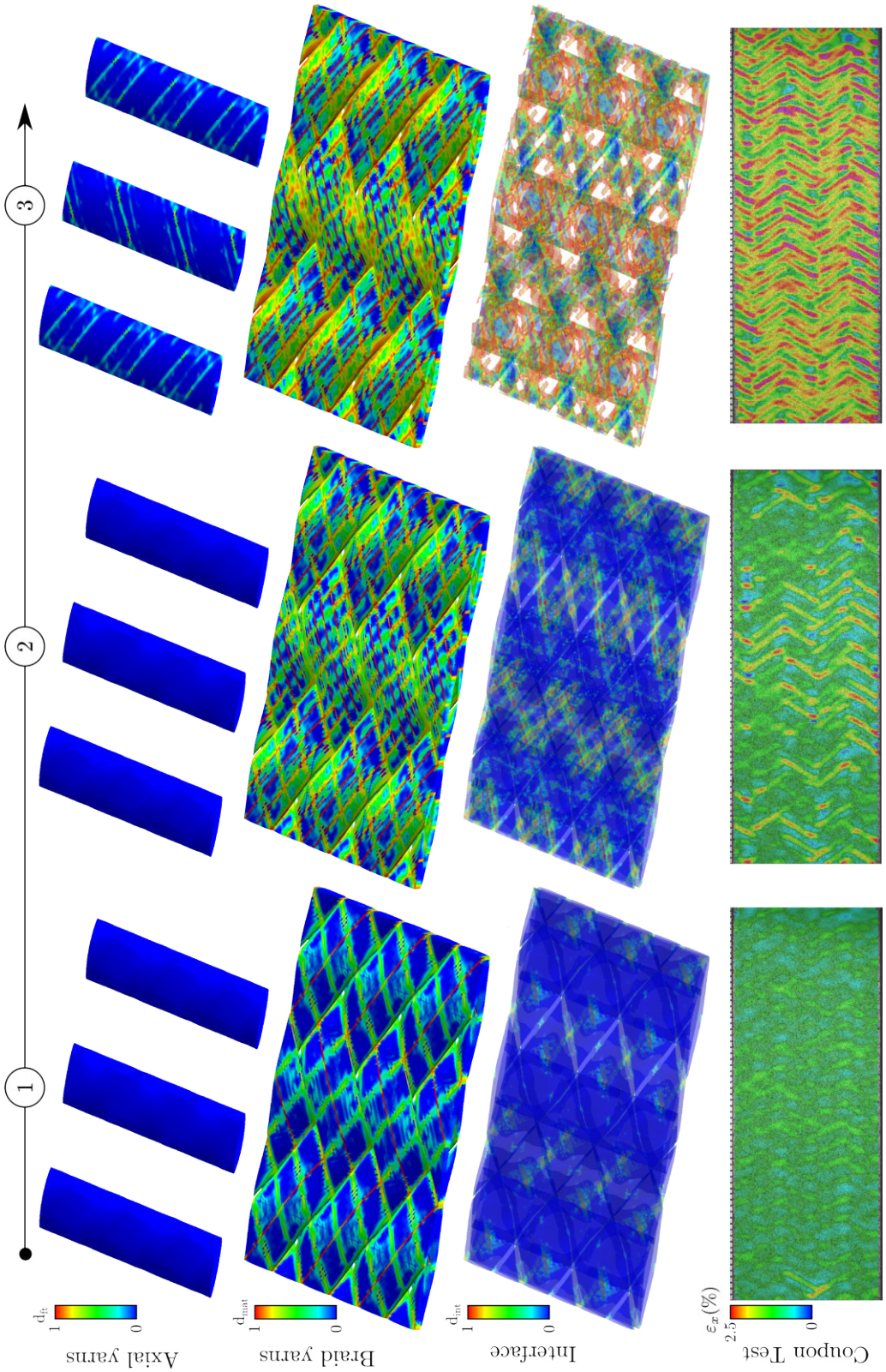

Fig. 5.9: Predicted damage morphology and DIC strain field for the [0/±60] architecture (nesting case 1) loaded in the axial direction (x)

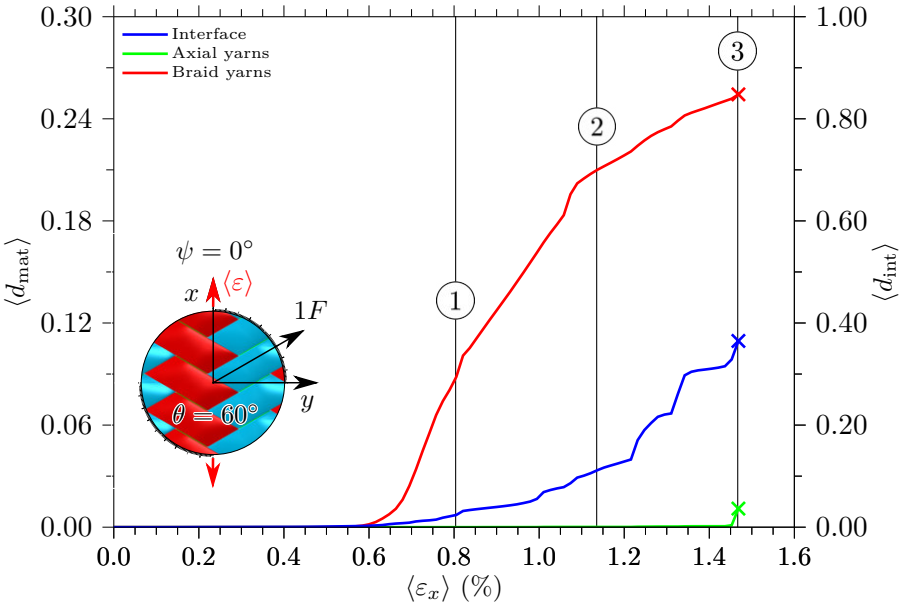

Fig. 5.10: Evolution of accumulated damage in the yarns and the interface for the [0/±60] architecture (nesting case 1) loaded in the axial direction (x)

the formation of new cracks is observed persistently in the experiments, the tangent modulus of the stress-train curves subsequently converges back to its initial magnitude. This phenomenon may be the product of two overlying mechanisms: Firstly, with increasing compliance due to softening in the braid yarns, more loads are redistributed into the axial fibres. Secondly, the appearance of multiple cracks removes constraints in the material and hence promotes further alignment of fibres in the load direction. While the model is capable of accurately rendering the first mechanism, an over-estimation of modulus degradation can be attributed to the constitutive law of the bundles not explicitly incorporating large fibre reorientations. Upon further loading to the third level, however, the overall tendency of damage saturation is well captured with a declining growth in the accumulated matrix damage variable. The measured ultimate strength agrees well with the predictions, if the first nesting case is considered. In the second stacking configuration, the higher degree of overall bundle distortion triggers a preliminary delamination of the slightly undulated axial yarns, which induces a catastrophic failure. Hence, a conservative strength prediction in relation to the experimental results is achieved. Although the progressive formation of a crack network across the entire coupon is driven by the variability of the underlying textile architecture, the unit cell modelling approach is capable of correctly rendering the overall damage morphology and its effect on the macroscopic constitutive response.

5.3.1.2 Uni-axial loading in the transverse direction (y, $\psi = 90°$)

In case the triaxial braided composites are loaded transverse to their axial fibre bundles, a strongly non-linear behaviour as shown in Fig. 5.11 is induced. Contrary to the previous load case, the material's constitutive response is not governed by the dominant stiffness contribution of the load aligned fibres, but rather by the combined off-axis response of the entirety of all mesoscopic phases. The [0/±45] architecture displayed in Fig. 5.11 (a) exhibits a gradual decrease in tangent modulus up to a stress of approximately 120 MPa, which is attributed to the non-linear in-plane shear contribution of the braid bundles to the overall stress-strain curve.

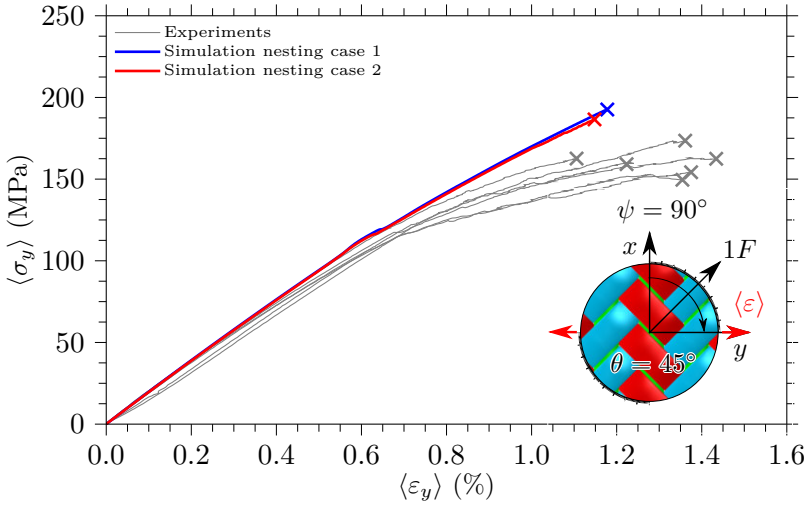

(a)

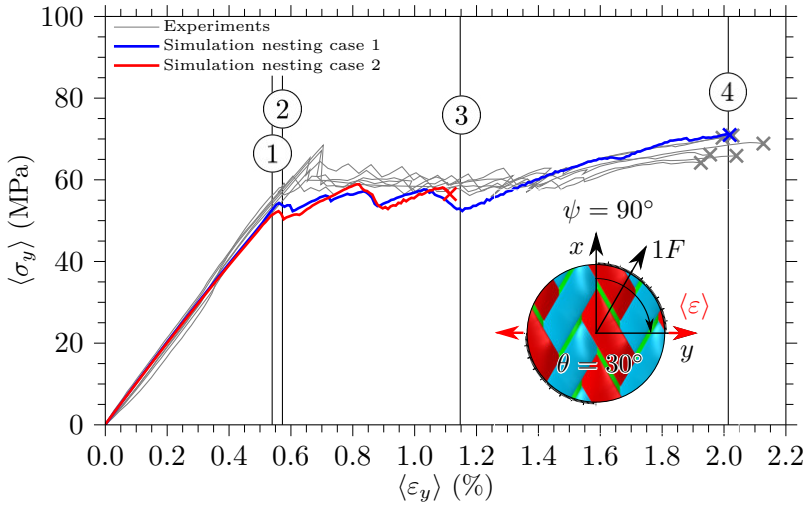

(b)

Fig. 5.11: Comparison of experimental and predicted homogenised stress-strain curves for the (a) [0/±45] and (b) [0/±30] architecture loaded in the transverse direction (y)

Above this threshold, their axial counterparts exhibit matrix cracking parallel to the fibre direction across the coupon width as a result of transverse tensile stresses. As the load is further increased, more cracks progressively localise at the cross-over points of braid yarns entangling a previously failed axial bundle. Again, their propagation is constrained by the underlying textile architecture at adjacent interfaces. As a consequence of this phenomenon, the stress-strain curve experiences a knee-point followed by a gradual stiffness degradation. This characteristic shape and the failure mechanism in the axial yarns are well captured by the numerical model. When a localisation band forms along the central axial bundle of the unit cell, secondary failure in the adjacent braid bundles due the redistributed loads is correctly predicted. However, with only a diffuse region of damage developing here, possibly attributed to the limitations of CDM to model crack interactions, the effect on the stress-strain curve is under-predicted. Still, its shape and failure strain match the experimental measurements.

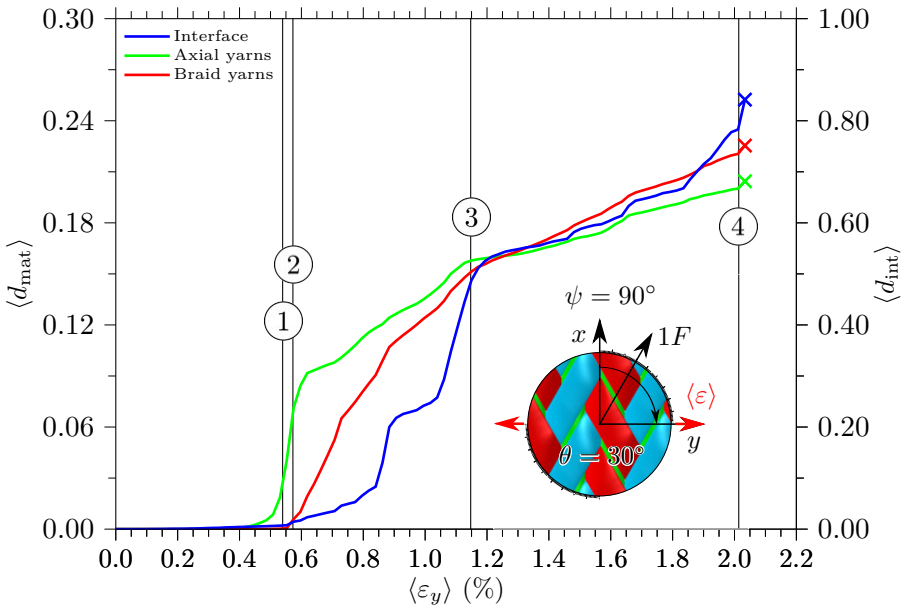

Fig. 5.12: Evolution of accumulated damage in the yarns and the interface for the [0/±30] architecture (nesting case 1) loaded in the transverse direction (y)

Although the damage morphology of the $[0/\pm 30]$ braid shown in Fig. 5.11 (b) follows a similar tendency, its effect on the stress-strain curve is considerably larger. Here, three separate domains in the constitutive behaviour are identified up to final failure: an approximately linear domain, a damage progression domain, and a saturation domain. As soon as the applied load reaches a critical level, a cluster of matrix cracks forms on the specimen surface. This event correlates with the first load drop, which marks the point of damage initiation at the end of the linear

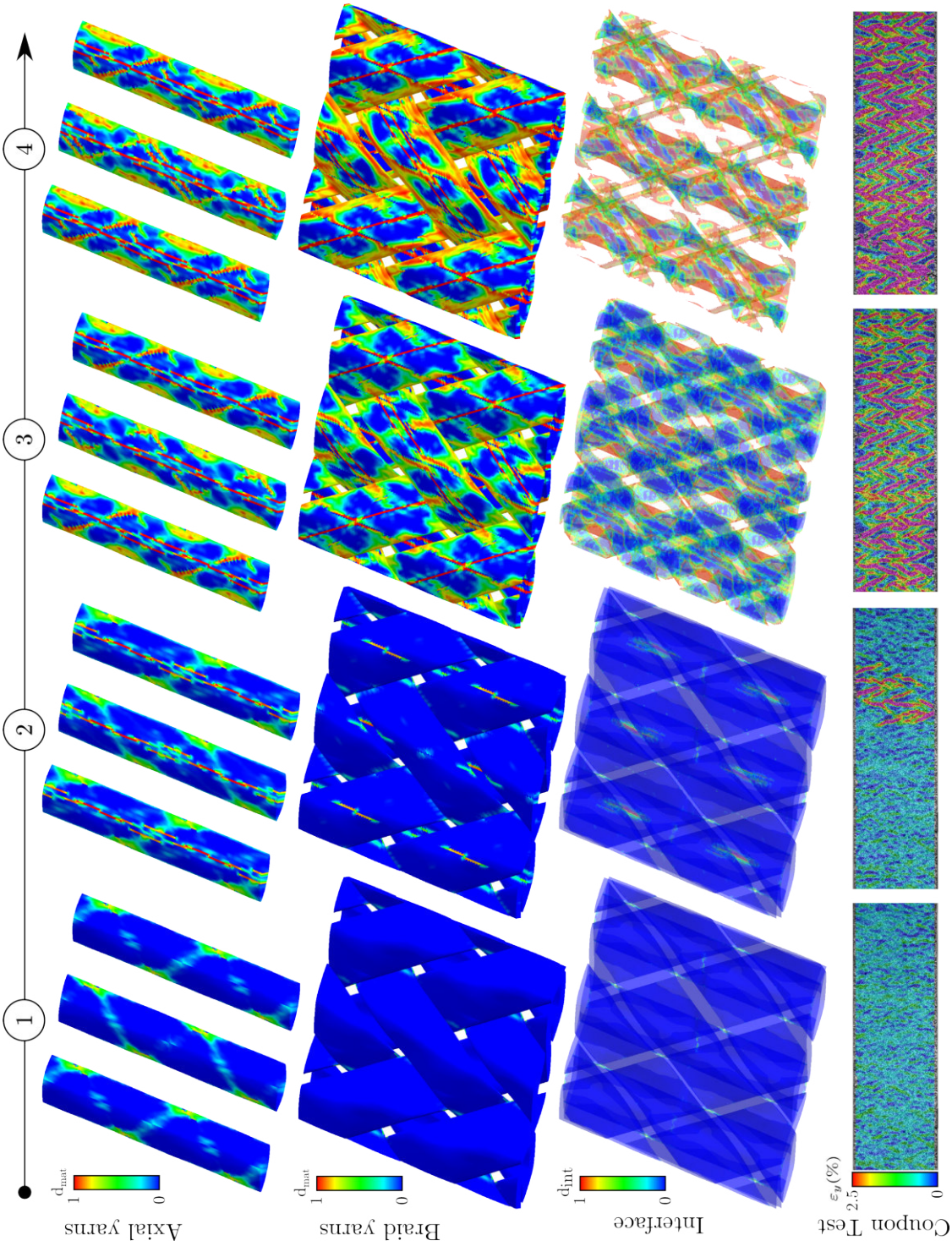

Fig. 5.13: Predicted damage morphology and DIC strain field for the [0/±30] architecture (nesting case 1) loaded in the transverse direction (y)

domain. By studying the detailed behaviour of the mesoscopic model in Fig. 5.13 and its associated damage accumulation in Fig. 5.12, the combined nature of this damage mechanism can be well explained: when failure localises rapidly in the

axial yarns close to the first two load level markers, comparable to a tunnelling matrix crack in the centre of the yarn, stresses are transferred through the interface into the surrounding braid bundles where they immediately trigger additional damage. Considering that the [0/±30] material features the highest bias angle of the fibres with respect to the off-axis angle and hence the lowest overall stiffness, the non-linear shape of the stress-strain curve is heavily affected by damage evolution. In the damage progression domain, the test samples exhibit a stable load plateau during the continuing development of matrix cracks over the entire coupon. This process coincides with a declining rate of damage growth predicted in the axial yarns, while damage in the braid bundles quickly accumulates as a result of localisation. During the continuous load redistribution, approximately half of the interfacial area delaminates. When the entire specimen is saturated with cracks in the experiments, a small increase in load can be observed before final failure due to the existing cracks exhibiting further growth. With the shifted plies in the second nesting configuration, the crack network coalesces such that a preliminary catastrophic failure within the plateau region is predicted. Contrarily, the experimental stress-strain curve and its mechanisms in the saturation domain are well captured by the first nesting case. In this phase, the intra-yarn and inter-yarn damage experience a receding growth, until the unit cell predicts final failure due to a catastrophic delamination in accordance with the measured failure stress and strain. Given the complexity of the failure morphology and its crucial effect on the mechanical response, the unit cell's capabilities are clearly demonstrated.

5.3.1.3 Uni-axial loading in the braid fibre direction ($1F$,$\psi = 30°, 45°$)

The test cases in braid fibre direction ($1F$) shown in Fig. 5.14 reveal a predominant effect of the fibre waviness on the mechanical behaviour. Initially, with one group of braid bundles aligned with the load direction, the [0/±45] and the [0/±30] braid topology respond approximately linearly-elastic up to an applied strain of $\langle\varepsilon_{1F}\rangle = 0.5\,\%$ in the experiments. Beyond this point, the measured stress-strain curves experience a stable load plateau as a result of several cascading failure events intrinsic to the textile architecture. One group of parallel braid bundles straightens along its longitudinal direction while progressively decreasing its initial waviness. Hence, crossing axial bundles are pushed in the through-the-thickness direction close to mutual intersection points while the deformation is constrained by opposing braid yarns and the support of adjacent plies. If the interface is not capable of sustaining additional inter-laminar stresses, a delamination forms abruptly along a single axial bundle across the specimen width followed by its out-of-plane pull-out.

During this mechanism highlighted by the DIC strain fields in Fig. 5.16, secondary matrix cracks become visible in the overlying braid direction. As the applied strain is further increased, the cascading bundle pull-outs fabricate a plateau-like shape of the stress-strain curve in all tested braid architectures. After the braided layers are fully debonded along their entire gage length, they act as separate entities, and the mechanical response is again governed by the straightening braid fibres aligned with the load direction. Contrarily to the [0/±30] case, the sustainable load before final failure can be approximately doubled compared to its plateau initiation value in the [0/±45] case.

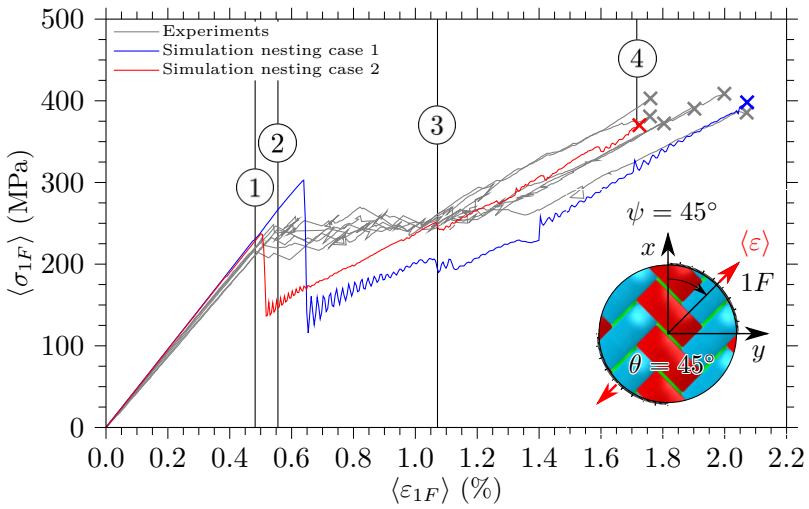

(a)

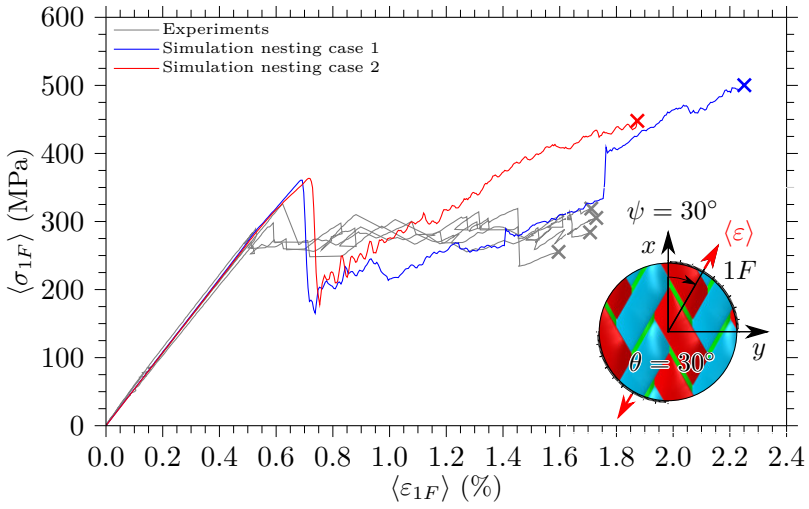

(b)

Fig. 5.14: Comparison of experimental and predicted homogenised stress-strain curves for the (a) [0/±45] and (b) [0/±30] architecture loaded in the braid fibre direction ($1F$)

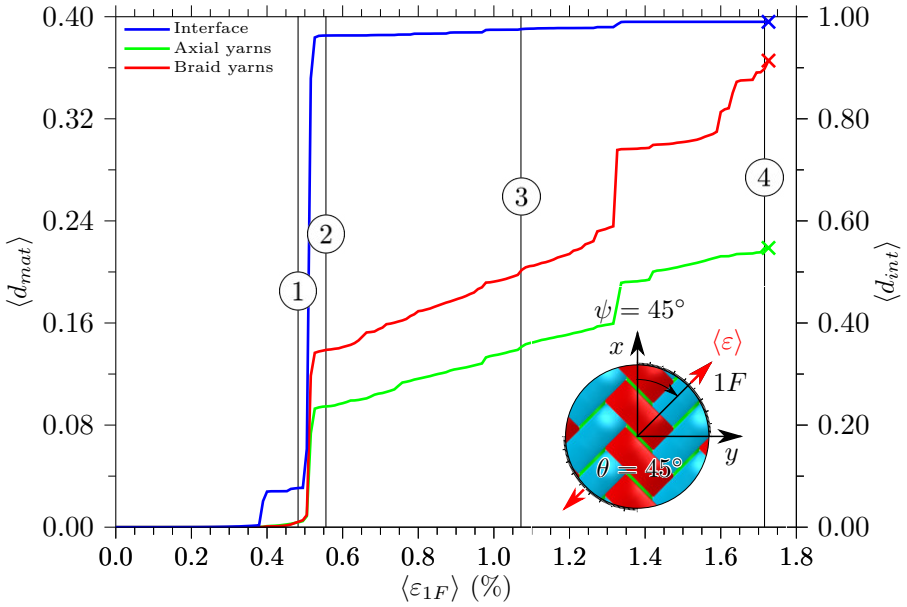

Fig. 5.15: Evolution of accumulated damage in the yarns and the interface for the [0/±45] architecture (nesting case 2) loaded in the braid fibre direction ($1F$)

Unlike many macroscopic approaches, such as equivalent laminate models based on classical lamination theory [2, 28], the proposed unit cell captures the textile induced failure mode. After an initially linear response identical to the mechanical tests, the pull-out mode of the materials shown in Fig. 5.14 was measured to initiate at a macroscopic stress level comparable to the numerical predictions. Among both nesting configurations, the second case follows its previous tendency of producing a lower initial peak stress that matches well the [0/±45] material. For the [0/±30] braid, the effect of the out-of-plane PBCs on the first load drop is negligible. Here, the onset of the pull-out induced stress plateau is slightly over-predicted, possibly due to a severe through-the-thickness stress gradient not captured by the out-of-plane periodicity [81]. For the three braid topologies under consideration, the first load drop in the stress-strain curve is triggered by the sudden formation of a large delamination zone in the unit cell model visualized in Fig. 5.16. The initial failure in the cohesive interface occurs primarily under mode I, close to the point where the intersecting braid yarns are heavily undulating.

The damage evolution curves shown in Fig. 5.15 reveal that the interface fails almost completely between the first and second indicated load levels. As in the experimental observations of secondary matrix cracking, the extensive debonding process and subsequent out-of-plane deformation are accompanied by a sudden accumulation of intra-yarn matrix damage. Here, the mesoscopic structure shows considerable distributed damage, but no clear localisation bands are visible. Con-

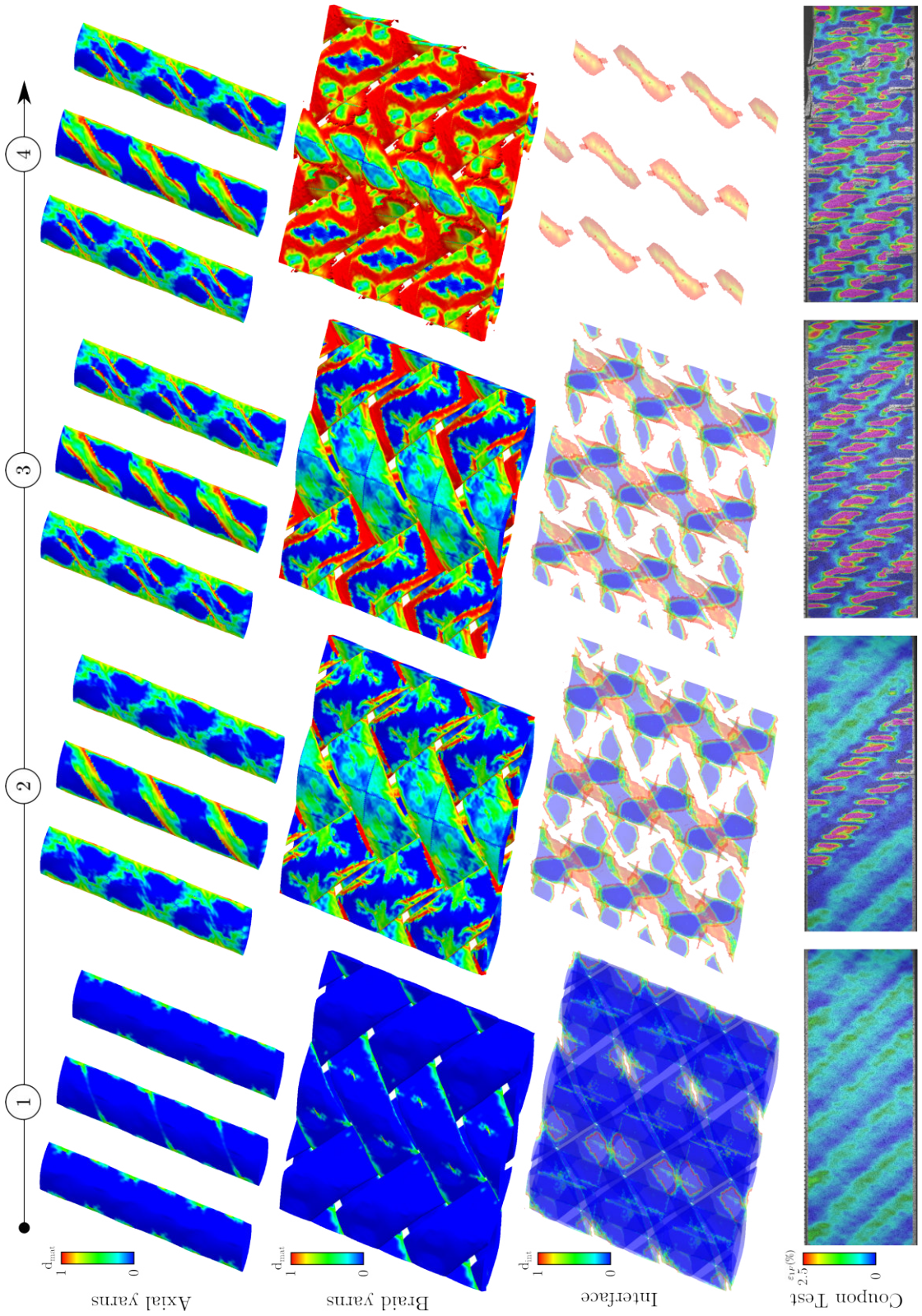

Fig. 5.16: Predicted damage morphology and DIC strain field for the [0/±45] architecture (nesting case 2) loaded in the braid fibre direction ($1F$)

trary to the cascading pull-out events experienced by the tensile specimens, the model's periodic boundaries imply a simultaneous bundle pull-out in an infinite array of repeating cells. As a consequence, the severity of the post-peak load drop and the associated localisation behaviour are over-estimated. Upon further straining, however, the stress capacity of the unit cell continuously increases at a slope comparable to the experimental post-plateau stiffness. Close to the end of the plateau-strain where the macroscopic stress level starts to increase again, the numerical predictions again capture the experimental response accurately. After all bundles have sustained severe secondary matrix cracking damage, the textile exhibits catastrophic failure when a localised fibre failure inside the load aligned yarns appears. Although the same failure mode was identified experimentally in the [0/±30] case, both the plateau initiation and the final failure stress level are over-predicted. While the model is capable of predicting the failure mode observed in the experiments qualitatively, this test case emphasises a limitation of the unit cell approach in addressing localisation and propagation of failure across a larger than the characteristic unit cell size.

5.3.2 Variable off-axis loading

Following the validation test cases, the mechanical response of the braid topologies is investigated under multiple uni-axial tensile off-axis load cases in order to identify transition regions in the failure morphology and further provide material failure envelopes for actual part design. By investigating the predicted stress-strain curves for the [0/±30] architecture shown in Fig. 5.17 (a), three principal mechanisms are identified. In case the load is applied along the axial principal material axis at an angle of $\psi = 0°$, ultimate failure of the braid is controlled by a catastrophic rupture of the load aligned bundles at the end of a linear constitutive response. Here, the small bias angle inherent to both braid fibre directions with respect to the uni-axial load inhibits the formation of matrix cracks before final failure. Following the absence of damage and its potential weakening effect on the load-carrying capability of axial yarns, the maximum strength of the [0/±30] configuration is achieved as a result of a predominant fibre tensile failure mode. However, with increasing misalignment of the load, the overall mechanical behaviour of the textile tends to be more and more affected by its interface. As the interfacial stresses grow quickly, localised delaminations promote a premature failure in the axial yarns accompanied by a degradation of the material strength. In case the off-axis angle and the braiding angle converge, a non-critical load drop followed by a characteristic growth in post-peak stress and strain marks the transition point into the textile

dominated bundle-pull out mode. For slightly greater off-axis angles, the bundle orientations of the multi-directional textile begin to redefine its failure morphology. Owing to the multi-axial stress state, the simultaneous formation of matrix cracks inside the axial and braid yarns accompanied by secondary damage along their interfaces translates into an early kink in the stress-strain curve. Since the initial stiffness of the braid gradually deteriorates as the load aligns with the transverse direction, the cumulative effect of damage on the stress-strain curve is amplified, until a plateau-like response with a strain to failure of up to 2 % is achieved for values greater than $\psi = 70°$.

The damage morphology of the [0/±45] braid presented in Fig. 5.17 (b) exhibits a similar behaviour. Due to its greater braiding angle, this topology responds in a much more balanced way when subjected to multi-axial loading. Although intra-yarn matrix cracking remains a primary failure mode, its contribution to the macroscopic non-linearity is confined to a portion of the gradual stiffness degradation for off-axis angles greater than $\psi = 60°$. For transverse tension, the axial bundles must sustain additional compressive stresses along their fibre direction due to the Poisson's effect. Hence, superimposed fibre splitting contributes to ultimate failure. Due to the absence of a competing failure mode, the bundle pull-out mechanism prevails over a considerable loading range from approximately $\psi = 30°$ to $\psi = 60°$, with the most pronounced plateau forming in the braid fibre direction, but with the initiation stress remaining largely insensitive to the load case.

Among the three triaxial braids under investigation, the least amount of non-linearity in the stress-strain curves is found in the [0/±60] braid shown in Fig. 5.17 (c). Owing to the evenly spaced in-plane yarn orientations, the macroscopic response under an arbitrary off-axis angle is assembled from a primary contribution of one load aligned bundle group, while the remainder can sustain multiple matrix cracks without triggering a catastrophic failure of the textile. For tension in axial direction, the two braid bundle directions accumulate damage equally in the context of a multi-axial stress state, such that a kink is generated in the stress-strain curve at about half of the strength. With the exception of a pull-out mode in close proximity to the braid fibre direction, the knee in the stress-strain curves gradually vanishes as the load vector rotates. Here, a less critical stress state delays the onset of matrix cracking in one group of braid bundles, while the rate of damage growth in the second group does not suffice for a noticeable non-linearity in the stress-strain curve. A comparable mechanism prevails for transverse loading. Although the matrix cracks and fibre splits start to develop at roughly two thirds of the failure load inside the axial bundles, any macroscopic effect is shielded by the

predominant load carrying and redistribution capabilities of the entangling braid fibres that ensure the integrity of the textile.

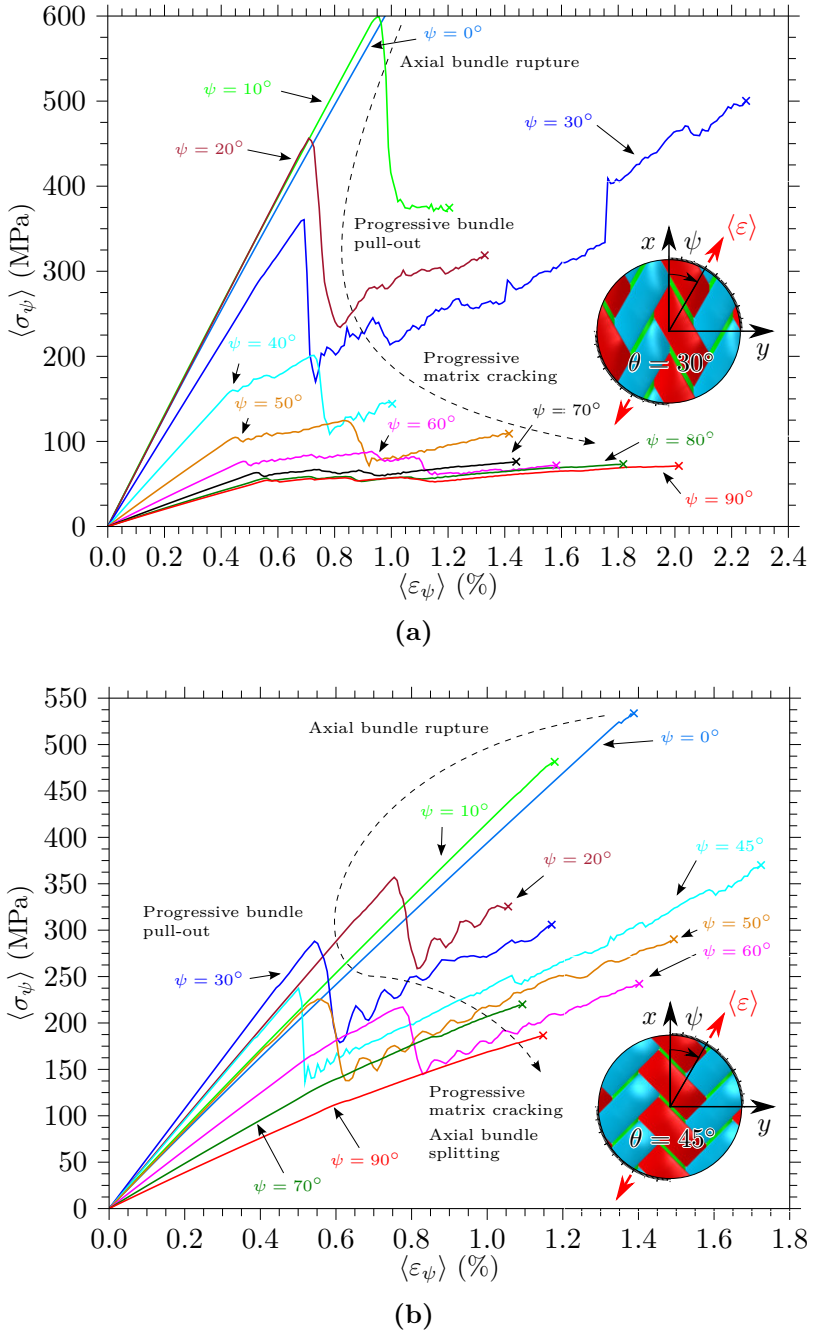

Fig. 5.17: Effect of variable off-axis loading on the predicted stress-strain curves for for (a) the [0/±30] braid (nesting case 1), (b) the [0/±45] braid (nesting case 2) and (c) the [0/±60] braid (nesting case 1)

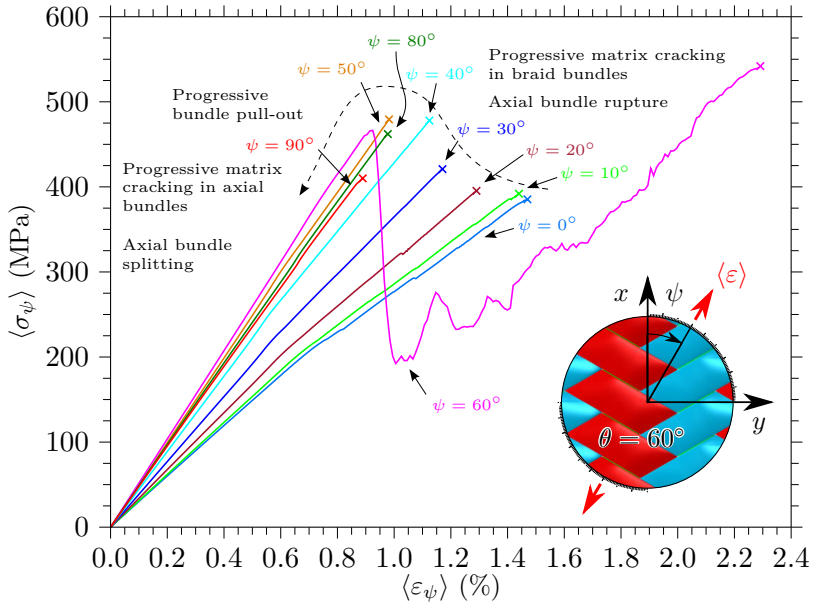

(c)

Fig. 5.17: continued: Effect of variable off-axis loading on the predicted stress-strain curves for for (a) the [0/±30] braid (nesting case 1), (b) the [0/±45] braid (nesting case 2) and (c) the [0/±60] braid (nesting case 1)

5.3.3 Effect of the braiding angle on the ultimate strength

Due to the high geometrical flexibility of the over-braiding process, it is often used to manufacture complex hollow parts that incorporate changing or asymmetric cross-sectional shapes. As a result, the textile and its mechanical properties gradually vary over the entire component, further complicating the structural design process. In order to investigate the sensitivity of the predicted macroscopic behaviour to the underlying textile architecture for a typical manufacturing process window, additional unit cell models are generated for braiding angles ranging from 25° to 65° in increments of 5°, with the input geometry obtained by a quadratic interpolation of Table 4.3.

The effect of the braiding angle on the material ultimate strength is shown in Fig. 5.18 for the uni-axial load cases in the axial (x), transverse (y) and braid fibre ($1F$) direction. Although the strength in the axial direction drops considerably with increasing braiding angle after a predominantly linear stress-strain response, it is consistently controlled by fibre failure in the axial bundles at a comparable failure strain. While the load carrying contribution of the braid bundles declines as their fibres exhibit a higher bias angle, the formation of matrix cracks in the latter close to a braiding angle of 50° induces a knee in the stress-strain response. Under transverse tension, a constant reduction of the degree of non-linearity is observed.

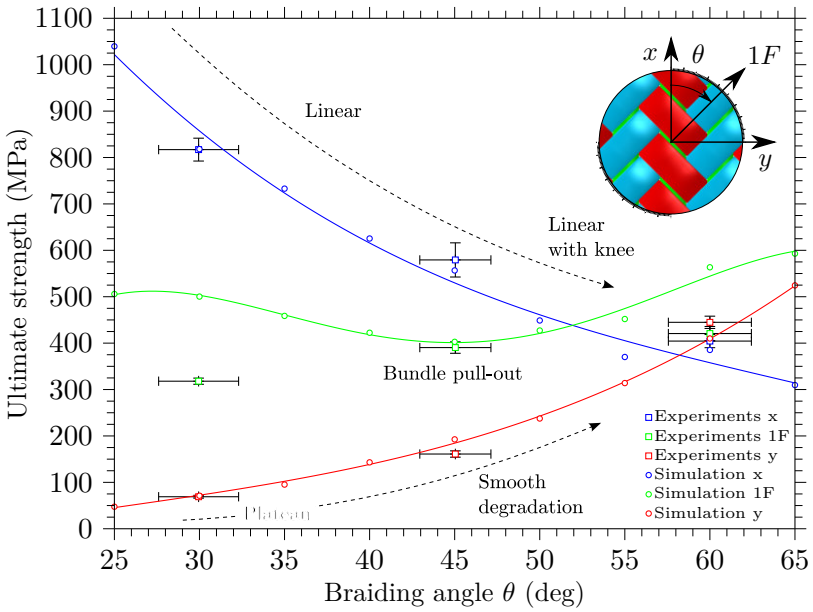

Fig. 5.18: Ultimate strength as a function of the braiding angle θ

For braiding angles below 35°, the rate of matrix cracking and interfacial damage growth adds substantial compliance to the material's matrix-dominated response, such that a constant stress level during an increase in strain is maintained. Following the growing stiffness contribution of the braid yarns, this plateau subsequently transitions into a smooth degradation of the stress-strain curve, until its effect becomes barely noticeable for braiding angles greater than 65°. In the braid fibre direction, progressive pull-out is encountered for any braiding angle, suggesting that this failure mechanism is triggered by a critical degree of braid bundle waviness present in all variations of the topology under investigation. The numerical model generally over-predicts the ultimate strength, with the exception of an excellent agreement for the [0/±45] case. This indicates that further improvements in the post-failure response are needed to better replicate the damage pattern introduced during the progressive nature of the bundle pull-out phenomenon.

5.4 Conclusions on non-linear mechanical response

In this chapter, a novel meso-scale simulation framework was applied to predict the non-linear mechanical response of triaxial braided composites under multiple loading conditions. By explicitly modelling the compaction process at low computational cost, unit cells with a realistic representation of the mesoscopic geometry were generated in a fully automated fashion. Using a 3D constitutive law to cap-

ture plasticity, damage initiation, and propagation inside the fibre bundles and cohesive zone modelling at the interfaces, the numerical predictions were validated against mechanical test of three braid architectures by comparing both stress-strain curves and damage morphology from DIC measurements. Further, the mechanical response was predicted under variable uni-axial off-axis load cases. Finally, the effect of the textile topology on the ultimate strength of the material was investigated. Based on the results presented in this study, the following conclusions can be formulated:

- Triaxial braided composites experienced significant non-linearity in their macroscopic constitutive response before final failure. This phenomenon was primarily attributed to a complex damage behaviour composed of two characteristic mechanisms. In the first one, matrix cracks developed progressively in the fibre bundles and induced subsequent inter-yarn fracture propagation, while the underlying textile architecture acted as a crack arresting grid and inhibited catastrophic failure. In both the experiments and the simulations, this failure mode manifested in a smooth degradation of the stress-strain curve up to the formation of a plateau for matrix dominated load cases. The second damage mechanism was found to be intrinsic to the textile architecture and prevailed in the presence of severe interfacial stresses, as was the case for loading parallel to the braid yarn direction. Here, a stable plateau in the stress-strain curves was correlated with a rapid formation of a large-scale delamination followed by progressive bundle pull-out, highlighting that the meso-scale strongly affects the mechanical behaviour at the macro-scale.
- Considering the good agreement of predicted and measured stress-strain curves and damage mechanisms, the capabilities of the unit cell modelling strategy were demonstrated. Although the investigated braid topologies exhibited considerable geometric variability, a unit cell modelling approach with a compacted geometry model built from average input parameters was capable of correctly predicting the homogenised constitutive response, localisation, and damage evolution by means of a combined CDM and CZM approach. Compared to damage, plasticity in the bundles was found to have a negligible impact on the stress-strain behaviour. The textile induced bundle pull-out mechanism was captured qualitatively. The capability to explicitly model its progressive nature and the associated stress-strain plateau, possibly by means of a statistical RVE, would imply a multiplication of the current computational cost at a comparable fidelity and was not the primary focus of this work. Regarding the effect of the nesting configuration on the homogenised

response, it was found that axial shifting of adjacent layers in the second configuration consistently yielded a lower ultimate strength prediction. While the nesting configuration was found to affect the criticality of damage initiation and catastrophic failure, the load redistribution during damage propagation in the braid followed a comparable pattern.

- The meso-scale framework described can be used as a general modelling approach for conducting numerical simulations of other textile composites. Aside from providing a valuable insight into how damage propagation is affected by the meso-structure, the predicted stress-strain curves can be used to calibrate macroscopic material models suitable for large-scale impact and crash simulations of braided composites.

6 Conclusions and future work

The primary aim of this thesis was to develop a high-fidelity simulation tool for virtually predicting the non-linear mechanical response of triaxial braided composites. In the first step, multiple braid architectures were investigated experimentally under multi-axial stress states. Different experimental techniques were applied to quantify the effects of the textile architecture and its heterogeneity on the surface strain fields, to identify and locate constituent failure mechanisms and to investigate damage initiation and development as a basis for modelling. With the the driving physical mechanisms behind the material non-linearity identified, a meso-scale simulation framework was developed which generates unit cell models of triaxial braided composites with a realistic internal geometry by explicitly modelling the manufacturing process. After validating the simulation framework against experimental data in terms of the internal geometry, elastic properties, non-linear behaviour, and damage morphology, the material response was predicted under variable uni-axial off-axis load cases and the effect of the textile topology on the ultimate strength of the material was investigated. The meso-scale framework described in this thesis can be used as a general modelling approach for conducting numerical simulations of other textile composites. Aside from providing a valuable insight into how damage propagation is affected by the meso-structure, the predicted stress-strain curves can be used to calibrate macroscopic material models suitable for large-scale impact and crash simulations of braided composites.

6.1 Conclusions

In chapter 3, the damage and failure behaviour of triaxial braided composites was investigated under multi-axial stress states introduced through uni-axial off-axis tests. Digital image correlation measurement techniques were used to quantify the effects of the textile architecture and its heterogeneity on the strain field, to identify and locate constituent failure mechanisms and to investigate damage initiation and development. Microsections of the specimen were analysed for the purpose of geometrical material characterisation and assessment of failure mech-

anisms in the thickness direction. The evolution of the damage variable and the accumulated inelastic strain was quantified using incremental loading/unloading experiments. A high-speed camera was employed in order to study the dynamic nature of catastrophic failure. The triaxial braids exhibited severe non-linearities in the mechanical response before final failure. This phenomenon was primarily attributed to a complex damage behaviour composed of two characteristic mechanisms. In the first one, matrix cracks developed progressively in the yarns that were not aligned with the load direction. While the underlying textile architecture was found to slightly reduce the elastic properties compared to equivalent tape laminates, it functions as a natural crack arresting grid and restricts the propagation of cracks to in between adjacent intersecting yarns, thus reducing their criticality. Loads can be redistributed without catastrophic failure of the material. In addition, a possible crack deflection can cause additional energy absorption. As a result of this mechanism, braids under certain load conditions were capable of withstanding a high strain to failure, even if a large portion of the specimen surface was saturated with matrix cracks. The accompanying mechanical behaviour can be desirable in the design of crash absorbing or pseudo-ductile materials. An additional failure mode intrinsic to the textile architecture was encountered for loading in the heavily undulated braid yarn direction. Due to yarn straightening induced out-of-plane deformations, braided composites were found to fail as a result of large scale delaminations accompanied by progressive fibre bundle pull-out. This information served as a baseline for the development of a numerical model for predicting the non-linear constitutive behaviour of braided composites. Having identified the failure morphology to be severely affected by the underlying textile architecture, the necessity of a meso-scale modelling approach became evident. In addition to a realistic representation of the internal geometry after compaction of multiple braided layers, the potential development of a bundle pull-out mode requires failure to not only be captured inside the yarns or matrix pockets, but also at their respective interfaces.

In chapter 4, a novel simulation framework for accurate predictions of the the mechanical response of triaxial braided composites was proposed. Realistic FE unit cell models were generated through an automated bottom-up simulation work-flow: local volumetric interpenetrations present in the initial stage of the model were resolved in a fictitious thermal step. Subsequently, a compaction simulation was performed to the desired target fibre volume fraction using flexible membranes for improved computational efficiency. Special out-of-plane periodic boundary conditions allowed an implicit consideration of the compaction of multiple braid plies in different nesting configurations which allowed capturing global FVFs of $55 - 60\%$

while using intra-yarn fibre volume fractions obtained from experiments. In the last step, a tetrahedral matrix pocket mesh was created from a CAD reconstruction of the deformed textile. A novel meshing methodology was developed to incorporate branching cohesive yarn-to-yarn and yarn-to matrix interfaces without the need of introducing an artificial matrix mesh of finite thickness. The framework was validated by detailed comparison with experimental results. First, the unit cell geometry was compared to the detailed reconstruction of the actual bundle geometry from μCT measurements for three braid architectures, with a nominal braiding angle of 30°, 45° and 60°. Subsequently, the predictive capability of the approach and its robustness were demonstrated by successfully generating models in an automatic fashion for braiding angles ranging from 25° to 65°. These models were successfully used to predict the elastic properties obtained experimentally. The excellent correlation of experiments and unit cell predictions underlined the framework's potential for damage modelling.

In chapter 5, the meso-scale simulation framework was applied to predict the non-linear mechanical response of triaxial braided composites under multiple loading conditions. Using a 3D constitutive law to capture plasticity, damage initiation, and propagation inside the fibre bundles and cohesive zone modelling at the interfaces, the numerical predictions were validated against mechanical test of three braid architectures by comparing both stress-strain curves and damage morphology from DIC measurements. Further, the mechanical response was predicted under variable uni-axial off-axis load cases. Finally, the effect of the textile topology on the ultimate strength of the material was investigated. To summarise the previous results, the following conclusions can be formulated:

- Triaxial braided composites experienced significant non-linearity in their macroscopic constitutive response before final failure. This phenomenon was primarily attributed to a complex damage behaviour composed of two characteristic mechanisms. In the first one, matrix cracks developed progressively in the fibre bundles and induced subsequent inter-yarn fracture propagation, while the underlying textile architecture acted as a crack arresting grid and inhibited catastrophic failure. In both the experiments and the simulations, this failure mode manifested in a smooth degradation of the stress-strain curve up to the formation of a plateau for matrix dominated load cases. The second damage mechanism was found to be intrinsic to the textile architecture and prevailed in the presence of severe interfacial stresses, as was the case for loading parallel to the braid yarn direction. Here, a stable plateau in the stress-strain curves was correlated with a rapid formation of a large-scale

delamination followed by progressive bundle pull-out, highlighting that the meso-scale strongly affects the mechanical behaviour at the macro-scale.

- With the excellent correlation of the predicted and measured stress-strain curves and damage mechanisms, the capabilities of the unit cell modelling framework were demonstrated. Although the investigated braid topologies exhibited considerable geometric variability, a unit cell modelling approach with a compacted geometry model built from average input parameters was capable of correctly predicting the homogenised constitutive response, localisation, and damage evolution by means of a combined CDM and CZM approach. Compared to damage, plasticity in the bundles was found to have a negligible impact on the stress-strain behaviour. The textile induced bundle pull-out mechanism was captured qualitatively. The capability to explicitly model its progressive nature and the associated stress-strain plateau, possibly by means of a statistical RVE, would imply a multiplication of the current computational cost at a comparable fidelity and was not the primary focus of this work. Regarding the effect of the nesting configuration on the homogenised response, it was found that axial shifting of adjacent layers in the second configuration consistently yielded a lower ultimate strength prediction.
- The meso-scale framework described in this work can be used as a general modelling approach for conducting numerical simulations of other textile composites. Aside from providing a valuable insight into how damage propagation is affected by the meso-structure, the predicted stress-strain curves can be used to calibrate macroscopic material models suitable for large-scale impact and crash simulations of braided composites.

6.2 Potential future work

6.2.0.1 Experimental material characterisation

- **Compression testing**
  In order to obtain representative stress-curves for triaxial braided composites under compressive loading, the most appropriate test method has to be identified. With its limited gage length and specimen width, the combined loading compression (CLC) fixture according to ASTM D 6641 may not yield satisfactory results for a wide range of braided composites. Considering the crack growth tends to be governed by the underlying textile architecture,

cracks may be forced to propagate into the clamped regions of the specimen, causing a combination of non-physical failure patterns and material properties. A larger specimen might be necessary in order to not artificially constrain crack growth and hence obtain representative stress-strain curves in a robust fashion. One possibility worth investigating could be a modified version of open-hole compression testing according to ASTM D 6484. Adding custom made transparent lateral supports for vision onto the entire gage length would further allow the investigation of damage propagation by full-field strain measurement techniques under compressive loading.

- **Additional non-destructive test methods**
  In-situ computed tomography is a powerful non-destructive testing method to study the damage inside the material during progressive loading. By tracking the nucleation and propagation of cracks, their phenomenology and effect on the macroscopic behaviour can be studied. Since cracks and delaminations are identified while the specimen is under load, crack-closure effects during microscopy of damaged specimens are avoided. A topic of particular interest are crack migration phenomena between different bundle orientations: Despite different in-plane fibre orientations, inter-connected matrix cracks are observed in regions of direct yarn-to-yarn contact when investigating microsections of damaged specimens. These cracks extend through individual bundles, branch into localised delaminations at the bundle interface and subsequently connect with a matrix crack in a neighbouring bundle. By better understanding the interaction among different damage mechanisms, the fidelity and robustness of future models can be drastically improved.

- **Additional investigations on progressive fibre pull-out failure mode**
  In order to further strengthen the findings on the progressive bundle pull-out mechanism for loading parallel to the braid fibre direction, additional testing with a variable specimen width is proposed. Since the occurrence of this failure mode was initially not expected, only a single specimen width was tested. Hence, a potential dependency of the results on the coupon dimensions could not be eliminated. However, considering that the three braid architectures under investigation experienced the same failure mode despite their unequal unit cell quantity per specimen width, it may be concluded that bundle pull-out is a failure mode intrinsic to braided composites and that the specimen width was sufficient to obtain a representative material response.

6.2.0.2 Meso-scale modelling

- **Improving runtime and robustness of the modelling framework**
  A large part of the modelling framework's pre-processing work flow is currently implemented within the Abaqus/CAE Python API environment. Core functionalities, such as the yarn meshing procedure and the generation of the matrix pockets by CAD geometry reconstruction are fully automated, but rely on the performance of built-in Abaqus/CAE functionalities. Unfortunately, with its original development dating back to the 1990s, Abaqus/CAE does not support multi-threaded operations and fails at handling large quantities of geometric elements. For example, the yarn meshing algorithm can suffer from am excessive run-time for very fine meshes, since the pre-processor cannot handle the quantity of elements involved in the geometric partitioning procedure. During the CAD reconstruction of the matrix pockets geometry, complex shapes may induce a large run-times or failure of the built-in boolean operation functionalities. The mediocre performance seems to be a result of an older ACIS geometry kernel implementation. Possible future improvements may switching to more advanced pre-processors which still allow for fully automated work-flows, such as ANSA (BETA CAE Systems), Hypermesh (Altair), the 3DEXPERIENCE Platform (Dassault), CATIA V5/V6 (Dassault) or Abaqus/CAE with improved user-developed functionalities.
- **Application to woven and other textile composites**
  With the fully automatic implementation, the meso-scale framework can be extended to other textile composites, such as woven or biaxial braided composites. For the latter, only slight modifications are necessary, including the removal of axial bundles and small adjustments to the characteristic undulation path. 2D woven composites are coincident to a 45° biaxial braid, with a convenient definition of the warp and weft direction after rotating the principal coordinate system.
- **Explicit representation of multiple nested plies**
  The through-the-thickness boundary conditions, including layer shifts and nesting affect the initiation and propagation of damage. In the presented model, two different nesting configurations were considered implicitly with a special set of out-of-plane PBCs, both during the compaction simulation and the mechanical analysis. While the current implementation focuses on minimum computational expense, numerical studies with an explicit representation of the textile stack are proposed in order to capture the effect of the through-the thickness stress gradient on damage initiation and propaga-

tion. Additionally, the stochastic variability of the textile architecture can be addressed by assembling laminates from unit cells with varying geometry characteristics.

- **Higher order periodic boundary conditions during compaction simulation**
  During the compaction simulation, the periodic displacement boundary conditions do not enforce curvature continuity to adjacent elements inside the unit cell. During highly localised compaction, this can cause kinks in the surface curvature across the periodic boundaries and lead to localised stress concentrations. As a future work-around, the solid mesh of the yarns can be wrapped with a thin dummy shell mesh, such that the periodic boundary conditions acting on displacements can be extended to rotational degrees of freedom. Hence, a smooth surface curvature is ensured across all cell boundaries.
- **Studying the effect of the unit cell size on damage localisation**
  The exploitation of internal material symmetries to minimize the simulation domain also implies that a specific type of periodicity is enforced on the predicted damage pattern. Additional numerical studies on the implications of exploiting arbitrary symmetries for modelling damage and strain localisation are necessary for reduced unit cells.
- **Discrete representation of cracks inside the unit cell**
  The formation of damage in the material is currently simulated using a continuum damage mechanics approach. High-fidelity approaches, such as the Floating Node Method represent discrete cracks by enriching finite elements with connectivities of geometrical entities. While the approach is accompanied by an increase in computational expense, the propagation of cracks and interactions of different failure mechanisms can be captured more accurately.

6.2.0.3 Macro-scale modelling

- **Implicit consideration of the textile architecture through reduced-order constitutive laws**
  The efficient simulation of composite structures manufactured from braided composites requires developing new reduced-order constitutive laws. For the sake of numerical efficiency and in the context of shell element discretisation, one proposed approach involves formulating a constitutive relation based on internal damage state variables that are obtained a priori from the meso-

scale model through homogenisation. Another approach relies on extending the previously introduced approach of virtually separating the braided composite into an equivalent tape laminate using classical lamination theory and modifying individual ply material properties, such that the overall constitutive of the meso-scale model is matched. Hence, the effect of the textile architecture is implicitly incorporated on the macro-scale.

A Implementation of periodic boundary conditions

A.1 General procedure

The implementation of periodic boundary conditions into finite element models is often a challenging and time consuming task. This section provides basic guidelines for their implementation into finite element models in the form of a 'cooking recipe'. Details on the theory and their derivation in the absence of bending and twisting can be found in [65, 66, 70]. An extension for solid-to-shell homogenisation is given in [96].

The overall implementation procedure can be subdivided into several main steps:

1 **Identification and selection of a suitable unit cell as shown in Fig. A.1** after assessing

- the overall computational expense
- the complexity of generating a mesh that satisfies all periodicity requirements
- the potential effect for modelling damage propagation when internal symmetries and periodicity are exploited in reduced unit cells
- the feasibility of different out-of-plane boundary conditions, their implications for textile nesting configurations, and the compatibility of in-plane and out-of-plane periodic boundary conditions for reduced unit cells
- the feasibility of different textile stacking and nesting configurations in case a compaction simulation is explicitly performed with multiple layers
- the admissible applied strain or stress tensor for reduced unit cells

2 **in the absence of rigid body motions, evaluate the relationship of each periodic boundary with respective neighbouring cell or sub-**

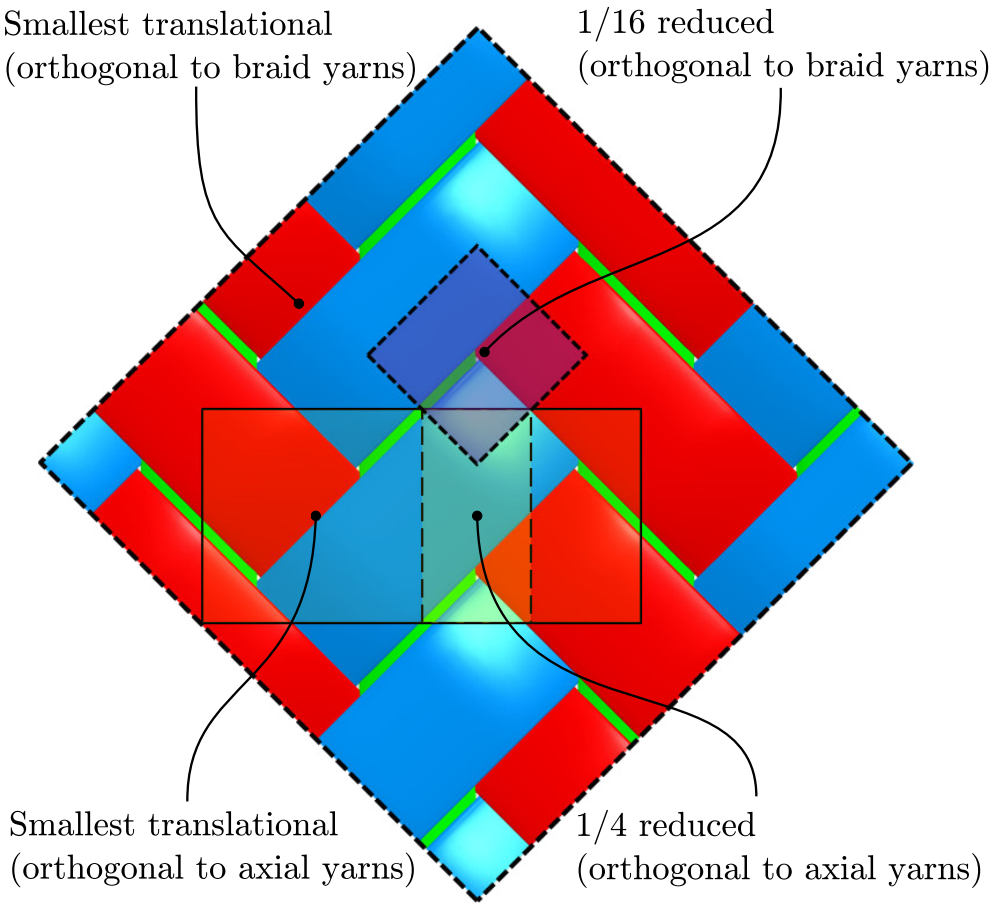

Fig. A.1: Selection of unit cell type for a 2×2 triaxial braided composite

domain by finding the unknown parameters in

$$\mathbf{u}(A) - \gamma \mathbf{T}\mathbf{u}(\hat{A}) = - \langle \mathbf{F} \rangle \, \mathbf{T}\mathbf{x}^{\mathbf{O}_{\hat{\mathbf{E}}}}$$

- determine the transformation matrices $\mathbf{T}$ at each periodic boundary as shown in Table A.1.
- determine the load reversal factors γ at each periodic boundary to check the admissibility of potential applied volume averaged deformation gradient tensors $\langle \mathbf{F} \rangle$ in Table A.1 by solving for γ in

  $$\langle \mathbf{F} \rangle = \gamma \mathbf{T} \, \langle \mathbf{F} \rangle \, \mathbf{T}^T$$

  If no solution for γ exists at any periodic boundary, the given strain tensor will not be admissible.
- determine the translation vector $\mathbf{x}^{\mathbf{O}_{\hat{\mathbf{E}}}}$ and the periodic displacement field $\mathbf{u}(A)$ and $\mathbf{u}(\hat{A})$ at each periodic boundary as is displayed in Table A.2. In

case of out-of-plane periodicity, the additional equations are summarised in Table A.3.

- with all parameters determined, evaluate the PBC equations to obtain all master coupling equations between the periodic boundary faces.
- in case of modelling displacement (strain) controlled off-axis loading, the full strain tensor in off-axis coordinates is not known a priori, as the model must be able to deform freely in any direction other than the load direction, such that Poisson's effects and shear-extension couplings are captured accurately. In order to reproduce this case, the external loading term on the right side is extended by transforming an arbitrary deformation gradient tensors $\langle \mathbf{F} \rangle$ from off-axis coordinates into principal coordinates using the transformation matrix $\mathbf{T}_\psi$ with the off-axis loading angle ψ. In this case, the periodic boundary conditions are extended to:

$$\mathbf{u}(A) - \gamma \mathbf{T}\mathbf{u}(\hat{A}) = -\mathbf{T}_\psi^{-\mathbf{1}} \langle \mathbf{F} \rangle \mathbf{T}\mathbf{x}^{\mathbf{O}_{\hat{\mathbf{E}}}}$$

Table A.1: In-plane sub-domain admissibility for 1/4 rUC (orthogonal to axial yarns)

	$\hat{E}_1$	$\hat{E}_2$	$\hat{E}_3$	$\hat{E}_4$
$\mathbf{T_i}$	$\begin{bmatrix} 1 & 0 & 0 \\ 0 & 1 & 0 \\ 0 & 0 & 1 \end{bmatrix}$	$\begin{bmatrix} -1 & 0 & 0 \\ 0 & -1 & 0 \\ 0 & 0 & 1 \end{bmatrix}$	$\begin{bmatrix} 1 & 0 & 0 \\ 0 & 1 & 0 \\ 0 & 0 & 1 \end{bmatrix}$	$\begin{bmatrix} -1 & 0 & 0 \\ 0 & -1 & 0 \\ 0 & 0 & -1 \end{bmatrix}$
$\left\langle \begin{bmatrix} \varepsilon_1 & \varepsilon_{12} & \varepsilon_{13} \\ \varepsilon_{12} & \varepsilon_2 & \varepsilon_{23} \\ \varepsilon_{13} & \varepsilon_{23} & \varepsilon_3 \end{bmatrix} \right\rangle$	$\gamma_1 = 1$	$\gamma_2 \neq \pm 1$	$\gamma_3 = 1$	$\gamma_4 = 1$
$\left\langle \begin{bmatrix} \varepsilon_1 & \varepsilon_{12} & 0 \\ \varepsilon_{12} & \varepsilon_2 & 0 \\ 0 & 0 & \varepsilon_3 \end{bmatrix} \right\rangle$	$\gamma_1 = 1$	$\gamma_2 = 1$	$\gamma_3 = 1$	$\gamma_4 = 1$
$\left\langle \begin{bmatrix} 0 & 0 & \varepsilon_{13} \\ 0 & 0 & \varepsilon_{23} \\ \varepsilon_{13} & \varepsilon_{23} & 0 \end{bmatrix} \right\rangle$	$\gamma_1 = 1$	$\gamma_2 = -1$	$\gamma_3 = 1$	$\gamma_4 = 1$

Table A.2: In-plane PBCs for 1/4 rUC (orthogonal to axial yarns)

	$\hat{E}_1$	$\hat{E}_2$	$\hat{E}_3$	$\hat{E}_4$
$\mathbf{T_i}$	$\begin{bmatrix} 1 & 0 & 0 \\ 0 & 1 & 0 \\ 0 & 0 & 1 \end{bmatrix}$	$\begin{bmatrix} -1 & 0 & 0 \\ 0 & -1 & 0 \\ 0 & 0 & 1 \end{bmatrix}$	$\begin{bmatrix} 1 & 0 & 0 \\ 0 & 1 & 0 \\ 0 & 0 & 1 \end{bmatrix}$	$\begin{bmatrix} -1 & 0 & 0 \\ 0 & -1 & 0 \\ 0 & 0 & -1 \end{bmatrix}$
$x^{O_{\hat{E}}}$	$\begin{bmatrix} -h_{rUC} \\ 0 \\ 0 \end{bmatrix}$	$\begin{bmatrix} 0 \\ -w_{rUC} \\ 0 \end{bmatrix}$	$\begin{bmatrix} h_{rUC} \\ 0 \\ 0 \end{bmatrix}$	$\begin{bmatrix} 0 \\ w_{rUC} \\ 0 \end{bmatrix}$
$x^{\hat{A}}$	$\begin{bmatrix} -h_{rUC}/2 \\ -w_{rUC}/2 \le y \le w_{rUC}/2 \\ -t_{rUC}/2 \le z \le t_{rUC}/2 \end{bmatrix}$	$\begin{bmatrix} -h_{rUC}/2 \le x \le h_{rUC}/2 \\ -w_{rUC}/2 \\ -t_{rUC}/2 \le z \le t_{rUC}/2 \end{bmatrix}$	$\begin{bmatrix} h_{rUC}/2 \\ -w_{rUC}/2 \le y \le w_{rUC}/2 \\ -t_{rUC}/2 \le z \le t_{rUC}/2 \end{bmatrix}$	$\begin{bmatrix} -h_{rUC}/2 \le x \le h_{rUC}/2 \\ w_{rUC}/2 \\ -t_{rUC}/2 \le z \le t_{rUC}/2 \end{bmatrix}$
x^{A}	$\begin{bmatrix} x_1^{\hat{A}} + h_{rUC} \\ x_2^{\hat{A}} \\ x_3^{\hat{A}} \end{bmatrix}$	$\begin{bmatrix} -x_1^{\hat{A}} \\ -x_2^{\hat{A}} - w_{rUC} \\ x_3^{\hat{A}} \end{bmatrix}$	$\begin{bmatrix} x_1^{\hat{A}} - h_{rUC} \\ x_2^{\hat{A}} \\ x_3^{\hat{A}} \end{bmatrix}$	$\begin{bmatrix} -x_1^{\hat{A}} \\ -x_2^{\hat{A}} + w_{rUC} \\ -x_3^{\hat{A}} \end{bmatrix}$

Table A.3: Out-of-plane PBCs for 1/4 rUC (orthogonal to axial yarns) in nesting case I: **T**=-1,-1,-1 ; $x_{shift} = 0$, $y_{shift} = 0$, nesting case II: **T**=-1,-1,-1 ; $x_{shift} = h_{rUC}/2$, $y_{shift} = 0$

	$\hat{E}_{5,N1}$	$\hat{E}_{6,N1}$	$\hat{E}_{5,I,N2}$	$\hat{E}_{5,II,N2}$	$\hat{E}_{6,I,N2}$	$\hat{E}_{6,II,N2}$
$\mathbf{T_i}$	$\begin{bmatrix} -1 & 0 & 0 \\ 0 & -1 & 0 \\ 0 & 0 & -1 \end{bmatrix}$	$\begin{bmatrix} -1 & 0 & 0 \\ 0 & -1 & 0 \\ 0 & 0 & 1 \end{bmatrix}$	$\begin{bmatrix} -1 & 0 & 0 \\ 0 & -1 & 0 \\ 0 & 0 & -1 \end{bmatrix}$	$\begin{bmatrix} -1 & 0 & 0 \\ 0 & -1 & 0 \\ 0 & 0 & -1 \end{bmatrix}$	$\begin{bmatrix} -1 & 0 & 0 \\ 0 & -1 & 0 \\ 0 & 0 & 1 \end{bmatrix}$	$\begin{bmatrix} -1 & 0 & 0 \\ 0 & -1 & 0 \\ 0 & 0 & 1 \end{bmatrix}$
$x^{O_{\hat{E}}}$	$\begin{bmatrix} 0 \\ 0 \\ \bar{t}_{rUC} \end{bmatrix}$	$\begin{bmatrix} 0 \\ 0 \\ -\bar{t}_{rUC} \end{bmatrix}$	$\begin{bmatrix} h_{rUC}/2 \\ 0 \\ \bar{t}_{rUC} \end{bmatrix}$	$\begin{bmatrix} -h_{rUC}/2 \\ 0 \\ \bar{t}_{rUC} \end{bmatrix}$	$\begin{bmatrix} -h_{rUC}/2 \\ 0 \\ -\bar{t}_{rUC} \end{bmatrix}$	$\begin{bmatrix} h_{rUC}/2 \\ 0 \\ -\bar{t}_{rUC} \end{bmatrix}$
$x^{\hat{A}}$	$\begin{bmatrix} -h_{rUC}/2 \le x \le h_{rUC}/2 \\ -w_{rUC}/2 \le y \le w_{rUC}/2 \\ \bar{t}_{rUC}/2 \end{bmatrix}$	$\begin{bmatrix} -h_{rUC}/2 \le x \le h_{rUC}/2 \\ -w_{rUC}/2 \le y \le w_{rUC}/2 \\ -\bar{t}_{rUC}/2 \end{bmatrix}$	$\begin{bmatrix} 0 \le x \le h_{rUC}/2 \\ -w_{rUC}/2 \le y \le w_{rUC}/2 \\ \bar{t}_{rUC}/2 \end{bmatrix}$	$\begin{bmatrix} -h_{rUC}/2 \le x \le 0 \\ -w_{rUC}/2 \le y \le w_{rUC}/2 \\ \bar{t}_{rUC}/2 \end{bmatrix}$	$\begin{bmatrix} -h_{rUC}/2 \le x \le 0 \\ -w_{rUC}/2 \le y \le w_{rUC}/2 \\ -\bar{t}_{rUC}/2 \end{bmatrix}$	$\begin{bmatrix} 0 \le x \le h_{rUC}/2 \\ -w_{rUC}/2 \le y \le w_{rUC}/2 \\ -\bar{t}_{rUC}/2 \end{bmatrix}$
x^{A}	$\begin{bmatrix} -x_1^{\hat{A}} \\ -x_2^{\hat{A}} \\ -x_3^{\hat{A}} + \bar{t}_{rUC} \end{bmatrix}$	$\begin{bmatrix} -x_1^{\hat{A}} \\ -x_2^{\hat{A}} \\ x_3^{\hat{A}} + \bar{t}_{rUC} \end{bmatrix}$	$\begin{bmatrix} -x_1^{\hat{A}} + h_{rUC}/2 \\ -x_2^{\hat{A}} \\ -x_3^{\hat{A}} + \bar{t}_{rUC} \end{bmatrix}$	$\begin{bmatrix} -x_1^{\hat{A}} - h_{rUC}/2 \\ -x_2^{\hat{A}} \\ -x_3^{\hat{A}} + \bar{t}_{rUC} \end{bmatrix}$	$\begin{bmatrix} -x_1^{\hat{A}} - h_{rUC}/2 \\ -x_2^{\hat{A}} \\ x_3^{\hat{A}} + \bar{t}_{rUC} \end{bmatrix}$	$\begin{bmatrix} -x_1^{\hat{A}} + h_{rUC}/2 \\ -x_2^{\hat{A}} \\ x_3^{\hat{A}} + \bar{t}_{rUC} \end{bmatrix}$

3 Determine a consistent system of linear equations

- from the periodic master equations, determine a consistent nomenclature of faces (isolated periodic boundary), edges (sharing two periodic boundaries) and vertices (sharing three periodic boundaries) for the unit cell displayed in Fig. A.2. In case of reduced unit cells, periodic faces may need to be further subdivided according to the master equations,

such that all internal symmetries are satisfied. As a result, additional edges and vertices are generated and need to be treated separately.

- for edges and vertices sharing more than a single periodic boundary (or result from a subdivision of a face), the individual equations need to be combined and condensed in order to generate a set of linear independent equations. Since many finite element codes allow coupling of master and slave nodes only in such a way that each slave node may only be used once (in order to minimise over-constraints and chains of constraints), an admissible system of linear equations must be derived. In case a node set is used more than once as a slave node set in Abaqus/Implicit, an error is directly issued. In Abaqus/Explicit, no direct error is returned, but the pre-processor crashes after several hours of run-time while unsuccessfully trying to resolve over-constraints prior to the beginning of the actual solution procedure. In a first step, write down all possible independent coupling equations for edges and vertices. Obtain new coupling equations by eliminating individual coefficients from substitution, subtraction or addition. A graphical representation of the coupling equations shown in Fig. A.3 describes how a system of equations is found that couples as many as possible to as few as possible master edges. The full implementation for faces, edges and vertices for a 1/4 reduced unit cell (orthogonal to axial yarns) including both out-of-plane nesting cases in summarised in Section A.2.

4 **Incorporate the periodic boundary conditions into the finite element model**

- create a mesh that satisfies the periodicity and symmetry requirements of the master coupling equations at all periodic boundaries. All previously determined faces, edges, and vertices must be represented in the model with at least a single node. In case a periodic mesh is cannot be obtained, a two-dimensional periodic dummy mesh can be created at the boundaries and then coupled to an arbitrary mesh inside the unit cell.
- create node sets for each face, edge, and vertex located at a periodic boundary.
- sort all node sets according to their nodal coordinates in the correct order. The node sorting must represent periodicity and potential symmetries at each boundary, such that each node will later be coupled to

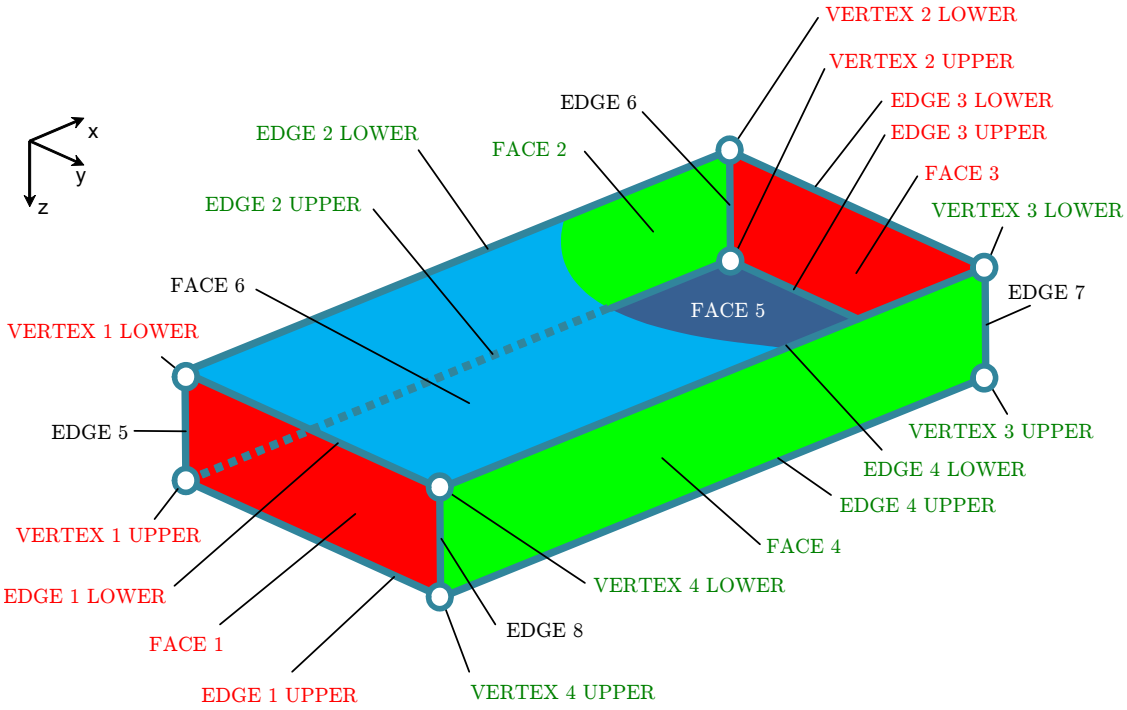

Fig. A.2: Definition of periodic faces, edges, and vertices on arbitrary periodic cell before evaluating internal symmetries

its correct partner node. Due to numerical inaccuracies in the nodal coordinates of structured meshes, the introduction of a search tolerance is strongly advised.

- apply coupling equations specific to the FE solver of choice. The order of the implementation in the solver input deck is irrelevant.
- use a double precision solution format in case an explicit solver is employed. Small inaccuracies in the nodal displacements may cause severe stress concentrations at the periodic boundaries.
- special care must be taken when PBCs are implemented in the commercial FE solver Abaqus/Explicit with the *Equation keyword. Within this environment, user-defined constraints are assembled in a global matrix for which a solution is obtained in every explicit time increment by means of an embedded penalty based implicit algorithm. Unlike in the implicit solver, however, the constraint equation solver in Abaqus/Explicit is not parallelised. Hence, a bottleneck controlled by the bandwidth of the constraint matrix is formed in the overall solution procedure. With a standard implementation of the PBCs, the run-time for a non-linear analysis of a single rUC increases by a factor of 20 compared to sim-

ple displacement boundary conditions and would nullify all benefits of the periodic model reduction. To overcome this issue, the constraint equation system is fully decoupled by introducing a phantom slave node for each physical node at a periodic boundary. Both entities are coupled using rigid one-dimensional truss elements to ensure displacement equivalence. The constraint equations are now independently formed at the isolated phantom slave nodes in order to obtain a straightforward solution for a minimum bandwidth matrix. As the task of overall coupling of the equation system is now distributed explicitly among several elements, the solution procedure can be subdivided between multiple CPUs. This methodology produces coincident run-times with and without activated PBCs and hence ensures the low computational expense of the unit cell.

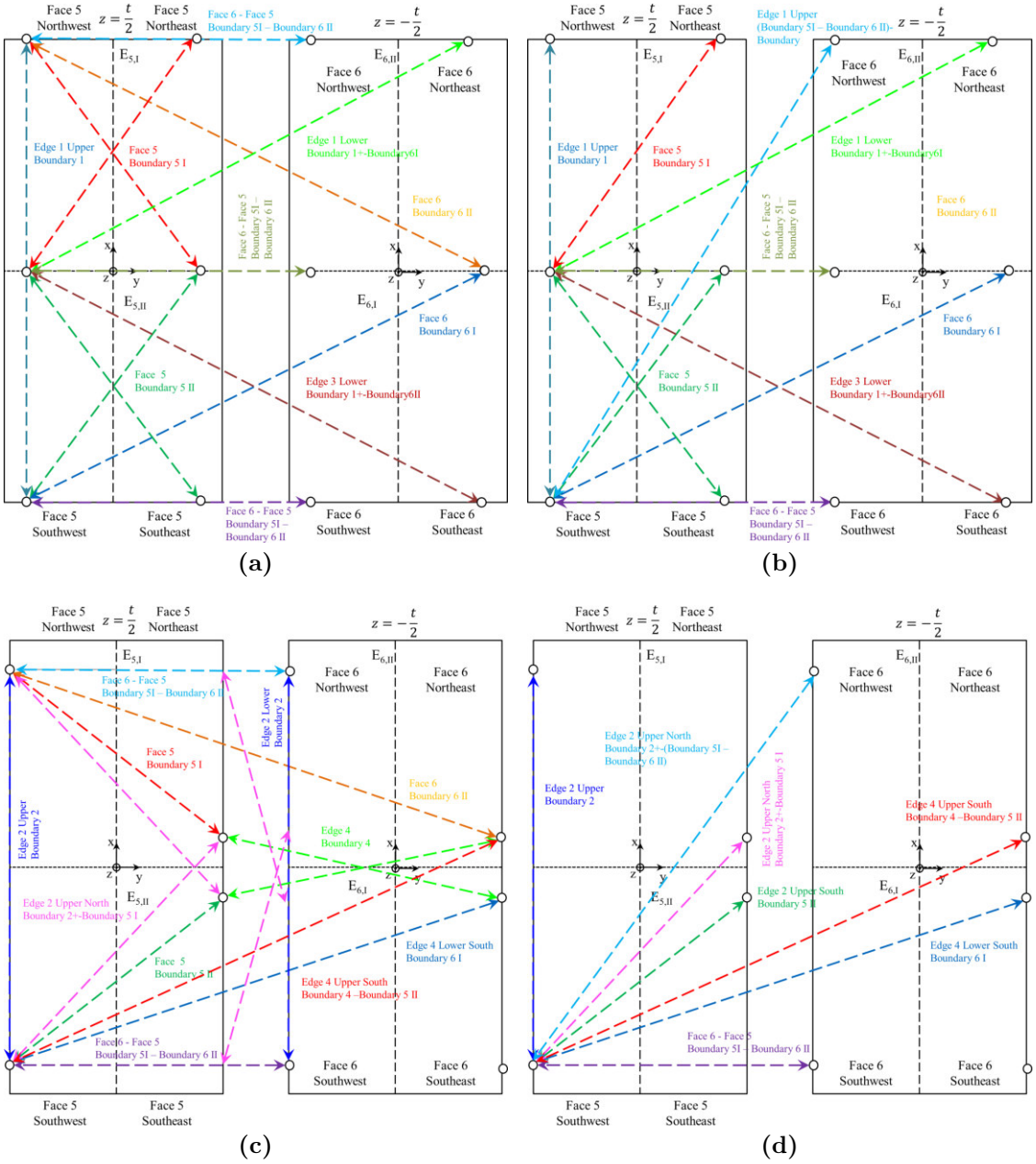

Fig. A.3: Combination of coupling equations for 1/4 rUC (orthogonal to axial yarns) for edges 2/4 and edges 1/3 (a),(c) raw coupling possibilities, (b),(d) solver implementation after condensation

A.2 Condensation and implementation of equations for 1/4 rUC

A.2.1 Faces

In-plane equations for faces

B1
$$\begin{bmatrix} u_1(h_{rUC}/2,y,z) \\ u_2(h_{rUC}/2,y,z) \\ u_3(h_{rUC}/2,y,z) \end{bmatrix} - \begin{bmatrix} u_1(-h_{rUC}/2,y,z) \\ u_2(-h_{rUC}/2,y,z) \\ u_3(-h_{rUC}/2,y,z) \end{bmatrix} = \begin{bmatrix} h_{rUC}(\varepsilon_1^\psi \cos(\psi)^2 + \varepsilon_2^\psi(1-\cos(\psi)^2) - \varepsilon_{12}^\psi \sin(2\psi)) \\ h_{rUC}(\varepsilon_1^\psi \sin(2\psi)/2 - \varepsilon_2^\psi \sin(2\psi)/2 + \varepsilon_{12}^\psi \cos(2\psi)) \\ 0 \end{bmatrix}$$

B2
$$\begin{bmatrix} u_1(-x,-w_{rUC}/2,z) \\ u_2(-x,-w_{rUC}/2,z) \\ u_3(-x,-w_{rUC}/2,z) \end{bmatrix} - \begin{bmatrix} -u_1(x,-w_{rUC}/2,z) \\ -u_2(x,-w_{rUC}/2,z) \\ u_3(x,-w_{rUC}/2,z) \end{bmatrix} = \begin{bmatrix} -w_{rUC}(\varepsilon_1^\psi \sin(2\psi)/2 - \varepsilon_2^\psi \sin(2\psi)/2 + \varepsilon_{12}^\psi \cos(2\psi)) \\ -w_{rUC}(\varepsilon_1^\psi(1-\cos(\psi)^2) + \varepsilon_2^\psi \cos(\psi)^2 + \varepsilon_{12}^\psi \sin(2\psi)) \\ 0 \end{bmatrix}$$

B3
$$\begin{bmatrix} u_1(-h_{rUC}/2,y,z) \\ u_2(-h_{rUC}/2,y,z) \\ u_3(-h_{rUC}/2,y,z) \end{bmatrix} - \begin{bmatrix} u_1(h_{rUC}/2,y,z) \\ u_2(h_{rUC}/2,y,z) \\ u_3(h_{rUC}/2,y,z) \end{bmatrix} = \begin{bmatrix} -h_{rUC}(\varepsilon_1^\psi \cos(\psi)^2 + \varepsilon_2^\psi(1-\cos(\psi)^2) - \varepsilon_{12}^\psi \sin(2\psi)) \\ -h_{rUC}(\varepsilon_1^\psi \sin(2\psi)/2 - \varepsilon_2^\psi \sin(2\psi)/2 + \varepsilon_{12}^\psi \cos(2\psi)) \\ 0 \end{bmatrix}$$

B4
$$\begin{bmatrix} u_1(-x,w_{rUC}/2,-z) \\ u_2(-x,w_{rUC}/2,-z) \\ u_3(-x,w_{rUC}/2,-z) \end{bmatrix} + \begin{bmatrix} u_1(x,w_{rUC}/2,z) \\ u_2(x,w_{rUC}/2,z) \\ u_3(x,w_{rUC}/2,z) \end{bmatrix} = \begin{bmatrix} w_{rUC}(\varepsilon_1^\psi \sin(2\psi)/2 - \varepsilon_2^\psi \sin(2\psi)/2 + \varepsilon_{12}^\psi \cos(2\psi)) \\ w_{rUC}(\varepsilon_1^\psi(1-\cos(\psi)^2) + \varepsilon_2^\psi \cos(\psi)^2 + \varepsilon_{12}^\psi \sin(2\psi)) \\ 0 \end{bmatrix}$$

Out-of-plane equations for faces nesting case I

B5
$$\begin{bmatrix} u_1(-x,-y,\bar{t}_{rUC}/2) \\ u_2(-x,-y,\bar{t}_{rUC}/2) \\ u_3(-x,-y,\bar{t}_{rUC}/2) \end{bmatrix} + \begin{bmatrix} u_1(x,y,\bar{t}_{rUC}/2) \\ u_2(x,y,\bar{t}_{rUC}/2) \\ u_3(x,y,\bar{t}_{rUC}/2) \end{bmatrix} = \begin{bmatrix} 0 \\ 0 \\ \varepsilon_3 \cdot \bar{t}_{rUC} \end{bmatrix}$$

B6
$$\begin{bmatrix} u_1(-x,-y,\bar{t}_{rUC}/2) \\ u_2(-x,-y,\bar{t}_{rUC}/2) \\ u_3(-x,-y,\bar{t}_{rUC}/2) \end{bmatrix} + \begin{bmatrix} u_1(x,y,-\bar{t}_{rUC}/2) \\ u_2(x,y,-\bar{t}_{rUC}/2) \\ -u_3(x,y,-\bar{t}_{rUC}/2) \end{bmatrix} = \begin{bmatrix} 0 \\ 0 \\ \varepsilon_3 \cdot \bar{t}_{rUC} \end{bmatrix}$$

Out-of-plane master equations for faces nesting case II

B5I
$$\begin{bmatrix} u_1(-x+h_{rUC}/2,-y,\overline{t}_{rUC}/2) \\ u_2(-x+h_{rUC}/2,-y,\overline{t}_{rUC}/2) \\ u_3(-x+h_{rUC}/2,-y,\overline{t}_{rUC}/2) \end{bmatrix} + \begin{bmatrix} u_1(x,y,\overline{t}_{rUC}/2) \\ u_2(x,y,\overline{t}_{rUC}/2) \\ u_3(x,y,\overline{t}_{rUC}/2) \end{bmatrix} = \begin{bmatrix} h_{rUC}(\varepsilon_1^{\psi}\cos(\psi)^2+\varepsilon_2^{\psi}(1-\cos(\psi)^2)-\varepsilon_{12}^{\psi}\sin(2\psi))/2 \\ h_{rUC}((\varepsilon_1^{\psi}\sin(2\psi))/2-(\varepsilon_2^{\psi}\sin(2\psi))/2+\varepsilon_{12}^{\psi}\cos(2\psi))/2 \\ \varepsilon_3\overline{t}_{rUC} \end{bmatrix}$$

B5II
$$\begin{bmatrix} u_1(-x-h_{rUC}/2,-y,\overline{t}_{rUC}/2) \\ u_2(-x-h_{rUC}/2,-y,\overline{t}_{rUC}/2) \\ u_3(-x-h_{rUC}/2,-y,\overline{t}_{rUC}/2) \end{bmatrix} + \begin{bmatrix} u_1(x,y,\overline{t}_{rUC}/2) \\ u_2(x,y,\overline{t}_{rUC}/2) \\ u_3(x,y,\overline{t}_{rUC}/2) \end{bmatrix} = \begin{bmatrix} -h_{rUC}(\varepsilon_1^{\psi}\cos(\psi)^2+\varepsilon_2^{\psi}(1-\cos(\psi)^2)-\varepsilon_{12}^{\psi}\sin(2\psi))/2 \\ -h_{rUC}((\varepsilon_1^{\psi}\sin(2\psi))/2-(\varepsilon_2^{\psi}\sin(2\psi))/2+\varepsilon_{12}^{\psi}\cos(2\psi))/2 \\ \varepsilon_3\overline{t}_{rUC} \end{bmatrix}$$

B6I
$$\begin{bmatrix} u_1(-x-h_{rUC}/2,-y,\overline{t}_{rUC}/2) \\ u_2(-x-h_{rUC}/2,-y,\overline{t}_{rUC}/2) \\ u_3(-x-h_{rUC}/2,-y,\overline{t}_{rUC}/2) \end{bmatrix} + \begin{bmatrix} u_1(x,y,-\overline{t}_{rUC}/2) \\ u_2(x,y,-\overline{t}_{rUC}/2) \\ -u_3(x,y,-\overline{t}_{rUC}/2) \end{bmatrix} = \begin{bmatrix} -h_{rUC}(\varepsilon_1^{\psi}\cos(\psi)^2+\varepsilon_2^{\psi}(1-\cos(\psi)^2)-\varepsilon_{12}^{\psi}\sin(2\psi))/2 \\ -h_{rUC}((\varepsilon_1^{\psi}\sin(2\psi))/2-(\varepsilon_2^{\psi}\sin(2\psi))/2+\varepsilon_{12}^{\psi}\cos(2\psi))/2 \\ \varepsilon_3\overline{t}_{rUC} \end{bmatrix}$$

B6II
$$\begin{bmatrix} u_1(-x+h_{rUC}/2,-y,\overline{t}_{rUC}/2) \\ u_2(-x+h_{rUC}/2,-y,\overline{t}_{rUC}/2) \\ u_3(-x+h_{rUC}/2,-y,\overline{t}_{rUC}/2) \end{bmatrix} + \begin{bmatrix} u_1(x,y,-\overline{t}_{rUC}/2) \\ u_2(x,y,-\overline{t}_{rUC}/2) \\ -u_3(x,y,-\overline{t}_{rUC}/2) \end{bmatrix} = \begin{bmatrix} h_{rUC}(\varepsilon_1^{\psi}\cos(\psi)^2+\varepsilon_2^{\psi}(1-\cos(\psi)^2)-\varepsilon_{12}^{\psi}\sin(2\psi))/2 \\ h_{rUC}((\varepsilon_1^{\psi}\sin(2\psi))/2-(\varepsilon_2^{\psi}\sin(2\psi))/2+\varepsilon_{12}^{\psi}\cos(2\psi))/2 \\ \varepsilon_3\overline{t}_{rUC} \end{bmatrix}$$

A.2.1.1 In-plane faces - special cases

Face 2 Center $u(x,y,z)=u(0,-w_{rUC}/2,z)$

B2
$$\begin{bmatrix} 2\cdot u_1(0,-w_{rUC}/2,z) \\ u_2(0,-w_{rUC}/2,z) \\ u_3(0,-w_{rUC}/2,z) \end{bmatrix} - \begin{bmatrix} -u_1(0,-w_{rUC}/2,z) \\ -u_2(0,-w_{rUC}/2,z) \\ u_3(0,-w_{rUC}/2,z) \end{bmatrix} = \begin{bmatrix} -w_{rUC}(\varepsilon_1^{\psi}\sin(2\psi)/2-\varepsilon_2^{\psi}\sin(2\psi)/2+\varepsilon_{12}^{\psi}\cos(2\psi)) \\ -w_{rUC}(\varepsilon_1^{\psi}(1-\cos(\psi)^2)+\varepsilon_2^{\psi}\cos(\psi)^2+\varepsilon_{12}^{\psi}\sin(2\psi)) \\ 0 \end{bmatrix}$$

B2
$$\begin{bmatrix} 2\cdot u_1(0,-w_{rUC}/2,z) \\ 2\cdot u_2(0,-w_{rUC}/2,z) \\ 0 \end{bmatrix} = \begin{bmatrix} -w_{rUC}(\varepsilon_1^{\psi}\sin(2\psi)/2-\varepsilon_2^{\psi}\sin(2\psi)/2+\varepsilon_{12}^{\psi}\cos(2\psi)) \\ -w_{rUC}(\varepsilon_1^{\psi}(1-\cos(\psi)^2)+\varepsilon_2^{\psi}\cos(\psi)^2+\varepsilon_{12}^{\psi}\sin(2\psi)) \\ 0 \end{bmatrix}$$

Face 4 Center $u(x,y,z) = u(0, w_{rUC}/2, z)$

B4
$$\begin{bmatrix} u_1(0, w_{rUC}/2, -z) \\ u_2(0, w_{rUC}/2, -z) \\ u_3(0, w_{rUC}/2, -z) \end{bmatrix} + \begin{bmatrix} u_1(0, w_{rUC}/2, z) \\ u_2(0, w_{rUC}/2, z) \\ u_3(0, w_{rUC}/2, z) \end{bmatrix} = \begin{bmatrix} w_{rUC}(\varepsilon_1^\psi \sin(2\psi)/2 - \varepsilon_2^\psi \sin(2\psi)/2 + \varepsilon_{12}^\psi \cos(2\psi)) \\ w_{rUC}(\varepsilon_1^\psi (1-\cos(\psi)^2) + \varepsilon_2^\psi \cos(\psi)^2 + \varepsilon_{12}^\psi \sin(2\psi)) \\ 0 \end{bmatrix}$$

Face 4 Center Center $u(x,y,z) = u(0, w_{rUC}/2, 0)$

B4
$$\begin{bmatrix} u_1(0, w_{rUC}/2, 0) \\ u_2(0, w_{rUC}/2, 0) \\ u_3(0, w_{rUC}/2, 0) \end{bmatrix} + \begin{bmatrix} u_1(0, w_{rUC}/2, 0) \\ u_2(0, w_{rUC}/2, 0) \\ u_3(0, w_{rUC}/2, 0) \end{bmatrix} = \begin{bmatrix} w_{rUC}(\varepsilon_1^\psi \sin(2\psi)/2 - \varepsilon_2^\psi \sin(2\psi)/2 + \varepsilon_{12}^\psi \cos(2\psi)) \\ w_{rUC}(\varepsilon_1^\psi (1-\cos(\psi)^2) + \varepsilon_2^\psi \cos(\psi)^2 + \varepsilon_{12}^\psi \sin(2\psi)) \\ 0 \end{bmatrix}$$

B4
$$\begin{bmatrix} 2 \cdot u_1(0, w_{rUC}/2, 0) \\ 2 \cdot u_2(0, w_{rUC}/2, 0) \\ 2 \cdot u_3(0, w_{rUC}/2, 0) \end{bmatrix} = \begin{bmatrix} w_{rUC}(\varepsilon_1^\psi \sin(2\psi)/2 - \varepsilon_2^\psi \sin(2\psi)/2 + \varepsilon_{12}^\psi \cos(2\psi)) \\ w_{rUC}(\varepsilon_1^\psi (1-\cos(\psi)^2) + \varepsilon_2^\psi \cos(\psi)^2 + \varepsilon_{12}^\psi \sin(2\psi)) \\ 0 \end{bmatrix}$$

A.2.2 Edges

A.2.2.1 In-plane edges

Edge 5 = B1 ∩ B2, $u(x,y,z) = u(-h_{rUC}/2, -w_{rUC}/2, z)$

B1
$$\begin{bmatrix} u_1(h_{rUC}/2, -w_{rUC}/2, z) \\ u_2(h_{rUC}/2, -w_{rUC}/2, z) \\ u_3(h_{rUC}/2, -w_{rUC}/2, z) \end{bmatrix} - \begin{bmatrix} u_1(-h_{rUC}/2, -w_{rUC}/2, z) \\ u_2(-h_{rUC}/2, -w_{rUC}/2, z) \\ u_3(-h_{rUC}/2, -w_{rUC}/2, z) \end{bmatrix} = \begin{bmatrix} h_{rUC}(\varepsilon_1^\psi \cos(\psi)^2 + \varepsilon_2^\psi (1-\cos(\psi)^2) - \varepsilon_{12}^\psi \sin(2\psi)) \\ h_{rUC}(\varepsilon_1^\psi \sin(2\psi)/2 - \varepsilon_2^\psi \sin(2\psi)/2 + \varepsilon_{12}^\psi \cos(2\psi)) \\ 0 \end{bmatrix}$$

B2
$$\begin{bmatrix} u_1(h_{rUC}/2, -w_{rUC}/2, z) \\ u_2(h_{rUC}/2, -w_{rUC}/2, z) \\ u_3(h_{rUC}/2, -w_{rUC}/2, z) \end{bmatrix} - \begin{bmatrix} -u_1(-h_{rUC}/2, -w_{rUC}/2, z) \\ -u_2(-h_{rUC}/2, -w_{rUC}/2, z) \\ u_3(-h_{rUC}/2, -w_{rUC}/2, z) \end{bmatrix} = \begin{bmatrix} -w_{rUC}(\varepsilon_1^\psi \sin(2\psi)/2 - \varepsilon_2^\psi \sin(2\psi)/2 + \varepsilon_{12}^\psi \cos(2\psi)) \\ -w_{rUC}(\varepsilon_1^\psi (1-\cos(\psi)^2) + \varepsilon_2^\psi \cos(\psi)^2 + \varepsilon_{12}^\psi \sin(2\psi)) \\ 0 \end{bmatrix}$$

B1-B2
$$\begin{bmatrix} -2 \cdot u_1(-h_{rUC}/2, -w_{rUC}/2, z) \\ -2 \cdot u_2(-h_{rUC}/2, -w_{rUC}/2, z) \\ 0 \end{bmatrix} = \begin{bmatrix} h_{rUC}(\varepsilon_1^\psi \cos(\psi)^2 + \varepsilon_2^\psi (1-\cos(\psi)^2) - \varepsilon_{12}^\psi \sin(2\psi)) + w_{rUC}(\varepsilon_1^\psi \sin(2\psi)/2 - \varepsilon_2^\psi \sin(2\psi)/2 + \varepsilon_{12}^\psi \cos(2\psi)) \\ h_{rUC}(\varepsilon_1^\psi \sin(2\psi)/2 - \varepsilon_2^\psi \sin(2\psi)/2 + \varepsilon_{12}^\psi \cos(2\psi)) + w_{rUC}(\varepsilon_1^\psi (1-\cos(\psi)^2) + \varepsilon_2^\psi \cos(\psi)^2 + \varepsilon_{12}^\psi \sin(2\psi)) \\ 0 \end{bmatrix}$$

Edge 5 = B1 ∩ B2, $u(x,y,z) = u(-h_{rUC}/2, -w_{rUC}/2, z)$

B1+B2
$$\begin{bmatrix} 2\cdot u_1(h_{rUC}/2,-w_{rUC}/2,z) \\ 2\cdot u_2(h_{rUC}/2,-w_{rUC}/2,z) \\ 2\cdot u_3(h_{rUC}/2,-w_{rUC}/2,z) \end{bmatrix} - \begin{bmatrix} 0 \\ 0 \\ 2\cdot u_3(-h_{rUC}/2,-w_{rUC}/2,z) \end{bmatrix} = \begin{bmatrix} h_{rUC}(\varepsilon_1^\psi\cos(\psi)^2 + \varepsilon_2^\psi(1-\cos(\psi)^2) - \varepsilon_{12}^\psi\sin(2\psi)) - w_{rUC}(\varepsilon_1^\psi\sin(2\psi)/2 - \varepsilon_2^\psi\sin(2\psi)/2 + \varepsilon_{12}^\psi\cos(2\psi)) \\ h_{rUC}(\varepsilon_1^\psi\sin(2\psi)/2 - \varepsilon_2^\psi\sin(2\psi)/2 + \varepsilon_{12}^\psi\cos(2\psi)) - w_{rUC}(\varepsilon_1^\psi(1-\cos(\psi)^2) + \varepsilon_2^\psi\cos(\psi)^2 + \varepsilon_{12}^\psi\sin(2\psi)) \\ 0 \end{bmatrix}$$

Edge 6 = B2 ∩ B3, $u(x,y,z) = u(h_{rUC}/2, -w_{rUC}/2, z)$

B2
$$\begin{bmatrix} u_1(h_{rUC}/2,-w_{rUC}/2,z) \\ u_2(h_{rUC}/2,-w_{rUC}/2,z) \\ u_3(h_{rUC}/2,-w_{rUC}/2,z) \end{bmatrix} - \begin{bmatrix} -u_1(-h_{rUC}/2,-w_{rUC}/2,z) \\ -u_2(-h_{rUC}/2,-w_{rUC}/2,z) \\ u_3(-h_{rUC}/2,-w_{rUC}/2,z) \end{bmatrix} = \begin{bmatrix} -w_{rUC}(\varepsilon_1^\psi\sin(2\psi)/2 - \varepsilon_2^\psi\sin(2\psi)/2 + \varepsilon_{12}^\psi\cos(2\psi)) \\ -w_{rUC}(\varepsilon_1^\psi(1-\cos(\psi)^2) + \varepsilon_2^\psi\cos(\psi)^2 + \varepsilon_{12}^\psi\sin(2\psi)) \\ 0 \end{bmatrix}$$

B3
$$\begin{bmatrix} u_1(-h_{rUC}/2,-w_{rUC}/2,z) \\ u_2(-h_{rUC}/2,-w_{rUC}/2,z) \\ u_3(-h_{rUC}/2,-w_{rUC}/2,z) \end{bmatrix} - \begin{bmatrix} u_1(h_{rUC}/2,-w_{rUC}/2,z) \\ u_2(h_{rUC}/2,-w_{rUC}/2,z) \\ u_3(h_{rUC}/2,-w_{rUC}/2,z) \end{bmatrix} = \begin{bmatrix} -h_{rUC}(\varepsilon_1^\psi\cos(\psi)^2 + \varepsilon_2^\psi(1-\cos(\psi)^2) - \varepsilon_{12}^\psi\sin(2\psi)) \\ -h_{rUC}(\varepsilon_1^\psi\sin(2\psi)/2 - \varepsilon_2^\psi\sin(2\psi)/2 + \varepsilon_{12}^\psi\cos(2\psi)) \\ 0 \end{bmatrix}$$

B2-B3
$$\begin{bmatrix} 0 \\ 0 \\ -2\cdot u_3(-h_{rUC}/2,-w_{rUC}/2,z) \end{bmatrix} + \begin{bmatrix} 2\cdot u_1(h_{rUC}/2,-w_{rUC}/2,z) \\ 2\cdot u_2(h_{rUC}/2,-w_{rUC}/2,z) \\ 2\cdot u_3(h_{rUC}/2,-w_{rUC}/2,z) \end{bmatrix} = \begin{bmatrix} -w_{rUC}(\varepsilon_1^\psi\sin(2\psi)/2 - \varepsilon_2^\psi\sin(2\psi)/2 + \varepsilon_{12}^\psi\cos(2\psi)) + h_{rUC}(\varepsilon_1^\psi\cos(\psi)^2 + \varepsilon_2^\psi(1-\cos(\psi)^2) - \varepsilon_{12}^\psi\sin(2\psi)) \\ -w_{rUC}(\varepsilon_1^\psi(1-\cos(\psi)^2) + \varepsilon_2^\psi\cos(\psi)^2 + \varepsilon_{12}^\psi\sin(2\psi)) + h_{rUC}(\varepsilon_1^\psi\sin(2\psi)/2 - \varepsilon_2^\psi\sin(2\psi)/2 + \varepsilon_{12}^\psi\cos(2\psi)) \\ 0 \end{bmatrix}$$

B2+B3
$$\begin{bmatrix} 2\cdot u_1(-h_{rUC}/2,-w_{rUC}/2,z) \\ 2\cdot u_2(-h_{rUC}/2,-w_{rUC}/2,z) \\ 0 \end{bmatrix} = \begin{bmatrix} -w_{rUC}(\varepsilon_1^\psi\sin(2\psi)/2 - \varepsilon_2^\psi\sin(2\psi)/2 + \varepsilon_{12}^\psi\cos(2\psi)) - h_{rUC}(\varepsilon_1^\psi\cos(\psi)^2 + \varepsilon_2^\psi(1-\cos(\psi)^2) - \varepsilon_{12}^\psi\sin(2\psi)) \\ -w_{rUC}(\varepsilon_1^\psi(1-\cos(\psi)^2) + \varepsilon_2^\psi\cos(\psi)^2 + \varepsilon_{12}^\psi\sin(2\psi)) - h_{rUC}(\varepsilon_1^\psi\sin(2\psi)/2 - \varepsilon_2^\psi\sin(2\psi)/2 + \varepsilon_{12}^\psi\cos(2\psi)) \\ 0 \end{bmatrix}$$

Edge 7 = B3 ∩ B4, $u(x,y,z) = u(h_{rUC}/2, w_{rUC}/2, z)$

B3
$$\begin{bmatrix} u_1(-h_{rUC}/2,w_{rUC}/2,z) \\ u_2(-h_{rUC}/2,w_{rUC}/2,z) \\ u_3(-h_{rUC}/2,w_{rUC}/2,z) \end{bmatrix} - \begin{bmatrix} u_1(h_{rUC}/2,w_{rUC}/2,z) \\ u_2(h_{rUC}/2,w_{rUC}/2,z) \\ u_3(h_{rUC}/2,w_{rUC}/2,z) \end{bmatrix} = \begin{bmatrix} -h_{rUC}(\varepsilon_1^\psi\cos(\psi)^2 + \varepsilon_2^\psi(1-\cos(\psi)^2) - \varepsilon_{12}^\psi\sin(2\psi)) \\ -h_{rUC}(\varepsilon_1^\psi\sin(2\psi)/2 - \varepsilon_2^\psi\sin(2\psi)/2 + \varepsilon_{12}^\psi\cos(2\psi)) \\ 0 \end{bmatrix}$$

B4
$$\begin{bmatrix} u_1(-h_{rUC}/2,w_{rUC}/2,-z) \\ u_2(-h_{rUC}/2,w_{rUC}/2,-z) \\ u_3(-h_{rUC}/2,w_{rUC}/2,-z) \end{bmatrix} + \begin{bmatrix} u_1(h_{rUC}/2,w_{rUC}/2,z) \\ u_2(h_{rUC}/2,w_{rUC}/2,z) \\ u_3(h_{rUC}/2,w_{rUC}/2,z) \end{bmatrix} = \begin{bmatrix} w_{rUC}(\varepsilon_1^\psi\sin(2\psi)/2 - \varepsilon_2^\psi\sin(2\psi)/2 + \varepsilon_{12}^\psi\cos(2\psi)) \\ w_{rUC}(\varepsilon_1^\psi(1-\cos(\psi)^2) + \varepsilon_2^\psi\cos(\psi)^2 + \varepsilon_{12}^\psi\sin(2\psi)) \\ 0 \end{bmatrix}$$

Edge 7 = B3 ∩ B4, $u(x,y,z) = u(h_{rUC}/2, w_{rUC}/2, z)$

$$\text{B3-B4}\quad \begin{bmatrix} u_1(-h_{rUC}/2, w_{rUC}/2, z) \\ u_2(-h_{rUC}/2, w_{rUC}/2, z) \\ u_3(-h_{rUC}/2, w_{rUC}/2, z) \end{bmatrix} - \begin{bmatrix} u_1(-h_{rUC}/2, w_{rUC}/2, -z) \\ u_2(-h_{rUC}/2, w_{rUC}/2, -z) \\ u_3(-h_{rUC}/2, w_{rUC}/2, -z) \end{bmatrix} = \begin{bmatrix} 2\cdot u_1(h_{rUC}/2, w_{rUC}/2, z) \\ 2\cdot u_2(h_{rUC}/2, w_{rUC}/2, z) \\ 2\cdot u_3(h_{rUC}/2, w_{rUC}/2, z) \end{bmatrix}$$

$$\begin{bmatrix} -h_{rUC}(\varepsilon_1^\psi \cos(\psi)^2 + \varepsilon_2^\psi(1-\cos(\psi)^2) - \varepsilon_{12}^\psi \sin(2\psi)) - w_{rUC}(\varepsilon_1^\psi \sin(2\psi)/2 - \varepsilon_2^\psi \sin(2\psi)/2 + \varepsilon_{12}^\psi \cos(2\psi)) \\ -h_{rUC}(\varepsilon_1^\psi \sin(2\psi)/2 - \varepsilon_2^\psi \sin(2\psi)/2 + \varepsilon_{12}^\psi \cos(2\psi)) - w_{rUC}(\varepsilon_1^\psi(1-\cos(\psi)^2) + \varepsilon_2^\psi \cos(\psi)^2 + \varepsilon_{12}^\psi \sin(2\psi)) \\ 0 \end{bmatrix}$$

$$\text{B3+B4}\quad \begin{bmatrix} u_1(-h_{rUC}/2, w_{rUC}/2, z) \\ u_2(-h_{rUC}/2, w_{rUC}/2, z) \\ u_3(-h_{rUC}/2, w_{rUC}/2, z) \end{bmatrix} + \begin{bmatrix} u_1(-h_{rUC}/2, w_{rUC}/2, -z) \\ u_2(-h_{rUC}/2, w_{rUC}/2, -z) \\ u_3(-h_{rUC}/2, w_{rUC}/2, -z) \end{bmatrix} = \begin{bmatrix} -h_{rUC}(\varepsilon_1^\psi \cos(\psi)^2 + \varepsilon_2^\psi(1-\cos(\psi)^2) - \varepsilon_{12}^\psi \sin(2\psi)) + w_{rUC}(\varepsilon_1^\psi \sin(2\psi)/2 - \varepsilon_2^\psi \sin(2\psi)/2 + \varepsilon_{12}^\psi \cos(2\psi)) \\ -h_{rUC}(\varepsilon_1^\psi \sin(2\psi)/2 - \varepsilon_2^\psi \sin(2\psi)/2 + \varepsilon_{12}^\psi \cos(2\psi)) + w_{rUC}(\varepsilon_1^\psi(1-\cos(\psi)^2) + \varepsilon_2^\psi \cos(\psi)^2 + \varepsilon_{12}^\psi \sin(2\psi)) \\ 0 \end{bmatrix}$$

Edge 7 Center = B3 ∩ B4, $u(x,y,z) = u(h_{rUC}/2, w_{rUC}/2, 0)$

$$\text{B3-B4}\quad \begin{bmatrix} u_1(-h_{rUC}/2, w_{rUC}/2, 0) \\ u_2(-h_{rUC}/2, w_{rUC}/2, 0) \\ u_3(-h_{rUC}/2, w_{rUC}/2, 0) \end{bmatrix} - \begin{bmatrix} 2\cdot u_1(h_{rUC}/2, w_{rUC}/2, 0) \\ 2\cdot u_2(h_{rUC}/2, w_{rUC}/2, 0) \\ 2\cdot u_3(h_{rUC}/2, w_{rUC}/2, 0) \end{bmatrix} = \begin{bmatrix} u_1(-h_{rUC}/2, w_{rUC}/2, 0) \\ u_2(-h_{rUC}/2, w_{rUC}/2, 0) \\ u_3(-h_{rUC}/2, w_{rUC}/2, 0) \end{bmatrix}$$

$$\begin{bmatrix} -h_{rUC}(\varepsilon_1^\psi \cos(\psi)^2 + \varepsilon_2^\psi(1-\cos(\psi)^2) - \varepsilon_{12}^\psi \sin(2\psi)) - w_{rUC}(\varepsilon_1^\psi \sin(2\psi)/2 - \varepsilon_2^\psi \sin(2\psi)/2 + \varepsilon_{12}^\psi \cos(2\psi)) \\ -h_{rUC}(\varepsilon_1^\psi \sin(2\psi)/2 - \varepsilon_2^\psi \sin(2\psi)/2 + \varepsilon_{12}^\psi \cos(2\psi)) - w_{rUC}(\varepsilon_1^\psi(1-\cos(\psi)^2) + \varepsilon_2^\psi \cos(\psi)^2 + \varepsilon_{12}^\psi \sin(2\psi)) \\ 0 \end{bmatrix}$$

$$\text{B3+B4}\quad \begin{bmatrix} u_1(-h_{rUC}/2, w_{rUC}/2, 0) \\ u_2(-h_{rUC}/2, w_{rUC}/2, 0) \\ u_3(-h_{rUC}/2, w_{rUC}/2, 0) \end{bmatrix} + \begin{bmatrix} u_1(-h_{rUC}/2, w_{rUC}/2, 0) \\ u_2(-h_{rUC}/2, w_{rUC}/2, 0) \\ u_3(-h_{rUC}/2, w_{rUC}/2, 0) \end{bmatrix} = \begin{bmatrix} -h_{rUC}(\varepsilon_1^\psi \cos(\psi)^2 + \varepsilon_2^\psi(1-\cos(\psi)^2) - \varepsilon_{12}^\psi \sin(2\psi)) + w_{rUC}(\varepsilon_1^\psi \sin(2\psi)/2 - \varepsilon_2^\psi \sin(2\psi)/2 + \varepsilon_{12}^\psi \cos(2\psi)) \\ -h_{rUC}(\varepsilon_1^\psi \sin(2\psi)/2 - \varepsilon_2^\psi \sin(2\psi)/2 + \varepsilon_{12}^\psi \cos(2\psi)) + w_{rUC}(\varepsilon_1^\psi(1-\cos(\psi)^2) + \varepsilon_2^\psi \cos(\psi)^2 + \varepsilon_{12}^\psi \sin(2\psi)) \\ 0 \end{bmatrix}$$

$$\text{B3-B4}\quad \begin{bmatrix} -2\cdot u_1(h_{rUC}/2, w_{rUC}/2, 0) \\ -2\cdot u_2(h_{rUC}/2, w_{rUC}/2, 0) \\ -2\cdot u_3(h_{rUC}/2, w_{rUC}/2, 0) \end{bmatrix} = \begin{bmatrix} -h_{rUC}(\varepsilon_1^\psi \cos(\psi)^2 + \varepsilon_2^\psi(1-\cos(\psi)^2) - \varepsilon_{12}^\psi \sin(2\psi)) - w_{rUC}(\varepsilon_1^\psi \sin(2\psi)/2 - \varepsilon_2^\psi \sin(2\psi)/2 + \varepsilon_{12}^\psi \cos(2\psi)) \\ -h_{rUC}(\varepsilon_1^\psi \sin(2\psi)/2 - \varepsilon_2^\psi \sin(2\psi)/2 + \varepsilon_{12}^\psi \cos(2\psi)) - w_{rUC}(\varepsilon_1^\psi(1-\cos(\psi)^2) + \varepsilon_2^\psi \cos(\psi)^2 + \varepsilon_{12}^\psi \sin(2\psi)) \\ 0 \end{bmatrix}$$

$$\text{B3+B4}\quad \begin{bmatrix} 2\cdot u_1(-h_{rUC}/2, w_{rUC}/2, 0) \\ 2\cdot u_2(-h_{rUC}/2, w_{rUC}/2, 0) \\ 2\cdot u_3(-h_{rUC}/2, w_{rUC}/2, 0) \end{bmatrix} = \begin{bmatrix} -h_{rUC}(\varepsilon_1^\psi \cos(\psi)^2 + \varepsilon_2^\psi(1-\cos(\psi)^2) - \varepsilon_{12}^\psi \sin(2\psi)) + w_{rUC}(\varepsilon_1^\psi \sin(2\psi)/2 - \varepsilon_2^\psi \sin(2\psi)/2 + \varepsilon_{12}^\psi \cos(2\psi)) \\ -h_{rUC}(\varepsilon_1^\psi \sin(2\psi)/2 - \varepsilon_2^\psi \sin(2\psi)/2 + \varepsilon_{12}^\psi \cos(2\psi)) + w_{rUC}(\varepsilon_1^\psi(1-\cos(\psi)^2) + \varepsilon_2^\psi \cos(\psi)^2 + \varepsilon_{12}^\psi \sin(2\psi)) \\ 0 \end{bmatrix}$$

Edge 8 = B4 ∩ B1, $u(x,y,z) = u(-h_{rUC}/2, w_{rUC}/2, z)$

$$\text{B4}\quad \begin{bmatrix} u_1(h_{rUC}/2, w_{rUC}/2, -z) \\ u_2(h_{rUC}/2, w_{rUC}/2, -z) \\ u_3(h_{rUC}/2, w_{rUC}/2, -z) \end{bmatrix} + \begin{bmatrix} u_1(-h_{rUC}/2, w_{rUC}/2, z) \\ u_2(-h_{rUC}/2, w_{rUC}/2, z) \\ u_3(-h_{rUC}/2, w_{rUC}/2, z) \end{bmatrix} = \begin{bmatrix} w_{rUC}(\varepsilon_1^\psi \sin(2\psi)/2 - \varepsilon_2^\psi \sin(2\psi)/2 + \varepsilon_{12}^\psi \cos(2\psi)) \\ w_{rUC}(\varepsilon_1^\psi(1-\cos(\psi)^2) + \varepsilon_2^\psi \cos(\psi)^2 + \varepsilon_{12}^\psi \sin(2\psi)) \\ 0 \end{bmatrix}$$

Edge 8 = B4 ∩ B1, $u(x,y,z) = u(-h_{rUC}/2, w_{rUC}/2, z)$

B1

$$\begin{bmatrix} u_1(h_{rUC}/2, w_{rUC}/2, z) \\ u_2(h_{rUC}/2, w_{rUC}/2, z) \\ u_3(h_{rUC}/2, w_{rUC}/2, z) \end{bmatrix} - \begin{bmatrix} u_1(-h_{rUC}/2, w_{rUC}/2, z) \\ u_2(-h_{rUC}/2, w_{rUC}/2, z) \\ u_3(-h_{rUC}/2, w_{rUC}/2, z) \end{bmatrix} = \begin{bmatrix} h_{rUC}(\varepsilon_1^\psi \cos(\psi)^2 + \varepsilon_2^\psi(1-\cos(\psi)^2) - \varepsilon_{12}^\psi \sin(2\psi)) \\ h_{rUC}(\varepsilon_1^\psi \sin(2\psi)/2 - \varepsilon_2^\psi \sin(2\psi)/2 + \varepsilon_{12}^\psi \cos(2\psi)) \\ 0 \end{bmatrix}$$

B4-B1

$$\begin{bmatrix} u_1(h_{rUC}/2, w_{rUC}/2, -z) \\ u_2(h_{rUC}/2, w_{rUC}/2, -z) \\ u_3(h_{rUC}/2, w_{rUC}/2, -z) \end{bmatrix} - \begin{bmatrix} u_1(h_{rUC}/2, w_{rUC}/2, z) \\ u_2(h_{rUC}/2, w_{rUC}/2, z) \\ u_3(h_{rUC}/2, w_{rUC}/2, z) \end{bmatrix} + \begin{bmatrix} 2\cdot u_1(-h_{rUC}/2, w_{rUC}/2, z) \\ 2\cdot u_2(-h_{rUC}/2, w_{rUC}/2, z) \\ 2\cdot u_3(-h_{rUC}/2, w_{rUC}/2, z) \end{bmatrix} = \begin{bmatrix} w_{rUC}(\varepsilon_1^\psi \sin(2\psi)/2 - \varepsilon_2^\psi \sin(2\psi)/2 + \varepsilon_{12}^\psi \cos(2\psi)) - h_{rUC}(\varepsilon_1^\psi \cos(\psi)^2 + \varepsilon_2^\psi(1-\cos(\psi)^2) - \varepsilon_{12}^\psi \sin(2\psi)) \\ w_{rUC}(\varepsilon_1^\psi(1-\cos(\psi)^2) + \varepsilon_2^\psi \cos(\psi)^2 + \varepsilon_{12}^\psi \sin(2\psi)) - h_{rUC}(\varepsilon_1^\psi \sin(2\psi)/2 - \varepsilon_2^\psi \sin(2\psi)/2 + \varepsilon_{12}^\psi \cos(2\psi)) \\ 0 \end{bmatrix}$$

B4+B1

$$\begin{bmatrix} u_1(h_{rUC}/2, w_{rUC}/2, -z) \\ u_2(h_{rUC}/2, w_{rUC}/2, -z) \\ u_3(h_{rUC}/2, w_{rUC}/2, -z) \end{bmatrix} + \begin{bmatrix} u_1(h_{rUC}/2, w_{rUC}/2, z) \\ u_2(h_{rUC}/2, w_{rUC}/2, z) \\ u_3(h_{rUC}/2, w_{rUC}/2, z) \end{bmatrix} = \begin{bmatrix} w_{rUC}(\varepsilon_1^\psi \sin(2\psi)/2 - \varepsilon_2^\psi \sin(2\psi)/2 + \varepsilon_{12}^\psi \cos(2\psi)) + h_{rUC}(\varepsilon_1^\psi \cos(\psi)^2 + \varepsilon_2^\psi(1-\cos(\psi)^2) - \varepsilon_{12}^\psi \sin(2\psi)) \\ w_{rUC}(\varepsilon_1^\psi(1-\cos(\psi)^2) + \varepsilon_2^\psi \cos(\psi)^2 + \varepsilon_{12}^\psi \sin(2\psi)) + h_{rUC}(\varepsilon_1^\psi \sin(2\psi)/2 - \varepsilon_2^\psi \sin(2\psi)/2 + \varepsilon_{12}^\psi \cos(2\psi)) \\ 0 \end{bmatrix}$$

Edge 8 Center= B4 ∩ B1, $u(x,y,z) = u(-h_{rUC}/2, w_{rUC}/2, 0)$

B4-B1

$$\begin{bmatrix} u_1(h_{rUC}/2, w_{rUC}/2, 0) \\ u_2(h_{rUC}/2, w_{rUC}/2, 0) \\ u_3(h_{rUC}/2, w_{rUC}/2, 0) \end{bmatrix} + \begin{bmatrix} 2\cdot u_1(-h_{rUC}/2, w_{rUC}/2, 0) \\ 2\cdot u_2(-h_{rUC}/2, w_{rUC}/2, 0) \\ 2\cdot u_3(-h_{rUC}/2, w_{rUC}/2, 0) \end{bmatrix} - \begin{bmatrix} u_1(h_{rUC}/2, w_{rUC}/2, 0) \\ u_2(h_{rUC}/2, w_{rUC}/2, 0) \\ u_3(h_{rUC}/2, w_{rUC}/2, 0) \end{bmatrix} = \begin{bmatrix} w_{rUC}(\varepsilon_1^\psi \sin(2\psi)/2 - \varepsilon_2^\psi \sin(2\psi)/2 + \varepsilon_{12}^\psi \cos(2\psi)) - h_{rUC}(\varepsilon_1^\psi \cos(\psi)^2 + \varepsilon_2^\psi(1-\cos(\psi)^2) - \varepsilon_{12}^\psi \sin(2\psi)) \\ w_{rUC}(\varepsilon_1^\psi(1-\cos(\psi)^2) + \varepsilon_2^\psi \cos(\psi)^2 + \varepsilon_{12}^\psi \sin(2\psi)) - h_{rUC}(\varepsilon_1^\psi \sin(2\psi)/2 - \varepsilon_2^\psi \sin(2\psi)/2 + \varepsilon_{12}^\psi \cos(2\psi)) \\ 0 \end{bmatrix}$$

B4+B1

$$\begin{bmatrix} u_1(h_{rUC}/2, w_{rUC}/2, 0) \\ u_2(h_{rUC}/2, w_{rUC}/2, 0) \\ u_3(h_{rUC}/2, w_{rUC}/2, 0) \end{bmatrix} + \begin{bmatrix} u_1(h_{rUC}/2, w_{rUC}/2, 0) \\ u_2(h_{rUC}/2, w_{rUC}/2, 0) \\ u_3(h_{rUC}/2, w_{rUC}/2, 0) \end{bmatrix} = \begin{bmatrix} w_{rUC}(\varepsilon_1^\psi \sin(2\psi)/2 - \varepsilon_2^\psi \sin(2\psi)/2 + \varepsilon_{12}^\psi \cos(2\psi)) + h_{rUC}(\varepsilon_1^\psi \cos(\psi)^2 + \varepsilon_2^\psi(1-\cos(\psi)^2) - \varepsilon_{12}^\psi \sin(2\psi)) \\ w_{rUC}(\varepsilon_1^\psi(1-\cos(\psi)^2) + \varepsilon_2^\psi \cos(\psi)^2 + \varepsilon_{12}^\psi \sin(2\psi)) + h_{rUC}(\varepsilon_1^\psi \sin(2\psi)/2 - \varepsilon_2^\psi \sin(2\psi)/2 + \varepsilon_{12}^\psi \cos(2\psi)) \\ 0 \end{bmatrix}$$

B4-B1

$$\begin{bmatrix} 2\cdot u_1(-h_{rUC}/2, w_{rUC}/2, 0) \\ 2\cdot u_2(-h_{rUC}/2, w_{rUC}/2, 0) \\ 2\cdot u_3(-h_{rUC}/2, w_{rUC}/2, 0) \end{bmatrix} = \begin{bmatrix} w_{rUC}(\varepsilon_1^\psi \sin(2\psi)/2 - \varepsilon_2^\psi \sin(2\psi)/2 + \varepsilon_{12}^\psi \cos(2\psi)) - h_{rUC}(\varepsilon_1^\psi \cos(\psi)^2 + \varepsilon_2^\psi(1-\cos(\psi)^2) - \varepsilon_{12}^\psi \sin(2\psi)) \\ w_{rUC}(\varepsilon_1^\psi(1-\cos(\psi)^2) + \varepsilon_2^\psi \cos(\psi)^2 + \varepsilon_{12}^\psi \sin(2\psi)) - h_{rUC}(\varepsilon_1^\psi \sin(2\psi)/2 - \varepsilon_2^\psi \sin(2\psi)/2 + \varepsilon_{12}^\psi \cos(2\psi)) \\ 0 \end{bmatrix}$$

B4+B1

$$\begin{bmatrix} 2\cdot u_1(h_{rUC}/2, w_{rUC}/2, 0) \\ 2\cdot u_2(h_{rUC}/2, w_{rUC}/2, 0) \\ 2\cdot u_3(h_{rUC}/2, w_{rUC}/2, 0) \end{bmatrix} = \begin{bmatrix} w_{rUC}(\varepsilon_1^\psi \sin(2\psi)/2 - \varepsilon_2^\psi \sin(2\psi)/2 + \varepsilon_{12}^\psi \cos(2\psi)) + h_{rUC}(\varepsilon_1^\psi \cos(\psi)^2 + \varepsilon_2^\psi(1-\cos(\psi)^2) - \varepsilon_{12}^\psi \sin(2\psi)) \\ w_{rUC}(\varepsilon_1^\psi(1-\cos(\psi)^2) + \varepsilon_2^\psi \cos(\psi)^2 + \varepsilon_{12}^\psi \sin(2\psi)) + h_{rUC}(\varepsilon_1^\psi \sin(2\psi)/2 - \varepsilon_2^\psi \sin(2\psi)/2 + \varepsilon_{12}^\psi \cos(2\psi)) \\ 0 \end{bmatrix}$$

A.2.2.2 Out-of-plane faces for nesting case I - special cases

Face 5 to Face 6 $u(x,y,z) = u(x,y,z)$

B5
$$\begin{bmatrix} u_1(-x,-y,\overline{t}_{rUC}/2) \\ u_2(-x,-y,\overline{t}_{rUC}/2) \\ u_3(-x,-y,\overline{t}_{rUC}/2) \end{bmatrix} + \begin{bmatrix} u_1(x,y,\overline{t}_{rUC}/2) \\ u_2(x,y,\overline{t}_{rUC}/2) \\ u_3(x,y,\overline{t}_{rUC}/2) \end{bmatrix} = \begin{bmatrix} 0 \\ 0 \\ \varepsilon_3 \cdot \overline{t}_{rUC} \end{bmatrix}$$

B6
$$\begin{bmatrix} u_1(-x,-y,\overline{t}_{rUC}/2) \\ u_2(-x,-y,\overline{t}_{rUC}/2) \\ u_3(-x,-y,\overline{t}_{rUC}/2) \end{bmatrix} + \begin{bmatrix} u_1(x,y,-\overline{t}_{rUC}/2) \\ u_2(x,y,-\overline{t}_{rUC}/2) \\ -u_3(x,y,-\overline{t}_{rUC}/2) \end{bmatrix} = \begin{bmatrix} 0 \\ 0 \\ \varepsilon_3 \cdot \overline{t}_{rUC} \end{bmatrix}$$

B5-B6
$$\begin{bmatrix} u_1(x,y,\overline{t}_{rUC}/2) \\ u_2(x,y,\overline{t}_{rUC}/2) \\ u_3(x,y,\overline{t}_{rUC}/2) \end{bmatrix} - \begin{bmatrix} u_1(x,y,-\overline{t}_{rUC}/2) \\ u_2(x,y,-\overline{t}_{rUC}/2) \\ -u_3(x,y,-\overline{t}_{rUC}/2) \end{bmatrix} = \begin{bmatrix} 0 \\ 0 \\ 0 \end{bmatrix}$$

Face 5 Center South to Face 5 Center North $u(x,y,z) = u(x,0,\overline{t}_{rUC}/2)$

B5
$$\begin{bmatrix} u_1(-x,0,\overline{t}_{rUC}/2) \\ u_2(-x,0,\overline{t}_{rUC}/2) \\ u_3(-x,0,\overline{t}_{rUC}/2) \end{bmatrix} + \begin{bmatrix} u_1(x,0,\overline{t}_{rUC}/2) \\ u_2(x,0,\overline{t}_{rUC}/2) \\ u_3(x,0,\overline{t}_{rUC}/2) \end{bmatrix} = \begin{bmatrix} 0 \\ 0 \\ \varepsilon_3 \cdot \overline{t}_{rUC} \end{bmatrix}$$

Face 6 Center South to Face 6 Center North $u(x,y,z) = u(x,0,-\overline{t}_{rUC}/2)$

B5C
$$\begin{bmatrix} u_1(-x,0,\overline{t}_{rUC}/2) \\ u_2(-x,0,\overline{t}_{rUC}/2) \\ u_3(-x,0,\overline{t}_{rUC}/2) \end{bmatrix} + \begin{bmatrix} u_1(x,0,\overline{t}_{rUC}/2) \\ u_2(x,0,\overline{t}_{rUC}/2) \\ u_3(x,0,\overline{t}_{rUC}/2) \end{bmatrix} = \begin{bmatrix} 0 \\ 0 \\ \varepsilon_3 \cdot \overline{t}_{rUC} \end{bmatrix}$$

B6C
$$\begin{bmatrix} u_1(-x,0,\overline{t}_{rUC}/2) \\ u_2(-x,0,\overline{t}_{rUC}/2) \\ u_3(-x,0,\overline{t}_{rUC}/2) \end{bmatrix} + \begin{bmatrix} u_1(x,0,-\overline{t}_{rUC}/2) \\ u_2(x,0,-\overline{t}_{rUC}/2) \\ -u_3(x,0,-\overline{t}_{rUC}/2) \end{bmatrix} = \begin{bmatrix} 0 \\ 0 \\ \varepsilon_3 \cdot \overline{t}_{rUC} \end{bmatrix}$$

Face 6 Center South to Face 6 Center North $u(x,y,z) = u(x,0,-\bar{t}_{rUC}/2)$

B5C-B6C
$$\begin{bmatrix} u_1(x,0,\bar{t}_{rUC}/2) \\ u_2(x,0,\bar{t}_{rUC}/2) \\ u_3(x,0,\bar{t}_{rUC}/2) \end{bmatrix} - \begin{bmatrix} u_1(x,0,-\bar{t}_{rUC}/2) \\ u_2(x,0,-\bar{t}_{rUC}/2) \\ -u_3(x,0,-\bar{t}_{rUC}/2) \end{bmatrix} = \begin{bmatrix} 0 \\ 0 \\ 0 \end{bmatrix}$$

Face 5 Center Center $u(x,y,z) = u(0,0,\bar{t}_{rUC}/2)$

B5CC
$$\begin{bmatrix} u_1(0,0,\bar{t}_{rUC}/2) \\ u_2(0,0,\bar{t}_{rUC}/2) \\ u_3(0,0,\bar{t}_{rUC}/2) \end{bmatrix} + \begin{bmatrix} u_1(0,0,\bar{t}_{rUC}/2) \\ u_2(0,0,\bar{t}_{rUC}/2) \\ u_3(0,0,\bar{t}_{rUC}/2) \end{bmatrix} = \begin{bmatrix} 0 \\ 0 \\ \varepsilon_3 \cdot \bar{t}_{rUC} \end{bmatrix}$$

B5CC
$$\begin{bmatrix} 2 \cdot u_1(0,0,\bar{t}_{rUC}/2) \\ 2 \cdot u_2(0,0,\bar{t}_{rUC}/2) \\ 2 \cdot u_3(0,0,\bar{t}_{rUC}/2) \end{bmatrix} = \begin{bmatrix} 0 \\ 0 \\ \varepsilon_3 \cdot \bar{t}_{rUC} \end{bmatrix}$$

Face 6 Center Center $u(x,y,z) = u(0,0,-\bar{t}_{rUC}/2)$

B6CC
$$\begin{bmatrix} u_1(0,0,\bar{t}_{rUC}/2) \\ u_2(0,0,\bar{t}_{rUC}/2) \\ u_3(0,0,\bar{t}_{rUC}/2) \end{bmatrix} + \begin{bmatrix} u_1(0,0,-\bar{t}_{rUC}/2) \\ u_2(0,0,-\bar{t}_{rUC}/2) \\ -u_3(0,0,-\bar{t}_{rUC}/2) \end{bmatrix} = \begin{bmatrix} 0 \\ 0 \\ \varepsilon_3 \cdot \bar{t}_{rUC} \end{bmatrix}$$

A.2.2.3 Out-of-plane faces for nesting case II - special cases

Face 5 to Face 6 $u(x,y,z) = u(x,y,\pm\bar{t}_{rUC}/2)$

B5I
$$\begin{bmatrix} u_1(-x+h_{rUC}/2,-y,\bar{t}_{rUC}/2) \\ u_2(-x+h_{rUC}/2,-y,\bar{t}_{rUC}/2) \\ u_3(-x+h_{rUC}/2,-y,\bar{t}_{rUC}/2) \end{bmatrix} + \begin{bmatrix} u_1(x,y,\bar{t}_{rUC}/2) \\ u_2(x,y,\bar{t}_{rUC}/2) \\ u_3(x,y,\bar{t}_{rUC}/2) \end{bmatrix} = \begin{bmatrix} h_{rUC}(\varepsilon_1^{\psi}\cos(\psi)^2 + \varepsilon_2^{\psi}(1-\cos(\psi)^2) - \varepsilon_{12}^{\psi}\sin(2\psi))/2 \\ h_{rUC}((\varepsilon_1^{\psi}\sin(2\psi))/2 - (\varepsilon_2^{\psi}\sin(2\psi))/2 + \varepsilon_{12}^{\psi}\cos(2\psi))/2 \\ \varepsilon_3\bar{t}_{rUC} \end{bmatrix}$$

B5II
$$\begin{bmatrix} u_1(-x-h_{rUC}/2,-y,\bar{t}_{rUC}/2) \\ u_2(-x-h_{rUC}/2,-y,\bar{t}_{rUC}/2) \\ u_3(-x-h_{rUC}/2,-y,\bar{t}_{rUC}/2) \end{bmatrix} + \begin{bmatrix} u_1(x,y,\bar{t}_{rUC}/2) \\ u_2(x,y,\bar{t}_{rUC}/2) \\ u_3(x,y,\bar{t}_{rUC}/2) \end{bmatrix} = \begin{bmatrix} -h_{rUC}(\varepsilon_1^{\psi}\cos(\psi)^2 + \varepsilon_2^{\psi}(1-\cos(\psi)^2) - \varepsilon_{12}^{\psi}\sin(2\psi))/2 \\ -h_{rUC}((\varepsilon_1^{\psi}\sin(2\psi))/2 - (\varepsilon_2^{\psi}\sin(2\psi))/2 + \varepsilon_{12}^{\psi}\cos(2\psi))/2 \\ \varepsilon_3\bar{t}_{rUC} \end{bmatrix}$$

Face 5 to Face 6 $u(x,y,z) = u(x,y,\pm\bar{t}_{rUC}/2)$

B6I
$$\begin{bmatrix} u_1(-x-h_{rUC}/2,-y,\bar{t}_{rUC}/2) \\ u_2(-x-h_{rUC}/2,-y,\bar{t}_{rUC}/2) \\ u_3(-x-h_{rUC}/2,-y,\bar{t}_{rUC}/2) \end{bmatrix} + \begin{bmatrix} u_1(x,y,-\bar{t}_{rUC}/2) \\ u_2(x,y,-\bar{t}_{rUC}/2) \\ -u_3(x,y,-\bar{t}_{rUC}/2) \end{bmatrix} = \begin{bmatrix} -h_{rUC}(\varepsilon_1^{\psi}\cos(\psi)^2 + \varepsilon_2^{\psi}(1-\cos(\psi)^2) - \varepsilon_{12}^{\psi}\sin(2\psi))/2 \\ -h_{rUC}((\varepsilon_1^{\psi}\sin(2\psi))/2 - (\varepsilon_2^{\psi}\sin(2\psi))/2 + \varepsilon_{12}^{\psi}\cos(2\psi))/2 \\ \varepsilon_3\bar{t}_{rUC} \end{bmatrix}$$

B6II
$$\begin{bmatrix} u_1(-x+h_{rUC}/2,-y,\bar{t}_{rUC}/2) \\ u_2(-x+h_{rUC}/2,-y,\bar{t}_{rUC}/2) \\ u_3(-x+h_{rUC}/2,-y,\bar{t}_{rUC}/2) \end{bmatrix} + \begin{bmatrix} u_1(x,y,-\bar{t}_{rUC}/2) \\ u_2(x,y,-\bar{t}_{rUC}/2) \\ -u_3(x,y,-\bar{t}_{rUC}/2) \end{bmatrix} = \begin{bmatrix} h_{rUC}(\varepsilon_1^{\psi}\cos(\psi)^2 + \varepsilon_2^{\psi}(1-\cos(\psi)^2) - \varepsilon_{12}^{\psi}\sin(2\psi))/2 \\ h_{rUC}((\varepsilon_1^{\psi}\sin(2\psi))/2 - (\varepsilon_2^{\psi}\sin(2\psi))/2 + \varepsilon_{12}^{\psi}\cos(2\psi))/2 \\ \varepsilon_3\bar{t}_{rUC} \end{bmatrix}$$

B5I-B6II
$$\begin{bmatrix} u_1(x,y,\bar{t}_{rUC}/2) \\ u_2(x,y,\bar{t}_{rUC}/2) \\ u_3(x,y,\bar{t}_{rUC}/2) \end{bmatrix} - \begin{bmatrix} u_1(x,y,-\bar{t}_{rUC}/2) \\ u_2(x,y,-\bar{t}_{rUC}/2) \\ -u_3(x,y,-\bar{t}_{rUC}/2) \end{bmatrix} = \begin{bmatrix} 0 \\ 0 \\ 0 \end{bmatrix}$$

B5II-B6I
$$\begin{bmatrix} u_1(x,y,\bar{t}_{rUC}/2) \\ u_2(x,y,\bar{t}_{rUC}/2) \\ u_3(x,y,\bar{t}_{rUC}/2) \end{bmatrix} - \begin{bmatrix} u_1(x,y,-\bar{t}_{rUC}/2) \\ u_2(x,y,-\bar{t}_{rUC}/2) \\ -u_3(x,y,-\bar{t}_{rUC}/2) \end{bmatrix} = \begin{bmatrix} 0 \\ 0 \\ 0 \end{bmatrix}$$

Face 5 to Face 6 South to North $u(x,y,z) = u(x,0,\pm\bar{t}_{rUC}/2)$

B5I
$$\begin{bmatrix} u_1(-x+h_{rUC}/2,0,\bar{t}_{rUC}/2) \\ u_2(-x+h_{rUC}/2,0,\bar{t}_{rUC}/2) \\ u_3(-x+h_{rUC}/2,0,\bar{t}_{rUC}/2) \end{bmatrix} + \begin{bmatrix} u_1(x,0,\bar{t}_{rUC}/2) \\ u_2(x,0,\bar{t}_{rUC}/2) \\ u_3(x,0,\bar{t}_{rUC}/2) \end{bmatrix} = \begin{bmatrix} h_{rUC}(\varepsilon_1^{\psi}\cos(\psi)^2 + \varepsilon_2^{\psi}(1-\cos(\psi)^2) - \varepsilon_{12}^{\psi}\sin(2\psi))/2 \\ h_{rUC}((\varepsilon_1^{\psi}\sin(2\psi))/2 - (\varepsilon_2^{\psi}\sin(2\psi))/2 + \varepsilon_{12}^{\psi}\cos(2\psi))/2 \\ \varepsilon_3\bar{t}_{rUC} \end{bmatrix}$$

B5II
$$\begin{bmatrix} u_1(-x-h_{rUC}/2,0,\bar{t}_{rUC}/2) \\ u_2(-x-h_{rUC}/2,0,\bar{t}_{rUC}/2) \\ u_3(-x-h_{rUC}/2,0,\bar{t}_{rUC}/2) \end{bmatrix} + \begin{bmatrix} u_1(x,0,\bar{t}_{rUC}/2) \\ u_2(x,0,\bar{t}_{rUC}/2) \\ u_3(x,0,\bar{t}_{rUC}/2) \end{bmatrix} = \begin{bmatrix} -h_{rUC}(\varepsilon_1^{\psi}\cos(\psi)^2 + \varepsilon_2^{\psi}(1-\cos(\psi)^2) - \varepsilon_{12}^{\psi}\sin(2\psi))/2 \\ -h_{rUC}((\varepsilon_1^{\psi}\sin(2\psi))/2 - (\varepsilon_2^{\psi}\sin(2\psi))/2 + \varepsilon_{12}^{\psi}\cos(2\psi))/2 \\ \varepsilon_3\bar{t}_{rUC} \end{bmatrix}$$

B6I
$$\begin{bmatrix} u_1(-x-h_{rUC}/2,0,\bar{t}_{rUC}/2) \\ u_2(-x-h_{rUC}/2,0,\bar{t}_{rUC}/2) \\ u_3(-x-h_{rUC}/2,,\bar{t}_{rUC}/2) \end{bmatrix} + \begin{bmatrix} u_1(x,0,-\bar{t}_{rUC}/2) \\ u_2(x,0,-\bar{t}_{rUC}/2) \\ -u_3(x,0,-\bar{t}_{rUC}/2) \end{bmatrix} = \begin{bmatrix} -h_{rUC}(\varepsilon_1^{\psi}\cos(\psi)^2 + \varepsilon_2^{\psi}(1-\cos(\psi)^2) - \varepsilon_{12}^{\psi}\sin(2\psi))/2 \\ -h_{rUC}((\varepsilon_1^{\psi}\sin(2\psi))/2 - (\varepsilon_2^{\psi}\sin(2\psi))/2 + \varepsilon_{12}^{\psi}\cos(2\psi))/2 \\ \varepsilon_3\bar{t}_{rUC} \end{bmatrix}$$

Face 5 to Face 6 South to North $u(x,y,z) = u(x,0,\pm\overline{t}_{rUC}/2)$

B6II
$$\begin{bmatrix} u_1(-x+h_{rUC}/2,0,\overline{t}_{rUC}/2) \\ u_2(-x+h_{rUC}/2,0,\overline{t}_{rUC}/2) \\ u_3(-x+h_{rUC}/2,0,\overline{t}_{rUC}/2) \end{bmatrix} + \begin{bmatrix} u_1(x,0,-\overline{t}_{rUC}/2) \\ u_2(x,0,-\overline{t}_{rUC}/2) \\ -u_3(x,0,-\overline{t}_{rUC}/2) \end{bmatrix} = \begin{bmatrix} h_{rUC}(\varepsilon_1^{\psi}\cos(\psi)^2 + \varepsilon_2^{\psi}(1-\cos(\psi)^2) - \varepsilon_{12}^{\psi}\sin(2\psi))/2 \\ h_{rUC}((\varepsilon_1^{\psi}\sin(2\psi))/2 - (\varepsilon_2^{\psi}\sin(2\psi))/2 + \varepsilon_{12}^{\psi}\cos(2\psi))/2 \\ \varepsilon_3\overline{t}_{rUC} \end{bmatrix}$$

B5I-B6II
$$\begin{bmatrix} u_1(x,0,\overline{t}_{rUC}/2) \\ u_2(x,0,\overline{t}_{rUC}/2) \\ u_3(x,0,\overline{t}_{rUC}/2) \end{bmatrix} - \begin{bmatrix} u_1(x,0,-\overline{t}_{rUC}/2) \\ u_2(x,0,-\overline{t}_{rUC}/2) \\ -u_3(x,0,-\overline{t}_{rUC}/2) \end{bmatrix} = \begin{bmatrix} 0 \\ 0 \\ 0 \end{bmatrix}$$

B5II-B6I
$$\begin{bmatrix} u_1(x,0,\overline{t}_{rUC}/2) \\ u_2(x,0,\overline{t}_{rUC}/2) \\ u_3(x,0,\overline{t}_{rUC}/2) \end{bmatrix} - \begin{bmatrix} u_1(x,0,-\overline{t}_{rUC}/2) \\ u_2(x,0,-\overline{t}_{rUC}/2) \\ -u_3(x,0,-\overline{t}_{rUC}/2) \end{bmatrix} = \begin{bmatrix} 0 \\ 0 \\ 0 \end{bmatrix}$$

Face 5 to Face 6 West to East $u(x,y,z) = u(0,y,\pm\overline{t}_{rUC}/2)$

B5I
$$\begin{bmatrix} u_1(h_{rUC}/2,-y,\overline{t}_{rUC}/2) \\ u_2(h_{rUC}/2,-y,\overline{t}_{rUC}/2) \\ u_3(h_{rUC}/2,-y,\overline{t}_{rUC}/2) \end{bmatrix} + \begin{bmatrix} u_1(0,y,\overline{t}_{rUC}/2) \\ u_2(0,y,\overline{t}_{rUC}/2) \\ u_3(0,y,\overline{t}_{rUC}/2) \end{bmatrix} = \begin{bmatrix} h_{rUC}(\varepsilon_1^{\psi}\cos(\psi)^2 + \varepsilon_2^{\psi}(1-\cos(\psi)^2) - \varepsilon_{12}^{\psi}\sin(2\psi))/2 \\ h_{rUC}((\varepsilon_1^{\psi}\sin(2\psi))/2 - (\varepsilon_2^{\psi}\sin(2\psi))/2 + \varepsilon_{12}^{\psi}\cos(2\psi))/2 \\ \varepsilon_3\overline{t}_{rUC} \end{bmatrix}$$

B5II
$$\begin{bmatrix} u_1(-h_{rUC}/2,-y,\overline{t}_{rUC}/2) \\ u_2(-h_{rUC}/2,-y,\overline{t}_{rUC}/2) \\ u_3(-h_{rUC}/2,-y,\overline{t}_{rUC}/2) \end{bmatrix} + \begin{bmatrix} u_1(0,y,\overline{t}_{rUC}/2) \\ u_2(0,y,\overline{t}_{rUC}/2) \\ u_3(0,y,\overline{t}_{rUC}/2) \end{bmatrix} = \begin{bmatrix} -h_{rUC}(\varepsilon_1^{\psi}\cos(\psi)^2 + \varepsilon_2^{\psi}(1-\cos(\psi)^2) - \varepsilon_{12}^{\psi}\sin(2\psi))/2 \\ -h_{rUC}((\varepsilon_1^{\psi}\sin(2\psi))/2 - (\varepsilon_2^{\psi}\sin(2\psi))/2 + \varepsilon_{12}^{\psi}\cos(2\psi))/2 \\ \varepsilon_3\overline{t}_{rUC} \end{bmatrix}$$

B6I
$$\begin{bmatrix} u_1(-h_{rUC}/2,-y,\overline{t}_{rUC}/2) \\ u_2(-h_{rUC}/2,-y,\overline{t}_{rUC}/2) \\ u_3(-h_{rUC}/2,-y,\overline{t}_{rUC}/2) \end{bmatrix} + \begin{bmatrix} u_1(0,y,-\overline{t}_{rUC}/2) \\ u_2(0,y,-\overline{t}_{rUC}/2) \\ -u_3(0,y,-\overline{t}_{rUC}/2) \end{bmatrix} = \begin{bmatrix} -h_{rUC}(\varepsilon_1^{\psi}\cos(\psi)^2 + \varepsilon_2^{\psi}(1-\cos(\psi)^2) - \varepsilon_{12}^{\psi}\sin(2\psi))/2 \\ -h_{rUC}((\varepsilon_1^{\psi}\sin(2\psi))/2 - (\varepsilon_2^{\psi}\sin(2\psi))/2 + \varepsilon_{12}^{\psi}\cos(2\psi))/2 \\ \varepsilon_3\overline{t}_{rUC} \end{bmatrix}$$

B6II
$$\begin{bmatrix} u_1(+h_{rUC}/2,-y,\overline{t}_{rUC}/2) \\ u_2(+h_{rUC}/2,-y,\overline{t}_{rUC}/2) \\ u_3(+h_{rUC}/2,-y,\overline{t}_{rUC}/2) \end{bmatrix} + \begin{bmatrix} u_1(0,y,-\overline{t}_{rUC}/2) \\ u_2(0,y,-\overline{t}_{rUC}/2) \\ -u_3(0,y,-\overline{t}_{rUC}/2) \end{bmatrix} = \begin{bmatrix} h_{rUC}(\varepsilon_1^{\psi}\cos(\psi)^2 + \varepsilon_2^{\psi}(1-\cos(\psi)^2) - \varepsilon_{12}^{\psi}\sin(2\psi))/2 \\ h_{rUC}((\varepsilon_1^{\psi}\sin(2\psi))/2 - (\varepsilon_2^{\psi}\sin(2\psi))/2 + \varepsilon_{12}^{\psi}\cos(2\psi))/2 \\ \varepsilon_3\overline{t}_{rUC} \end{bmatrix}$$

Face 5 to Face 6 West to East $u(x,y,z) = u(0,y,\pm\bar{t}_{rUC}/2)$

B5I-B6II	$\begin{bmatrix} u_1(0,y,\bar{t}_{rUC}/2) \\ u_2(0,y,\bar{t}_{rUC}/2) \\ u_3(0,y,\bar{t}_{rUC}/2) \end{bmatrix}$	$-$	$\begin{bmatrix} u_1(0,y,-\bar{t}_{rUC}/2) \\ u_2(0,y,-\bar{t}_{rUC}/2) \\ -u_3(0,y,-\bar{t}_{rUC}/2) \end{bmatrix}$	$=$	$\begin{bmatrix} 0 \\ 0 \\ 0 \end{bmatrix}$
B5II-B6I	$\begin{bmatrix} u_1(0,y,\bar{t}_{rUC}/2) \\ u_2(0,y,\bar{t}_{rUC}/2) \\ u_3(0,y,\bar{t}_{rUC}/2) \end{bmatrix}$	$-$	$\begin{bmatrix} u_1(0,y,-\bar{t}_{rUC}/2) \\ u_2(0,y,-\bar{t}_{rUC}/2) \\ -u_3(0,y,-\bar{t}_{rUC}/2) \end{bmatrix}$	$=$	$\begin{bmatrix} 0 \\ 0 \\ 0 \end{bmatrix}$

A.2.2.4 Combined in-plane and out-of-plane edges for nesting case I

Edge 1 Upper = B 1 ∩ B 5, $u(x,y,z) = u(-h_{rUC}/2,y,\bar{t}_{rUC}/2)$

B1	$\begin{bmatrix} u_1(h_{rUC}/2,y,\bar{t}_{rUC}/2) \\ u_2(h_{rUC}/2,y,\bar{t}_{rUC}/2) \\ u_3(h_{rUC}/2,y,\bar{t}_{rUC}/2) \end{bmatrix}$	$-$	$\begin{bmatrix} u_1(-h_{rUC}/2,y,\bar{t}_{rUC}/2) \\ u_2(-h_{rUC}/2,y,\bar{t}_{rUC}/2) \\ u_3(-h_{rUC}/2,y,\bar{t}_{rUC}/2) \end{bmatrix}$	$=$	$\begin{bmatrix} h_{rUC}(\varepsilon_1^\psi \cos(\psi)^2 + \varepsilon_2^\psi(1-\cos(\psi)^2) - \varepsilon_{12}^\psi \sin(2\psi)) \\ h_{rUC}(\varepsilon_1^\psi \sin(2\psi)/2 - \varepsilon_2^\psi \sin(2\psi)/2 + \varepsilon_{12}^\psi \cos(2\psi)) \\ 0 \end{bmatrix}$
B5	$\begin{bmatrix} u_1(h_{rUC}/2,-y,\bar{t}_{rUC}/2) \\ u_2(h_{rUC}/2,-y,\bar{t}_{rUC}/2) \\ u_3(h_{rUC}/2,-y,\bar{t}_{rUC}/2) \end{bmatrix}$	$+$	$\begin{bmatrix} u_1(-h_{rUC}/2,y,\bar{t}_{rUC}/2) \\ u_2(-h_{rUC}/2,y,\bar{t}_{rUC}/2) \\ u_3(-h_{rUC}/2,y,\bar{t}_{rUC}/2) \end{bmatrix}$	$=$	$\begin{bmatrix} 0 \\ 0 \\ \varepsilon_3 \cdot \bar{t}_{rUC} \end{bmatrix}$
B1+B5	$\begin{bmatrix} u_1(h_{rUC}/2,y,\bar{t}_{rUC}/2) \\ u_2(h_{rUC}/2,y,\bar{t}_{rUC}/2) \\ u_3(h_{rUC}/2,y,\bar{t}_{rUC}/2) \end{bmatrix}$	$+$	$\begin{bmatrix} u_1(h_{rUC}/2,-y,\bar{t}_{rUC}/2) \\ u_2(h_{rUC}/2,-y,\bar{t}_{rUC}/2) \\ u_3(h_{rUC}/2,-y,\bar{t}_{rUC}/2) \end{bmatrix}$	$=$	$\begin{bmatrix} h_{rUC}(\varepsilon_1^\psi \cos(\psi)^2 + \varepsilon_2^\psi(1-\cos(\psi)^2) - \varepsilon_{12}^\psi \sin(2\psi)) \\ h_{rUC}(\varepsilon_1^\psi \sin(2\psi)/2 - \varepsilon_2^\psi \sin(2\psi)/2 + \varepsilon_{12}^\psi \cos(2\psi)) \\ \varepsilon_3 \cdot \bar{t}_{rUC} \end{bmatrix}$

Edge 3 Upper = B 3 ∩ B 5, $u(x,y,z) = u(h_{rUC}/2,y,\bar{t}_{rUC}/2)$

B3	$\begin{bmatrix} u_1(-h_{rUC}/2,y,\bar{t}_{rUC}/2) \\ u_2(-h_{rUC}/2,y,\bar{t}_{rUC}/2) \\ u_3(-h_{rUC}/2,y,\bar{t}_{rUC}/2) \end{bmatrix}$	$-$	$\begin{bmatrix} u_1(h_{rUC}/2,y,\bar{t}_{rUC}/2) \\ u_2(h_{rUC}/2,y,\bar{t}_{rUC}/2) \\ u_3(h_{rUC}/2,y,\bar{t}_{rUC}/2) \end{bmatrix}$	$=$	$\begin{bmatrix} -h_{rUC}(\varepsilon_1^\psi \cos(\psi)^2 + \varepsilon_2^\psi(1-\cos(\psi)^2) - \varepsilon_{12}^\psi \sin(2\psi)) \\ -h_{rUC}(\varepsilon_1^\psi \sin(2\psi)/2 - \varepsilon_2^\psi \sin(2\psi)/2 + \varepsilon_{12}^\psi \cos(2\psi)) \\ 0 \end{bmatrix}$

Edge 3 Upper = B 3 ∩ B 5, $u(x,y,z) = u(h_{rUC}/2, y, \bar{t}_{rUC}/2)$

B5
$$\begin{bmatrix} u_1(-h_{rUC}/2,-y,\bar{t}_{rUC}/2) \\ u_2(-h_{rUC}/2,-y,\bar{t}_{rUC}/2) \\ u_3(-h_{rUC}/2,-y,\bar{t}_{rUC}/2) \end{bmatrix} + \begin{bmatrix} u_1(h_{rUC}/2,y,\bar{t}_{rUC}/2) \\ u_2(h_{rUC}/2,y,\bar{t}_{rUC}/2) \\ u_3(h_{rUC}/2,y,\bar{t}_{rUC}/2) \end{bmatrix} = \begin{bmatrix} 0 \\ 0 \\ \varepsilon_3 \cdot \bar{t}_{rUC} \end{bmatrix}$$

B3+B5
$$\begin{bmatrix} u_1(-h_{rUC}/2,y,\bar{t}_{rUC}/2) \\ u_2(-h_{rUC}/2,y,\bar{t}_{rUC}/2) \\ u_3(-h_{rUC}/2,y,\bar{t}_{rUC}/2) \end{bmatrix} + \begin{bmatrix} u_1(-h_{rUC}/2,-y,\bar{t}_{rUC}/2) \\ u_2(-h_{rUC}/2,-y,\bar{t}_{rUC}/2) \\ u_3(-h_{rUC}/2,-y,\bar{t}_{rUC}/2) \end{bmatrix} = \begin{bmatrix} -h_{rUC}(\varepsilon_1^\psi \cos(\psi)^2 + \varepsilon_2^\psi(1-\cos(\psi)^2) - \varepsilon_{12}^\psi \sin(2\psi)) \\ -h_{rUC}(\varepsilon_1^\psi \sin(2\psi)/2 - \varepsilon_2^\psi \sin(2\psi)/2 + \varepsilon_{12}^\psi \cos(2\psi)) \\ \varepsilon_3 \cdot \bar{t}_{rUC} \end{bmatrix}$$

Edge 1 Lower = B 1 ∩ B 6, $u(x,y,z) = u(-h_{rUC}/2, y, -\bar{t}_{rUC}/2)$

B1
$$\begin{bmatrix} u_1(h_{rUC}/2,y,-\bar{t}_{rUC}/2) \\ u_2(h_{rUC}/2,y,-\bar{t}_{rUC}/2) \\ u_3(h_{rUC}/2,y,-\bar{t}_{rUC}/2) \end{bmatrix} - \begin{bmatrix} u_1(-h_{rUC}/2,y,-\bar{t}_{rUC}/2) \\ u_2(-h_{rUC}/2,y,-\bar{t}_{rUC}/2) \\ u_3(-h_{rUC}/2,y,-\bar{t}_{rUC}/2) \end{bmatrix} = \begin{bmatrix} h_{rUC}(\varepsilon_1^\psi \cos(\psi)^2 + \varepsilon_2^\psi(1-\cos(\psi)^2) - \varepsilon_{12}^\psi \sin(2\psi)) \\ h_{rUC}(\varepsilon_1^\psi \sin(2\psi)/2 - \varepsilon_2^\psi \sin(2\psi)/2 + \varepsilon_{12}^\psi \cos(2\psi)) \\ 0 \end{bmatrix}$$

B6
$$\begin{bmatrix} u_1(-h_{rUC}/2,y,-\bar{t}_{rUC}/2) \\ u_2(-h_{rUC}/2,y,-\bar{t}_{rUC}/2) \\ -u_3(-h_{rUC}/2,y,-\bar{t}_{rUC}/2) \end{bmatrix} + \begin{bmatrix} u_1(h_{rUC}/2,-y,\bar{t}_{rUC}/2) \\ u_2(h_{rUC}/2,-y,\bar{t}_{rUC}/2) \\ u_3(h_{rUC}/2,-y,\bar{t}_{rUC}/2) \end{bmatrix} = \begin{bmatrix} 0 \\ 0 \\ \varepsilon_3 \cdot \bar{t}_{rUC} \end{bmatrix}$$

B1-B6
$$\begin{bmatrix} u_1(h_{rUC}/2,y,-\bar{t}_{rUC}/2) \\ u_2(h_{rUC}/2,y,-\bar{t}_{rUC}/2) \\ u_3(h_{rUC}/2,y,-\bar{t}_{rUC}/2) \end{bmatrix} - \begin{bmatrix} 2\cdot u_1(-h_{rUC}/2,y,-\bar{t}_{rUC}/2) \\ 2\cdot u_2(-h_{rUC}/2,y,-\bar{t}_{rUC}/2) \\ 0 \end{bmatrix} - \begin{bmatrix} u_1(h_{rUC}/2,-y,\bar{t}_{rUC}/2) \\ u_2(h_{rUC}/2,-y,\bar{t}_{rUC}/2) \\ u_3(h_{rUC}/2,-y,\bar{t}_{rUC}/2) \end{bmatrix} = \begin{bmatrix} h_{rUC}(\varepsilon_1^\psi \cos(\psi)^2 + \varepsilon_2^\psi(1-\cos(\psi)^2) - \varepsilon_{12}^\psi \sin(2\psi)) \\ h_{rUC}(\varepsilon_1^\psi \sin(2\psi)/2 - \varepsilon_2^\psi \sin(2\psi)/2 + \varepsilon_{12}^\psi \cos(2\psi)) \\ -\varepsilon_3 \cdot \bar{t}_{rUC} \end{bmatrix}$$

B1+B6
$$\begin{bmatrix} u_1(h_{rUC}/2,y,-\bar{t}_{rUC}/2) \\ u_2(h_{rUC}/2,y,-\bar{t}_{rUC}/2) \\ u_3(h_{rUC}/2,y,-\bar{t}_{rUC}/2) \end{bmatrix} - \begin{bmatrix} 0 \\ 0 \\ 2\cdot u_3(-h_{rUC}/2,y,-\bar{t}_{rUC}/2) \end{bmatrix} + \begin{bmatrix} u_1(h_{rUC}/2,-y,\bar{t}_{rUC}/2) \\ u_2(h_{rUC}/2,-y,\bar{t}_{rUC}/2) \\ u_3(h_{rUC}/2,-y,\bar{t}_{rUC}/2) \end{bmatrix} = \begin{bmatrix} h_{rUC}(\varepsilon_1^\psi \cos(\psi)^2 + \varepsilon_2^\psi(1-\cos(\psi)^2) - \varepsilon_{12}^\psi \sin(2\psi)) \\ h_{rUC}(\varepsilon_1^\psi \sin(2\psi)/2 - \varepsilon_2^\psi \sin(2\psi)/2 + \varepsilon_{12}^\psi \cos(2\psi)) \\ \varepsilon_3 \cdot \bar{t}_{rUC} \end{bmatrix}$$

B5-B6
$$- \begin{bmatrix} u_1(-h_{rUC}/2,y,-\bar{t}_{rUC}/2) \\ u_2(-h_{rUC}/2,y,-\bar{t}_{rUC}/2) \\ -u_3(-h_{rUC}/2,y,-\bar{t}_{rUC}/2) \end{bmatrix} + \begin{bmatrix} u_1(-h_{rUC}/2,y,\bar{t}_{rUC}/2) \\ u_2(-h_{rUC}/2,y,\bar{t}_{rUC}/2) \\ u_3(-h_{rUC}/2,y,\bar{t}_{rUC}/2) \end{bmatrix} = \begin{bmatrix} 0 \\ 0 \\ 0 \end{bmatrix}$$

Edge 1 Lower = B 1 ∩ B 6, $u(x,y,z) = u(-h_{rUC}/2, y, -\bar{t}_{rUC}/2)$

B5-B6+B1

$$\begin{bmatrix} u_1(-h_{rUC}/2, y, \bar{t}_{rUC}/2) \\ u_2(-h_{rUC}/2, y, \bar{t}_{rUC}/2) \\ u_3(-h_{rUC}/2, y, \bar{t}_{rUC}/2) \end{bmatrix} - \begin{bmatrix} -2 \cdot u_1(h_{rUC}/2, y, -\bar{t}_{rUC}/2) \\ -2 \cdot u_2(h_{rUC}/2, y, -\bar{t}_{rUC}/2) \\ 0 \end{bmatrix} + \begin{bmatrix} u_1(h_{rUC}/2, y, -\bar{t}_{rUC}/2) \\ u_2(h_{rUC}/2, y, -\bar{t}_{rUC}/2) \\ u_3(h_{rUC}/2, y, -\bar{t}_{rUC}/2) \end{bmatrix} = \begin{bmatrix} h_{rUC}(\varepsilon_1^{\psi} \cos(\psi)^2 + \varepsilon_2^{\psi}(1-\cos(\psi)^2) - \varepsilon_{12}^{\psi} \sin(2\psi)) \\ h_{rUC}(\varepsilon_1^{\psi} \sin(2\psi)/2 - \varepsilon_2^{\psi} \sin(2\psi)/2 + \varepsilon_{12}^{\psi} \cos(2\psi)) \\ 0 \end{bmatrix}$$

B5-B6-B1

$$\begin{bmatrix} u_1(-h_{rUC}/2, y, \bar{t}_{rUC}/2) \\ u_2(-h_{rUC}/2, y, \bar{t}_{rUC}/2) \\ u_3(-h_{rUC}/2, y, \bar{t}_{rUC}/2) \end{bmatrix} - \begin{bmatrix} 0 \\ 0 \\ -2 \cdot u_3(h_{rUC}/2, y, -\bar{t}_{rUC}/2) \end{bmatrix} - \begin{bmatrix} u_1(h_{rUC}/2, y, -\bar{t}_{rUC}/2) \\ u_2(h_{rUC}/2, y, -\bar{t}_{rUC}/2) \\ u_3(h_{rUC}/2, y, -\bar{t}_{rUC}/2) \end{bmatrix} = \begin{bmatrix} -h_{rUC}(\varepsilon_1^{\psi} \cos(\psi)^2 + \varepsilon_2^{\psi}(1-\cos(\psi)^2) - \varepsilon_{12}^{\psi} \sin(2\psi)) \\ -h_{rUC}(\varepsilon_1^{\psi} \sin(2\psi)/2 - \varepsilon_2^{\psi} \sin(2\psi)/2 + \varepsilon_{12}^{\psi} \cos(2\psi)) \\ 0 \end{bmatrix}$$

Edge 3 Lower = B 3 ∩ B 6, $u(x,y,z) = u(h_{rUC}/2, y, -\bar{t}_{rUC}/2)$

B3

$$\begin{bmatrix} u_1(-h_{rUC}/2, y, -\bar{t}_{rUC}/2) \\ u_2(-h_{rUC}/2, y, -\bar{t}_{rUC}/2) \\ u_3(-h_{rUC}/2, y, -\bar{t}_{rUC}/2) \end{bmatrix} - \begin{bmatrix} u_1(h_{rUC}/2, y, -\bar{t}_{rUC}/2) \\ u_2(h_{rUC}/2, y, -\bar{t}_{rUC}/2) \\ u_3(h_{rUC}/2, y, -\bar{t}_{rUC}/2) \end{bmatrix} = \begin{bmatrix} -h_{rUC}(\varepsilon_1^{\psi} \cos(\psi)^2 + \varepsilon_2^{\psi}(1-\cos(\psi)^2) - \varepsilon_{12}^{\psi} \sin(2\psi)) \\ -h_{rUC}(\varepsilon_1^{\psi} \sin(2\psi)/2 - \varepsilon_2^{\psi} \sin(2\psi)/2 + \varepsilon_{12}^{\psi} \cos(2\psi)) \\ 0 \end{bmatrix}$$

B6

$$\begin{bmatrix} u_1(-h_{rUC}/2, -y, \bar{t}_{rUC}/2) \\ u_2(-h_{rUC}/2, -y, \bar{t}_{rUC}/2) \\ u_3(-h_{rUC}/2, -y, \bar{t}_{rUC}/2) \end{bmatrix} + \begin{bmatrix} u_1(h_{rUC}/2, y, -\bar{t}_{rUC}/2) \\ u_2(h_{rUC}/2, y, -\bar{t}_{rUC}/2) \\ -u_3(h_{rUC}/2, y, -\bar{t}_{rUC}/2) \end{bmatrix} = \begin{bmatrix} 0 \\ 0 \\ \varepsilon_3 \cdot \bar{t}_{rUC} \end{bmatrix}$$

B3-B6

$$\begin{bmatrix} u_1(-h_{rUC}/2, y, -\bar{t}_{rUC}/2) \\ u_2(-h_{rUC}/2, y, -\bar{t}_{rUC}/2) \\ u_3(-h_{rUC}/2, y, -\bar{t}_{rUC}/2) \end{bmatrix} - \begin{bmatrix} u_1(-h_{rUC}/2, -y, \bar{t}_{rUC}/2) \\ u_2(-h_{rUC}/2, -y, \bar{t}_{rUC}/2) \\ u_3(-h_{rUC}/2, -y, \bar{t}_{rUC}/2) \end{bmatrix} - \begin{bmatrix} 2 \cdot u_1(h_{rUC}/2, y, -\bar{t}_{rUC}/2) \\ 2 \cdot u_2(h_{rUC}/2, y, -\bar{t}_{rUC}/2) \\ 0 \end{bmatrix} = \begin{bmatrix} -h_{rUC}(\varepsilon_1^{\psi} \cos(\psi)^2 + \varepsilon_2^{\psi}(1-\cos(\psi)^2) - \varepsilon_{12}^{\psi} \sin(2\psi)) \\ -h_{rUC}(\varepsilon_1^{\psi} \sin(2\psi)/2 - \varepsilon_2^{\psi} \sin(2\psi)/2 + \varepsilon_{12}^{\psi} \cos(2\psi)) \\ -\varepsilon_3 \cdot \bar{t}_{rUC} \end{bmatrix}$$

B3+B6

$$\begin{bmatrix} u_1(-h_{rUC}/2, y, -\bar{t}_{rUC}/2) \\ u_2(-h_{rUC}/2, y, -\bar{t}_{rUC}/2) \\ u_3(-h_{rUC}/2, y, -\bar{t}_{rUC}/2) \end{bmatrix} + \begin{bmatrix} u_1(-h_{rUC}/2, -y, \bar{t}_{rUC}/2) \\ u_2(-h_{rUC}/2, -y, \bar{t}_{rUC}/2) \\ u_3(-h_{rUC}/2, -y, \bar{t}_{rUC}/2) \end{bmatrix} - \begin{bmatrix} 0 \\ 0 \\ 2 \cdot u_3(h_{rUC}/2, y, -\bar{t}_{rUC}/2) \end{bmatrix} = \begin{bmatrix} -h_{rUC}(\varepsilon_1^{\psi} \cos(\psi)^2 + \varepsilon_2^{\psi}(1-\cos(\psi)^2) - \varepsilon_{12}^{\psi} \sin(2\psi)) \\ -h_{rUC}(\varepsilon_1^{\psi} \sin(2\psi)/2 - \varepsilon_2^{\psi} \sin(2\psi)/2 + \varepsilon_{12}^{\psi} \cos(2\psi)) \\ \varepsilon_3 \cdot \bar{t}_{rUC} \end{bmatrix}$$

Edge 1 Upper Center = B 1 ∩ B 5, $u(x,y,z) = u(-h_{rUC}/2, 0, \bar{t}_{rUC}/2)$

B1

$$\begin{bmatrix} u_1(h_{rUC}/2, 0, \bar{t}_{rUC}/2) \\ u_2(h_{rUC}/2, 0, \bar{t}_{rUC}/2) \\ u_3(h_{rUC}/2, 0, \bar{t}_{rUC}/2) \end{bmatrix} - \begin{bmatrix} u_1(-h_{rUC}/2, 0, \bar{t}_{rUC}/2) \\ u_2(-h_{rUC}/2, 0, \bar{t}_{rUC}/2) \\ u_3(-h_{rUC}/2, 0, \bar{t}_{rUC}/2) \end{bmatrix} = \begin{bmatrix} h_{rUC}(\varepsilon_1^{\psi} \cos(\psi)^2 + \varepsilon_2^{\psi}(1-\cos(\psi)^2) - \varepsilon_{12}^{\psi} \sin(2\psi)) \\ h_{rUC}(\varepsilon_1^{\psi} \sin(2\psi)/2 - \varepsilon_2^{\psi} \sin(2\psi)/2 + \varepsilon_{12}^{\psi} \cos(2\psi)) \\ 0 \end{bmatrix}$$

Edge 1 Upper Center = B 1 ∩ B 5, $u(x,y,z) = u(-h_{rUC}/2, 0, \overline{t}_{rUC}/2)$

B5
$$\begin{bmatrix} u_1(h_{rUC}/2,0,\overline{t}_{rUC}/2) \\ u_2(h_{rUC}/2,0,\overline{t}_{rUC}/2) \\ u_3(h_{rUC}/2,0,\overline{t}_{rUC}/2) \end{bmatrix} + \begin{bmatrix} u_1(-h_{rUC}/2,0,\overline{t}_{rUC}/2) \\ u_2(-h_{rUC}/2,0,\overline{t}_{rUC}/2) \\ u_3(-h_{rUC}/2,0,\overline{t}_{rUC}/2) \end{bmatrix} = \begin{bmatrix} 0 \\ 0 \\ \varepsilon_3 \cdot \overline{t}_{rUC} \end{bmatrix}$$

B1-B5
$$\begin{bmatrix} -2 \cdot u_1(-h_{rUC}/2,0,\overline{t}_{rUC}/2) \\ -2 \cdot u_2(-h_{rUC}/2,0,\overline{t}_{rUC}/2) \\ -2 \cdot u_3(-h_{rUC}/2,0,\overline{t}_{rUC}/2) \end{bmatrix} = \begin{bmatrix} h_{rUC}(\varepsilon_1^{\psi}\cos(\psi)^2 + \varepsilon_2^{\psi}(1-\cos(\psi)^2) - \varepsilon_{12}^{\psi}\sin(2\psi)) \\ h_{rUC}(\varepsilon_1^{\psi}\sin(2\psi)/2 - \varepsilon_2^{\psi}\sin(2\psi)/2 + \varepsilon_{12}^{\psi}\cos(2\psi)) \\ -\varepsilon_3 \cdot \overline{t}_{rUC} \end{bmatrix}$$

B1+B5
$$\begin{bmatrix} 2 \cdot u_1(h_{rUC}/2,0,\overline{t}_{rUC}/2) \\ 2 \cdot u_2(h_{rUC}/2,0,\overline{t}_{rUC}/2) \\ 2 \cdot u_3(h_{rUC}/2,0,\overline{t}_{rUC}/2) \end{bmatrix} = \begin{bmatrix} h_{rUC}(\varepsilon_1^{\psi}\cos(\psi)^2 + \varepsilon_2^{\psi}(1-\cos(\psi)^2) - \varepsilon_{12}^{\psi}\sin(2\psi)) \\ h_{rUC}(\varepsilon_1^{\psi}\sin(2\psi)/2 - \varepsilon_2^{\psi}\sin(2\psi)/2 + \varepsilon_{12}^{\psi}\cos(2\psi)) \\ \varepsilon_3 \cdot \overline{t}_{rUC} \end{bmatrix}$$

Edge 1 Lower Center = B 1 ∩ B 6, $u(x,y,z) = u(-h_{rUC}/2, 0, -\overline{t}_{rUC}/2)$

B1
$$\begin{bmatrix} u_1(h_{rUC}/2,0,-\overline{t}_{rUC}/2) \\ u_2(h_{rUC}/2,0,-\overline{t}_{rUC}/2) \\ u_3(h_{rUC}/2,0,-\overline{t}_{rUC}/2) \end{bmatrix} - \begin{bmatrix} u_1(-h_{rUC}/2,0,-\overline{t}_{rUC}/2) \\ u_2(-h_{rUC}/2,0,-\overline{t}_{rUC}/2) \\ u_3(-h_{rUC}/2,0,-\overline{t}_{rUC}/2) \end{bmatrix} = \begin{bmatrix} h_{rUC}(\varepsilon_1^{\psi}\cos(\psi)^2 + \varepsilon_2^{\psi}(1-\cos(\psi)^2) - \varepsilon_{12}^{\psi}\sin(2\psi)) \\ h_{rUC}(\varepsilon_1^{\psi}\sin(2\psi)/2 - \varepsilon_2^{\psi}\sin(2\psi)/2 + \varepsilon_{12}^{\psi}\cos(2\psi)) \\ 0 \end{bmatrix}$$

B6
$$\begin{bmatrix} u_1(h_{rUC}/2,0,\overline{t}_{rUC}/2) \\ u_2(h_{rUC}/2,0,\overline{t}_{rUC}/2) \\ u_3(h_{rUC}/2,0,\overline{t}_{rUC}/2) \end{bmatrix} + \begin{bmatrix} u_1(-h_{rUC}/2,0,-\overline{t}_{rUC}/2) \\ u_2(-h_{rUC}/2,0,-\overline{t}_{rUC}/2) \\ -u_3(-h_{rUC}/2,0,-\overline{t}_{rUC}/2) \end{bmatrix} = \begin{bmatrix} 0 \\ 0 \\ \varepsilon_3 \cdot \overline{t}_{rUC} \end{bmatrix}$$

B5-B6
$$\begin{bmatrix} u_1(-h_{rUC}/2,0,\overline{t}_{rUC}/2) \\ u_2(-h_{rUC}/2,0,\overline{t}_{rUC}/2) \\ u_3(-h_{rUC}/2,0,\overline{t}_{rUC}/2) \end{bmatrix} - \begin{bmatrix} u_1(-h_{rUC}/2,0,-\overline{t}_{rUC}/2) \\ u_2(-h_{rUC}/2,0,-\overline{t}_{rUC}/2) \\ -u_3(-h_{rUC}/2,0,-\overline{t}_{rUC}/2) \end{bmatrix} = \begin{bmatrix} 0 \\ 0 \\ 0 \end{bmatrix}$$

Edge 2 Upper = B 2 ∩ B 5, $u(x,y,z) = u(x, -w_{rUC}/2, \overline{t}_{rUC}/2)$

B2
$$\begin{bmatrix} u_1(-x,-w_{rUC}/2,\overline{t}_{rUC}/2) \\ u_2(-x,-w_{rUC}/2,\overline{t}_{rUC}/2) \\ u_3(-x,-w_{rUC}/2,\overline{t}_{rUC}/2) \end{bmatrix} - \begin{bmatrix} -u_1(x,-w_{rUC}/2,\overline{t}_{rUC}/2) \\ -u_2(x,-w_{rUC}/2,\overline{t}_{rUC}/2) \\ u_3(x,-w_{rUC}/2,\overline{t}_{rUC}/2) \end{bmatrix} = \begin{bmatrix} -w_{rUC}(\varepsilon_1^{\psi}\sin(2\psi)/2 - \varepsilon_2^{\psi}\sin(2\psi)/2 + \varepsilon_{12}^{\psi}\cos(2\psi)) \\ -w_{rUC}(\varepsilon_1^{\psi}(1-\cos(\psi)^2) + \varepsilon_2^{\psi}\cos(\psi)^2 + \varepsilon_{12}^{\psi}\sin(2\psi)) \\ 0 \end{bmatrix}$$

Edge 2 Upper = B 2 ∩ B 5, $u(x,y,z) = u(x,-w_{rUC}/2,\overline{t}_{rUC}/2)$

B5				$\begin{bmatrix} u_1(-x,w_{rUC}/2,\overline{t}_{rUC}/2) \\ u_2(-x,w_{rUC}/2,\overline{t}_{rUC}/2) \\ u_3(-x,w_{rUC}/2,\overline{t}_{rUC}/2) \end{bmatrix}$	$+$	$\begin{bmatrix} u_1(x,-w_{rUC}/2,\overline{t}_{rUC}/2) \\ u_2(x,-w_{rUC}/2,\overline{t}_{rUC}/2) \\ u_3(x,-w_{rUC}/2,\overline{t}_{rUC}/2) \end{bmatrix}$	$=$	$\begin{bmatrix} 0 \\ 0 \\ \varepsilon_3 \cdot \overline{t}_{rUC} \end{bmatrix}$
B2-B5	$\begin{bmatrix} u_1(-x,-w_{rUC}/2,\overline{t}_{rUC}/2) \\ u_2(-x,-w_{rUC}/2,\overline{t}_{rUC}/2) \\ u_3(-x,-w_{rUC}/2,\overline{t}_{rUC}/2) \end{bmatrix}$	$-$	$\begin{bmatrix} u_1(-x,w_{rUC}/2,\overline{t}_{rUC}/2) \\ u_2(-x,w_{rUC}/2,\overline{t}_{rUC}/2) \\ u_3(-x,w_{rUC}/2,\overline{t}_{rUC}/2) \end{bmatrix}$	$-$	$\begin{bmatrix} 0 \\ 0 \\ 2 \cdot u_3(x,-w_{rUC}/2,\overline{t}_{rUC}/2) \end{bmatrix}$	$=$	$\begin{bmatrix} -w_{rUC}(\varepsilon_1^{\psi}\sin(2\psi)/2 - \varepsilon_2^{\psi}\sin(2\psi)/2 + \varepsilon_{12}^{\psi}\cos(2\psi)) \\ -w_{rUC}(\varepsilon_1^{\psi}(1-\cos(\psi)^2) + \varepsilon_2^{\psi}\cos(\psi)^2 + \varepsilon_{12}^{\psi}\sin(2\psi)) \\ -\varepsilon_3 \cdot \overline{t}_{rUC} \end{bmatrix}$
B2+B5	$\begin{bmatrix} u_1(-x,-w_{rUC}/2,\overline{t}_{rUC}/2) \\ u_2(-x,-w_{rUC}/2,\overline{t}_{rUC}/2) \\ u_3(-x,-w_{rUC}/2,\overline{t}_{rUC}/2) \end{bmatrix}$	$+$	$\begin{bmatrix} u_1(-x,w_{rUC}/2,\overline{t}_{rUC}/2) \\ u_2(-x,w_{rUC}/2,\overline{t}_{rUC}/2) \\ u_3(-x,w_{rUC}/2,\overline{t}_{rUC}/2) \end{bmatrix}$	$+$	$\begin{bmatrix} 2 \cdot u_1(x,-w_{rUC}/2,\overline{t}_{rUC}/2) \\ 2 \cdot u_2(x,-w_{rUC}/2,\overline{t}_{rUC}/2) \\ 0 \end{bmatrix}$	$=$	$\begin{bmatrix} -w_{rUC}(\varepsilon_1^{\psi}\sin(2\psi)/2 - \varepsilon_2^{\psi}\sin(2\psi)/2 + \varepsilon_{12}^{\psi}\cos(2\psi)) \\ -w_{rUC}(\varepsilon_1^{\psi}(1-\cos(\psi)^2) + \varepsilon_2^{\psi}\cos(\psi)^2 + \varepsilon_{12}^{\psi}\sin(2\psi)) \\ +\varepsilon_3 \cdot \overline{t}_{rUC} \end{bmatrix}$
B2±B5	$\begin{bmatrix} u_1(-x,-w_{rUC}/2,\overline{t}_{rUC}/2) \\ u_2(-x,-w_{rUC}/2,\overline{t}_{rUC}/2) \\ u_3(-x,-w_{rUC}/2,\overline{t}_{rUC}/2) \end{bmatrix}$				$-$	$\begin{bmatrix} u_1(-x,w_{rUC}/2,\overline{t}_{rUC}/2) \\ u_2(-x,w_{rUC}/2,\overline{t}_{rUC}/2) \\ -u_3(-x,w_{rUC}/2,\overline{t}_{rUC}/2) \end{bmatrix}$	$=$	$\begin{bmatrix} -w_{rUC}(\varepsilon_1^{\psi}\sin(2\psi)/2 - \varepsilon_2^{\psi}\sin(2\psi)/2 + \varepsilon_{12}^{\psi}\cos(2\psi)) \\ -w_{rUC}(\varepsilon_1^{\psi}(1-\cos(\psi)^2) + \varepsilon_2^{\psi}\cos(\psi)^2 + \varepsilon_{12}^{\psi}\sin(2\psi)) \\ \varepsilon_3 \cdot \overline{t}_{rUC} \end{bmatrix}$
B6				$\begin{bmatrix} u_1(-x,w_{rUC}/2,\overline{t}_{rUC}/2) \\ u_2(-x,w_{rUC}/2,\overline{t}_{rUC}/2) \\ u_3(-x,w_{rUC}/2,\overline{t}_{rUC}/2) \end{bmatrix}$	$+$	$\begin{bmatrix} u_1(x,-w_{rUC}/2,-\overline{t}_{rUC}/2) \\ u_2(x,-w_{rUC}/2,-\overline{t}_{rUC}/2) \\ -u_3(x,-w_{rUC}/2,-\overline{t}_{rUC}/2) \end{bmatrix}$	$=$	$\begin{bmatrix} 0 \\ 0 \\ \varepsilon_3 \cdot \overline{t}_{rUC} \end{bmatrix}$
(B2±B5)±B6	$\begin{bmatrix} u_1(-x,-w_{rUC}/2,\overline{t}_{rUC}/2) \\ u_2(-x,-w_{rUC}/2,\overline{t}_{rUC}/2) \\ u_3(-x,-w_{rUC}/2,\overline{t}_{rUC}/2) \end{bmatrix}$				$+$	$\begin{bmatrix} u_1(x,-w_{rUC}/2,-\overline{t}_{rUC}/2) \\ u_2(x,-w_{rUC}/2,-\overline{t}_{rUC}/2) \\ u_3(x,-w_{rUC}/2,-\overline{t}_{rUC}/2) \end{bmatrix}$	$=$	$\begin{bmatrix} -w_{rUC}(\varepsilon_1^{\psi}\sin(2\psi)/2 - \varepsilon_2^{\psi}\sin(2\psi)/2 + \varepsilon_{12}^{\psi}\cos(2\psi)) \\ -w_{rUC}(\varepsilon_1^{\psi}(1-\cos(\psi)^2) + \varepsilon_2^{\psi}\cos(\psi)^2 + \varepsilon_{12}^{\psi}\sin(2\psi)) \\ -\varepsilon_3 \cdot \overline{t}_{rUC} \end{bmatrix}$
B5-B6			$-$	$\begin{bmatrix} u_1(x,-w_{rUC}/2,-\overline{t}_{rUC}/2) \\ u_2(x,-w_{rUC}/2,-\overline{t}_{rUC}/2) \\ -u_3(x,-w_{rUC}/2,-\overline{t}_{rUC}/2) \end{bmatrix}$	$+$	$\begin{bmatrix} u_1(x,-w_{rUC}/2,\overline{t}_{rUC}/2) \\ u_2(x,-w_{rUC}/2,\overline{t}_{rUC}/2) \\ u_3(x,-w_{rUC}/2,\overline{t}_{rUC}/2) \end{bmatrix}$	$=$	$\begin{bmatrix} 0 \\ 0 \\ 0 \end{bmatrix}$

Edge 2 Lower = B 2 ∩ B 6, $u(x,y,z) = u(x,-w_{rUC}/2,-\overline{t}_{rUC}/2)$

Edge 2 Lower = B 2 ∩ B 6, $u(x,y,z) = u(x,-w_{rUC}/2,-\overline{t}_{rUC}/2)$

B2
$$\begin{bmatrix} u_1(-x,-w_{rUC}/2,-\overline{t}_{rUC}/2) \\ u_2(-x,-w_{rUC}/2,-\overline{t}_{rUC}/2) \\ u_3(-x,-w_{rUC}/2,-\overline{t}_{rUC}/2) \end{bmatrix} - \begin{bmatrix} -u_1(x,-w_{rUC}/2,-\overline{t}_{rUC}/2) \\ -u_2(x,-w_{rUC}/2,-\overline{t}_{rUC}/2) \\ u_3(x,-w_{rUC}/2,-\overline{t}_{rUC}/2) \end{bmatrix} = \begin{bmatrix} -w_{rUC}(\varepsilon_1^{\psi}\sin(2\psi)/2 - \varepsilon_2^{\psi}\sin(2\psi)/2 + \varepsilon_{12}^{\psi}\cos(2\psi)) \\ -w_{rUC}(\varepsilon_1^{\psi}(1-\cos(\psi)^2) + \varepsilon_2^{\psi}\cos(\psi)^2 + \varepsilon_{12}^{\psi}\sin(2\psi)) \\ 0 \end{bmatrix}$$

B6
$$\begin{bmatrix} u_1(-x,w_{rUC}/2,\overline{t}_{rUC}/2) \\ u_2(-x,w_{rUC}/2,\overline{t}_{rUC}/2) \\ u_3(-x,w_{rUC}/2,\overline{t}_{rUC}/2) \end{bmatrix} + \begin{bmatrix} u_1(x,-w_{rUC}/2,-\overline{t}_{rUC}/2) \\ u_2(x,-w_{rUC}/2,-\overline{t}_{rUC}/2) \\ -u_3(x,-w_{rUC}/2,-\overline{t}_{rUC}/2) \end{bmatrix} = \begin{bmatrix} 0 \\ 0 \\ \varepsilon_3 \cdot \overline{t}_{rUC} \end{bmatrix}$$

B2-B6
$$\begin{bmatrix} u_1(-x,-w_{rUC}/2,-\overline{t}_{rUC}/2) \\ u_2(-x,-w_{rUC}/2,-\overline{t}_{rUC}/2) \\ u_3(-x,-w_{rUC}/2,-\overline{t}_{rUC}/2) \end{bmatrix} - \begin{bmatrix} u_1(-x,w_{rUC}/2,\overline{t}_{rUC}/2) \\ u_2(-x,w_{rUC}/2,\overline{t}_{rUC}/2) \\ u_3(-x,w_{rUC}/2,\overline{t}_{rUC}/2) \end{bmatrix} = \begin{bmatrix} -w_{rUC}(\varepsilon_1^{\psi}\sin(2\psi)/2 - \varepsilon_2^{\psi}\sin(2\psi)/2 + \varepsilon_{12}^{\psi}\cos(2\psi)) \\ -w_{rUC}(\varepsilon_1^{\psi}(1-\cos(\psi)^2) + \varepsilon_2^{\psi}\cos(\psi)^2 + \varepsilon_{12}^{\psi}\sin(2\psi)) \\ -\varepsilon_3 \cdot \overline{t}_{rUC} \end{bmatrix}$$

Edge 4 Upper = B 4 ∩ B 5, $u(x,y,z) = u(x,w_{rUC}/2,\overline{t}_{rUC}/2)$

B4
$$\begin{bmatrix} u_1(-x,w_{rUC}/2,-\overline{t}_{rUC}/2) \\ u_2(-x,w_{rUC}/2,-\overline{t}_{rUC}/2) \\ u_3(-x,w_{rUC}/2,-\overline{t}_{rUC}/2) \end{bmatrix} + \begin{bmatrix} u_1(x,w_{rUC}/2,\overline{t}_{rUC}/2) \\ u_2(x,w_{rUC}/2,\overline{t}_{rUC}/2) \\ u_3(x,w_{rUC}/2,\overline{t}_{rUC}/2) \end{bmatrix} = \begin{bmatrix} w_{rUC}(\varepsilon_1^{\psi}\sin(2\psi)/2 - \varepsilon_2^{\psi}\sin(2\psi)/2 + \varepsilon_{12}^{\psi}\cos(2\psi)) \\ w_{rUC}(\varepsilon_1^{\psi}(1-\cos(\psi)^2) + \varepsilon_2^{\psi}\cos(\psi)^2 + \varepsilon_{12}^{\psi}\sin(2\psi)) \\ 0 \end{bmatrix}$$

B5
$$\begin{bmatrix} u_1(-x,-w_{rUC}/2,\overline{t}_{rUC}/2) \\ u_2(-x,-w_{rUC}/2,\overline{t}_{rUC}/2) \\ u_3(-x,-w_{rUC}/2,\overline{t}_{rUC}/2) \end{bmatrix} + \begin{bmatrix} u_1(x,w_{rUC}/2,\overline{t}_{rUC}/2) \\ u_2(x,w_{rUC}/2,\overline{t}_{rUC}/2) \\ u_3(x,w_{rUC}/2,\overline{t}_{rUC}/2) \end{bmatrix} = \begin{bmatrix} 0 \\ 0 \\ \varepsilon_3 \cdot \overline{t}_{rUC} \end{bmatrix}$$

B4-B5
$$\begin{bmatrix} u_1(-x,w_{rUC}/2,-\overline{t}_{rUC}/2) \\ u_2(-x,w_{rUC}/2,-\overline{t}_{rUC}/2) \\ u_3(-x,w_{rUC}/2,-\overline{t}_{rUC}/2) \end{bmatrix} - \begin{bmatrix} u_1(-x,-w_{rUC}/2,\overline{t}_{rUC}/2) \\ u_2(-x,-w_{rUC}/2,\overline{t}_{rUC}/2) \\ u_3(-x,-w_{rUC}/2,\overline{t}_{rUC}/2) \end{bmatrix} = \begin{bmatrix} w_{rUC}(\varepsilon_1^{\psi}\sin(2\psi)/2 - \varepsilon_2^{\psi}\sin(2\psi)/2 + \varepsilon_{12}^{\psi}\cos(2\psi)) \\ w_{rUC}(\varepsilon_1^{\psi}(1-\cos(\psi)^2) + \varepsilon_2^{\psi}\cos(\psi)^2 + \varepsilon_{12}^{\psi}\sin(2\psi)) \\ -\varepsilon_3 \cdot \overline{t}_{rUC} \end{bmatrix}$$

Edge 4 Lower = B 4 ∩ B 6, $u(x,y,z) = u(x,w_{rUC}/2,-\overline{t}_{rUC}/2)$

B4
$$\begin{bmatrix} u_1(-x,w_{rUC}/2,\overline{t}_{rUC}/2) \\ u_2(-x,w_{rUC}/2,\overline{t}_{rUC}/2) \\ u_3(-x,w_{rUC}/2,\overline{t}_{rUC}/2) \end{bmatrix} + \begin{bmatrix} u_1(x,w_{rUC}/2,-\overline{t}_{rUC}/2) \\ u_2(x,w_{rUC}/2,-\overline{t}_{rUC}/2) \\ u_3(x,w_{rUC}/2,-\overline{t}_{rUC}/2) \end{bmatrix} = \begin{bmatrix} w_{rUC}(\varepsilon_1^{\psi}\sin(2\psi)/2 - \varepsilon_2^{\psi}\sin(2\psi)/2 + \varepsilon_{12}^{\psi}\cos(2\psi)) \\ w_{rUC}(\varepsilon_1^{\psi}(1-\cos(\psi)^2) + \varepsilon_2^{\psi}\cos(\psi)^2 + \varepsilon_{12}^{\psi}\sin(2\psi)) \\ 0 \end{bmatrix}$$

Edge 4 Lower = B 4 ∩ B 6, $u(x,y,z) = u(x, w_{rUC}/2, -\bar{t}_{rUC}/2)$

$$\text{B6} \qquad \begin{bmatrix} u_1(x, w_{rUC}/2, -\bar{t}_{rUC}/2) \\ u_2(x, w_{rUC}/2, -\bar{t}_{rUC}/2) \\ -u_3(x, w_{rUC}/2, -\bar{t}_{rUC}/2) \end{bmatrix} + \begin{bmatrix} u_1(-x, -w_{rUC}/2, \bar{t}_{rUC}/2) \\ u_2(-x, -w_{rUC}/2, \bar{t}_{rUC}/2) \\ u_3(-x, -w_{rUC}/2, \bar{t}_{rUC}/2) \end{bmatrix} = \begin{bmatrix} 0 \\ 0 \\ \varepsilon_3 \cdot \bar{t}_{rUC} \end{bmatrix}$$

$$\text{B4-B6} \qquad \begin{bmatrix} u_1(-x, w_{rUC}/2, \bar{t}_{rUC}/2) \\ u_2(-x, w_{rUC}/2, \bar{t}_{rUC}/2) \\ u_3(-x, w_{rUC}/2, \bar{t}_{rUC}/2) \end{bmatrix} + \begin{bmatrix} 0 \\ 0 \\ 2 \cdot u_3(x, w_{rUC}/2, -\bar{t}_{rUC}/2) \end{bmatrix} - \begin{bmatrix} u_1(-x, -w_{rUC}/2, \bar{t}_{rUC}/2) \\ u_2(-x, -w_{rUC}/2, \bar{t}_{rUC}/2) \\ u_3(-x, -w_{rUC}/2, \bar{t}_{rUC}/2) \end{bmatrix} = \begin{bmatrix} w_{rUC}(\varepsilon_1^{\psi} \sin(2\psi)/2 - \varepsilon_2^{\psi} \sin(2\psi)/2 + \varepsilon_{12}^{\psi} \cos(2\psi)) \\ w_{rUC}(\varepsilon_1^{\psi}(1-\cos(\psi)^2) + \varepsilon_2^{\psi} \cos(\psi)^2 + \varepsilon_{12}^{\psi} \sin(2\psi)) \\ -\varepsilon_3 \cdot \bar{t}_{rUC} \end{bmatrix}$$

$$\text{B4+B6} \qquad \begin{bmatrix} u_1(-x, w_{rUC}/2, \bar{t}_{rUC}/2) \\ u_2(-x, w_{rUC}/2, \bar{t}_{rUC}/2) \\ u_3(-x, w_{rUC}/2, \bar{t}_{rUC}/2) \end{bmatrix} + \begin{bmatrix} 2 \cdot u_1(x, w_{rUC}/2, -\bar{t}_{rUC}/2) \\ 2 \cdot u_2(x, w_{rUC}/2, -\bar{t}_{rUC}/2) \\ 0 \end{bmatrix} + \begin{bmatrix} u_1(-x, -w_{rUC}/2, \bar{t}_{rUC}/2) \\ u_2(-x, -w_{rUC}/2, \bar{t}_{rUC}/2) \\ u_3(-x, -w_{rUC}/2, \bar{t}_{rUC}/2) \end{bmatrix} = \begin{bmatrix} w_{rUC}(\varepsilon_1^{\psi} \sin(2\psi)/2 - \varepsilon_2^{\psi} \sin(2\psi)/2 + \varepsilon_{12}^{\psi} \cos(2\psi)) \\ w_{rUC}(\varepsilon_1^{\psi}(1-\cos(\psi)^2) + \varepsilon_2^{\psi} \cos(\psi)^2 + \varepsilon_{12}^{\psi} \sin(2\psi)) \\ \varepsilon_3 \cdot \bar{t}_{rUC} \end{bmatrix}$$

Edge 2 Upper Center = B 2 ∩ B 5, $u(x,y,z) = u(0, -w_{rUC}/2, \bar{t}_{rUC}/2)$

$$\text{B2} \qquad \begin{bmatrix} 2 \cdot u_1(0, -w_{rUC}/2, \bar{t}_{rUC}/2) \\ 2 \cdot u_2(0, -w_{rUC}/2, \bar{t}_{rUC}/2) \\ 0 \end{bmatrix} = \begin{bmatrix} -w_{rUC}(\varepsilon_1^{\psi} \sin(2\psi)/2 - \varepsilon_2^{\psi} \sin(2\psi)/2 + \varepsilon_{12}^{\psi} \cos(2\psi)) \\ -w_{rUC}(\varepsilon_1^{\psi}(1-\cos(\psi)^2) + \varepsilon_2^{\psi} \cos(\psi)^2 + \varepsilon_{12}^{\psi} \sin(2\psi)) \\ 0 \end{bmatrix}$$

$$\text{B5} \qquad \begin{bmatrix} u_1(0, -w_{rUC}/2, \bar{t}_{rUC}/2) \\ u_2(0, -w_{rUC}/2, \bar{t}_{rUC}/2) \\ u_3(0, -w_{rUC}/2, \bar{t}_{rUC}/2) \end{bmatrix} + \begin{bmatrix} u_1(0, w_{rUC}/2, \bar{t}_{rUC}/2) \\ u_2(0, w_{rUC}/2, \bar{t}_{rUC}/2) \\ u_3(0, w_{rUC}/2, \bar{t}_{rUC}/2) \end{bmatrix} = \begin{bmatrix} 0 \\ 0 \\ \varepsilon_3 \cdot \bar{t}_{rUC} \end{bmatrix}$$

$$\text{B2±B5} \qquad \begin{bmatrix} u_1(0, -w_{rUC}/2, \bar{t}_{rUC}/2) \\ u_2(0, -w_{rUC}/2, \bar{t}_{rUC}/2) \\ u_3(0, -w_{rUC}/2, \bar{t}_{rUC}/2) \end{bmatrix} - \begin{bmatrix} u_1(0, w_{rUC}/2, \bar{t}_{rUC}/2) \\ u_2(0, w_{rUC}/2, \bar{t}_{rUC}/2) \\ -u_3(0, w_{rUC}/2, \bar{t}_{rUC}/2) \end{bmatrix} = \begin{bmatrix} -w_{rUC}(\varepsilon_1^{\psi} \sin(2\psi)/2 - \varepsilon_2^{\psi} \sin(2\psi)/2 + \varepsilon_{12}^{\psi} \cos(2\psi)) \\ -w_{rUC}(\varepsilon_1^{\psi}(1-\cos(\psi)^2) + \varepsilon_2^{\psi} \cos(\psi)^2 + \varepsilon_{12}^{\psi} \sin(2\psi)) \\ \varepsilon_3 \cdot \bar{t}_{rUC} \end{bmatrix}$$

Edge 2 Lower Center = B 4 ∩ B 5, $u(x,y,z) = u(0, w_{rUC}/2, -\bar{t}_{rUC}/2)$

$$\text{B2} \qquad \begin{bmatrix} 2 \cdot u_1(0, -w_{rUC}/2, -\bar{t}_{rUC}/2) \\ 2 \cdot u_2(0, -w_{rUC}/2, -\bar{t}_{rUC}/2) \\ 0 \end{bmatrix} = \begin{bmatrix} -w_{rUC}(\varepsilon_1^{\psi} \sin(2\psi)/2 - \varepsilon_2^{\psi} \sin(2\psi)/2 + \varepsilon_{12}^{\psi} \cos(2\psi)) \\ -w_{rUC}(\varepsilon_1^{\psi}(1-\cos(\psi)^2) + \varepsilon_2^{\psi} \cos(\psi)^2 + \varepsilon_{12}^{\psi} \sin(2\psi)) \\ 0 \end{bmatrix}$$

Edge 2 Lower Center = B 4 ∩ B 5, $u(x,y,z) = u(0, w_{rUC}/2, -\overline{t}_{rUC}/2)$

B6
$$\begin{bmatrix} u_1(0,-w_{rUC}/2,-\overline{t}_{rUC}/2) \\ u_2(0,-w_{rUC}/2,-\overline{t}_{rUC}/2) \\ -u_3(0,-w_{rUC}/2,-\overline{t}_{rUC}/2) \end{bmatrix} + \begin{bmatrix} u_1(0,w_{rUC}/2,\overline{t}_{rUC}/2) \\ u_2(0,w_{rUC}/2,\overline{t}_{rUC}/2) \\ u_3(0,w_{rUC}/2,\overline{t}_{rUC}/2) \end{bmatrix} = \begin{bmatrix} 0 \\ 0 \\ \varepsilon_3 \cdot \overline{t}_{rUC} \end{bmatrix}$$

B2-B6
$$\begin{bmatrix} u_1(0,-w_{rUC}/2,-\overline{t}_{rUC}/2) \\ u_2(0,-w_{rUC}/2,-\overline{t}_{rUC}/2) \\ u_3(0,-w_{rUC}/2,-\overline{t}_{rUC}/2) \end{bmatrix} - \begin{bmatrix} u_1(0,w_{rUC}/2,\overline{t}_{rUC}/2) \\ u_2(0,w_{rUC}/2,\overline{t}_{rUC}/2) \\ u_3(0,w_{rUC}/2,\overline{t}_{rUC}/2) \end{bmatrix} = \begin{bmatrix} -w_{rUC}(\varepsilon_1^{\psi}\sin(2\psi)/2 - \varepsilon_2^{\psi}\sin(2\psi)/2 + \varepsilon_{12}^{\psi}\cos(2\psi)) \\ -w_{rUC}(\varepsilon_1^{\psi}(1-\cos(\psi)^2) + \varepsilon_2^{\psi}\cos(\psi)^2 + \varepsilon_{12}^{\psi}\sin(2\psi)) \\ -\varepsilon_3 \cdot \overline{t}_{rUC} \end{bmatrix}$$

Edge 4 Upper Center = B 4 ∩ B 5, $u(x,y,z) = u(0, w_{rUC}/2, \overline{t}_{rUC}/2)$

B4
$$\begin{bmatrix} u_1(0,w_{rUC}/2,-\overline{t}_{rUC}/2) \\ u_2(0,w_{rUC}/2,-\overline{t}_{rUC}/2) \\ u_3(0,w_{rUC}/2,-\overline{t}_{rUC}/2) \end{bmatrix} + \begin{bmatrix} u_1(0,w_{rUC}/2,\overline{t}_{rUC}/2) \\ u_2(0,w_{rUC}/2,\overline{t}_{rUC}/2) \\ u_3(0,w_{rUC}/2,\overline{t}_{rUC}/2) \end{bmatrix} = \begin{bmatrix} w_{rUC}(\varepsilon_1^{\psi}\sin(2\psi)/2 - \varepsilon_2^{\psi}\sin(2\psi)/2 + \varepsilon_{12}^{\psi}\cos(2\psi)) \\ w_{rUC}(\varepsilon_1^{\psi}(1-\cos(\psi)^2) + \varepsilon_2^{\psi}\cos(\psi)^2 + \varepsilon_{12}^{\psi}\sin(2\psi)) \\ 0 \end{bmatrix}$$

B5
$$\begin{bmatrix} u_1(0,-w_{rUC}/2,\overline{t}_{rUC}/2) \\ u_2(0,-w_{rUC}/2,\overline{t}_{rUC}/2) \\ u_3(0,-w_{rUC}/2,\overline{t}_{rUC}/2) \end{bmatrix} + \begin{bmatrix} u_1(0,w_{rUC}/2,\overline{t}_{rUC}/2) \\ u_2(0,w_{rUC}/2,\overline{t}_{rUC}/2) \\ u_3(x,w_{rUC}/2,\overline{t}_{rUC}/2) \end{bmatrix} = \begin{bmatrix} 0 \\ 0 \\ \varepsilon_3 \cdot \overline{t}_{rUC} \end{bmatrix}$$

B4-B5
$$\begin{bmatrix} u_1(0,w_{rUC}/2,-\overline{t}_{rUC}/2) \\ u_2(0,w_{rUC}/2,-\overline{t}_{rUC}/2) \\ u_3(0,w_{rUC}/2,-\overline{t}_{rUC}/2) \end{bmatrix} - \begin{bmatrix} u_1(0,-w_{rUC}/2,\overline{t}_{rUC}/2) \\ u_2(0,-w_{rUC}/2,\overline{t}_{rUC}/2) \\ u_3(0,-w_{rUC}/2,\overline{t}_{rUC}/2) \end{bmatrix} = \begin{bmatrix} w_{rUC}(\varepsilon_1^{\psi}\sin(2\psi)/2 - \varepsilon_2^{\psi}\sin(2\psi)/2 + \varepsilon_{12}^{\psi}\cos(2\psi)) \\ w_{rUC}(\varepsilon_1^{\psi}(1-\cos(\psi)^2) + \varepsilon_2^{\psi}\cos(\psi)^2 + \varepsilon_{12}^{\psi}\sin(2\psi)) \\ -\varepsilon_3 \cdot \overline{t}_{rUC} \end{bmatrix}$$

Edge 4 Lower Center = B 4 ∩ B 6, $u(x,y,z) = u(0, w_{rUC}/2, -\overline{t}_{rUC}/2)$

B4
$$\begin{bmatrix} u_1(0,w_{rUC}/2,\overline{t}_{rUC}/2) \\ u_2(0,w_{rUC}/2,\overline{t}_{rUC}/2) \\ u_3(0,w_{rUC}/2,\overline{t}_{rUC}/2) \end{bmatrix} + \begin{bmatrix} u_1(0,w_{rUC}/2,-\overline{t}_{rUC}/2) \\ u_2(0,w_{rUC}/2,-\overline{t}_{rUC}/2) \\ u_3(0,w_{rUC}/2,-\overline{t}_{rUC}/2) \end{bmatrix} = \begin{bmatrix} w_{rUC}(\varepsilon_1^{\psi}\sin(2\psi)/2 - \varepsilon_2^{\psi}\sin(2\psi)/2 + \varepsilon_{12}^{\psi}\cos(2\psi)) \\ w_{rUC}(\varepsilon_1^{\psi}(1-\cos(\psi)^2) + \varepsilon_2^{\psi}\cos(\psi)^2 + \varepsilon_{12}^{\psi}\sin(2\psi)) \\ 0 \end{bmatrix}$$

B6
$$\begin{bmatrix} u_1(0,-w_{rUC}/2,\overline{t}_{rUC}/2) \\ u_2(0,-w_{rUC}/2,\overline{t}_{rUC}/2) \\ u_3(0,-w_{rUC}/2,\overline{t}_{rUC}/2) \end{bmatrix} + \begin{bmatrix} u_1(0,w_{rUC}/2,-\overline{t}_{rUC}/2) \\ u_2(0,w_{rUC}/2,-\overline{t}_{rUC}/2) \\ -u_3(0,w_{rUC}/2,-\overline{t}_{rUC}/2) \end{bmatrix} = \begin{bmatrix} 0 \\ 0 \\ \varepsilon_3 \cdot \overline{t}_{rUC} \end{bmatrix}$$

Edge 4 Lower Center = B 4 ∩ B 6, $u(x,y,z) = u(0, w_{rUC}/2, -\bar{t}_{rUC}/2)$

B4-B6

$$\begin{bmatrix} u_1(0, w_{rUC}/2, \bar{t}_{rUC}/2) \\ u_2(0, w_{rUC}/2, \bar{t}_{rUC}/2) \\ u_3(0, w_{rUC}/2, \bar{t}_{rUC}/2) \end{bmatrix} - \begin{bmatrix} u_1(0, -w_{rUC}/2, \bar{t}_{rUC}/2) \\ u_2(0, -w_{rUC}/2, \bar{t}_{rUC}/2) \\ u_3(0, -w_{rUC}/2, \bar{t}_{rUC}/2) \end{bmatrix} + \begin{bmatrix} 0 \\ 0 \\ 2 \cdot u_3(0, w_{rUC}/2, -\bar{t}_{rUC}/2) \end{bmatrix} = \begin{bmatrix} w_{rUC}(\varepsilon_1^{\psi} \sin(2\psi)/2 - \varepsilon_2^{\psi} \sin(2\psi)/2 + \varepsilon_{12}^{\psi} \cos(2\psi)) \\ w_{rUC}(\varepsilon_1^{\psi}(1 - \cos(\psi)^2) + \varepsilon_2^{\psi} \cos(\psi)^2 + \varepsilon_{12}^{\psi} \sin(2\psi)) \\ -\varepsilon_3 \cdot \bar{t}_{rUC} \end{bmatrix}$$

B4+B6

$$\begin{bmatrix} u_1(0, w_{rUC}/2, \bar{t}_{rUC}/2) \\ u_2(0, w_{rUC}/2, \bar{t}_{rUC}/2) \\ u_3(0, w_{rUC}/2, \bar{t}_{rUC}/2) \end{bmatrix} + \begin{bmatrix} u_1(0, -w_{rUC}/2, \bar{t}_{rUC}/2) \\ u_2(0, -w_{rUC}/2, \bar{t}_{rUC}/2) \\ u_3(0, -w_{rUC}/2, \bar{t}_{rUC}/2) \end{bmatrix} + \begin{bmatrix} 2 \cdot u_1(0, w_{rUC}/2, -\bar{t}_{rUC}/2) \\ 2 \cdot u_2(x, w_{rUC}/2, -\bar{t}_{rUC}/2) \\ 0 \end{bmatrix} = \begin{bmatrix} w_{rUC}(\varepsilon_1^{\psi} \sin(2\psi)/2 - \varepsilon_2^{\psi} \sin(2\psi)/2 + \varepsilon_{12}^{\psi} \cos(2\psi)) \\ w_{rUC}(\varepsilon_1^{\psi}(1 - \cos(\psi)^2) + \varepsilon_2^{\psi} \cos(\psi)^2 + \varepsilon_{12}^{\psi} \sin(2\psi)) \\ \varepsilon_3 \cdot \bar{t}_{rUC} \end{bmatrix}$$

A.2.2.5 Combined in-plane and out-of-plane edges for nesting case II

Edge 1 Upper = B1 ∩ B5II, $u(x,y,z) = u(-h_{rUC}/2, y, \bar{t}_{rUC}/2)$

B1

$$\begin{bmatrix} u_1(h_{rUC}/2, y, \bar{t}_{rUC}/2) \\ u_2(h_{rUC}/2, y, \bar{t}_{rUC}/2) \\ u_3(h_{rUC}/2, y, \bar{t}_{rUC}/2) \end{bmatrix} - \begin{bmatrix} u_1(-h_{rUC}/2, y, \bar{t}_{rUC}/2) \\ u_2(-h_{rUC}/2, y, \bar{t}_{rUC}/2) \\ u_3(-h_{rUC}/2, y, \bar{t}_{rUC}/2) \end{bmatrix} = \begin{bmatrix} h_{rUC}(\varepsilon_1^\psi \cos(\psi)^2 + \varepsilon_2^\psi (1-\cos(\psi)^2) - \varepsilon_{12}^\psi \sin(2\psi)) \\ h_{rUC}(\varepsilon_1^\psi \sin(2\psi)/2 - \varepsilon_2^\psi \sin(2\psi)/2 + \varepsilon_{12}^\psi \cos(2\psi)) \\ 0 \end{bmatrix}$$

B5II

$$\begin{bmatrix} u_1(0, -y, \bar{t}_{rUC}/2) \\ u_2(0, -y, \bar{t}_{rUC}/2) \\ u_3(0, -y, \bar{t}_{rUC}/2) \end{bmatrix} + \begin{bmatrix} u_1(-h_{rUC}/2, y, \bar{t}_{rUC}/2) \\ u_2(-h_{rUC}/2, y, \bar{t}_{rUC}/2) \\ u_3(-h_{rUC}/2, y, \bar{t}_{rUC}/2) \end{bmatrix} = \begin{bmatrix} -h_{rUC}(\varepsilon_1^\psi \cos(\psi)^2 + \varepsilon_2^\psi (1-\cos(\psi)^2) - \varepsilon_{12}^\psi \sin(2\psi))/2 \\ -h_{rUC}((\varepsilon_1^\psi \sin(2\psi))/2 - (\varepsilon_2^\psi \sin(2\psi))/2 + \varepsilon_{12}^\psi \cos(2\psi))/2 \\ \varepsilon_3 \bar{t}_{rUC} \end{bmatrix}$$

B1+B5II

$$\begin{bmatrix} u_1(h_{rUC}/2, y, \bar{t}_{rUC}/2) \\ u_2(h_{rUC}/2, y, \bar{t}_{rUC}/2) \\ u_3(h_{rUC}/2, y, \bar{t}_{rUC}/2) \end{bmatrix} + \begin{bmatrix} u_1(0, -y, \bar{t}_{rUC}/2) \\ u_2(0, -y, \bar{t}_{rUC}/2) \\ u_3(0, -y, \bar{t}_{rUC}/2) \end{bmatrix} = \begin{bmatrix} h_{rUC}(\varepsilon_1^\psi \cos(\psi)^2 + \varepsilon_2^\psi (1-\cos(\psi)^2) - \varepsilon_{12}^\psi \sin(2\psi))/2 \\ h_{rUC}((\varepsilon_1^\psi \sin(2\psi))/2 - (\varepsilon_2^\psi \sin(2\psi))/2 + \varepsilon_{12}^\psi \cos(2\psi))/2 \\ \varepsilon_3 \bar{t}_{rUC} \end{bmatrix}$$

B5II-B6I

$$\begin{bmatrix} u_1(h_{rUC}/2, y, \bar{t}_{rUC}/2) \\ u_2(h_{rUC}/2, y, \bar{t}_{rUC}/2) \\ u_3(h_{rUC}/2, y, \bar{t}_{rUC}/2) \end{bmatrix} - \begin{bmatrix} u_1(h_{rUC}/2, y, -\bar{t}_{rUC}/2) \\ u_2(h_{rUC}/2, y, -\bar{t}_{rUC}/2) \\ -u_3(h_{rUC}/2, y, -\bar{t}_{rUC}/2) \end{bmatrix} = \begin{bmatrix} 0 \\ 0 \\ 0 \end{bmatrix}$$

(B5II-B6I)-B1

$$- \begin{bmatrix} u_1(h_{rUC}/2, y, -\bar{t}_{rUC}/2) \\ u_2(h_{rUC}/2, y, -\bar{t}_{rUC}/2) \\ -u_3(h_{rUC}/2, y, -\bar{t}_{rUC}/2) \end{bmatrix} + \begin{bmatrix} u_1(-h_{rUC}/2, y, \bar{t}_{rUC}/2) \\ u_2(-h_{rUC}/2, y, \bar{t}_{rUC}/2) \\ u_3(-h_{rUC}/2, y, \bar{t}_{rUC}/2) \end{bmatrix} = \begin{bmatrix} -h_{rUC}(\varepsilon_1^\psi \cos(\psi)^2 + \varepsilon_2^\psi (1-\cos(\psi)^2) - \varepsilon_{12}^\psi \sin(2\psi)) \\ -h_{rUC}(\varepsilon_1^\psi \sin(2\psi)/2 - \varepsilon_2^\psi \sin(2\psi)/2 + \varepsilon_{12}^\psi \cos(2\psi)) \\ 0 \end{bmatrix}$$

Edge 1 Lower = B1 ∩ B6I, $u(x,y,z) = u(-h_{rUC}/2, y, -\bar{t}_{rUC}/2)$

B1

$$\begin{bmatrix} u_1(h_{rUC}/2, y, -\bar{t}_{rUC}/2) \\ u_2(h_{rUC}/2, y, -\bar{t}_{rUC}/2) \\ u_3(h_{rUC}/2, y, -\bar{t}_{rUC}/2) \end{bmatrix} - \begin{bmatrix} u_1(-h_{rUC}/2, y, -\bar{t}_{rUC}/2) \\ u_2(-h_{rUC}/2, y, -\bar{t}_{rUC}/2) \\ u_3(-h_{rUC}/2, y, -\bar{t}_{rUC}/2) \end{bmatrix} = \begin{bmatrix} h_{rUC}(\varepsilon_1^\psi \cos(\psi)^2 + \varepsilon_2^\psi (1-\cos(\psi)^2) - \varepsilon_{12}^\psi \sin(2\psi)) \\ h_{rUC}(\varepsilon_1^\psi \sin(2\psi)/2 - \varepsilon_2^\psi \sin(2\psi)/2 + \varepsilon_{12}^\psi \cos(2\psi)) \\ 0 \end{bmatrix}$$

B6I

$$\begin{bmatrix} u_1(0, -y, \bar{t}_{rUC}/2) \\ u_2(0, -y, \bar{t}_{rUC}/2) \\ u_3(0, -y, \bar{t}_{rUC}/2) \end{bmatrix} + \begin{bmatrix} u_1(-h_{rUC}/2, y, -\bar{t}_{rUC}/2) \\ u_2(-h_{rUC}/2, y, -\bar{t}_{rUC}/2) \\ -u_3(-h_{rUC}/2, y, -\bar{t}_{rUC}/2) \end{bmatrix} = \begin{bmatrix} -h_{rUC}(\varepsilon_1^\psi \cos(\psi)^2 + \varepsilon_2^\psi (1-\cos(\psi)^2) - \varepsilon_{12}^\psi \sin(2\psi))/2 \\ -h_{rUC}((\varepsilon_1^\psi \sin(2\psi))/2 - (\varepsilon_2^\psi \sin(2\psi))/2 + \varepsilon_{12}^\psi \cos(2\psi))/2 \\ \varepsilon_3 \bar{t}_{rUC} \end{bmatrix}$$

Edge 1 Lower = B1 ∩ B6I, $u(x,y,z) = u(-h_{rUC}/2, y, -\bar{t}_{rUC}/2)$

B1+B6I

$$\begin{bmatrix} u_1(h_{rUC}/2, y, -\bar{t}_{rUC}/2) \\ u_2(h_{rUC}/2, y, -\bar{t}_{rUC}/2) \\ u_3(h_{rUC}/2, y, -\bar{t}_{rUC}/2) \end{bmatrix} + \begin{bmatrix} u_1(0, -y, \bar{t}_{rUC}/2) \\ u_2(0, -y, \bar{t}_{rUC}/2) \\ u_3(0, -y, \bar{t}_{rUC}/2) \end{bmatrix} - \begin{bmatrix} 0 \\ 0 \\ 2 \cdot u_3(-h_{rUC}/2, y, -\bar{t}_{rUC}/2) \end{bmatrix} = \begin{bmatrix} h_{rUC}(\varepsilon_1^{\psi} \cos(\psi)^2 + \varepsilon_2^{\psi}(1-\cos(\psi)^2) - \varepsilon_{12}^{\psi} \sin(2\psi))/2 \\ h_{rUC}((\varepsilon_1^{\psi} \sin(2\psi))/2 - (\varepsilon_2^{\psi} \sin(2\psi))/2 + \varepsilon_{12}^{\psi} \cos(2\psi))/2 \\ \varepsilon_3 \bar{t}_{rUC} \end{bmatrix}$$

B1-B6I

$$\begin{bmatrix} u_1(h_{rUC}/2, y, -\bar{t}_{rUC}/2) \\ u_2(h_{rUC}/2, y, -\bar{t}_{rUC}/2) \\ u_3(h_{rUC}/2, y, -\bar{t}_{rUC}/2) \end{bmatrix} - \begin{bmatrix} u_1(0, -y, \bar{t}_{rUC}/2) \\ u_2(0, -y, \bar{t}_{rUC}/2) \\ u_3(0, -y, \bar{t}_{rUC}/2) \end{bmatrix} - \begin{bmatrix} 2 \cdot u_1(-h_{rUC}/2, y, -\bar{t}_{rUC}/2) \\ 2 \cdot u_2(-h_{rUC}/2, y, -\bar{t}_{rUC}/2) \\ 0 \end{bmatrix} = \begin{bmatrix} 3/2 \cdot h_{rUC}(\varepsilon_1^{\psi} \cos(\psi)^2 + \varepsilon_2^{\psi}(1-\cos(\psi)^2) - \varepsilon_{12}^{\psi} \sin(2\psi)) \\ 3/2 \cdot h_{rUC}(\varepsilon_1^{\psi} \sin(2\psi)/2 - \varepsilon_2^{\psi} \sin(2\psi)/2 + \varepsilon_{12}^{\psi} \cos(2\psi)) \\ -\varepsilon_3 \bar{t}_{rUC} \end{bmatrix}$$

Edge 3 Upper = B3 ∩ B5I, $u(x,y,z) = u(h_{rUC}/2, y, \bar{t}_{rUC}/2)$

B3

$$\begin{bmatrix} u_1(-h_{rUC}/2, y, \bar{t}_{rUC}/2) \\ u_2(-h_{rUC}/2, y, \bar{t}_{rUC}/2) \\ u_3(-h_{rUC}/2, y, \bar{t}_{rUC}/2) \end{bmatrix} - \begin{bmatrix} u_1(h_{rUC}/2, y, \bar{t}_{rUC}/2) \\ u_2(h_{rUC}/2, y, \bar{t}_{rUC}/2) \\ u_3(h_{rUC}/2, y, \bar{t}_{rUC}/2) \end{bmatrix} = \begin{bmatrix} -h_{rUC}(\varepsilon_1^{\psi} \cos(\psi)^2 + \varepsilon_2^{\psi}(1-\cos(\psi)^2) - \varepsilon_{12}^{\psi} \sin(2\psi)) \\ -h_{rUC}(\varepsilon_1^{\psi} \sin(2\psi)/2 - \varepsilon_2^{\psi} \sin(2\psi)/2 + \varepsilon_{12}^{\psi} \cos(2\psi)) \\ 0 \end{bmatrix}$$

B5I

$$\begin{bmatrix} u_1(0, -y, \bar{t}_{rUC}/2) \\ u_2(0, -y, \bar{t}_{rUC}/2) \\ u_3(0, -y, \bar{t}_{rUC}/2) \end{bmatrix} + \begin{bmatrix} u_1(h_{rUC}/2, y, \bar{t}_{rUC}/2) \\ u_2(h_{rUC}/2, y, \bar{t}_{rUC}/2) \\ u_3(h_{rUC}/2, y, \bar{t}_{rUC}/2) \end{bmatrix} = \begin{bmatrix} h_{rUC}(\varepsilon_1^{\psi} \cos(\psi)^2 + \varepsilon_2^{\psi}(1-\cos(\psi)^2) - \varepsilon_{12}^{\psi} \sin(2\psi))/2 \\ h_{rUC}((\varepsilon_1^{\psi} \sin(2\psi))/2 - (\varepsilon_2^{\psi} \sin(2\psi))/2 + \varepsilon_{12}^{\psi} \cos(2\psi))/2 \\ \varepsilon_3 \bar{t}_{rUC} \end{bmatrix}$$

B3+B5I

$$\begin{bmatrix} u_1(-h_{rUC}/2, y, \bar{t}_{rUC}/2) \\ u_2(-h_{rUC}/2, y, \bar{t}_{rUC}/2) \\ u_3(-h_{rUC}/2, y, \bar{t}_{rUC}/2) \end{bmatrix} + \begin{bmatrix} u_1(0, -y, \bar{t}_{rUC}/2) \\ u_2(0, -y, \bar{t}_{rUC}/2) \\ u_3(0, -y, \bar{t}_{rUC}/2) \end{bmatrix} = \begin{bmatrix} -h_{rUC}(\varepsilon_1^{\psi} \cos(\psi)^2 + \varepsilon_2^{\psi}(1-\cos(\psi)^2) - \varepsilon_{12}^{\psi} \sin(2\psi))/2 \\ -h_{rUC}((\varepsilon_1^{\psi} \sin(2\psi))/2 - (\varepsilon_2^{\psi} \sin(2\psi))/2 + \varepsilon_{12}^{\psi} \cos(2\psi))/2 \\ \varepsilon_3 \bar{t}_{rUC} \end{bmatrix}$$

Edge 3 Lower = B3 ∩ B6II, $u(x,y,z) = u(h_{rUC}/2, y, -\bar{t}_{rUC}/2)$

B3

$$\begin{bmatrix} u_1(-h_{rUC}/2, y, -\bar{t}_{rUC}/2) \\ u_2(-h_{rUC}/2, y, -\bar{t}_{rUC}/2) \\ u_3(-h_{rUC}/2, y, -\bar{t}_{rUC}/2) \end{bmatrix} - \begin{bmatrix} u_1(h_{rUC}/2, y, -\bar{t}_{rUC}/2) \\ u_2(h_{rUC}/2, y, -\bar{t}_{rUC}/2) \\ u_3(h_{rUC}/2, y, -\bar{t}_{rUC}/2) \end{bmatrix} = \begin{bmatrix} -h_{rUC}(\varepsilon_1^{\psi} \cos(\psi)^2 + \varepsilon_2^{\psi}(1-\cos(\psi)^2) - \varepsilon_{12}^{\psi} \sin(2\psi)) \\ -h_{rUC}(\varepsilon_1^{\psi} \sin(2\psi)/2 - \varepsilon_2^{\psi} \sin(2\psi)/2 + \varepsilon_{12}^{\psi} \cos(2\psi)) \\ 0 \end{bmatrix}$$

B6II

$$\begin{bmatrix} u_1(h_{rUC}/2, y, -\bar{t}_{rUC}/2) \\ u_2(h_{rUC}/2, y, -\bar{t}_{rUC}/2) \\ -u_3(h_{rUC}/2, y, -\bar{t}_{rUC}/2) \end{bmatrix} + \begin{bmatrix} u_1(0, -y, \bar{t}_{rUC}/2) \\ u_2(0, -y, \bar{t}_{rUC}/2) \\ u_3(0, -y, \bar{t}_{rUC}/2) \end{bmatrix} = \begin{bmatrix} h_{rUC}(\varepsilon_1^{\psi} \cos(\psi)^2 + \varepsilon_2^{\psi}(1-\cos(\psi)^2) - \varepsilon_{12}^{\psi} \sin(2\psi))/2 \\ h_{rUC}((\varepsilon_1^{\psi} \sin(2\psi))/2 - (\varepsilon_2^{\psi} \sin(2\psi))/2 + \varepsilon_{12}^{\psi} \cos(2\psi))/2 \\ \varepsilon_3 \bar{t}_{rUC} \end{bmatrix}$$

Edge 3 Lower = B3 ∩ B6II, $u(x,y,z) = u(h_{rUC}/2, y, -\overline{t}_{rUC}/2)$

B3+B6II

$$\begin{bmatrix} u_1(-h_{rUC}/2, y, -\overline{t}_{rUC}/2) \\ u_2(-h_{rUC}/2, y, -\overline{t}_{rUC}/2) \\ u_3(-h_{rUC}/2, y, -\overline{t}_{rUC}/2) \end{bmatrix} - \begin{bmatrix} 0 \\ 0 \\ 2 \cdot u_3(h_{rUC}/2, y, -\overline{t}_{rUC}/2) \end{bmatrix} + \begin{bmatrix} u_1(0, -y, \overline{t}_{rUC}/2) \\ u_2(0, -y, \overline{t}_{rUC}/2) \\ u_3(0, -y, \overline{t}_{rUC}/2) \end{bmatrix} = \begin{bmatrix} -h_{rUC}(\varepsilon_1^\psi \cos(\psi)^2 + \varepsilon_2^\psi (1-\cos(\psi)^2) - \varepsilon_{12}^\psi \sin(2\psi))/2 \\ -h_{rUC}((\varepsilon_1^\psi \sin(2\psi))/2 - (\varepsilon_2^\psi \sin(2\psi))/2 + \varepsilon_{12}^\psi \cos(2\psi))/2 \\ \varepsilon_3 \overline{t}_{rUC} \end{bmatrix}$$

B3-B6II

$$\begin{bmatrix} u_1(-h_{rUC}/2, y, -\overline{t}_{rUC}/2) \\ u_2(-h_{rUC}/2, y, -\overline{t}_{rUC}/2) \\ u_3(-h_{rUC}/2, y, -\overline{t}_{rUC}/2) \end{bmatrix} - \begin{bmatrix} 2 \cdot u_1(h_{rUC}/2, y, -\overline{t}_{rUC}/2) \\ 2 \cdot u_2(h_{rUC}/2, y, -\overline{t}_{rUC}/2) \\ 0 \end{bmatrix} - \begin{bmatrix} u_1(0, -y, \overline{t}_{rUC}/2) \\ u_2(0, -y, \overline{t}_{rUC}/2) \\ u_3(0, -y, \overline{t}_{rUC}/2) \end{bmatrix} = \begin{bmatrix} -3/2 \cdot h_{rUC}(\varepsilon_1^\psi \cos(\psi)^2 + \varepsilon_2^\psi (1-\cos(\psi)^2) - \varepsilon_{12}^\psi \sin(2\psi))/2 \\ -3/2 \cdot h_{rUC}((\varepsilon_1^\psi \sin(2\psi))/2 - (\varepsilon_2^\psi \sin(2\psi))/2 + \varepsilon_{12}^\psi \cos(2\psi))/2 \\ -\varepsilon_3 \overline{t}_{rUC} \end{bmatrix}$$

Edge 2 Upper North = B2 ∩ B5I, $u(x,y,z) = u(x, -w_{rUC}/2, \overline{t}_{rUC}/2)$

B2

$$\begin{bmatrix} u_1(-x, -w_{rUC}/2, \overline{t}_{rUC}/2) \\ u_2(-x, -w_{rUC}/2, \overline{t}_{rUC}/2) \\ u_3(-x, -w_{rUC}/2, \overline{t}_{rUC}/2) \end{bmatrix} - \begin{bmatrix} -u_1(x, -w_{rUC}/2, \overline{t}_{rUC}/2) \\ -u_2(x, -w_{rUC}/2, \overline{t}_{rUC}/2) \\ u_3(x, -w_{rUC}/2, \overline{t}_{rUC}/2) \end{bmatrix} = \begin{bmatrix} -w_{rUC}(\varepsilon_1^\psi \sin(2\psi)/2 - \varepsilon_2^\psi \sin(2\psi)/2 + \varepsilon_{12}^\psi \cos(2\psi)) \\ -w_{rUC}(\varepsilon_1^\psi (1-\cos(\psi)^2) + \varepsilon_2^\psi \cos(\psi)^2 + \varepsilon_{12}^\psi \sin(2\psi)) \\ 0 \end{bmatrix}$$

B5I

$$\begin{bmatrix} u_1(-x + h_{rUC}/2, w_{rUC}/2, \overline{t}_{rUC}/2) \\ u_2(-x + h_{rUC}/2, w_{rUC}/2, \overline{t}_{rUC}/2) \\ u_3(-x + h_{rUC}/2, w_{rUC}/2, \overline{t}_{rUC}/2) \end{bmatrix} + \begin{bmatrix} u_1(x, -w_{rUC}/2, \overline{t}_{rUC}/2) \\ u_2(x, -w_{rUC}/2, \overline{t}_{rUC}/2) \\ u_3(x, -w_{rUC}/2, \overline{t}_{rUC}/2) \end{bmatrix} = \begin{bmatrix} h_{rUC}(\varepsilon_1^\psi \cos(\psi)^2 + \varepsilon_2^\psi (1-\cos(\psi)^2) - \varepsilon_{12}^\psi \sin(2\psi))/2 \\ h_{rUC}((\varepsilon_1^\psi \sin(2\psi))/2 - (\varepsilon_2^\psi \sin(2\psi))/2 + \varepsilon_{12}^\psi \cos(2\psi))/2 \\ \varepsilon_3 \overline{t}_{rUC} \end{bmatrix}$$

B2 − B5I
B2 − B5I
B2 + B5I

$$\begin{bmatrix} u_1(-x, -w_{rUC}/2, \overline{t}_{rUC}/2) \\ u_2(-x, -w_{rUC}/2, \overline{t}_{rUC}/2) \\ u_3(-x, -w_{rUC}/2, \overline{t}_{rUC}/2) \end{bmatrix} - \begin{bmatrix} u_1(-x + h_{rUC}/2, w_{rUC}/2, \overline{t}_{rUC}/2) \\ u_2(-x + h_{rUC}/2, w_{rUC}/2, \overline{t}_{rUC}/2) \\ -u_3(-x + h_{rUC}/2, w_{rUC}/2, \overline{t}_{rUC}/2) \end{bmatrix} = \begin{bmatrix} -h_{rUC}(\varepsilon_1^\psi \cos(\psi)^2 + \varepsilon_2^\psi (1-\cos(\psi)^2) - \varepsilon_{12}^\psi \sin(2\psi))/2 - w_{rUC}(\varepsilon_1^\psi \sin(2\psi)/2 - \varepsilon_2^\psi \sin(2\psi)/2 + \varepsilon_{12}^\psi \cos(2\psi)) \\ -h_{rUC}((\varepsilon_1^\psi \sin(2\psi))/2 - (\varepsilon_2^\psi \sin(2\psi))/2 + \varepsilon_{12}^\psi \cos(2\psi))/2 - w_{rUC}(\varepsilon_1^\psi (1-\cos(\psi)^2) + \varepsilon_2^\psi \cos(\psi)^2 + \varepsilon_{12}^\psi \sin(2\psi)) \\ \varepsilon_3 \overline{t}_{rUC} \end{bmatrix}$$

B5I-B6II

$$\begin{bmatrix} u_1(x, -w_{rUC}/2, \overline{t}_{rUC}/2) \\ u_2(x, -w_{rUC}/2, \overline{t}_{rUC}/2) \\ u_3(x, -w_{rUC}/2, \overline{t}_{rUC}/2) \end{bmatrix} - \begin{bmatrix} u_1(x, -w_{rUC}/2, -\overline{t}_{rUC}/2) \\ u_2(x, -w_{rUC}/2, -\overline{t}_{rUC}/2) \\ -u_3(x, -w_{rUC}/2, -\overline{t}_{rUC}/2) \end{bmatrix} = \begin{bmatrix} 0 \\ 0 \\ 0 \end{bmatrix}$$

B2 − (B5I-B6II)
B2 − (B5I-B6II)
B2 + (B5I-B6II)

$$\begin{bmatrix} u_1(-x, -w_{rUC}/2, \overline{t}_{rUC}/2) \\ u_2(-x, -w_{rUC}/2, \overline{t}_{rUC}/2) \\ u_3(-x, -w_{rUC}/2, \overline{t}_{rUC}/2) \end{bmatrix} + \begin{bmatrix} u_1(x, -w_{rUC}/2, -\overline{t}_{rUC}/2) \\ u_2(x, -w_{rUC}/2, -\overline{t}_{rUC}/2) \\ u_3(x, -w_{rUC}/2, -\overline{t}_{rUC}/2) \end{bmatrix} = \begin{bmatrix} -w_{rUC}(\varepsilon_1^\psi \sin(2\psi)/2 - \varepsilon_2^\psi \sin(2\psi)/2 + \varepsilon_{12}^\psi \cos(2\psi)) \\ -w_{rUC}(\varepsilon_1^\psi (1-\cos(\psi)^2) + \varepsilon_2^\psi \cos(\psi)^2 + \varepsilon_{12}^\psi \sin(2\psi)) \\ 0 \end{bmatrix}$$

Edge 2 Upper South = B2 ∩ B5I, $u(x,y,z) = u(x,-w_{rUC}/2,\overline{t}_{rUC}/2)$

B2
$$\begin{bmatrix} u_1(-x,-w_{rUC}/2,\overline{t}_{rUC}/2) \\ u_2(-x,-w_{rUC}/2,\overline{t}_{rUC}/2) \\ u_3(-x,-w_{rUC}/2,\overline{t}_{rUC}/2) \end{bmatrix} - \begin{bmatrix} -u_1(x,-w_{rUC}/2,\overline{t}_{rUC}/2) \\ -u_2(x,-w_{rUC}/2,\overline{t}_{rUC}/2) \\ u_3(x,-w_{rUC}/2,\overline{t}_{rUC}/2) \end{bmatrix} = \begin{bmatrix} -w_{rUC}(\varepsilon_1^{\psi}\sin(2\psi)/2 - \varepsilon_2^{\psi}\sin(2\psi)/2 + \varepsilon_{12}^{\psi}\cos(2\psi)) \\ -w_{rUC}(\varepsilon_1^{\psi}(1-\cos(\psi)^2) + \varepsilon_2^{\psi}\cos(\psi)^2 + \varepsilon_{12}^{\psi}\sin(2\psi)) \\ 0 \end{bmatrix}$$

B5II
$$\begin{bmatrix} u_1(-x-h_{rUC}/2,w_{rUC}/2,\overline{t}_{rUC}/2) \\ u_2(-x-h_{rUC}/2,w_{rUC}/2,\overline{t}_{rUC}/2) \\ u_3(-x-h_{rUC}/2,w_{rUC}/2,\overline{t}_{rUC}/2) \end{bmatrix} + \begin{bmatrix} u_1(x,-w_{rUC}/2,\overline{t}_{rUC}/2) \\ u_2(x,-w_{rUC}/2,\overline{t}_{rUC}/2) \\ u_3(x,-w_{rUC}/2,\overline{t}_{rUC}/2) \end{bmatrix} = \begin{bmatrix} -h_{rUC}(\varepsilon_1^{\psi}\cos(\psi)^2 + \varepsilon_2^{\psi}(1-\cos(\psi)^2) - \varepsilon_{12}^{\psi}\sin(2\psi))/2 \\ -h_{rUC}((\varepsilon_1^{\psi}\sin(2\psi))/2 - (\varepsilon_2^{\psi}\sin(2\psi))/2 + \varepsilon_{12}^{\psi}\cos(2\psi))/2 \\ \varepsilon_3\overline{t}_{rUC} \end{bmatrix}$$

B2 − B5II
B2 − B5II
B2 + B5II
$$\begin{bmatrix} u_1(-x,-w_{rUC}/2,\overline{t}_{rUC}/2) \\ u_2(-x,-w_{rUC}/2,\overline{t}_{rUC}/2) \\ u_3(-x,-w_{rUC}/2,\overline{t}_{rUC}/2) \end{bmatrix} - \begin{bmatrix} u_1(-x-h_{rUC}/2,w_{rUC}/2,\overline{t}_{rUC}/2) \\ u_2(-x-h_{rUC}/2,w_{rUC}/2,\overline{t}_{rUC}/2) \\ -u_3(-x-h_{rUC}/2,w_{rUC}/2,\overline{t}_{rUC}/2) \end{bmatrix} = \begin{bmatrix} h_{rUC}(\varepsilon_1^{\psi}\cos(\psi)^2 + \varepsilon_2^{\psi}(1-\cos(\psi)^2) - \varepsilon_{12}^{\psi}\sin(2\psi))/2 - w_{rUC}(\varepsilon_1^{\psi}\sin(2\psi)/2 - \varepsilon_2^{\psi}\sin(2\psi)/2 + \varepsilon_{12}^{\psi}\cos(2\psi)) \\ h_{rUC}((\varepsilon_1^{\psi}\sin(2\psi))/2 - (\varepsilon_2^{\psi}\sin(2\psi))/2 + \varepsilon_{12}^{\psi}\cos(2\psi))/2 - w_{rUC}(\varepsilon_1^{\psi}(1-\cos(\psi)^2) + \varepsilon_2^{\psi}\cos(\psi)^2 + \varepsilon_{12}^{\psi}\sin(2\psi)) \\ \varepsilon_3\overline{t}_{rUC} \end{bmatrix}$$

Edge 2 Lower North = B2 ∩ B6II, $u(x,y,z) = u(x,-w_{rUC}/2,-\overline{t}_{rUC}/2)$

B2
$$\begin{bmatrix} u_1(-x,-w_{rUC}/2,-\overline{t}_{rUC}/2) \\ u_2(-x,-w_{rUC}/2,-\overline{t}_{rUC}/2) \\ u_3(-x,-w_{rUC}/2,-\overline{t}_{rUC}/2) \end{bmatrix} - \begin{bmatrix} -u_1(x,-w_{rUC}/2,-\overline{t}_{rUC}/2) \\ -u_2(x,-w_{rUC}/2,-\overline{t}_{rUC}/2) \\ u_3(x,-w_{rUC}/2,-\overline{t}_{rUC}/2) \end{bmatrix} = \begin{bmatrix} -w_{rUC}(\varepsilon_1^{\psi}\sin(2\psi)/2 - \varepsilon_2^{\psi}\sin(2\psi)/2 + \varepsilon_{12}^{\psi}\cos(2\psi)) \\ -w_{rUC}(\varepsilon_1^{\psi}(1-\cos(\psi)^2) + \varepsilon_2^{\psi}\cos(\psi)^2 + \varepsilon_{12}^{\psi}\sin(2\psi)) \\ 0 \end{bmatrix}$$

B6II
$$\begin{bmatrix} u_1(-x+h_{rUC}/2,w_{rUC}/2,\overline{t}_{rUC}/2) \\ u_2(-x+h_{rUC}/2,w_{rUC}/2,\overline{t}_{rUC}/2) \\ u_3(-x+h_{rUC}/2,w_{rUC}/2,\overline{t}_{rUC}/2) \end{bmatrix} + \begin{bmatrix} u_1(x,-w_{rUC}/2,-\overline{t}_{rUC}/2) \\ u_2(x,-w_{rUC}/2,-\overline{t}_{rUC}/2) \\ -u_3(x,-w_{rUC}/2,-\overline{t}_{rUC}/2) \end{bmatrix} = \begin{bmatrix} h_{rUC}(\varepsilon_1^{\psi}\cos(\psi)^2 + \varepsilon_2^{\psi}(1-\cos(\psi)^2) - \varepsilon_{12}^{\psi}\sin(2\psi))/2 \\ h_{rUC}((\varepsilon_1^{\psi}\sin(2\psi))/2 - (\varepsilon_2^{\psi}\sin(2\psi))/2 + \varepsilon_{12}^{\psi}\cos(2\psi))/2 \\ \varepsilon_3\overline{t}_{rUC} \end{bmatrix}$$

B2-B6II
$$\begin{bmatrix} u_1(-x,-w_{rUC}/2,-\overline{t}_{rUC}/2) \\ u_2(-x,-w_{rUC}/2,-\overline{t}_{rUC}/2) \\ u_3(-x,-w_{rUC}/2,-\overline{t}_{rUC}/2) \end{bmatrix} - \begin{bmatrix} u_1(-x+h_{rUC}/2,w_{rUC}/2,\overline{t}_{rUC}/2) \\ u_2(-x+h_{rUC}/2,w_{rUC}/2,\overline{t}_{rUC}/2) \\ u_3(-x+h_{rUC}/2,w_{rUC}/2,\overline{t}_{rUC}/2) \end{bmatrix} = \begin{bmatrix} -h_{rUC}(\varepsilon_1^{\psi}\cos(\psi)^2 + \varepsilon_2^{\psi}(1-\cos(\psi)^2) - \varepsilon_{12}^{\psi}\sin(2\psi))/2 - w_{rUC}(\varepsilon_1^{\psi}\sin(2\psi)/2 - \varepsilon_2^{\psi}\sin(2\psi)/2 + \varepsilon_{12}^{\psi}\cos(2\psi)) \\ -h_{rUC}((\varepsilon_1^{\psi}\sin(2\psi))/2 - (\varepsilon_2^{\psi}\sin(2\psi))/2 + \varepsilon_{12}^{\psi}\cos(2\psi))/2 - w_{rUC}(\varepsilon_1^{\psi}(1-\cos(\psi)^2) + \varepsilon_2^{\psi}\cos(\psi)^2 + \varepsilon_{12}^{\psi}\sin(2\psi)) \\ -\varepsilon_3\overline{t}_{rUC} \end{bmatrix}$$

Edge 2 Lower South = B2 ∩ B6I, $u(x,y,z) = u(x,-w_{rUC}/2,-\overline{t}_{rUC}/2)$

B2
$$\begin{bmatrix} u_1(-x,-w_{rUC}/2,-\overline{t}_{rUC}/2) \\ u_2(-x,-w_{rUC}/2,-\overline{t}_{rUC}/2) \\ u_3(-x,-w_{rUC}/2,-\overline{t}_{rUC}/2) \end{bmatrix} - \begin{bmatrix} -u_1(x,-w_{rUC}/2,-\overline{t}_{rUC}/2) \\ -u_2(x,-w_{rUC}/2,-\overline{t}_{rUC}/2) \\ u_3(x,-w_{rUC}/2,-\overline{t}_{rUC}/2) \end{bmatrix} = \begin{bmatrix} -w_{rUC}(\varepsilon_1^{\psi}\sin(2\psi)/2 - \varepsilon_2^{\psi}\sin(2\psi)/2 + \varepsilon_{12}^{\psi}\cos(2\psi)) \\ -w_{rUC}(\varepsilon_1^{\psi}(1-\cos(\psi)^2) + \varepsilon_2^{\psi}\cos(\psi)^2 + \varepsilon_{12}^{\psi}\sin(2\psi)) \\ 0 \end{bmatrix}$$

Edge 2 Lower South = B2 ∩ B6I, $u(x,y,z) = u(x,-w_{rUC}/2,-\overline{t}_{rUC}/2)$

B6I
$$\begin{bmatrix} u_1(-x-h_{rUC}/2, w_{rUC}/2, \overline{t}_{rUC}/2) \\ u_2(-x-h_{rUC}/2, w_{rUC}/2, \overline{t}_{rUC}/2) \\ u_3(-x-h_{rUC}/2, w_{rUC}/2, \overline{t}_{rUC}/2) \end{bmatrix} + \begin{bmatrix} u_1(x, -w_{rUC}/2, -\overline{t}_{rUC}/2) \\ u_2(x, -w_{rUC}/2, -\overline{t}_{rUC}/2) \\ -u_3(x, -w_{rUC}/2, -\overline{t}_{rUC}/2) \end{bmatrix} = \begin{bmatrix} -h_{rUC}(\varepsilon_1^{\psi}\cos(\psi)^2 + \varepsilon_2^{\psi}(1-\cos(\psi)^2) - \varepsilon_{12}^{\psi}\sin(2\psi))/2 \\ -h_{rUC}((\varepsilon_1^{\psi}\sin(2\psi))/2 - (\varepsilon_2^{\psi}\sin(2\psi))/2 + \varepsilon_{12}^{\psi}\cos(2\psi))/2 \\ \varepsilon_3\overline{t}_{rUC} \end{bmatrix}$$

B2-B6I
$$\begin{bmatrix} u_1(-x, -w_{rUC}/2, -\overline{t}_{rUC}/2) \\ u_2(-x, -w_{rUC}/2, -\overline{t}_{rUC}/2) \\ u_3(-x, -w_{rUC}/2, -\overline{t}_{rUC}/2) \end{bmatrix} - \begin{bmatrix} u_1(-x-h_{rUC}/2, w_{rUC}/2, \overline{t}_{rUC}/2) \\ u_2(-x-h_{rUC}/2, w_{rUC}/2, \overline{t}_{rUC}/2) \\ u_3(-x-h_{rUC}/2, w_{rUC}/2, \overline{t}_{rUC}/2) \end{bmatrix} = \begin{bmatrix} h_{rUC}(\varepsilon_1^{\psi}\cos(\psi)^2 + \varepsilon_2^{\psi}(1-\cos(\psi)^2) - \varepsilon_{12}^{\psi}\sin(2\psi))/2 - w_{rUC}(\varepsilon_1^{\psi}\sin(2\psi)/2 - \varepsilon_2^{\psi}\sin(2\psi)/2 + \varepsilon_{12}^{\psi}\cos(2\psi)) \\ h_{rUC}((\varepsilon_1^{\psi}\sin(2\psi))/2 - (\varepsilon_2^{\psi}\sin(2\psi))/2 + \varepsilon_{12}^{\psi}\cos(2\psi))/2 - w_{rUC}(\varepsilon_1^{\psi}(1-\cos(\psi)^2) + \varepsilon_2^{\psi}\cos(\psi)^2 + \varepsilon_{12}^{\psi}\sin(2\psi)) \\ -\varepsilon_3\overline{t}_{rUC} \end{bmatrix}$$

Edge 4 Upper North = B4 ∩ B5I, $u(x,y,z) = u(x,w_{rUC}/2,\overline{t}_{rUC}/2)$

B4
$$\begin{bmatrix} u_1(-x, w_{rUC}/2, -\overline{t}_{rUC}/2) \\ u_2(-x, w_{rUC}/2, -\overline{t}_{rUC}/2) \\ u_3(-x, w_{rUC}/2, -\overline{t}_{rUC}/2) \end{bmatrix} + \begin{bmatrix} u_1(x, w_{rUC}/2, \overline{t}_{rUC}/2) \\ u_2(x, w_{rUC}/2, \overline{t}_{rUC}/2) \\ u_3(x, w_{rUC}/2, \overline{t}_{rUC}/2) \end{bmatrix} = \begin{bmatrix} w_{rUC}(\varepsilon_1^{\psi}\sin(2\psi)/2 - \varepsilon_2^{\psi}\sin(2\psi)/2 + \varepsilon_{12}^{\psi}\cos(2\psi)) \\ w_{rUC}(\varepsilon_1^{\psi}(1-\cos(\psi)^2) + \varepsilon_2^{\psi}\cos(\psi)^2 + \varepsilon_{12}^{\psi}\sin(2\psi)) \\ 0 \end{bmatrix}$$

B5I
$$\begin{bmatrix} u_1(-x+h_{rUC}/2, -w_{rUC}/2, \overline{t}_{rUC}/2) \\ u_2(-x+h_{rUC}/2, -w_{rUC}/2, \overline{t}_{rUC}/2) \\ u_3(-x+h_{rUC}/2, -w_{rUC}/2, \overline{t}_{rUC}/2) \end{bmatrix} + \begin{bmatrix} u_1(x, w_{rUC}/2, \overline{t}_{rUC}/2) \\ u_2(x, w_{rUC}/2, \overline{t}_{rUC}/2) \\ u_3(x, w_{rUC}/2, \overline{t}_{rUC}/2) \end{bmatrix} = \begin{bmatrix} h_{rUC}(\varepsilon_1^{\psi}\cos(\psi)^2 + \varepsilon_2^{\psi}(1-\cos(\psi)^2) - \varepsilon_{12}^{\psi}\sin(2\psi))/2 \\ h_{rUC}((\varepsilon_1^{\psi}\sin(2\psi))/2 - (\varepsilon_2^{\psi}\sin(2\psi))/2 + \varepsilon_{12}^{\psi}\cos(2\psi))/2 \\ \varepsilon_3\overline{t}_{rUC} \end{bmatrix}$$

B4-B5I
$$\begin{bmatrix} u_1(-x, w_{rUC}/2, -\overline{t}_{rUC}/2) \\ u_2(-x, w_{rUC}/2, -\overline{t}_{rUC}/2) \\ u_3(-x, w_{rUC}/2, -\overline{t}_{rUC}/2) \end{bmatrix} - \begin{bmatrix} u_1(-x+h_{rUC}/2, -w_{rUC}/2, \overline{t}_{rUC}/2) \\ u_2(-x+h_{rUC}/2, -w_{rUC}/2, \overline{t}_{rUC}/2) \\ u_3(-x+h_{rUC}/2, -w_{rUC}/2, \overline{t}_{rUC}/2) \end{bmatrix} = \begin{bmatrix} -h_{rUC}(\varepsilon_1^{\psi}\cos(\psi)^2 + \varepsilon_2^{\psi}(1-\cos(\psi)^2) - \varepsilon_{12}^{\psi}\sin(2\psi))/2 + w_{rUC}(\varepsilon_1^{\psi}\sin(2\psi)/2 - \varepsilon_2^{\psi}\sin(2\psi)/2 + \varepsilon_{12}^{\psi}\cos(2\psi)) \\ -h_{rUC}((\varepsilon_1^{\psi}\sin(2\psi))/2 - (\varepsilon_2^{\psi}\sin(2\psi))/2 + \varepsilon_{12}^{\psi}\cos(2\psi))/2 + w_{rUC}(\varepsilon_1^{\psi}(1-\cos(\psi)^2) + \varepsilon_2^{\psi}\cos(\psi)^2 + \varepsilon_{12}^{\psi}\sin(2\psi)) \\ -\varepsilon_3\overline{t}_{rUC} \end{bmatrix}$$

Edge 4 Upper South = B4 ∩ B5II, $u(x,y,z) = u(x,w_{rUC}/2,\overline{t}_{rUC}/2)$

B4
$$\begin{bmatrix} u_1(-x, w_{rUC}/2, -\overline{t}_{rUC}/2) \\ u_2(-x, w_{rUC}/2, -\overline{t}_{rUC}/2) \\ u_3(-x, w_{rUC}/2, -\overline{t}_{rUC}/2) \end{bmatrix} + \begin{bmatrix} u_1(x, w_{rUC}/2, \overline{t}_{rUC}/2) \\ u_2(x, w_{rUC}/2, \overline{t}_{rUC}/2) \\ u_3(x, w_{rUC}/2, \overline{t}_{rUC}/2) \end{bmatrix} = \begin{bmatrix} w_{rUC}(\varepsilon_1^{\psi}\sin(2\psi)/2 - \varepsilon_2^{\psi}\sin(2\psi)/2 + \varepsilon_{12}^{\psi}\cos(2\psi)) \\ w_{rUC}(\varepsilon_1^{\psi}(1-\cos(\psi)^2) + \varepsilon_2^{\psi}\cos(\psi)^2 + \varepsilon_{12}^{\psi}\sin(2\psi)) \\ 0 \end{bmatrix}$$

B5II
$$\begin{bmatrix} u_1(-x-h_{rUC}/2, -w_{rUC}/2, \overline{t}_{rUC}/2) \\ u_2(-x-h_{rUC}/2, -w_{rUC}/2, \overline{t}_{rUC}/2) \\ u_3(-x-h_{rUC}/2, -w_{rUC}/2, \overline{t}_{rUC}/2) \end{bmatrix} + \begin{bmatrix} u_1(x, w_{rUC}/2, \overline{t}_{rUC}/2) \\ u_2(x, w_{rUC}/2, \overline{t}_{rUC}/2) \\ u_3(x, w_{rUC}/2, \overline{t}_{rUC}/2) \end{bmatrix} = \begin{bmatrix} -h_{rUC}(\varepsilon_1^{\psi}\cos(\psi)^2 + \varepsilon_2^{\psi}(1-\cos(\psi)^2) - \varepsilon_{12}^{\psi}\sin(2\psi))/2 \\ -h_{rUC}((\varepsilon_1^{\psi}\sin(2\psi))/2 - (\varepsilon_2^{\psi}\sin(2\psi))/2 + \varepsilon_{12}^{\psi}\cos(2\psi))/2 \\ \varepsilon_3\overline{t}_{rUC} \end{bmatrix}$$

Edge 4 Upper South = B4 ∩ B5II, $u(x,y,z) = u(x, w_{rUC}/2, \overline{t}_{rUC}/2)$

B4-B5II
$$\begin{bmatrix} u_1(-x, w_{rUC}/2, -\overline{t}_{rUC}/2) \\ u_2(-x, w_{rUC}/2, -\overline{t}_{rUC}/2) \\ u_3(-x, w_{rUC}/2, -\overline{t}_{rUC}/2) \end{bmatrix} - \begin{bmatrix} u_1(-x-h_{rUC}/2, -w_{rUC}/2, \overline{t}_{rUC}/2) \\ u_2(-x-h_{rUC}/2, -w_{rUC}/2, \overline{t}_{rUC}/2) \\ u_3(-x-h_{rUC}/2, -w_{rUC}/2, \overline{t}_{rUC}/2) \end{bmatrix} = \begin{bmatrix} h_{rUC}(\varepsilon_1^\psi \cos(\psi)^2 + \varepsilon_2^\psi(1-\cos(\psi)^2) - \varepsilon_{12}^\psi \sin(2\psi))/2 + w_{rUC}(\varepsilon_1^\psi \sin(2\psi)/2 - \varepsilon_2^\psi \sin(2\psi)/2 + \varepsilon_{12}^\psi \cos(2\psi)) \\ h_{rUC}((\varepsilon_1^\psi \sin(2\psi))/2 - (\varepsilon_2^\psi \sin(2\psi))/2 + \varepsilon_{12}^\psi \cos(2\psi))/2 + w_{rUC}(\varepsilon_1^\psi(1-\cos(\psi)^2) + \varepsilon_2^\psi \cos(\psi)^2 + \varepsilon_{12}^\psi \sin(2\psi)) \\ -\varepsilon_3 \overline{t}_{rUC} \end{bmatrix}$$

Edge 4 Lower North = B4 ∩ B6II, $u(x,y,z) = u(x, w_{rUC}/2, -\overline{t}_{rUC}/2)$

B4
$$\begin{bmatrix} u_1(-x, w_{rUC}/2, \overline{t}_{rUC}/2) \\ u_2(-x, w_{rUC}/2, \overline{t}_{rUC}/2) \\ u_3(-x, w_{rUC}/2, \overline{t}_{rUC}/2) \end{bmatrix} + \begin{bmatrix} u_1(x, w_{rUC}/2, -\overline{t}_{rUC}/2) \\ u_2(x, w_{rUC}/2, -\overline{t}_{rUC}/2) \\ u_3(x, w_{rUC}/2, -\overline{t}_{rUC}/2) \end{bmatrix} = \begin{bmatrix} w_{rUC}(\varepsilon_1^\psi \sin(2\psi)/2 - \varepsilon_2^\psi \sin(2\psi)/2 + \varepsilon_{12}^\psi \cos(2\psi)) \\ w_{rUC}(\varepsilon_1^\psi(1-\cos(\psi)^2) + \varepsilon_2^\psi \cos(\psi)^2 + \varepsilon_{12}^\psi \sin(2\psi)) \\ 0 \end{bmatrix}$$

B6II
$$\begin{bmatrix} u_1(-x+h_{rUC}/2, -w_{rUC}/2, \overline{t}_{rUC}/2) \\ u_2(-x+h_{rUC}/2, -w_{rUC}/2, \overline{t}_{rUC}/2) \\ u_3(-x+h_{rUC}/2, -w_{rUC}/2, \overline{t}_{rUC}/2) \end{bmatrix} + \begin{bmatrix} u_1(x, w_{rUC}/2, -\overline{t}_{rUC}/2) \\ u_2(x, w_{rUC}/2, -\overline{t}_{rUC}/2) \\ -u_3(x, w_{rUC}/2, -\overline{t}_{rUC}/2) \end{bmatrix} = \begin{bmatrix} h_{rUC}(\varepsilon_1^\psi \cos(\psi)^2 + \varepsilon_2^\psi(1-\cos(\psi)^2) - \varepsilon_{12}^\psi \sin(2\psi))/2 \\ h_{rUC}((\varepsilon_1^\psi \sin(2\psi))/2 - (\varepsilon_2^\psi \sin(2\psi))/2 + \varepsilon_{12}^\psi \cos(2\psi))/2 \\ \varepsilon_3 \overline{t}_{rUC} \end{bmatrix}$$

B4 − B6II
B4 − B6II
B4 + B6II
$$\begin{bmatrix} u_1(-x, w_{rUC}/2, \overline{t}_{rUC}/2) \\ u_2(-x, w_{rUC}/2, \overline{t}_{rUC}/2) \\ u_3(-x, w_{rUC}/2, \overline{t}_{rUC}/2) \end{bmatrix} - \begin{bmatrix} u_1(-x+h_{rUC}/2, -w_{rUC}/2, \overline{t}_{rUC}/2) \\ u_2(-x+h_{rUC}/2, -w_{rUC}/2, \overline{t}_{rUC}/2) \\ -u_3(-x+h_{rUC}/2, -w_{rUC}/2, \overline{t}_{rUC}/2) \end{bmatrix} = \begin{bmatrix} -h_{rUC}(\varepsilon_1^\psi \cos(\psi)^2 + \varepsilon_2^\psi(1-\cos(\psi)^2) - \varepsilon_{12}^\psi \sin(2\psi))/2 + w_{rUC}(\varepsilon_1^\psi \sin(2\psi)/2 - \varepsilon_2^\psi \sin(2\psi)/2 + \varepsilon_{12}^\psi \cos(2\psi)) \\ -h_{rUC}((\varepsilon_1^\psi \sin(2\psi))/2 - (\varepsilon_2^\psi \sin(2\psi))/2 + \varepsilon_{12}^\psi \cos(2\psi))/2 + w_{rUC}(\varepsilon_1^\psi(1-\cos(\psi)^2) + \varepsilon_2^\psi \cos(\psi)^2 + \varepsilon_{12}^\psi \sin(2\psi)) \\ \varepsilon_3 \overline{t}_{rUC} \end{bmatrix}$$

Edge 4 Lower South = B4 ∩ B6I, $u(x,y,z) = u(x, w_{rUC}/2, -\overline{t}_{rUC}/2)$

B4
$$\begin{bmatrix} u_1(-x, w_{rUC}/2, \overline{t}_{rUC}/2) \\ u_2(-x, w_{rUC}/2, \overline{t}_{rUC}/2) \\ u_3(-x, w_{rUC}/2, \overline{t}_{rUC}/2) \end{bmatrix} + \begin{bmatrix} u_1(x, w_{rUC}/2, -\overline{t}_{rUC}/2) \\ u_2(x, w_{rUC}/2, -\overline{t}_{rUC}/2) \\ u_3(x, w_{rUC}/2, -\overline{t}_{rUC}/2) \end{bmatrix} = \begin{bmatrix} w_{rUC}(\varepsilon_1^\psi \sin(2\psi)/2 - \varepsilon_2^\psi \sin(2\psi)/2 + \varepsilon_{12}^\psi \cos(2\psi)) \\ w_{rUC}(\varepsilon_1^\psi(1-\cos(\psi)^2) + \varepsilon_2^\psi \cos(\psi)^2 + \varepsilon_{12}^\psi \sin(2\psi)) \\ 0 \end{bmatrix}$$

B6I
$$\begin{bmatrix} u_1(-x-h_{rUC}/2, -w_{rUC}/2, \overline{t}_{rUC}/2) \\ u_2(-x-h_{rUC}/2, -w_{rUC}/2, \overline{t}_{rUC}/2) \\ u_3(-x-h_{rUC}/2, -w_{rUC}/2, \overline{t}_{rUC}/2) \end{bmatrix} + \begin{bmatrix} u_1(x, w_{rUC}/2, -\overline{t}_{rUC}/2) \\ u_2(x, w_{rUC}/2, -\overline{t}_{rUC}/2) \\ -u_3(x, w_{rUC}/2, -\overline{t}_{rUC}/2) \end{bmatrix} = \begin{bmatrix} -h_{rUC}(\varepsilon_1^\psi \cos(\psi)^2 + \varepsilon_2^\psi(1-\cos(\psi)^2) - \varepsilon_{12}^\psi \sin(2\psi))/2 \\ -h_{rUC}((\varepsilon_1^\psi \sin(2\psi))/2 - (\varepsilon_2^\psi \sin(2\psi))/2 + \varepsilon_{12}^\psi \cos(2\psi))/2 \\ \varepsilon_3 \overline{t}_{rUC} \end{bmatrix}$$

B4 − B6I
B4 − B6I
B4 + B6I
$$\begin{bmatrix} u_1(-x, w_{rUC}/2, \overline{t}_{rUC}/2) \\ u_2(-x, w_{rUC}/2, \overline{t}_{rUC}/2) \\ u_3(-x, w_{rUC}/2, \overline{t}_{rUC}/2) \end{bmatrix} - \begin{bmatrix} u_1(-x-h_{rUC}/2, -w_{rUC}/2, \overline{t}_{rUC}/2) \\ u_2(-x-h_{rUC}/2, -w_{rUC}/2, \overline{t}_{rUC}/2) \\ -u_3(-x-h_{rUC}/2, -w_{rUC}/2, \overline{t}_{rUC}/2) \end{bmatrix} = \begin{bmatrix} h_{rUC}(\varepsilon_1^\psi \cos(\psi)^2 + \varepsilon_2^\psi(1-\cos(\psi)^2) - \varepsilon_{12}^\psi \sin(2\psi))/2 + w_{rUC}(\varepsilon_1^\psi \sin(2\psi)/2 - \varepsilon_2^\psi \sin(2\psi)/2 + \varepsilon_{12}^\psi \cos(2\psi)) \\ h_{rUC}((\varepsilon_1^\psi \sin(2\psi))/2 - (\varepsilon_2^\psi \sin(2\psi))/2 + \varepsilon_{12}^\psi \cos(2\psi))/2 + w_{rUC}(\varepsilon_1^\psi(1-\cos(\psi)^2) + \varepsilon_2^\psi \cos(\psi)^2 + \varepsilon_{12}^\psi \sin(2\psi)) \\ -\varepsilon_3 \overline{t}_{rUC} \end{bmatrix}$$

A.2.3 Vertices

Face 5 to Face 6 Center Center $u(x,y,z) = u(0,0,\pm\bar{t}_{rUC}/2)$

B5I
$$\begin{bmatrix} u_1(h_{rUC}/2,0,\bar{t}_{rUC}/2) \\ u_2(h_{rUC}/2,0,\bar{t}_{rUC}/2) \\ u_3(h_{rUC}/2,0,\bar{t}_{rUC}/2) \end{bmatrix} + \begin{bmatrix} u_1(0,0,\bar{t}_{rUC}/2) \\ u_2(0,0,\bar{t}_{rUC}/2) \\ u_3(0,0,\bar{t}_{rUC}/2) \end{bmatrix} = \begin{bmatrix} h_{rUC}(\varepsilon_1^\psi \cos(\psi)^2 + \varepsilon_2^\psi(1-\cos(\psi)^2) - \varepsilon_{12}^\psi \sin(2\psi))/2 \\ h_{rUC}((\varepsilon_1^\psi \sin(2\psi))/2 - (\varepsilon_2^\psi \sin(2\psi))/2 + \varepsilon_{12}^\psi \cos(2\psi))/2 \\ \varepsilon_3 \bar{t}_{rUC} \end{bmatrix}$$

B5II
$$\begin{bmatrix} u_1(-h_{rUC}/2,0,\bar{t}_{rUC}/2) \\ u_2(-h_{rUC}/2,0,\bar{t}_{rUC}/2) \\ u_3(-h_{rUC}/2,0,\bar{t}_{rUC}/2) \end{bmatrix} + \begin{bmatrix} u_1(0,0,\bar{t}_{rUC}/2) \\ u_2(0,0,\bar{t}_{rUC}/2) \\ u_3(0,0,\bar{t}_{rUC}/2) \end{bmatrix} = \begin{bmatrix} -h_{rUC}(\varepsilon_1^\psi \cos(\psi)^2 + \varepsilon_2^\psi(1-\cos(\psi)^2) - \varepsilon_{12}^\psi \sin(2\psi))/2 \\ -h_{rUC}((\varepsilon_1^\psi \sin(2\psi))/2 - (\varepsilon_2^\psi \sin(2\psi))/2 + \varepsilon_{12}^\psi \cos(2\psi))/2 \\ \varepsilon_3 \bar{t}_{rUC} \end{bmatrix}$$

B6I
$$\begin{bmatrix} u_1(-h_{rUC}/2,0,\bar{t}_{rUC}/2) \\ u_2(-h_{rUC}/2,0,\bar{t}_{rUC}/2) \\ u_3(-h_{rUC}/2,0,\bar{t}_{rUC}/2) \end{bmatrix} + \begin{bmatrix} u_1(0,0,-\bar{t}_{rUC}/2) \\ u_2(0,0,-\bar{t}_{rUC}/2) \\ -u_3(0,0,-\bar{t}_{rUC}/2) \end{bmatrix} = \begin{bmatrix} -h_{rUC}(\varepsilon_1^\psi \cos(\psi)^2 + \varepsilon_2^\psi(1-\cos(\psi)^2) - \varepsilon_{12}^\psi \sin(2\psi))/2 \\ -h_{rUC}((\varepsilon_1^\psi \sin(2\psi))/2 - (\varepsilon_2^\psi \sin(2\psi))/2 + \varepsilon_{12}^\psi \cos(2\psi))/2 \\ \varepsilon_3 \bar{t}_{rUC} \end{bmatrix}$$

B6II
$$\begin{bmatrix} u_1(h_{rUC}/2,0,\bar{t}_{rUC}/2) \\ u_2(h_{rUC}/2,0,\bar{t}_{rUC}/2) \\ u_3(h_{rUC}/2,0,\bar{t}_{rUC}/2) \end{bmatrix} + \begin{bmatrix} u_1(0,0,-\bar{t}_{rUC}/2) \\ u_2(0,0,-\bar{t}_{rUC}/2) \\ -u_3(0,0,-\bar{t}_{rUC}/2) \end{bmatrix} = \begin{bmatrix} h_{rUC}(\varepsilon_1^\psi \cos(\psi)^2 + \varepsilon_2^\psi(1-\cos(\psi)^2) - \varepsilon_{12}^\psi \sin(2\psi))/2 \\ h_{rUC}((\varepsilon_1^\psi \sin(2\psi))/2 - (\varepsilon_2^\psi \sin(2\psi))/2 + \varepsilon_{12}^\psi \cos(2\psi))/2 \\ \varepsilon_3 \bar{t}_{rUC} \end{bmatrix}$$

B5I-B6II
$$\begin{bmatrix} u_1(0,0,\bar{t}_{rUC}/2) \\ u_2(0,0,\bar{t}_{rUC}/2) \\ u_3(0,0,\bar{t}_{rUC}/2) \end{bmatrix} - \begin{bmatrix} u_1(0,0,-\bar{t}_{rUC}/2) \\ u_2(0,0,-\bar{t}_{rUC}/2) \\ -u_3(0,0,-\bar{t}_{rUC}/2) \end{bmatrix} = \begin{bmatrix} 0 \\ 0 \\ 0 \end{bmatrix}$$

B5II-B6I
$$\begin{bmatrix} u_1(0,0,\bar{t}_{rUC}/2) \\ u_2(0,0,\bar{t}_{rUC}/2) \\ u_3(0,0,\bar{t}_{rUC}/2) \end{bmatrix} - \begin{bmatrix} u_1(0,0,-\bar{t}_{rUC}/2) \\ u_2(0,0,-\bar{t}_{rUC}/2) \\ -u_3(0,0,-\bar{t}_{rUC}/2) \end{bmatrix} = \begin{bmatrix} 0 \\ 0 \\ 0 \end{bmatrix}$$

Edge 1 Upper Center = B1 ∩ B5II, $u(x,y,z) = u(-h_{rUC}/2,0,\bar{t}_{rUC}/2)$

B1
$$\begin{bmatrix} u_1(h_{rUC}/2,0,\bar{t}_{rUC}/2) \\ u_2(h_{rUC}/2,0,\bar{t}_{rUC}/2) \\ u_3(h_{rUC}/2,0,\bar{t}_{rUC}/2) \end{bmatrix} - \begin{bmatrix} u_1(-h_{rUC}/2,0,\bar{t}_{rUC}/2) \\ u_2(-h_{rUC}/2,0,\bar{t}_{rUC}/2) \\ u_3(-h_{rUC}/2,0,\bar{t}_{rUC}/2) \end{bmatrix} = \begin{bmatrix} h_{rUC}(\varepsilon_1^\psi \cos(\psi)^2 + \varepsilon_2^\psi(1-\cos(\psi)^2) - \varepsilon_{12}^\psi \sin(2\psi)) \\ h_{rUC}(\varepsilon_1^\psi \sin(2\psi)/2 - \varepsilon_2^\psi \sin(2\psi)/2 + \varepsilon_{12}^\psi \cos(2\psi)) \\ 0 \end{bmatrix}$$

Edge 1 Upper Center = B1 ∩ B5II, $u(x,y,z) = u(-h_{rUC}/2, 0, \bar{t}_{rUC}/2)$

B5II
$$\begin{bmatrix} u_1(0,0,\bar{t}_{rUC}/2) \\ u_2(0,0,\bar{t}_{rUC}/2) \\ u_3(0,0,\bar{t}_{rUC}/2) \end{bmatrix} + \begin{bmatrix} u_1(-h_{rUC}/2,0,\bar{t}_{rUC}/2) \\ u_2(-h_{rUC}/2,0,\bar{t}_{rUC}/2) \\ u_3(-h_{rUC}/2,0,\bar{t}_{rUC}/2) \end{bmatrix} = \begin{bmatrix} -h_{rUC}(\varepsilon_1^{\psi}\cos(\psi)^2 + \varepsilon_2^{\psi}(1-\cos(\psi)^2) - \varepsilon_{12}^{\psi}\sin(2\psi))/2 \\ -h_{rUC}((\varepsilon_1^{\psi}\sin(2\psi))/2 - (\varepsilon_2^{\psi}\sin(2\psi))/2 + \varepsilon_{12}^{\psi}\cos(2\psi))/2 \\ \varepsilon_3\bar{t}_{rUC} \end{bmatrix}$$

B1+B5II
$$\begin{bmatrix} u_1(h_{rUC}/2,0,\bar{t}_{rUC}/2) \\ u_2(h_{rUC}/2,0,\bar{t}_{rUC}/2) \\ u_3(h_{rUC}/2,0,\bar{t}_{rUC}/2) \end{bmatrix} + \begin{bmatrix} u_1(0,0,\bar{t}_{rUC}/2) \\ u_2(0,0,\bar{t}_{rUC}/2) \\ u_3(0,0,\bar{t}_{rUC}/2) \end{bmatrix} = \begin{bmatrix} h_{rUC}(\varepsilon_1^{\psi}\cos(\psi)^2 + \varepsilon_2^{\psi}(1-\cos(\psi)^2) - \varepsilon_{12}^{\psi}\sin(2\psi))/2 \\ h_{rUC}((\varepsilon_1^{\psi}\sin(2\psi))/2 - (\varepsilon_2^{\psi}\sin(2\psi))/2 + \varepsilon_{12}^{\psi}\cos(2\psi))/2 \\ \varepsilon_3\bar{t}_{rUC} \end{bmatrix}$$

(B5II-B6I)-B1
$$- \begin{bmatrix} u_1(h_{rUC}/2,0,-\bar{t}_{rUC}/2) \\ u_2(h_{rUC}/2,0,-\bar{t}_{rUC}/2) \\ -u_3(h_{rUC}/2,0,-\bar{t}_{rUC}/2) \end{bmatrix} + \begin{bmatrix} u_1(-h_{rUC}/2,0,\bar{t}_{rUC}/2) \\ u_2(-h_{rUC}/2,0,\bar{t}_{rUC}/2) \\ u_3(-h_{rUC}/2,0,\bar{t}_{rUC}/2) \end{bmatrix} = \begin{bmatrix} -h_{rUC}(\varepsilon_1^{\psi}\cos(\psi)^2 + \varepsilon_2^{\psi}(1-\cos(\psi)^2) - \varepsilon_{12}^{\psi}\sin(2\psi)) \\ -h_{rUC}(\varepsilon_1^{\psi}\sin(2\psi)/2 - \varepsilon_2^{\psi}\sin(2\psi)/2 + \varepsilon_{12}^{\psi}\cos(2\psi)) \\ 0 \end{bmatrix}$$

Edge 1 Lower Center = B1 ∩ B6I, $u(x,y,z) = u(-h_{rUC}/2, 0, -\bar{t}_{rUC}/2)$

B1
$$\begin{bmatrix} u_1(h_{rUC}/2,0,-\bar{t}_{rUC}/2) \\ u_2(h_{rUC}/2,0,-\bar{t}_{rUC}/2) \\ u_3(h_{rUC}/2,0,-\bar{t}_{rUC}/2) \end{bmatrix} - \begin{bmatrix} u_1(-h_{rUC}/2,0,-\bar{t}_{rUC}/2) \\ u_2(-h_{rUC}/2,0,-\bar{t}_{rUC}/2) \\ u_3(-h_{rUC}/2,0,-\bar{t}_{rUC}/2) \end{bmatrix} = \begin{bmatrix} h_{rUC}(\varepsilon_1^{\psi}\cos(\psi)^2 + \varepsilon_2^{\psi}(1-\cos(\psi)^2) - \varepsilon_{12}^{\psi}\sin(2\psi)) \\ h_{rUC}(\varepsilon_1^{\psi}\sin(2\psi)/2 - \varepsilon_2^{\psi}\sin(2\psi)/2 + \varepsilon_{12}^{\psi}\cos(2\psi)) \\ 0 \end{bmatrix}$$

B6I Implicit
$$\begin{bmatrix} u_1(0,0,-\bar{t}_{rUC}/2) \\ u_2(0,0,-\bar{t}_{rUC}/2) \\ u_3(0,0,-\bar{t}_{rUC}/2) \end{bmatrix} + \begin{bmatrix} u_1(-h_{rUC}/2,0,-\bar{t}_{rUC}/2) \\ u_2(-h_{rUC}/2,0,-\bar{t}_{rUC}/2) \\ u_3(-h_{rUC}/2,0,-\bar{t}_{rUC}/2) \end{bmatrix} = \begin{bmatrix} -h_{rUC}(\varepsilon_1^{\psi}\cos(\psi)^2 + \varepsilon_2^{\psi}(1-\cos(\psi)^2) - \varepsilon_{12}^{\psi}\sin(2\psi))/2 \\ -h_{rUC}((\varepsilon_1^{\psi}\sin(2\psi))/2 - (\varepsilon_2^{\psi}\sin(2\psi))/2 + \varepsilon_{12}^{\psi}\cos(2\psi))/2 \\ -\varepsilon_3\bar{t}_{rUC} \end{bmatrix}$$

B1+B6I
$$\begin{bmatrix} u_1(h_{rUC}/2,0,-\bar{t}_{rUC}/2) \\ u_2(h_{rUC}/2,0,-\bar{t}_{rUC}/2) \\ u_3(h_{rUC}/2,0,-\bar{t}_{rUC}/2) \end{bmatrix} + \begin{bmatrix} u_1(0,0,-\bar{t}_{rUC}/2) \\ u_2(0,0,-\bar{t}_{rUC}/2) \\ u_3(0,0,-\bar{t}_{rUC}/2) \end{bmatrix} = \begin{bmatrix} -h_{rUC}(\varepsilon_1^{\psi}\cos(\psi)^2 + \varepsilon_2^{\psi}(1-\cos(\psi)^2) - \varepsilon_{12}^{\psi}\sin(2\psi))/2 \\ -h_{rUC}((\varepsilon_1^{\psi}\sin(2\psi))/2 - (\varepsilon_2^{\psi}\sin(2\psi))/2 + \varepsilon_{12}^{\psi}\cos(2\psi))/2 \\ -\varepsilon_3\bar{t}_{rUC} \end{bmatrix}$$

Edge 3 Upper Center = B3 ∩ B5I, $u(x,y,z) = u(h_{rUC}/2, 0, \bar{t}_{rUC}/2)$

B3
$$\begin{bmatrix} u_1(-h_{rUC}/2,y,\bar{t}_{rUC}/2) \\ u_2(-h_{rUC}/2,0,\bar{t}_{rUC}/2) \\ u_3(-h_{rUC}/2,0,\bar{t}_{rUC}/2) \end{bmatrix} - \begin{bmatrix} u_1(h_{rUC}/2,0,\bar{t}_{rUC}/2) \\ u_2(h_{rUC}/2,0,\bar{t}_{rUC}/2) \\ u_3(h_{rUC}/2,0,\bar{t}_{rUC}/2) \end{bmatrix} = \begin{bmatrix} -h_{rUC}(\varepsilon_1^{\psi}\cos(\psi)^2 + \varepsilon_2^{\psi}(1-\cos(\psi)^2) - \varepsilon_{12}^{\psi}\sin(2\psi)) \\ -h_{rUC}(\varepsilon_1^{\psi}\sin(2\psi)/2 - \varepsilon_2^{\psi}\sin(2\psi)/2 + \varepsilon_{12}^{\psi}\cos(2\psi)) \\ 0 \end{bmatrix}$$

Edge 3 Upper Center = B3 ∩ B5I, $u(x,y,z) = u(h_{rUC}/2, 0, \overline{t}_{rUC}/2)$

B5I
$$\begin{bmatrix} u_1(0,0,\overline{t}_{rUC}/2) \\ u_2(0,0,\overline{t}_{rUC}/2) \\ u_3(0,0,\overline{t}_{rUC}/2) \end{bmatrix} + \begin{bmatrix} u_1(h_{rUC}/2,0,\overline{t}_{rUC}/2) \\ u_2(h_{rUC}/2,0,\overline{t}_{rUC}/2) \\ u_3(h_{rUC}/2,0,\overline{t}_{rUC}/2) \end{bmatrix} = \begin{bmatrix} h_{rUC}(\varepsilon_1^{\psi}\cos(\psi)^2 + \varepsilon_2^{\psi}(1-\cos(\psi)^2) - \varepsilon_{12}^{\psi}\sin(2\psi))/2 \\ h_{rUC}((\varepsilon_1^{\psi}\sin(2\psi))/2 - (\varepsilon_2^{\psi}\sin(2\psi))/2 + \varepsilon_{12}^{\psi}\cos(2\psi))/2 \\ \varepsilon_3\overline{t}_{rUC} \end{bmatrix}$$

B3+B5I
$$\begin{bmatrix} u_1(-h_{rUC}/2,0,\overline{t}_{rUC}/2) \\ u_2(-h_{rUC}/2,0,\overline{t}_{rUC}/2) \\ u_3(-h_{rUC}/2,0,\overline{t}_{rUC}/2) \end{bmatrix} + \begin{bmatrix} u_1(0,0,\overline{t}_{rUC}/2) \\ u_2(0,0,\overline{t}_{rUC}/2) \\ u_3(0,0,\overline{t}_{rUC}/2) \end{bmatrix} = \begin{bmatrix} -h_{rUC}(\varepsilon_1^{\psi}\cos(\psi)^2 + \varepsilon_2^{\psi}(1-\cos(\psi)^2) - \varepsilon_{12}^{\psi}\sin(2\psi))/2 \\ -h_{rUC}((\varepsilon_1^{\psi}\sin(2\psi))/2 - (\varepsilon_2^{\psi}\sin(2\psi))/2 + \varepsilon_{12}^{\psi}\cos(2\psi))/2 \\ \varepsilon_3\overline{t}_{rUC} \end{bmatrix}$$

Edge 3 Lower Center = B3 ∩ B6II, $u(x,y,z) = u(h_{rUC}/2, 0, -\overline{t}_{rUC}/2)$

B3
$$\begin{bmatrix} u_1(-h_{rUC}/2,0,-\overline{t}_{rUC}/2) \\ u_2(-h_{rUC}/2,0,-\overline{t}_{rUC}/2) \\ u_3(-h_{rUC}/2,0,-\overline{t}_{rUC}/2) \end{bmatrix} - \begin{bmatrix} u_1(h_{rUC}/2,0,-\overline{t}_{rUC}/2) \\ u_2(h_{rUC}/2,0,-\overline{t}_{rUC}/2) \\ u_3(h_{rUC}/2,0,-\overline{t}_{rUC}/2) \end{bmatrix} = \begin{bmatrix} -h_{rUC}(\varepsilon_1^{\psi}\cos(\psi)^2 + \varepsilon_2^{\psi}(1-\cos(\psi)^2) - \varepsilon_{12}^{\psi}\sin(2\psi)) \\ -h_{rUC}(\varepsilon_1^{\psi}\sin(2\psi)/2 - \varepsilon_2^{\psi}\sin(2\psi)/2 + \varepsilon_{12}^{\psi}\cos(2\psi)) \\ 0 \end{bmatrix}$$

B6II Implicit
$$\begin{bmatrix} u_1(0,0,-\overline{t}_{rUC}/2) \\ u_2(0,0,-\overline{t}_{rUC}/2) \\ u_3(0,0,-\overline{t}_{rUC}/2) \end{bmatrix} + \begin{bmatrix} u_1(h_{rUC}/2,0,-\overline{t}_{rUC}/2) \\ u_2(h_{rUC}/2,0,-\overline{t}_{rUC}/2) \\ u_3(h_{rUC}/2,0,-\overline{t}_{rUC}/2) \end{bmatrix} = \begin{bmatrix} h_{rUC}(\varepsilon_1^{\psi}\cos(\psi)^2 + \varepsilon_2^{\psi}(1-\cos(\psi)^2) - \varepsilon_{12}^{\psi}\sin(2\psi))/2 \\ h_{rUC}((\varepsilon_1^{\psi}\sin(2\psi))/2 - (\varepsilon_2^{\psi}\sin(2\psi))/2 + \varepsilon_{12}^{\psi}\cos(2\psi))/2 \\ -\varepsilon_3\overline{t}_{rUC} \end{bmatrix}$$

B3+B6II
$$\begin{bmatrix} u_1(-h_{rUC}/2,0,-\overline{t}_{rUC}/2) \\ u_2(-h_{rUC}/2,0,-\overline{t}_{rUC}/2) \\ u_3(-h_{rUC}/2,0,-\overline{t}_{rUC}/2) \end{bmatrix} + \begin{bmatrix} u_1(0,0,-\overline{t}_{rUC}/2) \\ u_2(0,0,-\overline{t}_{rUC}/2) \\ u_3(0,0,-\overline{t}_{rUC}/2) \end{bmatrix} = \begin{bmatrix} -h_{rUC}(\varepsilon_1^{\psi}\cos(\psi)^2 + \varepsilon_2^{\psi}(1-\cos(\psi)^2) - \varepsilon_{12}^{\psi}\sin(2\psi))/2 \\ -h_{rUC}((\varepsilon_1^{\psi}\sin(2\psi))/2 - (\varepsilon_2^{\psi}\sin(2\psi))/2 + \varepsilon_{12}^{\psi}\cos(2\psi))/2 \\ -\varepsilon_3\overline{t}_{rUC} \end{bmatrix}$$

Vertex 1 Upper $u(x,y,z) = u(-h_{rUC}/2, -w_{rUC}/2, \pm\overline{t}_{rUC}/2)$

B1
$$\begin{bmatrix} u_1(h_{rUC}/2,-w_{rUC}/2,\overline{t}_{rUC}/2) \\ u_2(h_{rUC}/2,-w_{rUC}/2,\overline{t}_{rUC}/2) \\ u_3(h_{rUC}/2,-w_{rUC}/2,\overline{t}_{rUC}/2) \end{bmatrix} - \begin{bmatrix} u_1(-h_{rUC}/2,-w_{rUC}/2,\overline{t}_{rUC}/2) \\ u_2(-h_{rUC}/2,-w_{rUC}/2,\overline{t}_{rUC}/2) \\ u_3(-h_{rUC}/2,-w_{rUC}/2,\overline{t}_{rUC}/2) \end{bmatrix} = \begin{bmatrix} h_{rUC}(\varepsilon_1^{\psi}\cos(\psi)^2 + \varepsilon_2^{\psi}(1-\cos(\psi)^2) - \varepsilon_{12}^{\psi}\sin(2\psi)) \\ h_{rUC}(\varepsilon_1^{\psi}\sin(2\psi)/2 - \varepsilon_2^{\psi}\sin(2\psi)/2 + \varepsilon_{12}^{\psi}\cos(2\psi)) \\ 0 \end{bmatrix}$$

B2
$$\begin{bmatrix} u_1(h_{rUC}/2,-w_{rUC}/2,\overline{t}_{rUC}/2) \\ u_2(h_{rUC}/2,-w_{rUC}/2,\overline{t}_{rUC}/2) \\ u_3(h_{rUC}/2,-w_{rUC}/2,\overline{t}_{rUC}/2) \end{bmatrix} - \begin{bmatrix} -u_1(-h_{rUC}/2,-w_{rUC}/2,\overline{t}_{rUC}/2) \\ -u_2(-h_{rUC}/2,-w_{rUC}/2,\overline{t}_{rUC}/2) \\ u_3(-h_{rUC}/2,-w_{rUC}/2,\overline{t}_{rUC}/2) \end{bmatrix} = \begin{bmatrix} -w_{rUC}(\varepsilon_1^{\psi}\sin(2\psi)/2 - \varepsilon_2^{\psi}\sin(2\psi)/2 + \varepsilon_{12}^{\psi}\cos(2\psi)) \\ -w_{rUC}(\varepsilon_1^{\psi}(1-\cos(\psi)^2) + \varepsilon_2^{\psi}\cos(\psi)^2 + \varepsilon_{12}^{\psi}\sin(2\psi)) \\ 0 \end{bmatrix}$$

Vertex 1 Upper $u(x,y,z) = u(-h_{rUC}/2, -w_{rUC}/2, \pm\overline{t}_{rUC}/2)$

B1-B2

$$\begin{bmatrix} -2\cdot u_1(-h_{rUC}/2,\,-w_{rUC}/2,\,\overline{t}_{rUC}/2) \\ -2\cdot u_2(-h_{rUC}/2,\,-w_{rUC}/2,\,\overline{t}_{rUC}/2) \\ 0 \end{bmatrix} = \begin{bmatrix} h_{rUC}(\varepsilon_1^\psi\cos(\psi)^2 + \varepsilon_2^\psi(1-\cos(\psi)^2) - \varepsilon_{12}^\psi\sin(2\psi)) + w_{rUC}(\varepsilon_1^\psi\sin(2\psi)/2 - \varepsilon_2^\psi\sin(2\psi)/2 + \varepsilon_{12}^\psi\cos(2\psi)) \\ h_{rUC}(\varepsilon_1^\psi\sin(2\psi)/2 - \varepsilon_2^\psi\sin(2\psi)/2 + \varepsilon_{12}^\psi\cos(2\psi)) + w_{rUC}(\varepsilon_1^\psi(1-\cos(\psi)^2) + \varepsilon_2^\psi\cos(\psi)^2 + \varepsilon_{12}^\psi\sin(2\psi)) \\ 0 \end{bmatrix}$$

B1+B2

$$\begin{bmatrix} 2\cdot u_1(h_{rUC}/2,\,-w_{rUC}/2,\,\overline{t}_{rUC}/2) \\ 2\cdot u_2(h_{rUC}/2,\,-w_{rUC}/2,\,\overline{t}_{rUC}/2) \\ 2\cdot u_3(h_{rUC}/2,\,-w_{rUC}/2,\,\overline{t}_{rUC}/2) \end{bmatrix} = \begin{bmatrix} h_{rUC}(\varepsilon_1^\psi\cos(\psi)^2 + \varepsilon_2^\psi(1-\cos(\psi)^2) - \varepsilon_{12}^\psi\sin(2\psi)) - w_{rUC}(\varepsilon_1^\psi\sin(2\psi)/2 - \varepsilon_2^\psi\sin(2\psi)/2 + \varepsilon_{12}^\psi\cos(2\psi)) \\ h_{rUC}(\varepsilon_1^\psi\sin(2\psi)/2 - \varepsilon_2^\psi\sin(2\psi)/2 + \varepsilon_{12}^\psi\cos(2\psi)) - w_{rUC}(\varepsilon_1^\psi(1-\cos(\psi)^2) + \varepsilon_2^\psi\cos(\psi)^2 + \varepsilon_{12}^\psi\sin(2\psi)) \\ 0 \end{bmatrix}$$

B1+2·B2

$$\begin{bmatrix} 3\cdot u_1(h_{rUC}/2,\,-w_{rUC}/2,\,\overline{t}_{rUC}/2) \\ 3\cdot u_2(h_{rUC}/2,\,-w_{rUC}/2,\,\overline{t}_{rUC}/2) \\ 3\cdot u_3(h_{rUC}/2,\,-w_{rUC}/2,\,\overline{t}_{rUC}/2) \end{bmatrix} + \begin{bmatrix} u_1(-h_{rUC}/2,\,-w_{rUC}/2,\,\overline{t}_{rUC}/2) \\ u_2(-h_{rUC}/2,\,-w_{rUC}/2,\,\overline{t}_{rUC}/2) \\ -3\cdot u_3(-h_{rUC}/2,\,-w_{rUC}/2,\,\overline{t}_{rUC}/2) \end{bmatrix} = \begin{bmatrix} h_{rUC}(\varepsilon_1^\psi\cos(\psi)^2 + \varepsilon_2^\psi(1-\cos(\psi)^2) - \varepsilon_{12}^\psi\sin(2\psi)) - 2w_{rUC}(\varepsilon_1^\psi\sin(2\psi)/2 - \varepsilon_2^\psi\sin(2\psi)/2 + \varepsilon_{12}^\psi\cos(2\psi)) \\ h_{rUC}(\varepsilon_1^\psi\sin(2\psi)/2 - \varepsilon_2^\psi\sin(2\psi)/2 + \varepsilon_{12}^\psi\cos(2\psi)) - 2w_{rUC}(\varepsilon_1^\psi(1-\cos(\psi)^2) + \varepsilon_2^\psi\cos(\psi)^2 + \varepsilon_{12}^\psi\sin(2\psi)) \\ 0 \end{bmatrix}$$

B5I-B6II

$$\begin{bmatrix} u_1(h_{rUC}/2,\,-w_{rUC}/2,\,\overline{t}_{rUC}/2) \\ u_2(h_{rUC}/2,\,-w_{rUC}/2,\,\overline{t}_{rUC}/2) \\ u_3(h_{rUC}/2,\,-w_{rUC}/2,\,\overline{t}_{rUC}/2) \end{bmatrix} - \begin{bmatrix} u_1(h_{rUC}/2,\,-w_{rUC}/2,\,-\overline{t}_{rUC}/2) \\ u_2(h_{rUC}/2,\,-w_{rUC}/2,\,-\overline{t}_{rUC}/2) \\ -u_3(h_{rUC}/2,\,-w_{rUC}/2,\,-\overline{t}_{rUC}/2) \end{bmatrix} = \begin{bmatrix} 0 \\ 0 \\ 0 \end{bmatrix}$$

(B1+2·B2) −3·(B5I-B6II)

$$\begin{bmatrix} u_1(-h_{rUC}/2,\,-w_{rUC}/2,\,\overline{t}_{rUC}/2) \\ u_2(-h_{rUC}/2,\,-w_{rUC}/2,\,\overline{t}_{rUC}/2) \\ -3\cdot u_3(-h_{rUC}/2,\,-w_{rUC}/2,\,\overline{t}_{rUC}/2) \end{bmatrix} + \begin{bmatrix} 3\cdot u_1(h_{rUC}/2,\,-w_{rUC}/2,\,-\overline{t}_{rUC}/2) \\ 3\cdot u_2(h_{rUC}/2,\,-w_{rUC}/2,\,-\overline{t}_{rUC}/2) \\ -3\cdot u_3(h_{rUC}/2,\,-w_{rUC}/2,\,-\overline{t}_{rUC}/2) \end{bmatrix} = \begin{bmatrix} h_{rUC}(\varepsilon_1^\psi\cos(\psi)^2 + \varepsilon_2^\psi(1-\cos(\psi)^2) - \varepsilon_{12}^\psi\sin(2\psi)) - 2w_{rUC}(\varepsilon_1^\psi\sin(2\psi)/2 - \varepsilon_2^\psi\sin(2\psi)/2 + \varepsilon_{12}^\psi\cos(2\psi)) \\ h_{rUC}(\varepsilon_1^\psi\sin(2\psi)/2 - \varepsilon_2^\psi\sin(2\psi)/2 + \varepsilon_{12}^\psi\cos(2\psi)) - 2w_{rUC}(\varepsilon_1^\psi(1-\cos(\psi)^2) + \varepsilon_2^\psi\cos(\psi)^2 + \varepsilon_{12}^\psi\sin(2\psi)) \\ 0 \end{bmatrix}$$

B5I

$$\begin{bmatrix} u_1(h_{rUC}/2,\,-y,\,\overline{t}_{rUC}/2) \\ u_2(h_{rUC}/2,\,-y,\,\overline{t}_{rUC}/2) \\ u_3(h_{rUC}/2,\,-y,\,\overline{t}_{rUC}/2) \end{bmatrix} + \begin{bmatrix} u_1(0,\,y,\,\overline{t}_{rUC}/2) \\ u_2(0,\,y,\,\overline{t}_{rUC}/2) \\ u_3(0,\,y,\,\overline{t}_{rUC}/2) \end{bmatrix} = \begin{bmatrix} h_{rUC}(\varepsilon_1^\psi\cos(\psi)^2 + \varepsilon_2^\psi(1-\cos(\psi)^2) - \varepsilon_{12}^\psi\sin(2\psi))/2 \\ h_{rUC}((\varepsilon_1^\psi\sin(2\psi))/2 - (\varepsilon_2^\psi\sin(2\psi))/2 + \varepsilon_{12}^\psi\cos(2\psi))/2 \\ \varepsilon_3\overline{t}_{rUC} \end{bmatrix}$$

B5II

$$\begin{bmatrix} u_1(-h_{rUC}/2,\,-y,\,\overline{t}_{rUC}/2) \\ u_2(-h_{rUC}/2,\,-y,\,\overline{t}_{rUC}/2) \\ u_3(-h_{rUC}/2,\,-y,\,\overline{t}_{rUC}/2) \end{bmatrix} + \begin{bmatrix} u_1(0,\,y,\,\overline{t}_{rUC}/2) \\ u_2(0,\,y,\,\overline{t}_{rUC}/2) \\ u_3(0,\,y,\,\overline{t}_{rUC}/2) \end{bmatrix} = \begin{bmatrix} -h_{rUC}(\varepsilon_1^\psi\cos(\psi)^2 + \varepsilon_2^\psi(1-\cos(\psi)^2) - \varepsilon_{12}^\psi\sin(2\psi))/2 \\ -h_{rUC}((\varepsilon_1^\psi\sin(2\psi))/2 - (\varepsilon_2^\psi\sin(2\psi))/2 + \varepsilon_{12}^\psi\cos(2\psi))/2 \\ \varepsilon_3\overline{t}_{rUC} \end{bmatrix}$$

Vertex 1 Upper $u(x,y,z) = u(-h_{rUC}/2, -w_{rUC}/2, \pm\overline{t}_{rUC}/2)$

B6I
$$\begin{bmatrix} u_1(-h_{rUC}/2,\,-y,\,\overline{t}_{rUC}/2) \\ u_2(-h_{rUC}/2,\,-y,\,\overline{t}_{rUC}/2) \\ u_3(-h_{rUC}/2,\,-y,\,\overline{t}_{rUC}/2) \end{bmatrix} + \begin{bmatrix} u_1(0,\,y,\,-\overline{t}_{rUC}/2) \\ u_2(0,\,y,\,-\overline{t}_{rUC}/2) \\ -u_3(0,\,y,\,-\overline{t}_{rUC}/2) \end{bmatrix} = \begin{bmatrix} -h_{rUC}(\varepsilon_1^{\psi}\cos(\psi)^2 + \varepsilon_2^{\psi}(1-\cos(\psi)^2) - \varepsilon_{12}^{\psi}\sin(2\psi))/2 \\ -h_{rUC}((\varepsilon_1^{\psi}\sin(2\psi))/2 - (\varepsilon_2^{\psi}\sin(2\psi))/2 + \varepsilon_{12}^{\psi}\cos(2\psi))/2 \\ \varepsilon_3\overline{t}_{rUC} \end{bmatrix}$$

B6II
$$\begin{bmatrix} u_1(+h_{rUC}/2,\,-y,\,\overline{t}_{rUC}/2) \\ u_2(+h_{rUC}/2,\,-y,\,\overline{t}_{rUC}/2) \\ u_3(+h_{rUC}/2,\,-y,\,\overline{t}_{rUC}/2) \end{bmatrix} + \begin{bmatrix} u_1(0,\,y,\,-\overline{t}_{rUC}/2) \\ u_2(0,\,y,\,-\overline{t}_{rUC}/2) \\ -u_3(0,\,y,\,-\overline{t}_{rUC}/2) \end{bmatrix} = \begin{bmatrix} h_{rUC}(\varepsilon_1^{\psi}\cos(\psi)^2 + \varepsilon_2^{\psi}(1-\cos(\psi)^2) - \varepsilon_{12}^{\psi}\sin(2\psi))/2 \\ h_{rUC}((\varepsilon_1^{\psi}\sin(2\psi))/2 - (\varepsilon_2^{\psi}\sin(2\psi))/2 + \varepsilon_{12}^{\psi}\cos(2\psi))/2 \\ \varepsilon_3\overline{t}_{rUC} \end{bmatrix}$$

B5I-B6II
$$\begin{bmatrix} u_1(0,\,y,\,\overline{t}_{rUC}/2) \\ u_2(0,\,y,\,\overline{t}_{rUC}/2) \\ u_3(0,\,y,\,\overline{t}_{rUC}/2) \end{bmatrix} - \begin{bmatrix} u_1(0,\,y,\,-\overline{t}_{rUC}/2) \\ u_2(0,\,y,\,-\overline{t}_{rUC}/2) \\ -u_3(0,\,y,\,-\overline{t}_{rUC}/2) \end{bmatrix} = \begin{bmatrix} 0 \\ 0 \\ 0 \end{bmatrix}$$

(B5II-B6I)-B1
$$-\begin{bmatrix} u_1(h_{rUC}/2,\,y,\,-\overline{t}_{rUC}/2) \\ u_2(h_{rUC}/2,\,y,\,-\overline{t}_{rUC}/2) \\ -u_3(h_{rUC}/2,\,y,\,-\overline{t}_{rUC}/2) \end{bmatrix} + \begin{bmatrix} u_1(-h_{rUC}/2,\,y,\,\overline{t}_{rUC}/2) \\ u_2(-h_{rUC}/2,\,y,\,\overline{t}_{rUC}/2) \\ u_3(-h_{rUC}/2,\,y,\,\overline{t}_{rUC}/2) \end{bmatrix} = \begin{bmatrix} -h_{rUC}(\varepsilon_1^{\psi}\cos(\psi)^2 + \varepsilon_2^{\psi}(1-\cos(\psi)^2) - \varepsilon_{12}^{\psi}\sin(2\psi)) \\ -h_{rUC}(\varepsilon_1^{\psi}\sin(2\psi)/2 - \varepsilon_2^{\psi}\sin(2\psi)/2 + \varepsilon_{12}^{\psi}\cos(2\psi)) \\ 0 \end{bmatrix}$$

Edge 2 Upper Center = B2 ∩ B5I ∩ B5II, $u(x,y,z) = u(0, -w_{rUC}/2, \overline{t}_{rUC}/2)$

B2
$$\begin{bmatrix} u_1(0,\,-w_{rUC}/2,\,\overline{t}_{rUC}/2) \\ u_2(0,\,-w_{rUC}/2,\,\overline{t}_{rUC}/2) \\ u_3(0,\,-w_{rUC}/2,\,\overline{t}_{rUC}/2) \end{bmatrix} - \begin{bmatrix} -u_1(0,\,-w_{rUC}/2,\,\overline{t}_{rUC}/2) \\ -u_2(0,\,-w_{rUC}/2,\,\overline{t}_{rUC}/2) \\ u_3(0,\,-w_{rUC}/2,\,\overline{t}_{rUC}/2) \end{bmatrix} = \begin{bmatrix} -w_{rUC}(\varepsilon_1^{\psi}\sin(2\psi)/2 - \varepsilon_2^{\psi}\sin(2\psi)/2 + \varepsilon_{12}^{\psi}\cos(2\psi)) \\ -w_{rUC}(\varepsilon_1^{\psi}(1-\cos(\psi)^2) + \varepsilon_2^{\psi}\cos(\psi)^2 + \varepsilon_{12}^{\psi}\sin(2\psi)) \\ 0 \end{bmatrix}$$

B5I
$$\begin{bmatrix} u_1(h_{rUC}/2,\,w_{rUC}/2,\,\overline{t}_{rUC}/2) \\ u_2(h_{rUC}/2,\,w_{rUC}/2,\,\overline{t}_{rUC}/2) \\ u_3(h_{rUC}/2,\,w_{rUC}/2,\,\overline{t}_{rUC}/2) \end{bmatrix} + \begin{bmatrix} u_1(0,\,-w_{rUC}/2,\,\overline{t}_{rUC}/2) \\ u_2(0,\,-w_{rUC}/2,\,\overline{t}_{rUC}/2) \\ u_3(0,\,-w_{rUC}/2,\,\overline{t}_{rUC}/2) \end{bmatrix} = \begin{bmatrix} h_{rUC}(\varepsilon_1^{\psi}\cos(\psi)^2 + \varepsilon_2^{\psi}(1-\cos(\psi)^2) - \varepsilon_{12}^{\psi}\sin(2\psi))/2 \\ h_{rUC}((\varepsilon_1^{\psi}\sin(2\psi))/2 - (\varepsilon_2^{\psi}\sin(2\psi))/2 + \varepsilon_{12}^{\psi}\cos(2\psi))/2 \\ \varepsilon_3\overline{t}_{rUC} \end{bmatrix}$$

B5II
$$\begin{bmatrix} u_1(-h_{rUC}/2,\,w_{rUC}/2,\,\overline{t}_{rUC}/2) \\ u_2(-h_{rUC}/2,\,w_{rUC}/2,\,\overline{t}_{rUC}/2) \\ u_3(-h_{rUC}/2,\,w_{rUC}/2,\,\overline{t}_{rUC}/2) \end{bmatrix} + \begin{bmatrix} u_1(0,\,-w_{rUC}/2,\,\overline{t}_{rUC}/2) \\ u_2(0,\,-w_{rUC}/2,\,\overline{t}_{rUC}/2) \\ u_3(0,\,-w_{rUC}/2,\,\overline{t}_{rUC}/2) \end{bmatrix} = \begin{bmatrix} -h_{rUC}(\varepsilon_1^{\psi}\cos(\psi)^2 + \varepsilon_2^{\psi}(1-\cos(\psi)^2) - \varepsilon_{12}^{\psi}\sin(2\psi))/2 \\ -h_{rUC}((\varepsilon_1^{\psi}\sin(2\psi))/2 - (\varepsilon_2^{\psi}\sin(2\psi))/2 + \varepsilon_{12}^{\psi}\cos(2\psi))/2 \\ \varepsilon_3\overline{t}_{rUC} \end{bmatrix}$$

Edge 2 Upper Center = B2 ∩ B5I ∩ B5II, $u(x,y,z) = u(0,-w_{rUC}/2,\overline{t}_{rUC}/2)$

B2-B5I

$$\begin{bmatrix} u_1(0,-w_{rUC}/2,\overline{t}_{rUC}/2) \\ u_2(0,-w_{rUC}/2,\overline{t}_{rUC}/2) \\ -u_3(0,-w_{rUC}/2,\overline{t}_{rUC}/2) \end{bmatrix} - \begin{bmatrix} u_1(h_{rUC}/2,w_{rUC}/2,\overline{t}_{rUC}/2) \\ u_2(h_{rUC}/2,w_{rUC}/2,\overline{t}_{rUC}/2) \\ u_3(h_{rUC}/2,w_{rUC}/2,\overline{t}_{rUC}/2) \end{bmatrix} = \begin{bmatrix} -h_{rUC}(\varepsilon_1^{\psi}\cos(\psi)^2 + \varepsilon_2^{\psi}(1-\cos(\psi)^2) - \varepsilon_{12}^{\psi}\sin(2\psi))/2 - w_{rUC}(\varepsilon_1^{\psi}\sin(2\psi)/2 - \varepsilon_2^{\psi}\sin(2\psi)/2 + \varepsilon_{12}^{\psi}\cos(2\psi)) \\ -h_{rUC}((\varepsilon_1^{\psi}\sin(2\psi))/2 - (\varepsilon_2^{\psi}\sin(2\psi))/2 + \varepsilon_{12}^{\psi}\cos(2\psi))/2 - w_{rUC}(\varepsilon_1^{\psi}(1-\cos(\psi)^2) + \varepsilon_2^{\psi}\cos(\psi)^2 + \varepsilon_{12}^{\psi}\sin(2\psi)) \\ -\varepsilon_3\overline{t}_{rUC} \end{bmatrix}$$

B2-B5II

$$\begin{bmatrix} u_1(0,-w_{rUC}/2,\overline{t}_{rUC}/2) \\ u_2(0,-w_{rUC}/2,\overline{t}_{rUC}/2) \\ -u_3(0,-w_{rUC}/2,\overline{t}_{rUC}/2) \end{bmatrix} - \begin{bmatrix} u_1(-h_{rUC}/2,w_{rUC}/2,\overline{t}_{rUC}/2) \\ u_2(-h_{rUC}/2,w_{rUC}/2,\overline{t}_{rUC}/2) \\ u_3(-h_{rUC}/2,w_{rUC}/2,\overline{t}_{rUC}/2) \end{bmatrix} = \begin{bmatrix} h_{rUC}(\varepsilon_1^{\psi}\cos(\psi)^2 + \varepsilon_2^{\psi}(1-\cos(\psi)^2) - \varepsilon_{12}^{\psi}\sin(2\psi))/2 - w_{rUC}(\varepsilon_1^{\psi}\sin(2\psi)/2 - \varepsilon_2^{\psi}\sin(2\psi)/2 + \varepsilon_{12}^{\psi}\cos(2\psi)) \\ h_{rUC}((\varepsilon_1^{\psi}\sin(2\psi))/2 - (\varepsilon_2^{\psi}\sin(2\psi))/2 + \varepsilon_{12}^{\psi}\cos(2\psi))/2 - w_{rUC}(\varepsilon_1^{\psi}(1-\cos(\psi)^2) + \varepsilon_2^{\psi}\cos(\psi)^2 + \varepsilon_{12}^{\psi}\sin(2\psi)) \\ -\varepsilon_3\overline{t}_{rUC} \end{bmatrix}$$

Edge 2 Lower Center = B2 ∩ B6I ∩ B6II, $u(x,y,z) = u(0,-w_{rUC}/2,-\overline{t}_{rUC}/2)$

B2

$$\begin{bmatrix} u_1(0,-w_{rUC}/2,-\overline{t}_{rUC}/2) \\ u_2(0,-w_{rUC}/2,-\overline{t}_{rUC}/2) \\ u_3(0,-w_{rUC}/2,-\overline{t}_{rUC}/2) \end{bmatrix} - \begin{bmatrix} -u_1(0,-w_{rUC}/2,-\overline{t}_{rUC}/2) \\ -u_2(0,-w_{rUC}/2,-\overline{t}_{rUC}/2) \\ u_3(0,-w_{rUC}/2,-\overline{t}_{rUC}/2) \end{bmatrix} = \begin{bmatrix} -w_{rUC}(\varepsilon_1^{\psi}\sin(2\psi)/2 - \varepsilon_2^{\psi}\sin(2\psi)/2 + \varepsilon_{12}^{\psi}\cos(2\psi)) \\ -w_{rUC}(\varepsilon_1^{\psi}(1-\cos(\psi)^2) + \varepsilon_2^{\psi}\cos(\psi)^2 + \varepsilon_{12}^{\psi}\sin(2\psi)) \\ 0 \end{bmatrix}$$

B6I

$$\begin{bmatrix} u_1(-h_{rUC}/2,w_{rUC}/2,-\overline{t}_{rUC}/2) \\ u_2(-h_{rUC}/2,w_{rUC}/2,-\overline{t}_{rUC}/2) \\ u_3(-h_{rUC}/2,w_{rUC}/2,-\overline{t}_{rUC}/2) \end{bmatrix} + \begin{bmatrix} u_1(0,-w_{rUC}/2,-\overline{t}_{rUC}/2) \\ u_2(0,-w_{rUC}/2,-\overline{t}_{rUC}/2) \\ u_3(0,-w_{rUC}/2,-\overline{t}_{rUC}/2) \end{bmatrix} = \begin{bmatrix} -h_{rUC}(\varepsilon_1^{\psi}\cos(\psi)^2 + \varepsilon_2^{\psi}(1-\cos(\psi)^2) - \varepsilon_{12}^{\psi}\sin(2\psi))/2 \\ -h_{rUC}((\varepsilon_1^{\psi}\sin(2\psi))/2 - (\varepsilon_2^{\psi}\sin(2\psi))/2 + \varepsilon_{12}^{\psi}\cos(2\psi))/2 \\ \varepsilon_3\overline{t}_{rUC} \end{bmatrix}$$

B6II

$$\begin{bmatrix} u_1(h_{rUC}/2,w_{rUC}/2,-\overline{t}_{rUC}/2) \\ u_2(h_{rUC}/2,w_{rUC}/2,-\overline{t}_{rUC}/2) \\ u_3(h_{rUC}/2,w_{rUC}/2,-\overline{t}_{rUC}/2) \end{bmatrix} + \begin{bmatrix} u_1(0,-w_{rUC}/2,-\overline{t}_{rUC}/2) \\ u_2(0,-w_{rUC}/2,-\overline{t}_{rUC}/2) \\ u_3(0,-w_{rUC}/2,-\overline{t}_{rUC}/2) \end{bmatrix} = \begin{bmatrix} h_{rUC}(\varepsilon_1^{\psi}\cos(\psi)^2 + \varepsilon_2^{\psi}(1-\cos(\psi)^2) - \varepsilon_{12}^{\psi}\sin(2\psi))/2 \\ h_{rUC}((\varepsilon_1^{\psi}\sin(2\psi))/2 - (\varepsilon_2^{\psi}\sin(2\psi))/2 + \varepsilon_{12}^{\psi}\cos(2\psi))/2 \\ \varepsilon_3\overline{t}_{rUC} \end{bmatrix}$$

B2-B6I

$$\begin{bmatrix} u_1(0,-w_{rUC}/2,-\overline{t}_{rUC}/2) \\ u_2(0,-w_{rUC}/2,-\overline{t}_{rUC}/2) \\ -u_3(0,-w_{rUC}/2,-\overline{t}_{rUC}/2) \end{bmatrix} - \begin{bmatrix} u_1(-h_{rUC}/2,w_{rUC}/2,-\overline{t}_{rUC}/2) \\ u_2(-h_{rUC}/2,w_{rUC}/2,-\overline{t}_{rUC}/2) \\ u_3(-h_{rUC}/2,w_{rUC}/2,-\overline{t}_{rUC}/2) \end{bmatrix} = \begin{bmatrix} h_{rUC}(\varepsilon_1^{\psi}\cos(\psi)^2 + \varepsilon_2^{\psi}(1-\cos(\psi)^2) - \varepsilon_{12}^{\psi}\sin(2\psi))/2 - w_{rUC}(\varepsilon_1^{\psi}\sin(2\psi)/2 - \varepsilon_2^{\psi}\sin(2\psi)/2 + \varepsilon_{12}^{\psi}\cos(2\psi)) \\ h_{rUC}((\varepsilon_1^{\psi}\sin(2\psi))/2 - (\varepsilon_2^{\psi}\sin(2\psi))/2 + \varepsilon_{12}^{\psi}\cos(2\psi))/2 - w_{rUC}(\varepsilon_1^{\psi}(1-\cos(\psi)^2) + \varepsilon_2^{\psi}\cos(\psi)^2 + \varepsilon_{12}^{\psi}\sin(2\psi)) \\ -\varepsilon_3\overline{t}_{rUC} \end{bmatrix}$$

B2-B6II

$$\begin{bmatrix} u_1(0,-w_{rUC}/2,-\overline{t}_{rUC}/2) \\ u_2(0,-w_{rUC}/2,-\overline{t}_{rUC}/2) \\ -u_3(0,-w_{rUC}/2,-\overline{t}_{rUC}/2) \end{bmatrix} - \begin{bmatrix} u_1(h_{rUC}/2,w_{rUC}/2,-\overline{t}_{rUC}/2) \\ u_2(h_{rUC}/2,w_{rUC}/2,-\overline{t}_{rUC}/2) \\ u_3(h_{rUC}/2,w_{rUC}/2,-\overline{t}_{rUC}/2) \end{bmatrix} = \begin{bmatrix} -h_{rUC}(\varepsilon_1^{\psi}\cos(\psi)^2 + \varepsilon_2^{\psi}(1-\cos(\psi)^2) - \varepsilon_{12}^{\psi}\sin(2\psi))/2 - w_{rUC}(\varepsilon_1^{\psi}\sin(2\psi)/2 - \varepsilon_2^{\psi}\sin(2\psi)/2 + \varepsilon_{12}^{\psi}\cos(2\psi)) \\ -h_{rUC}((\varepsilon_1^{\psi}\sin(2\psi))/2 - (\varepsilon_2^{\psi}\sin(2\psi))/2 + \varepsilon_{12}^{\psi}\cos(2\psi))/2 - w_{rUC}(\varepsilon_1^{\psi}(1-\cos(\psi)^2) + \varepsilon_2^{\psi}\cos(\psi)^2 + \varepsilon_{12}^{\psi}\sin(2\psi)) \\ -\varepsilon_3\overline{t}_{rUC} \end{bmatrix}$$

Edge 4 Upper Center = B4 ∩ B5I ∩ B5II, $u(x,y,z) = u(0, w_{rUC}/2, \overline{t}_{rUC}/2)$

B4
$$\begin{bmatrix} u_1(0, w_{rUC}/2, -\overline{t}_{rUC}/2) \\ u_2(0, w_{rUC}/2, -\overline{t}_{rUC}/2) \\ u_3(0, w_{rUC}/2, -\overline{t}_{rUC}/2) \end{bmatrix} + \begin{bmatrix} u_1(0, w_{rUC}/2, \overline{t}_{rUC}/2) \\ u_2(0, w_{rUC}/2, \overline{t}_{rUC}/2) \\ u_3(0, w_{rUC}/2, \overline{t}_{rUC}/2) \end{bmatrix} = \begin{bmatrix} w_{rUC}(\varepsilon_1^{\psi} \sin(2\psi)/2 - \varepsilon_2^{\psi} \sin(2\psi)/2 + \varepsilon_{12}^{\psi} \cos(2\psi)) \\ w_{rUC}(\varepsilon_1^{\psi}(1-\cos(\psi)^2) + \varepsilon_2^{\psi} \cos(\psi)^2 + \varepsilon_{12}^{\psi} \sin(2\psi)) \\ 0 \end{bmatrix}$$

B5I
$$\begin{bmatrix} u_1(h_{rUC}/2, -w_{rUC}/2, \overline{t}_{rUC}/2) \\ u_2(h_{rUC}/2, -w_{rUC}/2, \overline{t}_{rUC}/2) \\ u_3(h_{rUC}/2, -w_{rUC}/2, \overline{t}_{rUC}/2) \end{bmatrix} + \begin{bmatrix} u_1(0, w_{rUC}/2, \overline{t}_{rUC}/2) \\ u_2(0, w_{rUC}/2, \overline{t}_{rUC}/2) \\ u_3(0, w_{rUC}/2, \overline{t}_{rUC}/2) \end{bmatrix} = \begin{bmatrix} h_{rUC}(\varepsilon_1^{\psi} \cos(\psi)^2 + \varepsilon_2^{\psi}(1-\cos(\psi)^2) - \varepsilon_{12}^{\psi} \sin(2\psi))/2 \\ h_{rUC}((\varepsilon_1^{\psi} \sin(2\psi))/2 - (\varepsilon_2^{\psi} \sin(2\psi))/2 + \varepsilon_{12}^{\psi} \cos(2\psi))/2 \\ \varepsilon_3 \overline{t}_{rUC} \end{bmatrix}$$

B5II
$$\begin{bmatrix} u_1(-h_{rUC}/2, -w_{rUC}/2, \overline{t}_{rUC}/2) \\ u_2(-h_{rUC}/2, -w_{rUC}/2, \overline{t}_{rUC}/2) \\ u_3(-h_{rUC}/2, -w_{rUC}/2, \overline{t}_{rUC}/2) \end{bmatrix} + \begin{bmatrix} u_1(0, w_{rUC}/2, \overline{t}_{rUC}/2) \\ u_2(0, w_{rUC}/2, \overline{t}_{rUC}/2) \\ u_3(0, w_{rUC}/2, \overline{t}_{rUC}/2) \end{bmatrix} = \begin{bmatrix} -h_{rUC}(\varepsilon_1^{\psi} \cos(\psi)^2 + \varepsilon_2^{\psi}(1-\cos(\psi)^2) - \varepsilon_{12}^{\psi} \sin(2\psi))/2 \\ -h_{rUC}((\varepsilon_1^{\psi} \sin(2\psi))/2 - (\varepsilon_2^{\psi} \sin(2\psi))/2 + \varepsilon_{12}^{\psi} \cos(2\psi))/2 \\ \varepsilon_3 \overline{t}_{rUC} \end{bmatrix}$$

Edge 4 Lower Center = B4 ∩ B6I ∩ B6II, $u(x,y,z) = u(0, w_{rUC}/2, -\overline{t}_{rUC}/2)$

B4
$$\begin{bmatrix} u_1(0, w_{rUC}/2, -\overline{t}_{rUC}/2) \\ u_2(0, w_{rUC}/2, -\overline{t}_{rUC}/2) \\ u_3(0, w_{rUC}/2, -\overline{t}_{rUC}/2) \end{bmatrix} + \begin{bmatrix} u_1(0, w_{rUC}/2, \overline{t}_{rUC}/2) \\ u_2(0, w_{rUC}/2, \overline{t}_{rUC}/2) \\ u_3(0, w_{rUC}/2, \overline{t}_{rUC}/2) \end{bmatrix} = \begin{bmatrix} w_{rUC}(\varepsilon_1^{\psi} \sin(2\psi)/2 - \varepsilon_2^{\psi} \sin(2\psi)/2 + \varepsilon_{12}^{\psi} \cos(2\psi)) \\ w_{rUC}(\varepsilon_1^{\psi}(1-\cos(\psi)^2) + \varepsilon_2^{\psi} \cos(\psi)^2 + \varepsilon_{12}^{\psi} \sin(2\psi)) \\ 0 \end{bmatrix}$$

B6I
$$\begin{bmatrix} u_1(-h_{rUC}/2, -w_{rUC}/2, -\overline{t}_{rUC}/2) \\ u_2(-h_{rUC}/2, -w_{rUC}/2, -\overline{t}_{rUC}/2) \\ u_3(-h_{rUC}/2, -w_{rUC}/2, -\overline{t}_{rUC}/2) \end{bmatrix} + \begin{bmatrix} u_1(0, w_{rUC}/2, -\overline{t}_{rUC}/2) \\ u_2(0, w_{rUC}/2, -\overline{t}_{rUC}/2) \\ u_3(0, w_{rUC}/2, -\overline{t}_{rUC}/2) \end{bmatrix} = \begin{bmatrix} -h_{rUC}(\varepsilon_1^{\psi} \cos(\psi)^2 + \varepsilon_2^{\psi}(1-\cos(\psi)^2) - \varepsilon_{12}^{\psi} \sin(2\psi))/2 \\ -h_{rUC}((\varepsilon_1^{\psi} \sin(2\psi))/2 - (\varepsilon_2^{\psi} \sin(2\psi))/2 + \varepsilon_{12}^{\psi} \cos(2\psi))/2 \\ \varepsilon_3 \overline{t}_{rUC} \end{bmatrix}$$

B6II
$$\begin{bmatrix} u_1(h_{rUC}/2, -w_{rUC}/2, -\overline{t}_{rUC}/2) \\ u_2(h_{rUC}/2, -w_{rUC}/2, -\overline{t}_{rUC}/2) \\ u_3(h_{rUC}/2, -w_{rUC}/2, -\overline{t}_{rUC}/2) \end{bmatrix} + \begin{bmatrix} u_1(0, w_{rUC}/2, -\overline{t}_{rUC}/2) \\ u_2(0, w_{rUC}/2, -\overline{t}_{rUC}/2) \\ u_3(0, w_{rUC}/2, -\overline{t}_{rUC}/2) \end{bmatrix} = \begin{bmatrix} h_{rUC}(\varepsilon_1^{\psi} \cos(\psi)^2 + \varepsilon_2^{\psi}(1-\cos(\psi)^2) - \varepsilon_{12}^{\psi} \sin(2\psi))/2 \\ h_{rUC}((\varepsilon_1^{\psi} \sin(2\psi))/2 - (\varepsilon_2^{\psi} \sin(2\psi))/2 + \varepsilon_{12}^{\psi} \cos(2\psi))/2 \\ \varepsilon_3 \overline{t}_{rUC} \end{bmatrix}$$

B4-B6I
$$\begin{bmatrix} u_1(0, w_{rUC}/2, \overline{t}_{rUC}/2) \\ u_2(0, w_{rUC}/2, \overline{t}_{rUC}/2) \\ u_3(0, w_{rUC}/2, \overline{t}_{rUC}/2) \end{bmatrix} - \begin{bmatrix} u_1(-h_{rUC}/2, -w_{rUC}/2, -\overline{t}_{rUC}/2) \\ u_2(-h_{rUC}/2, -w_{rUC}/2, -\overline{t}_{rUC}/2) \\ u_3(-h_{rUC}/2, -w_{rUC}/2, -\overline{t}_{rUC}/2) \end{bmatrix} = \begin{bmatrix} h_{rUC}(\varepsilon_1^{\psi} \cos(\psi)^2 + \varepsilon_2^{\psi}(1-\cos(\psi)^2) - \varepsilon_{12}^{\psi} \sin(2\psi))/2 + w_{rUC}(\varepsilon_1^{\psi} \sin(2\psi)/2 - \varepsilon_2^{\psi} \sin(2\psi)/2 + \varepsilon_{12}^{\psi} \cos(2\psi)) \\ h_{rUC}((\varepsilon_1^{\psi} \sin(2\psi))/2 - (\varepsilon_2^{\psi} \sin(2\psi))/2 + \varepsilon_{12}^{\psi} \cos(2\psi))/2 + w_{rUC}(\varepsilon_1^{\psi}(1-\cos(\psi)^2) + \varepsilon_2^{\psi} \cos(\psi)^2 + \varepsilon_{12}^{\psi} \sin(2\psi)) \\ -\varepsilon_3 \overline{t}_{rUC} \end{bmatrix}$$

Edge 4 Lower Center = B4 ∩ B6I ∩ B6II, $u(x,y,z) = u(0, w_rUC/2, -\bar{t}_rUC/2)$

B4-B6II

$$\begin{bmatrix} u_1(0, w_rUC/2, \bar{t}_rUC/2) \\ u_2(0, w_rUC/2, \bar{t}_rUC/2) \\ u_3(0, w_rUC/2, \bar{t}_rUC/2) \end{bmatrix} - \begin{bmatrix} u_1(h_rUC/2, -w_rUC/2, -\bar{t}_rUC/2) \\ u_2(h_rUC/2, -w_rUC/2, -\bar{t}_rUC/2) \\ u_3(h_rUC/2, -w_rUC/2, -\bar{t}_rUC/2) \end{bmatrix} = \begin{bmatrix} -h_rUC(\varepsilon_1^\psi \cos(\psi)^2 + \varepsilon_2^\psi(1-\cos(\psi)^2) - \varepsilon_{12}^\psi \sin(2\psi))/2 + w_rUC(\varepsilon_1^\psi \sin(2\psi)/2 - \varepsilon_2^\psi \sin(2\psi)/2 + \varepsilon_{12}^\psi \cos(2\psi)) \\ -h_rUC((\varepsilon_1^\psi \sin(2\psi)))/2 - (\varepsilon_2^\psi \sin(2\psi)))/2 + \varepsilon_{12}^\psi \cos(2\psi)))/2 + w_rUC(\varepsilon_1^\psi(1-\cos(\psi)^2) + \varepsilon_2^\psi \cos(\psi)^2 + \varepsilon_{12}^\psi \sin(2\psi)) \\ -\varepsilon_3 \bar{t}_rUC \end{bmatrix}$$

Bibliography

[1] T. Hans, J. Cichosz, M. Brand, and R. Hinterhölzl. Finite element simulation of the braiding process for arbitrary mandrel shapes. *Composites Part A: Applied Science and Manufacturing*, 77:124 – 132, Oct 2015.

[2] Jörg Cichosz, Tobias Wehrkamp-Richter, Hannes Körber, Roland Hinterhölzl, and Pedro P. Camanho. Failure and damage characterization of ($\pm 30^\circ$) biaxial braided composites under multiaxial stress states. *Composites Part A: Applied Science and Manufacturing*, 90:748–759, Nov 2016.

[3] M. Schubert. Vergleich eines resin transfer moulding epoxidharzsystems mit einem prepregharzsystem. *Verbundwerkstoffe*, pages 339 – 344, 2009.

[4] E. Marklund, L.E. Asp, and R. Olsson. Transverse strength of unidirectional non-crimp fabric composites: Multiscale modelling. *Composites Part B: Engineering*, 65:47 – 56, Oct 2014.

[5] ST Pinho, R Darvizeh, P Robinson, C Schuecker, and PP Camanho. Material and structural response of polymer-matrix fibre-reinforced composites. *Journal of Composite Materials*, 46(19-20):2313–2341, 2012.

[6] Jakob Gager. *Modeling and Simulation Concepts for Advanced Braided Composites*. Fortschritt-Berichte VDI. Reihe 18, Mechanik/Bruchmechanik. 2013.

[7] J.P. Carey. 1 - introduction to braided composites. In Jason P. Carey, editor, *Handbook of Advances in Braided Composite Materials*, pages 1 – 21. Woodhead Publishing, 2017.

[8] J.P. Carey, G.W. Melenka, A.J. Hunt, and C. Ayranci. 5 - introduction to braided composite material behavior. In Jason P. Carey, editor, *Handbook of Advances in Braided Composite Materials*, pages 207 – 237. Woodhead Publishing, 2017.

[9] G.W. Melenka, A.J. Hunt, J.H. van Ravenhorst, R. Akkerman, C.M. Pastore, F.K. Ko, M. Munro, and J.P. Carey. 3 - manufacturing processes for braided composite materials. In Jason P. Carey, editor, *Handbook of Advances in Braided Composite Materials*, pages 47 – 153. Woodhead Publishing, 2017.

[10] Ajit D. Kelkar and John D. Whitcomb. Characterization and structural behavior of braided composites. Technical Report DOT/FAA/AR-08/52, U.S. Department of Transportation, Federal Aviation Administration, 2009.

[11] John E. Masters and Peter G. Ifju. A phenomenological study of triaxially braided textile composites loaded in tension. *Composites Science and Technology*, 56(3):347 – 358, 1996.

[12] Jens U. Rosenbaum. *Flechten. Rationelle Fertigung faserverstärkter Kunststoffbauteile*. Verlag TÜV Rheinland, 1991.

[13] Brian N. Cox and Gerry Flanagan. Handbook of analytical methods for textile composites. NASA-CR-4750, NASA, 1997.

[14] G. w. Du and P. Popper. Analysis of a circular braiding process for complex shapes. *The Journal of The Textile Institute*, 85(3):316–337, 1994.

[15] J.H. van Ravenhorst and R. Akkerman. Circular braiding take-up speed generation using inverse kinematics. *Composites Part A: Applied Science and Manufacturing*, 64(Supplement C):147 – 158, 2014.

[16] Anthony K. Pickett, Justas Sirtautas, and Andreas Erber. Braiding simulation and prediction of mechanical properties. *Applied Composite Materials*, 16(6):345, Sep 2009.

[17] P. Potluri, A. Rawal, M. Rivaldi, and I. Porat. Geometrical modelling and control of a triaxial braiding machine for producing 3d preforms. *Composites Part A: Applied Science and Manufacturing*, 34(6):481 – 492, 2003. ICMAC 2001 - International Conference for Manufacturing of Advanced Composites.

[18] F. Heieck, F. Hermann, P. Middendorf, and K. Schladitz. Influence of the cover factor of 2d biaxial and triaxial braided carbon composites on their in-plane mechanical properties. *Composite Structures*, 163(Supplement C):114 – 122, 2017.

[19] P. Potluri and A. Manan. Mechanics of non-orthogonally interlaced textile composites. *Composites Part A: Applied Science and Manufacturing*, 38(4):1216 – 1226, 2007.

[20] Rajiv A. Naik. Failure analysis of woven and braided fabric reinforced composites. NASA-CR-194981, NASA, 1994.

[21] ASTM International. ASTM D3171 - Standard Test Methods for Constituent Content of Composite Materials, 2009.

[22] S.V. Lomov, I. Verpoest, T. Peeters, D. Roose, and M. Zako. Nesting in textile laminates: geometrical modelling of the laminate. *Composites Science and Technology*, 63(7):993 – 1007, 2003.

[23] A. Endruweit and A.C. Long. A model for the in-plane permeability of triaxially braided reinforcements. *Composites Part A: Applied Science and Manufacturing*, 42(2):165–172, 2011.

[24] Karin Birkefeld, Mirko Röder, Tjark von Reden, Martina Bulat, and Klaus Drechsler. Characterization of biaxial and triaxial braids: Fiber architecture and mechanical properties. *Applied Composite Materials*, 19(3):259–273, Jun 2012.

[25] Mike Braley and Molly Dingeldein. Advancements in braided materials technology. Technical report, A&P Technology, 2017.

[26] Yentl Swolfs, Ignaas Verpoest, and Larissa Gorbatikh. Maximising the hybrid effect in unidirectional hybrid composites. *Materials & Design*, 93(Supplement C):39 – 45, 2016.

[27] Dmitry S. Ivanov, Fabien Baudry, Björn Van Den Broucke, Stepan V. Lomov, Hang Xie, and Ignaas Verpoest. Failure analysis of triaxial braided composite. *Composites Science and Technology*, 69(9):1372 – 1380, Jul 2009.

[28] A.K. Pickett and M.R.C. Fouinneteau. Material characterisation and calibration of a meso-mechanical damage model for braid reinforced composites. *Composites Part A: Applied Science and Manufacturing*, 37(2):368 – 377, 2006. CompTest 2004.

[29] Carla McGregor, Reza Vaziri, Anoush Poursartip, and Xinran Xiao. Axial crushing of triaxially braided composite tubes at quasi-static and dynamic rates. *Composite Structures*, 157:197–206, dec 2016.

[30] Paul J. Falzon and Israel Herszberg. Mechanical performance of 2-d braided carbon/epoxy composites. *Composites Science and Technology*, 58(2):253 – 265, Jan 1998.

[31] Paul J Falzon, Israel Herszberg, Michael K Bannister, KH Leong, et al. Compression and compression-after-impact properties of 2-d braided carbon/epoxy composites. In *Proceedings of the First Australasian Congress on Applied Mechanics: ACAM-96*, page 297. Institution of Engineers, Australia, 1996.

[32] ASTM International. ASTM D3039 - Standard Test Method for Tensile Properties of Polymer Matrix Composite Materials, 2008.

[33] John E. Masters and Marc A. Portanova. Standard test methods for textile composites. Nasa contractor report 4751, NASA, 1996.

[34] Justin D. Littell, Wieslaw K. Binienda, Gary D. Roberts, and Robert K. Goldberg. Characterization of damage in triaxial braided composites under tensile loading. *Journal of Aerospace Engineering*, 22(3):270 – 279, Jul 2009.

[35] S.V. Lomov, D.S. Ivanov, T.C. Truong, I. Verpoest, F. Baudry, K. Vanden Bosche, and H. Xie. Experimental methodology of study of damage initiation and development in textile composites in uniaxial tensile test. *Composites Science and Technology*, 68(12):2340 – 2349, Sep 2008.

[36] Dmitry Ivanov, Sergey Ivanov, Stepan Lomov, and Ignaas Verpoest. Strain mapping analysis of textile composites. *Optics and Lasers in Engineering*, 47(3-4):360 – 370, Mar 2009.

[37] P Ladeveze and E LeDantec. Damage modelling of the elementary ply for laminated composites. *Composites Science and Technology*, 43(3):257 – 267, 1992.

[38] Stefan Thumfart, Werner Palfinger, and Christian Eitzinger. Accurate fibre orientation measurement for carbon fibre surfaces. *Lecture Notes in Computer Science*, pages 75 – 82, 2013.

[39] Lee W. Kohlman, Justin L. Bail, Gary D. Roberts, Jonathan A. Salem, Richard E. Martin, and Wieslaw K. Binienda. A notched coupon approach for tensile testing of braided composites. *Composites Part A: Applied Science and Manufacturing*, 43(10):1680 – 1688, Oct 2012.

[40] Pierre J. Minguet, Mark J. Fedro, and Christian K. Gunther. Test methods for textile composites. Nasa contractor report 4609, NASA, 1994.

[41] C.T. Sun and Ilsup Chung. An oblique end-tab design for testing off-axis composite specimens. *Composites*, 24(8):619 – 623, Nov 1993.

[42] Bing Pan, Kemao Qian, Huimin Xie, and Anand Asundi. Two-dimensional digital image correlation for in-plane displacement and strain measurement: a review. *Meas. Sci. Technol.*, 20(6), Apr 2009.

[43] GOM mbH, D-38106 Braunschweig. *GOM Aramis User Manual*, 6.1 edition, 2009.

[44] Joon-Hyung Byun. The analytical characterization of 2-d braided textile composites. *Composites Science and Technology*, 60(5):705 – 716, 2000.

[45] P. Potluri, A. Manan, M. Francke, and R.J. Day. Flexural and torsional behaviour of biaxial and triaxial braided composite structures. *Composite Structures*, 75(1-4):377 – 386, Sep 2006.

[46] C. C. Chamis. Simplified composite micromechanics equations for strength, fracture toughness, impact resistance and environmental effects. Technical report, NASA Technical Memorandum 83696, 1984.

[47] W. H.M. Van Dreumel and J. L.M. Kamp. Non hookean behaviour in the fibre direction of carbon-fibre composites and the influence of fibre waviness on the tensile properties. *Journal of Composite Materials*, 11(4):461 – 469, Oct 1977.

[48] I. M. Djordjevic, D. R. Sekulic, M. N. Mitric, and M. M. Stevanovic. Non-hookean elastic behavior and crystallite orientation in carbon fibers. *Journal of Composite Materials*, 44(14):1717 –1727, Jan 2010.

[49] Ulrich Mandel, Robin Taubert, and Roland Hinterhölzl. Three-dimensional nonlinear constitutive model for composites. *Composite Structures*, 142:78 – 86, 2016.

[50] Cagri Ayranci and Jason Carey. 2D braided composites: A review for stiffness critical applications. *Composite Structures*, 85(1):43 – 58, Sep 2008.

[51] Ignaas Verpoest and Stepan V. Lomov. Virtual textile composites software wisetex: Integration with micro-mechanical, permeability and structural analysis. *Composites Science and Technology*, 65:2563–2574, 2005. 20th Anniversary Special Issue.

[52] A.C. Long and L.P. Brown. 8 - modelling the geometry of textile reinforcements for composites: Texgen. In Philippe Boisse, editor, *Composite Reinforcements for Optimum Performance*, Woodhead Publishing Series in Composites Science and Engineering, pages 239–264. Woodhead Publishing, 2011.

[53] Stepan V. Lomov, Dmitry S. Ivanov, Ignaas Verpoest, Masaru Zako, Tetsusei Kurashiki, Hiroaki Nakai, and Satoru Hirosawa. Meso-fe modelling of textile composites: Road map, data flow and algorithms. *Composites Science and Technology*, 67(9):1870–1891, 2007.

[54] Su-Yuen Hsu. Literature reviews on modeling internal geometry of textile composites and rate-independent continuum damage. Technical Report NASA/TM-2011-217079, NASA Langley Research Center, Hampton, VA, United States, 2011.

[55] Gilles Hivet and Philippe Boisse. Consistent mesoscopic mechanical behaviour model for woven composite reinforcements in biaxial tension. *Composites Part*

B: Engineering, 39(2):345–361, 2008.

[56] Q.T. Nguyen, E. Vidal-Salle, P. Boisse, C.H. Park, A. Saouab, J. Breard, and G. Hivet. Mesoscopic scale analyses of textile composite reinforcement compaction. *Composites Part B: Engineering*, 44(1):231 – 241, 2013.

[57] G. Grail, M. Hirsekorn, A. Wendling, G. Hivet, and R. Hambli. Consistent finite element mesh generation for meso-scale modeling of textile composites with preformed and compacted reinforcements. *Composites Part A: Applied Science and Manufacturing*, 55(0):143–151, 2013.

[58] Bassam El Said, Steven Green, and Stephen R. Hallett. Kinematic modelling of 3d woven fabric deformation for structural scale features. *Composites Part A: Applied Science and Manufacturing*, 57(0):95–107, 2014.

[59] Guangming Zhou, Xuekun Sun, and Youqi Wang. Multi-chain digital element analysis in textile mechanics. *Composites Science and Technology*, 64(2):239–244, 2004.

[60] S.D. Green, M.Y. Matveev, A.C. Long, D. Ivanov, and S.R. Hallett. Mechanical modelling of 3d woven composites considering realistic unit cell geometry. *Composite Structures*, 118(0):284–293, 2014.

[61] A. Doitrand, C. Fagiano, F.-X. Irisarri, and M. Hirsekorn. Comparison between voxel and consistent meso-scale models of woven composites. *Composites Part A: Applied Science and Manufacturing*, 73(0):143–154, 2015.

[62] E. Potter, S.T. Pinho, P. Robinson, L. Iannucci, and A.J. McMillan. Mesh generation and geometrical modelling of 3D woven composites with variable tow cross-sections. *Computational Materials Science*, 51(1):103 – 111, Jan 2012.

[63] N. Naouar, E. Vidal-Sall, J. Schneider, E. Maire, and P. Boisse. Meso-scale FE analyses of textile composite reinforcement deformation based on x-ray computed tomography. *Composite Structures*, 116(0):165 – 176, 2014.

[64] J.C. Faes, A. Rezaei, W. Van Paepegem, and J. Degrieck. Accuracy of 2d fe models for prediction of crack initiation in nested textile composites with inhomogeneous intra-yarn fiber volume fractions. *Composite Structures*, 140:11–20, Apr 2016.

[65] N.V. De Carvalho, S.T. Pinho, and P. Robinson. Reducing the domain in the mechanical analysis of periodic structures, with application to woven composites. *Composites Science and Technology*, 71(7):969–979, 2011.

[66] Xiaodong Tang and John D. Whitcomb. General techniques for exploiting periodicity and symmetries in micromechanics analysis of textile composites. *Journal of Composite Materials*, 37(13):1167–1189, Jul 2003.

[67] R.D.B. Sevenois, D. Garoz, F.A. Gilabert, S.W.F. Spronk, S. Fonteyn, M. Heyndrickx, L. Pyl, D. Van Hemelrijck, J. Degrieck, and W. Van Paepegem. Avoiding interpenetrations and the importance of nesting in analytic geometry construction for representative unit cells of woven composite laminates. *Composites Science and Technology*, 136:119–132, Nov 2016.

[68] A.R. Melro, P.P. Camanho, F.M. Andrade Pires, and S.T. Pinho. Numerical simulation of the non-linear deformation of 5-harness satin weaves. *Computational Materials Science*, 61:116 – 126, Aug 2012.

[69] P. Römelt and P.R. Cunningham. A multi-scale finite element approach for modelling damage progression in woven composite structures. *Composite Structures*, 94(3):977 – 986, Feb 2012.

[70] N.V. De Carvalho, S.T. Pinho, and P. Robinson. Numerical modelling of woven composites: Biaxial loading. *Composites Part A: Applied Science and Manufacturing*, 43(8):1326–1337, 2012.

[71] S. Jacques, I. De Baere, and W. Van Paepegem. Application of periodic boundary conditions on multiple part finite element meshes for the meso-scale homogenization of textile fabric composites. *Composites Science and Technology*, 92(Supplement C):41 – 54, 2014.

[72] Chao Zhang, Wieslaw K. Binienda, Robert K. Goldberg, and Lee W. Kohlman. Meso-scale failure modeling of single layer triaxial braided composite using finite element method. *Composites Part A: Applied Science and Manufacturing*, 58:36 – 46, Mar 2014.

[73] Dassault Systèmes Simulia Corp., Providence, RI, USA. *Abaqus Documentation*, 2014.

[74] Xiaodong Tang, John D. Whitcomb, Ajit D. Kelkar, and Jitendra Tate. Progressive failure analysis of 2x2 braided composites exhibiting multiscale heterogeneity. *Composites Science and Technology*, 66(14):2580–2590, Nov 2006.

[75] Zdeněk P. Bažant and B. H. Oh. Crack band theory for fracture of concrete. *Matériaux et Construction*, 16(3):155–177, May 1983.

[76] Philippe Boisse, Alain Gasser, Benjamin Hagege, and Jean-Louis Billoet. Analysis of the mechanical behavior of woven fibrous material using virtual tests at the unit cell level. *Journal of Materials Science*, 40(22):5955–5962,

Nov 2005.

[77] P. Badel, E. Vidal-Sallé, E. Maire, and P. Boisse. Simulation and tomography analysis of textile composite reinforcement deformation at the mesoscopic scale. *Composites Science and Technology*, 68(12):2433–2440, sep 2008.

[78] A. Doitrand, C. Fagiano, V. Chiaruttini, F.H. Leroy, A. Mavel, and M. Hirsekorn. Experimental characterization and numerical modeling of damage at the mesoscopic scale of woven polymer matrix composites under quasi-static tensile loading. *Composites Science and Technology*, 119:1–11, Nov 2015.

[79] Tobias Wehrkamp-Richter, Roland Hinterhölzl, and Silvestre T Pinho. Damage and failure of triaxial braided composites under multi-axial stress states. *Composites Science and Technology*, 150:32–44, 2017.

[80] Johannes Weissenböck, Arindam Bhattacharya, Bernhard Plank, Christoph Heinzl, and Johann Kastner. Visual classification of braided and woven fiber bundles in x-ray computed tomography scanned carbon fiber reinforced polymer specimens. *Case Studies in Nondestructive Testing and Evaluation*, May 2016.

[81] Dmitry S. Ivanov, Stepan V. Lomov, Sergey G. Ivanov, and Ignaas Verpoest. Stress distribution in outer and inner plies of textile laminates and novel boundary conditions for unit cell analysis. *Composites Part A: Applied Science and Manufacturing*, 41(4):571–580, Apr 2010.

[82] AurÃ©lien Doitrand, Christian Fagiano, FranÃ§ois-Henri Leroy, Anne Mavel, and Martin Hirsekorn. On the influence of fabric layer shifts on the strain distributions in a multi-layer woven composite. *Composite Structures*, 145:15–25, Jun 2016.

[83] B. Gommers, I. Verpoest, and P. Van Houtte. The mori–tanaka method applied to textile composite materials. *Acta Materialia*, 46(6):2223 – 2235, 1998.

[84] E. Obert, F. Daghia, P. Ladeveze, and L. Ballere. Micro and meso modeling of woven composites: Transverse cracking kinetics and homogenization. *Composite Structures*, 117:212 – 221, Nov 2014.

[85] S.-Y. Hsu and R.-B. Cheng. Modeling geometry and progressive interfacial damage in textile composites. *Journal of Composite Materials*, 47(11):1343–1356, Jun 2012.

[86] AS Kaddour and MJ Hinton. Maturity of 3D failure criteria for fibre-reinforced composites: Comparison between theories and experiments: Part B of WWFE-II. *Journal of Composite Materials*, 47(6-7):925 – 966, 2013.

[87] Alexander E. Bogdanovich, Mehmet Karahan, Stepan V. Lomov, and Ignaas Verpoest. Quasi-static tensile behavior and damage of carbon/epoxy composite reinforced with 3D non-crimp orthogonal woven fabric. *Mechanics of Materials*, 62:14 – 31, 2013.

[88] Jean Lemaitre and Jean-Louis Chaboche. *Mechanics of solid materials*. Cambridge University Press (CUP), 1990.

[89] Milan Jirasek and Marco Bauer. Numerical aspects of the crack band approach. *Computers & Structures*, 110-111:60 – 78, Nov 2012.

[90] S.T. Pinho, L. Iannucci, and P. Robinson. Physically based failure models and criteria for laminated fibre-reinforced composites with emphasis on fibre kinking. Part II: FE implementation. *Composites Part A: Applied Science and Manufacturing*, 37(5):766 – 777, May 2006.

[91] Cheryl A. Rose, Carlos G. Davila, and Frank A. Leone. Analysis methods for progressive damage of composite structures. Technical Report NASA/TM–2013-218024, NASA Langley Research Center, Hampton, Virginia, 2013.

[92] R. Gutkin, M.L. Laffan, S.T. Pinho, P. Robinson, and P.T. Curtis. Modelling the R-curve effect and its specimen-dependence. *International Journal of Solids and Structures*, 48(11-12):1767 – 1777, Jun 2011.

[93] Joakim Schön. Coefficient of friction of composite delamination surfaces. *Wear*, 237(1):77 – 89, Jan 2000.

[94] X. P. Morelle, J. Chevalier, C. Bailly, T. Pardoen, and F. Lani. Mechanical characterization and modeling of the deformation and failure of the highly crosslinked RTM6 epoxy resin. *Mechanics of Time-Dependent Materials*, pages 1 – 36, 2017.

[95] A.R. Melro, P.P. Camanho, F.M. Andrade Pires, and S.T. Pinho. Micromechanical analysis of polymer composites reinforced by unidirectional fibres: Part i - constitutive modelling. *International Journal of Solids and Structures*, 50(11):1897 – 1905, 2013.

[96] L. Gigliotti and S.T. Pinho. Exploiting symmetries in solid-to-shell homogenization, with application to periodic pin-reinforced sandwich structures. *Composite Structures*, 132(Supplement C):995 – 1005, 2015.

B Publications

Peer-reviewed journal publications

[J1] T. Wehrkamp-Richter, R. Hinterhölzl, and S.T. Pinho. Damage and failure of triaxial braided composites under multi-axial stress states. *Composites Science and Technology*, 150 : 32 – 44, Sep 2017.

[J2] T. Wehrkamp-Richter, N.V. De Carvalho, and S.T. Pinho. A meso-scale framework for predicting the mechanical response of triaxial braided composites. *Composites Part A: Applied Science and Manufacturing*, 107 : 489−506, 2018.

[J3] T. Wehrkamp-Richter, N.V. De Carvalho, and S.T. Pinho. Predicting the non-linear mechanical response of triaxial braided composites. *Composites Part A: Applied Science and Manufacturing*, 114 : 117 – 135, 2018.

[J4] J. Cichosz, T. Wehrkamp-Richter, H. Körber, R. Hinterhölzl, and P.P. Camanho. Failure and damage characterization of (30°) biaxial braided composites under multiaxial stress states. *Composites Part A: Applied Science and Manufacturing*, 90 : 748 – 759, Nov 2016.

Conference publications

[C1] T. Wehrkamp-Richter, R. Hinterhölzl, and S.T. Pinho. Failure behaviour of triaxial braided composites. 17^{th} *European Conference on Composite Materials (ECCM-17)*, Munich, Germany, Jun 2016.

[C2] T. Wehrkamp-Richter, R. Hinterhölzl, and S.T. Pinho. Modelling the non-linear mechancial behaviour of triaxial braided composites. 20^{th} *International Conference on Composite Materials (ICCM-20)*, Copenhagen, Denmark, Jul 2015.

[C3] T. Wehrkamp-Richter, R. Hinterhölzl, and S.T. Pinho. On the numerical modelling of triaxial braided composites. 12^{th} *International Conference on Textile Composites (Texcomp-12)*, Raleigh, USA, May 2015.

[C4] T. Wehrkamp-Richter, J. Cichosz, R. Hinterhölzl, and K. Drechsler. Modeling strategies for triaxial braided carbon/epoxy composites. *International Symposium on Green Manufacturing and Applications (ISGMA 2013)*, Honolulu, USA, Jun 2013.

[C5] T. Wehrkamp-Richter, M. Humbs, D. Schultheiss, and R. Hinterhölzl. Damage characterization of triaxial braided composites under tension using full-field strain measurement. 19^{th} *International Conference on Composite Materials (ICCM-19)*, Montreal, Canada, Jul 2013.

[C6] T. Wehrkamp-Richter, and S.T. Pinho. On the Numerical Modelling of Triaxial Braided Composites, *Imperial College London Research Colloquium*, 2015.

[C7] T. Wehrkamp-Richter, M. Brand, P. Bockelmann, W. Ki, and R. Hinterhölzl. Design and Analysis of a Carbon Fibre Braided Stabilizer Bar. *The* 63^{rd} *World Congress on Carbon (Carbon2014)*, Jeju, Korea, Jun 2014.

[C8] T. Hogger, P. Winkler, and T. Wehrkamp-Richter. MAI Skelett/Multiskelett: A novel design philosophy based on truss elements . 17^{th} *European Conference on Composite Materials (ECCM-17)*, Munich, Germany, Jun 2016.

[C9] J. Cichosz, T. Wehrkamp-Richter, and R. Hinterhölzl. Material modeling of 2x2 braided composites using a beam approach. 15^{th} *European Conference on Composite Materials (ECCM-15)*, Venice, Italy, Jun 2012.

Invited seminar presentations

[T1] T. Wehrkamp-Richter, and S.T. Pinho. Festigkeitsvorhersage von Triaxialgeflechten. *Carbon Composites e.V. AG Engineering Symposium*, Augsburg, Germany, Nov 2016.

[T2] T. Wehrkamp-Richter, N.V. De Carvalho, S.T. Pinho, and R. Hinterhölzl. The Mechanical Response of Triaxial Braided Composites - Experiments and Modelling. *Seminar at NASA Langley Research Center*, Hampton, USA, May 2015.

[T3] T. Wehrkamp-Richter, S.T. Pinho, and R. Hinterhölzl. Numerical Modelling of the Mechanical Response of Triaxial Braided Composites. *Symposium on the occasion of the* 5^{th} *anniversary of the Institute for Carbon Composites*, Munich, Germany, Sep 2014.

[T4] T. Wehrkamp-Richter, J. Cichosz, and R. Hinterhölzl. Materialmodellierung von geflochtenen Verbundwerkstoffen: Forschungs- und Ingenieursansätze. *Carbon Composites e.V. AG Engineering Symposium*, Augsburg, Germany, Feb 2013.

Patents

[P1] T. Hogger, O. Konrad, P. Winkler, F. Koschnick, R. Blank, T. Wehrkamp-Richter and R. Hinterhölzl. Faserbauteil mit verbundenen Faserstäben, Patentanmeldung 102016111468.5.

C Supervised student thesis

During my employment at the Institute for Carbon Composites - Lehrstuhl für Carbon Composites - I supervised the following student theses:

[S1] P. Juretzko. Berechnung von Carbonfasergeflechten mit klassischer Laminattheorie. *Semester thesis, Lehrstuhl für Carbon Composites, TUM*, Mar 2013.

[S2] M. Humbs. Versagensverhalten von triaxialen Carbonfasergeflechten. *Semester thesis, Lehrstuhl für Carbon Composites, TUM*, Jan 2014.

[S3] F. Wilke. Simulation von UD-Materialverhalten an Einheitszellen mit stochastischer Faserverteilung. *Diploma thesis in cooperation with the Munich University of Applied Sciences, Lehrstuhl für Carbon Composites, TUM*, Mar 2014.

[S4] F. Zeller. Mechanische Charakerisierung von unidirektionalem kohlenstofffaserverstärktem Kunststoff. *Semester thesis, Lehrstuhl für Carbon Composites, TUM*, Jun 2014.

[S5] J. Stocker. Auslegung eines geflochtenen Fahrzeugstabilisators aus CFK. *Semester thesis, Lehrstuhl für Carbon Composites, TUM*, Jul 2014.

[S6] J. Achleitner. Struktursimulation von geflochtenen Faserverbundbauteilen unter Berücksichtigung von Fertigungseinflüssen. *Diploma thesis, Lehrstuhl für Carbon Composites, TUM*, Sep 2014.

[S7] A. Mundt. Entwicklung einer Matlab Routine zur geometrisch analytischen Flechtsimulation für die Faserverbundtechnologie. *Semester thesis, Lehrstuhl für Carbon Composites, TUM*, Jan 2015.

[S8] T. Hinterbrandner. FE Einheitszellenberechnung von Triaxialgeflechten auf Basis von Computertomografie. *Master thesis, Lehrstuhl für Carbon Composites, TUM*, Feb 2016.

[S9] P. Vollmer. Automatisierte Berechnung der effektiven elastischen Materialeigenschaften von Geweben auf Basis von FE Einheitszellen. *Semester thesis, Lehrstuhl für Carbon Composites, TUM*, Jul 2017.

[S10] E. Helfrich. Numerische Festigkeitsvorhersage von Triaxialgeflechten mithilfe von Netzsuperpositionsverfahren. *Semester thesis, Lehrstuhl für Carbon Composites, TUM*, Sep 2016.

Parts of the following theses contributed to the underlying doctoral thesis: [S2], [S8]